Theory of charge-spin conversion phenomena in two-dimensional electronic systems: from graphene heterostructures to Rashba-coupled interfaces

Alessandro Veneri

PhD

Physics, Engineering and Technology
University of York
March 2023

Abstract

Using the electron's spin in addition to its charge represents a promising avenue for future solid-state devices. The potential of this field of research, called spintronics, has been propelled by the advent of graphene and related atomically-thin materials, which have enabled unprecedented electric control over spin dynamics and spin-charge conversion effects in layer-by-layer systems.

This thesis aims to contribute towards a broader understanding of spin-dependent phenomena in two spintronic platforms of much current interest; honeycomb layers and interfaces hosting two-dimensional electron gases and topologically protected states. These systems are characterized by rich symmetry-breaking spin-orbit coupling effects, which render theoretical descriptions of electronic structure and spin transport highly nontrivial. Therefore, this work aims to develop a unified microscopic treatment that captures, on equal footing, disorder-limited spin dynamics and disorder-enhanced spin-charge conversion effects, two complementary phenomena at the heart of modern spintronics.

On the first front, we put forward a diagrammatic method that allows the derivation of space and time-dependent kinetic equations for generic 2D electronic systems. Applied to adatom-decorated graphene, it uncovers the interband spin-orbit scattering at the origin of sizable current-induced spin currents. Secondly, we study the possibility of acquiring twist-angle control over spin-charge conversion effects in novel graphene-based heterostructures, where a rotation angle between adjacent layers strongly modifies the spin texture of electronic bands, thus opening the possibility of realizing unconventional spin galvanic effects. Our formulation is also applied to studying spin-orbit torques in ferromagnet bilayers. We find that skew scattering from ubiquitous short-range impurities can produce significant damping-like torques, allowing for all-electrical magnetization switching of a nearby micromagnet.

Our work highlights the crucial role played by electronic structure modifications at interfaces in the generation of spin-dependent forces experienced by transport electrons and the necessity for an adequate treatment of impurity scattering for describing the behaviour of realistic spintronic materials.

Contents

List of Figures

Chapter 1

Acknowledgements

With no doubts, these PhD years have been the best of my life, having squeezed out everything they had to offer me. This period has given me terrific experiences, maybe painful at times, beautiful friendships, and has made me grow as a person. All of this, as is obvious, is made possible by the people I have met along the way and whom I, therefore, want to thank here.

First, my supervisor Aires, an exceptional physicist who offered me the means to be an independent professional in research and work. He always accompanied me with judgment, friendship, and kindness in my academic journey. Then, my "collaborators", even though this is a restrictive term to refer to beautiful friendships. Firstly, Frederico, one of my best friends and to whom I will be tied for the rest of my life. He was my mentor during the first years of my PhD, and I owe him much of my technical knowledge and the introduction to the "practical" world of research. But, above all, I owe him the beautiful moments we spent together. Secondly, David, with whom I wrote my first articles and worked with excitement on the same research topics. Our adventures in Chicago will permanently be engraved in my heart.

I now want to thank my closest friends, Alessietto, Alessio, and Riccardo. Contradicting my greatest fear in coming to England, our bond of love has further strengthened, and its solidity has always brightened my moments of solitude. The same goes for my family, who has always supported and accompanied me. So my dad, which introduced me to the scientific world, and my mom, whom I always asked for advice. I thank the best friendships that enlightened end enriched my life in these years, so Giulia (mannaggia a te), Francisco (I shared everything with you, my friend), Ornellina, Amy, Will and Ari (how have I been so lucky to have a second family?), Guilherme, Megan, and Santiago. I thank my second home, York, and everyone I drank coffee with, I chatted in the office or in corridors, played tennis, and worked with.

My deepest gratitude goes to Camilla, who always believed in me and pushed me with all her energy into this experience and to whom I owe everything.

Lastly, to my Giada, she gave me the strength to go through the last hardships of this journey and start walking a new path in my life.

These words of gratitude will never fully express the joy of having these people and

memories in my life, not just because of my incompetence in putting my thoughts into writing, for which I apologize, but because words won't ever express the full range of emotions that you have made me feel over these years.

1.1 Declaration

I, the author, confirm that this thesis is entirely my own original work and has not been presented for an award at any university. All sources used in this thesis are properly cited in the References section. Some of the material in this thesis has been adapted from articles published in the following scientific journals: Chapter 5 and 6 describe two collaborative works

- *Nonperturbative approach to interfacial spin-orbit torques induced by the Rashba effect*, Alessandro Veneri, David T. S. Perkins, and Aires Ferreira Phys. Rev. B 106, 235419
- *Twist angle controlled collinear Edelstein effect in van der Waals heterostructures*, Alessandro Veneri, David T. S. Perkins, Csaba G. Péterfalvi, and Aires Ferreira Phys. Rev. B 106, L081406.

I declare that I was the main contributor to the formulation of the research, including the calculations and interpretation of the results presented in the mentioned papers, being also the author of the first draft of the papers.

Chapter 2

Introduction

2.1 Spintronics

The study of materials guided by the principles of quantum mechanics, known as solid-state physics, is an ever-evolving field fueled by a constant discovery of new condensed-matter phenomena. An example of such materials are semiconductors, which nowadays play a central role in electronics and, therefore, modern technology. In the late 20^{th} century, an exciting sub-field of solid-state physics was born, inspired by the possibility of storing and manipulating information encoded in the electron spin. This modern area of research – dubbed spintronics – has already revolutionised random access memory (RAM) proposing devices with zero standby power dissipation, denser bit-cell, and better reading/writing performances [1, 2], and is poised to make its most significant leap yet. The overarching aim of spintronics is two-fold. The first is to establish a consistent theoretical framework that encompasses the study of i) magnetic structure and spin excitations, ii) the coupling of spin to other degrees of freedom (DOFs), and iii) the microscopic mechanisms underlying spin transport. The second goal is to realise these ideas in practical applications, such as information processing and data storage, where spintronics seeks to improve the capabilities of mainstream silicon-based electronics using new-generation devices [3].

Early research in spintronics had its focus on on the strong exchange interaction between conduction electron spins and magnetic moments of a ferromagnetic layer (FM), leading to the discovery of the giant magneto-resistance effect (GMR) in 1989 [4] and underpinning the development of spin-valve sensors, hard disk drives, and magnetoresistive RAM (MRAM). Recently, relativistic spin-orbit coupling (SOC) has attracted a great deal of attention from the community as it provides means to control the spin DOF by pure electrical means. The various manifestations of SOC – intrinsic SOC, random SOC induced by impurities, and symmetry-breaking SOC on surfaces and interfaces – were shown to play a significant role in many spin-dependent phenomena, including spin relaxation, [5, 6, 7, 8], current-induced spin-polarization (CISP) [9, 10, 11, 12], and current-induced spin-current (CISC) [13, 7, 14, 15].

An important task in this emergent field of research is to develop unified microscopic descriptions that account for the rich phenomenology displayed by spintronic

materials. For example, charge-spin interconversion effects have been traced back to a subtle interplay between band topology and spin-orbit scattering mechanisms. These manifestations of SOC are broadly classified as *intrinsic* and *extrinsic* depending on the specific role of disorder. Intrinsic effects arise from the relativistic electronic structure of the material investigated, where the impact of disorder is secondary. For instance, the resulting effective spin-orbit fields experienced by the electrons may be topological in nature, translating into a non-trivial Berry phase that affects the quasiclassical equation of motion and leads to purely-intrinsic spin currents, i.e., the intrinsic spin Hall effect [16]. We also include the Edelstein effect (EE) [17], in which an applied electric current generates a perpendicular spin polarization due to the entanglement of spin and orbital DOFs, courtesy of the symmetry-breaking Rashba interaction.

Extrinsic mechanisms, on the other hand, result from spin-dependent scattering of the electrons by randomly distributed impurities. For instance, spin-orbit-active scatterers can mediate the emergence of spin-polarized current and net spin polarization. In fact, upon interaction with the SOC-active impurities, wave packets are preferably deviated asymmetrically by an impurity, depending on the relative sign between their spin and angular momentum. This mechanism is called skew-scattering [18] and is responsible for the appearance of the extrinsic spin Hall effect (SHE) [19], consisting of the generation of a transverse spin-current by application of charge current, as well as more exotic variants of the EE effect, discovered in recent works [20].

Spin-charge dynamics is also addressed by current research, aiming to understand better the evolution of spin-related phenomena over time and space. Great importance is attributed to spin-relaxation, i.e., the disappearance of initial non-equilibrium spin accumulation, being ubiquitous in realistic media and crucial in experiments. This effect also relies entirely on the interplay between scattering processes and SOC [21].

In recent years, the focus of spin-orbitronics has been shifting from semiconductor heterostructures, quantum wells [22, 23, 24], and traditional metallic spintronic systems [25, 26] to recently discovered materials with exotic electronic properties. Examples are surfaces of 3D topological insulators (3D-TIs), graphene-based heterostructures, and graphene decorated with adatoms — all 2D systems with unconventional Dirac-like low-energy excitations that have attracted great interest due to their distinct potential to realize strong and gate-tunable SOC transport phenomena [27, 28, 29, 30, 31, 32, 33, 34].

This shift towards new materials has motivated some interesting methodology developments. A simple but relevant example is graphene. The vanishingly small density of states associated with its pristine band structure can be easily shown to favour strong (resonant) skew scattering contributions to the CISC, which in turn requires the use of linear-response frameworks that go beyond commonly employed ladder (Born) approximations. One of these frameworks is a SO(5) quantum diagrammatic technique, treating the low-energy band structure in an exact fashion and single-scattering events at all orders in the impurity potential. It has provided great insight into the physics of skew scattering, the validity of semiclassical treatments of coupled spin-charge transport, and the breakdown of perturbative approaches to studies of quantum contributions to CISC [31, 19, 35]. This SO(5) nonperturbative approach, treating sublattice and spin DOF on equal footing, has been subsequently extended to the study of rich transport phenom-

ena caused by the interplay of Rashba interaction, spin-valley coupling and magnetic proximity effects [36, 37, 8]. Extensions of the widely-used Boltzmann equation have also been instrumental in discovering and comprehending novel quantum effects, such as the anisotropic-spin precession mechanism (ASP), stemming from different components of a spin-dependent scattering potential and generating sizable CISP [38].

In this thesis, we will revise and extend these techniques, aiming to uncover new effects in systems of interest in spintronics. In particular, we develop a novel method, based on the diagrammatic treatment of the Kubo-Streda formula, to derive the complete set of spin and charge drift-diffusion and continuity-like equations non-perturbatively in the impurity potential for single-scattering events. We dub this technique *Diffuson Hamiltonian method*. The employment of this novel approach in studying graphene monolayers with random sources of local spin-orbit fields, will allow us to uncover the *interband spin-orbit scattering mechanism*, yielding to sizable current-induced spin-current which can overshadow the traditional skew scattering contribution. Our interest in charge-spin conversion mechanisms in graphene extends to the study of bilayer systems where graphene is placed atop a substrate. These systems are critical in spintronics due to the enhancement of uniform proximity effects. Specifically, we discover that twisted graphene-based Van der Waals (vdW) heterostructures support highly anisotropic spin-density-current responses enabling full control over the in-plane orientation of non-equilibrium electron spin. The last findings of our projects concern the physics of the spin-orbit torque, one of the most promising mechanisms for applications that exploits charge-to-spin conversions. We find that CISP induced at the interface of ferromagnetic bilayer systems produces a torque that allows magnetization switching, paving the way toward new generation RAMs.

2.2 Spin-orbit phenomena in solids

2.2.1 Spin-orbit interaction in solids

SOC is the driving force of coupled spin-charge transport, also being a key factor in spin relaxation. An intuitive interpretation of this interaction is provided by electrodynamics, where the origin of the SOC is traced back to the relativistic transformation of electromagnetic fields. This effect produces corrections to the electrons' energy levels of atomic spectra [39], band structures in solids (intrinsic and structure-induced SOC) [40, 41], and influences the electrons' interaction with impurities (extrinsic random SOC) [31, 38]. According to special relativity, the effective magnetic field that an electron orbiting a nucleus perceive in its rest frame is

$$\mathbf{B}_{\mathrm{SO}} = -\frac{\mathbf{v} \times \mathbf{E}}{c^2}, \tag{2.1}$$

where $\mathbf{E}$ is the electric field in the rest frame of the nucleus, $\mathbf{v}$ is the electron velocity, c is the speed of light, and we used $|\mathbf{v}| \ll c$ to approximate the Lorentz factor by unity. The existence of the particles' intrinsic magnetic moment, related to their spin, generates an interaction that enters the Hamiltonian as

$$H_{\mathrm{SOC}} = -\boldsymbol{\mu}_s \cdot \mathbf{B}_{\mathrm{SO}}, \tag{2.2}$$

where $\boldsymbol{\mu}_s = -(g_e/2m_e)\mathbf{S}$ is the electrons' magnetic moment and $\mathbf{S} = (\hbar/2)\mathbf{s}$ is the spin operator, with $\mathbf{s} = (s_x, s_y, s_z)$ the vector of Pauli matrices. The constants in Eq.(2.2) are the gyromagnetic factor of a free electron $g_e \simeq 2$, and the electron mass $m_e = 9.11 \times 10^{-31}\,\mathrm{kg}$. A subtle, but crucial, correction to Eq.(2.2) is offered by the Thomas precession, which is a relativistic modification to the angular velocity experienced by the electron in its rest frame [42]. It results in a new term in the Hamiltonian $\sim -\mathbf{S} \cdot \omega_T$, where $\omega_T = \mathbf{v} \times \mathbf{a}/2c^2$ is the Thomas angular frequency, and $\mathbf{a}$ is the centripetal acceleration.

Both relativistic corrections to the hydrogen atom and the effects of impurities can be described by a radial electric field $\mathbf{E} = -\partial_r V(r)\mathbf{r}/er$, where $V(r)$ is the electrostatic energy of the electron in the central field and $e = 1.6 \times 10^{-19}\,\mathrm{C}$ is the elementary charge. We also notice that the effective spin-orbit field can be cast as $\mathbf{B}_{\mathrm{SO}} \sim \mathbf{r} \times \mathbf{p} = \mathbf{L}$, where $\mathbf{p} = m_e\mathbf{v}$ is the electrons' momentum and $\mathbf{L}$ is the orbital angular momentum. Putting all the pieces together, the interaction Hamiltonian finally becomes

$$H^{\mathrm{rad}}_{\mathrm{SOC}} = -\frac{g_e}{4\,e\,m_e^2\,c^2}\,\frac{\partial_r V(r)}{r}\,\mathbf{L} \cdot \mathbf{S}, \tag{2.3}$$

where we used that $\mathbf{a} = e\mathbf{E}/m_e$. This simple equation already hints at the consequences of including the SOC interaction in crystalline solids.

Semiconductors with a zinc blende structure, such as GaAs, InSb, and CdTe, provide excellent examples since their dispersion relation can be (relatively) easily interfaced with the atomic interactions in the material via the extended Kane model [43, 44]. This theoretical framework shows that the valence band originates from bonding p-like states (orbital angular momentum $l = 1$) and the conduction band from antibonding s-like ($l = 0$) and p-like states. With the SOC taken into account, the spin and the orbital angular momenta are no longer good quantum numbers and the total angular momentum $\mathbf{J} = \mathbf{S} + \mathbf{L}$ must be introduced to diagonalize Eq.(2.3). One finds electronic states with $j = 1/2, 3/2$, which are split in energy and strongly modify the band structure by inducing significant band gaps (Fig.(2.1)).

Another example is pristine graphene, where the projection of Eq.(2.3) onto the manifold of π-orbital states yields an intrinsic spin-orbit interaction commonly referred to as Kane-Mele SOC [41, 45]. In this scenario, the spin of an electron initially in the p_z state at site A is flipped due to the intraatomic spin-orbit interaction. As a result, it transitions to a σ state at the same site. This electron then hops to an intermediate site B, facilitated by the spin-conserving σ bond in the system. Finally, at site B, the electron undergoes a second spin-flip transition, leading to its arrival at site C, which is the next-nearest neighbour to A. At this point, the electron is back in the p_z state with its original spin orientation intact [46]. The Kane-Mele interaction opens a small gap at graphene's Dirac points, rendering graphene a quantum spin Hall insulator [47].

In more exotic materials, the contribution of the SOC to the system's electronic band structure determines new quantum states of matter. For instance, in the family of Y_3XC solids [48] the choice of the X element (Ga, Tl) determines a TI or a Dirac

semi-metal phase, while in Sb_2Te_3, Bi_2Te_3, and Bi_2Se_3 the presence of a strong SOC establishes topological insulator features [49].

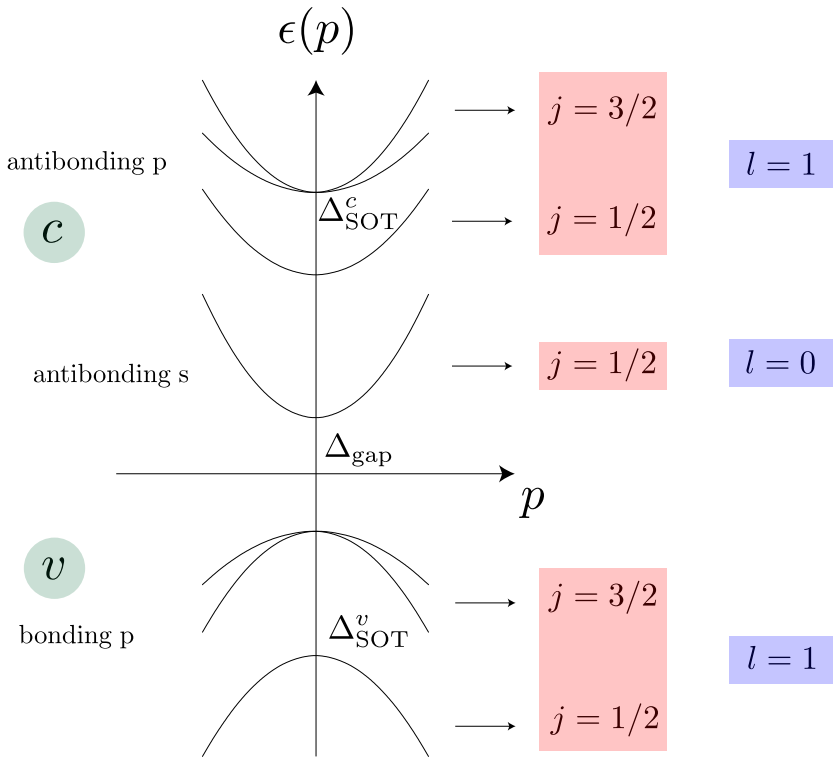

Figure 2.1: Qualitative sketch of the electronic structure of a sp_3-bonded semiconductor around the Γ point derived from the extended Kane model. The fundamental gap at $p = 0$ distinguishing bonding and antibonding states is Δ_{gap}, while $\Delta^{c\,(v)}_{\mathrm{SOT}}$ is the conduction "c" (valence "v") gap induced by SOC. Further splittings for $p \neq 0$ are still due to the SOC, and define heavy and light quasiparticles [21].

The intuitive picture of the SOC provided by Eq.(2.3) can be complemented by analysing the possible system's symmetries, either naturally present in the crystalline structure or specifically engineered. Broken symmetries are important because they can induce splittings in the spin DOF. To see that, we consider two essential symmetries in quantum mechanics; time-reversal T and inversion-symmetry I. If both are present, the system's energy bands $\epsilon_{n,s}(\mathbf{p})$, with n and s being the band and spin index $s = \uparrow, \downarrow$, are spin-degenerate:

$$\epsilon_{n,\uparrow(\downarrow)}(\mathbf{p}) \underset{T}{\rightarrow} \epsilon_{n,\downarrow(\uparrow)}(-\mathbf{p}) \underset{I}{\rightarrow} \epsilon_{n,\downarrow(\uparrow)}(\mathbf{p}), \tag{2.4}$$

which implies $\epsilon_{n,\uparrow(\downarrow)}(\mathbf{p}) = \epsilon_{n,\downarrow(\uparrow)}(\mathbf{p})$ and shows explicitly the spin degeneracy in the band structure. The presence of a Zeeman interaction induced by an external magnetic field

also breaks the time-reversal symmetry, leading to spin-split bands. In non-magnetic materials (time-reversal invariant systems), the lack of the inversion symmetry is at the origin of the splitting and is accompanied by the emergence of spin-orbit interactions. Notable examples are the Dresselhaus SOC, present in non-centrosymmetric bulks [50], the Rashba SOC, generated by breaking the mirror reflection symmetry about a plane, and the spin-valley SOC, appearing in honeycomb layers with broken sublattice symmetry (C_{3v} point group), such as group VI dichalcogenides and hexagonal BN [41, 51, 52].

A more realistic picture of the SOC in solids also considers local sources of spin-orbit interactions mediated by impurities, adatoms, and fluctuations in the spin-orbit field (e.g., due to interface roughness) [19, 53, 54]. Such interactions impact the coupled spin-charge dynamics along side with uniform (intrinsic) spin-orbit interactions, as shall be explored in-depth later in this thesis. For instance, magnetic or spin-orbit-active impurities activate a skew scattering mechanism that yields an extrinsic SHE and renormalizes the CISP. Additionally, random Rashba-type interactions also contribute to charge-spin interconversion effects through the ASP mechanism.

The SOC phenomenology heretofore investigated allows us to consider a more general expression for Eq.(2.3), namely

$$H_{\mathrm{SOC}} = \frac{g_e}{4\, e\, m_e^2\, c^2} \left(\boldsymbol{\nabla} V(\mathbf{r}) \times \mathbf{p}\right) \cdot \mathbf{S}, \tag{2.5}$$

where $V(\mathbf{r}) = V_0(\mathbf{r}) + V_{\mathrm{ext}}(\mathbf{r}) + V_{\mathrm{imp}}(\mathbf{r})$ gathers the effect of the periodic crystal potential V_0, the external applied potential V_{ext}, and the extrinsic term V_{imp} generated by quenched disorder in the system. Eq.(2.5) encompasses the SOC on the crystal's electronic band structure, originating from V_0 (intrinsic SOC) or periodic ad-atom insertions $V_{\mathrm{dis}}^{\mathrm{per}}$ (uniform extrinsic SOC), and local effects due to randomly distributed impurities in the sample, described by $V_{\mathrm{dis}}^{\mathrm{ran}}$ (random extrinsic SOC). It also describes symmetry-breaking SOC effects due to surfaces and interfaces.

The coupling between the spin and orbital DOFs will lead to detectable effects whenever Eq.(2.5) is a significant perturbation. It explains, for example, why random sources of SOC can affect the electron's trajectory in a spin-dependent fashion, i.e. skew scattering. A similar net effect occurs through the ASP mechanism, where quantum interference between different components of the scattering potential induces strong spin–momentum correlations. Another well-studied case occurs in systems dominated by spatially uniform symmetry-breaking SOC (also known as structure-induced SOC), where the the Fermi surface displays characteristic **k**-space spin textures. Consequently, the application of electric fields influences the electron's spin, leading to pure spin currents and non-equilibrium spin polarisation that accompany the steady-state electric current. Furthermore, in proximitised graphene systems endowed with well-defined spin-quantization axes around the Dirac points, skew scattering develops efficiently even in the absence of random SOC sources [55].

2.2.2 2D spintronics

The unusual and distinctive properties of low-dimensional solid-state systems garnered a lot of attention due to their technological potential. Here, we include zero-dimension

quantum dots (promising to fabricate single-electron transistors, new generation solar cells [56], etc.), one-dimension *carbon nanotubes* [57] (successfully employed in the medical [58] and tech sector [59]), and, most notably for spintronics applications, *two-dimensional systems*. Amongst them, two-dimensional gases (2DEG) are primarily used in traditional technologies, like MOSFETs and diodes, where electrons can move only in two dimensions of 3D multilayered apparatuses. However, these systems only scratch the surface of the possibilities that two-dimensionality can offer.

For instance, the topological order in bulk solids gives rise to the family of the 3D topological insulators (3D-TI), which behave as nonmagnetic insulators in their interior but possess metallic surface states. As a result, the electrons can flow only at the surface, which can be considered a new form of 2D metal [60, 61]. Interestingly, these systems exhibit an unusually robust coupling between the spin and momentum DOF, resulting in unprecedented spin-charge interconversion effects [62]. TIs are therefore considered excellent candidates for spintronics applications.

Another class of 2D systems are atomically-thin materials, which up until the early 2000s had only been thought as a pure abstraction. Naively, their experimental realisation seems to defy the Mermin-Wagner theorem, which states that long-wavelength fluctuations supress long-range order in one and two spatial dimensions [63]. As such, to many, the isolation of one-atom-thick graphene in 2004 [64] came to a surprise. The assumptions of the famous theorem are circumvented, most trickery, by anharmonic coupling between bending and stretching modes that facilitate rippled membranes living in the 3D space [65]. Beyond graphene, advances in nanofabrication opened the doors to the realization of monolayers starting from virtually any given bulk vdW material [66, 67], like insulators (e.g. hexagonal boron-nitride), semiconductors (e.g. group-VI transition metals dichalcogenides), and metals (e.g. NbS2). The unprecedented properties of these materials span from electrical and optical to structural [68].

In terms of spin-related phenomena, there is no shortage of wonder. Considering the case of graphene, the combination of high electronic mobility and ultra-small intrinsic SOC makes gives way to micrometer-long spin diffusion lengths [69, 70, 71], promising for spin transfer. On the contrary, group-VI TMDs possess strong spin-valley coupling which is exploitable for manipulating the spin degree of freedom of Dirac electrons in graphene/TMD heterostructures [37]. Also, being graphene an open surface, the adatom absorption of certain atomic species is also possible, opening the possibility of controlling graphene's SOC and generating new spin-related phenomena [38].

Before diving into the rich spin-orbit-coupled phenomena hosted by two-dimensional systems, we briefly review the paradigmatic Rashba-coupled 2DEG for illustrative purposes. The Hamiltonian reads as

$$H = p^2/2m + H_{\mathrm{R}}, \tag{2.6}$$

where

$$H_{\mathrm{R}} = \alpha_{\mathrm{R}}(\mathbf{s} \times \mathbf{p}) \cdot \hat{z}, \tag{2.7}$$

is the Rashba SOC (RSOC), α_{R} is the Rashba coupling constant reflecting the strength of the spin-orbit interaction, m is the effective mass of the electrons, and $\mathbf{p} = (p_x, p_y)$. This interaction lifts the spin degeneracy for $p \neq 0$, splitting the dispersion relation

into two subbands $\epsilon_\pm = p^2/2m \pm \alpha_R\, p$ as shown in Fig.(2.2a) [72, 73, 74]. The spin

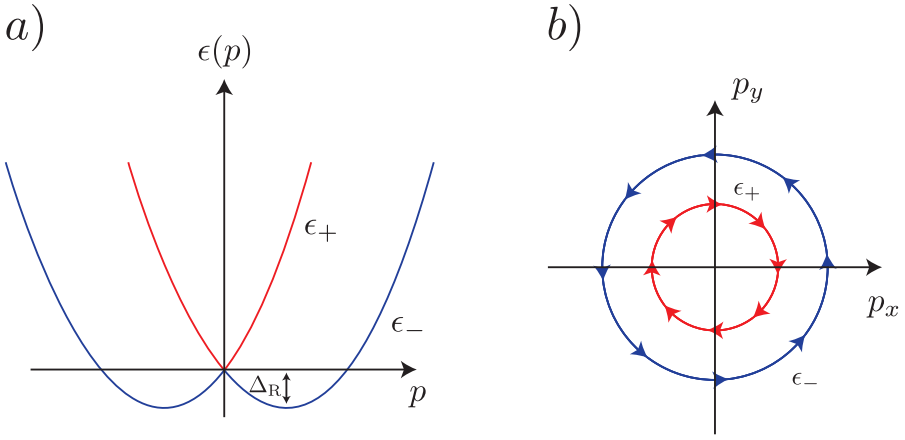

Figure 2.2: Effect of the Rashba spin-orbit interaction on the band structure of 2DEGs. (a) Spin-splitting and dispersion law for $\epsilon_\pm$. The quantity $\Delta_R = m\alpha^2/2\hbar^2$ is the distance between the minima of the two bands. (b) Rashba-induced spin texture for a positive Fermi energy crossing both bands. The arrows mimic the direction of the spin moment, and the tangential winding of the spin texture is a direct consequence of the transverse spin-momentum locking, as described by Eq.(2.8).

polarization associated with each spin-split band can be easily shown to be

$$\langle \mathbf{s} \rangle_{\mathbf{p},\chi} = \langle \mathbf{p}, \chi |\, \mathbf{s}\, | \mathbf{p}, \chi \rangle = \frac{\chi\, \alpha_R}{|\mathbf{p}|} \left(\mathbf{p} \times \hat{z} \right), \tag{2.8}$$

where $\chi = \pm$ corresponds to the upper (lower) band. This equation shows a specific spin-momentum locking in which the spin orientation is always orthogonal to the particle's momentum. Fig.(2.2b) shows a visualization of Eq.(2.8) at the Fermi level, i.e. the *spin texture*, where the momentum is replaced by the Fermi momentum, $\mathbf{p} \to \mathbf{p}_f$.

As discussed later, spin-momentum locking is at the origin of the Edelstein effect [17] and the Dyakonov-Perel spin-relaxation mechanism [7], making RSOC of paramount importance in spintronics. More sophisticated versions of these phenomena can be achieved by coupling the Rashba effect with the skew-scattering, as demonstrated in recent literature [20, 35], or by considering different spin textures (Fig.(2.3)), results of distinct SOC and interactions [75, 38] (see Chaps.(6) and 7)).

2.2.3 The skew-scattering mechanism

Collisions between electrons and randomly distributed impurities induce extrinsic spin-related phenomena that dominate the spin-charge response functions even in the dilute regime, i.e., when $p_f l \gg 1$, with l being the mean free path. Such scattering events are described quantum mechanically by the Lippmann-Swinger equation [78] which finds the final state $|\psi(p, \chi, V)\rangle$ of a diffused incident wave packet $|p, \chi\rangle$ and provides the related scattering cross section

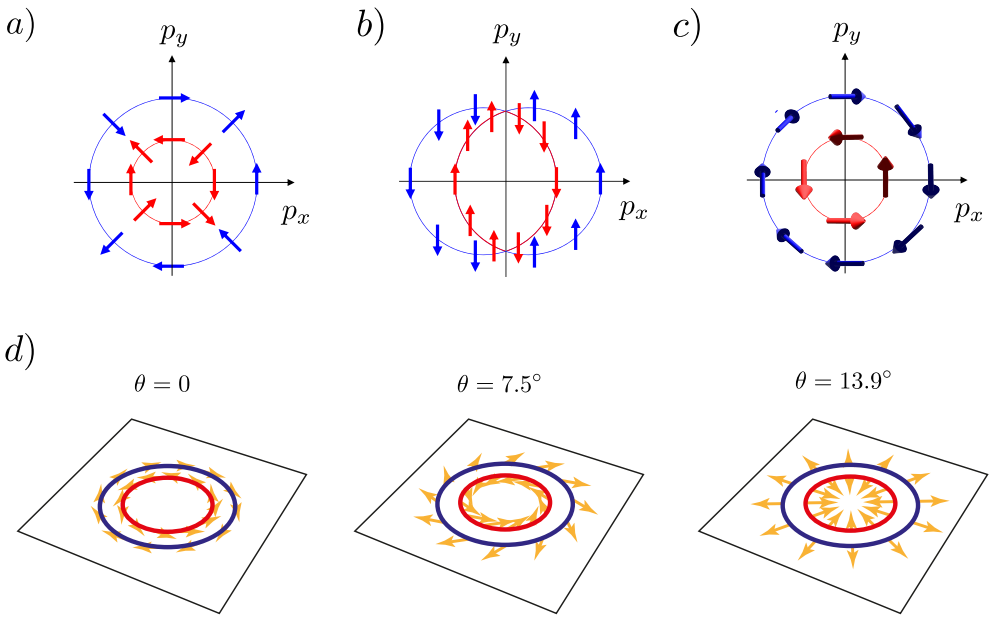

Figure 2.3: Fermi-surface spin textures associated with different symmetry-breaking SOC effects: Dresselhaus (a), persistent (b) [76], Rashba + Zeeman interaction (c) [8] and (d) RSOC in graphene/TMD heterostructures for different twist-angles [77]

.

$$\frac{d\sigma_{\chi\chi'}}{d\Omega} = |f(p'\chi', p\chi)|^2 , \tag{2.9}$$

where $f(p'\chi', p\chi) \sim \langle p', \chi'|V|\psi(p, \chi, V)\rangle$ is the *scattering amplitude* (entering the Fermi Golden Rule). Here, V is the impurity potential and χ, χ' are spin quantum numbers. Equation (2.9) is generally treated perturbatively, and in most literature within the first Born approximation (FBA) [79], where $f(p'\chi', p\chi) \sim \langle p', \chi'|V|p, \chi\rangle$. The inclusion of the SOC, either uniform or random, affects dramatically the scattering amplitudes in both spin-conserving and spin-flip channels [18], see Chap.(4) for further details. An adequate treatment beyond the FBA shows that, in rather general grounds, electrons are preferably deviated from impurities asymmetrically depending on the relative sign between their spin moment and orbital angular momentum. As a result, electron-impurity cross sections become asymmetrical, $\sigma_\chi(\theta) \neq \sigma_\chi(-\theta)$ (Fig.(2.4)).

At the lowest order, skew scattering is captured by retaining the third order in the scattering potential expansion. The effect is not necessarily weak, though, as it can be strongly enhanced in the resonant scattering regime (in which case nonperturbative T-matrix calculations are required [80, 19]).

2.2.4 Current-induced spin polarization

In gyrotropic media, where some components of polar vectors (like electric fields) and components of axial vectors (like spin moments) transform according to the same representation and are, therefore, related, the entanglement between the electrons' spin

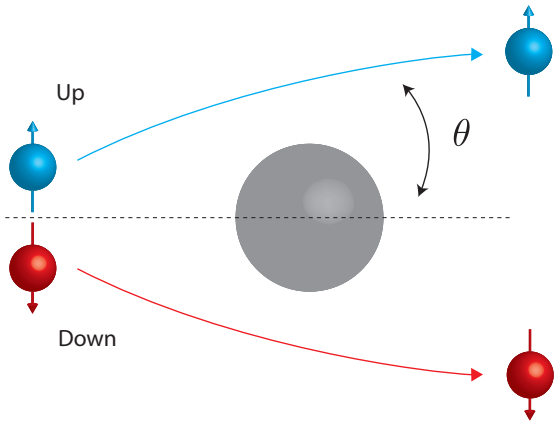

Figure 2.4: Semiclassical skew scattering mechanism. Particles with spin up (in blue) and down (in red) are deviated more likely to the left or right after a scattering event with an impurity (in grey).

and orbital DOFs with broken mirror symmetry, allows the appearance of a *current-induced spin polarization* (CISP), or inverse spin-Galvanic effect, a major focus of this thesis [81]. After experimental evidence of the phenomenon [82, 83], the first theoretical studies in semiconductors [17] explained the results by accounting for the RSOC in the effective quadratic Hamiltonian of two-dimensional systems, expressed by Eq.(2.6). According to this picture, the shifting of the Fermi rings, induced by an applied electric field $\mathbf{E}$, yields an out-of-equilibrium unbalance between spins oriented in opposite directions due to the spin-momentum locking (see Fig.(2.5)). In other words, the acceleration of the electrons in an external electric field generates a net spin polarisation of the electron gas perpendicular to $\mathbf{E}$.

According to linear-response theory, the non-equilibrium spin density is given by

$$\langle S_\mu \rangle = K_{\mu\nu} E_\nu, \tag{2.10}$$

where $\mu, \nu = x, y$ and $\langle ... \rangle$ stands for the statistical average. The conversion is entirely controlled by the 3×2 charge-spin linear-response tensor $\hat{K}$. For a Rashba-coupled 2DEG, only $xy(yx)$ components are nonzero, and $K_{xy} = -K_{yx}$ due to O(2) symmetry.

The CISP has a rich phenomenology. For example, systems with pure Dresselhaus SOC display a collinear Edelstein effect (i.e. $\mathbf{S} \propto \mathbf{E}$) due to their hedgehog spin textures, while more general anisotropic spin responses are achievable in twisted graphene-based heterostructures (see Chap.6). Spin-charge conversion processes are said to be *intrinsic* when they are driven by the $\mathbf{k}$-space spin texture of eigenstates. However, disorder corrections can generate important corrections to "intrinsic" spin responses. For example, skew scattering from scalar impurities in ferromagnetic Rashba-coupled systems activates collinear spin responses ($K_{xx(yy)}$) [20, 84]. As shown in Fig.(2.5c), electrons with opposite spin can be scattered asymmetrically, resulting in an unbalance between p_y and $-p_y$ electrons in the Fermi rings and thus a CISP collinear to the electric current $\langle J_x \rangle$. Finally, purely *extrinsic* CISP can be induced by heavy (spin-orbit-active) impurities even in host materials with low SOC (see Chapter 5).

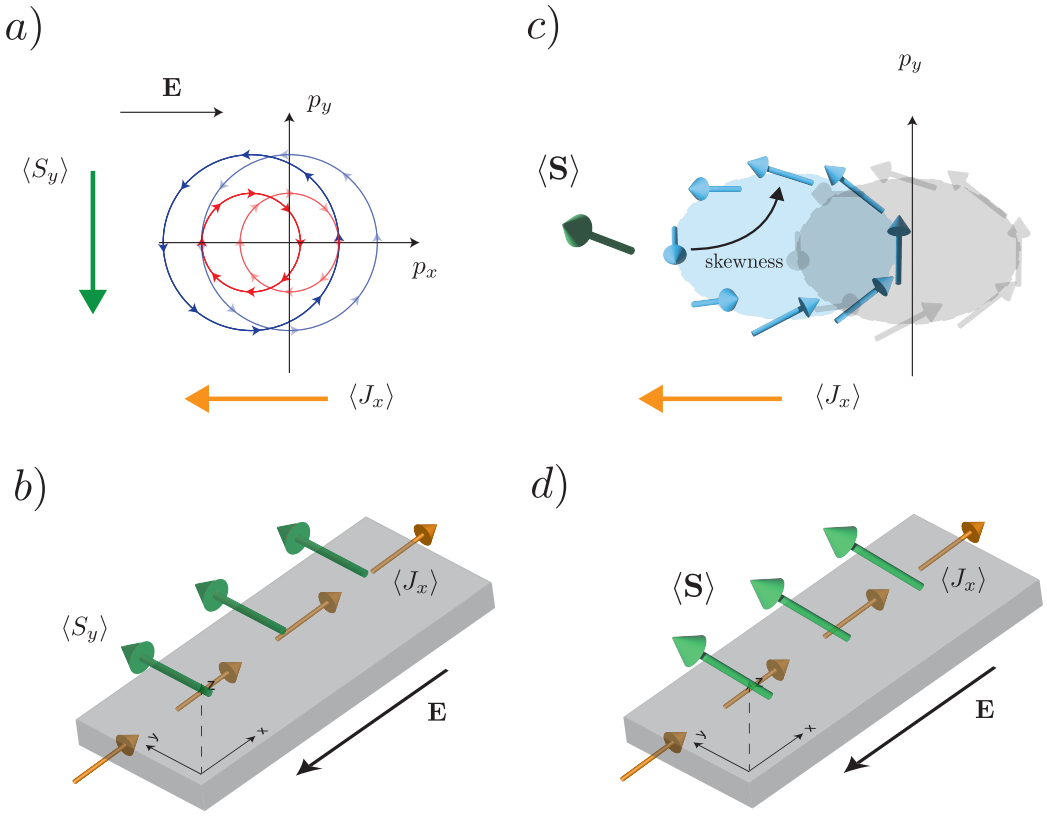

Figure 2.5: CISP driven by Rashba SOC (a-b) and Rashba SOC combined with magnetic exchange coupling (c-d). In momentum space, an applied electric field **E** distorts the Fermi surface (a), establishing an out-of-equilibrium spin accumulation $\langle S_y \rangle$ perpendicular to **E** (Edelstein effect). In (b), we show the real-space picture. In the presence of an out-of-plane component to the spin texture (c), the skew scattering kicks in and leads to an additional accumulation of spin collinear to the applied field–the resulting nonequilibrium spin-density is non-coplanar (d) [20].

The body of theoretical work produced so far [17, 89, 90, 91, 92, 93, 94, 95, 37] has supported experimental advances on several fronts, including spin-injectors, detectors [22, 85], and non-volatile memories [75, 96]. For example, a novel experimental setup, shown in Fig.(2.6), can detect the presence of macroscopic spin accumulations in NiFe/LAO/STO by exploiting the Onsager reciprocal effect of the EE (i.e., inverse-EE, or simply spin-to-charge conversion) [86]. Spin currents are injected via ferromagnetic resonance from the FM (NiFe) and then converted into electric current in a two-dimensional electronic system formed at the LAO interface. The spin-to-charge conversion can be controlled by an applied gate voltage, which modulates the strength of the RSOC.

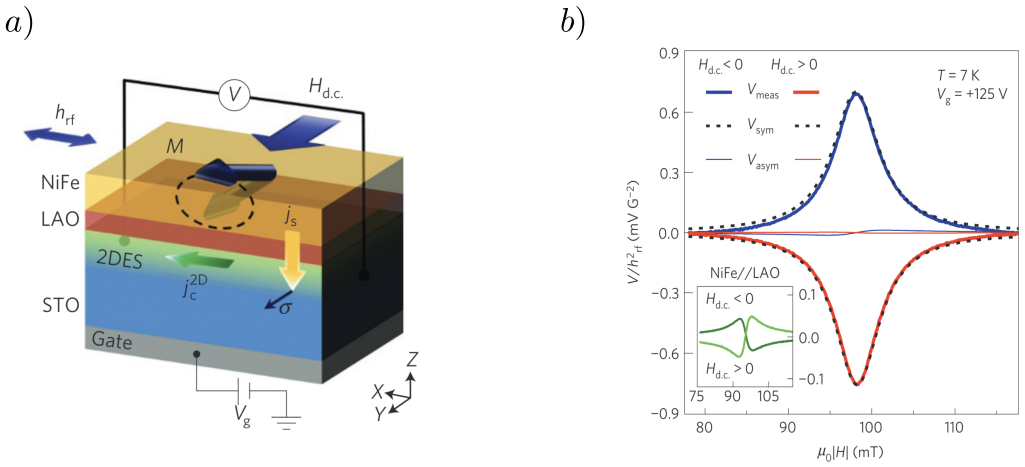

Figure 2.6: Setup (a) and measurement results (b) for detection and characterization of spin-to-charge conversions via ferromagnetic resonance in NiFe/LAO/STO samples [85] (see also [86, 87, 88]). A spin-accumulation is produced in the two-dimensional electron system. along with a spin-current j_s, pumped in from a ferromagnet (NiFe). These two effects are measured via inverse-SHE (ISHE) and inverse-EE (IEE) by detecting the electric voltage V as a function of the applied magnetic field $H_{d.c.}$. The asymmetric component results mainly from ISHE, while the symmetric part comes from IEE.

2.2.5 Spin relaxation

Spin-relaxation, i.e., the disappearance of an initial non-equilibrium spin accumulation over time, is another interesting aspect when considering the ramifications of SOC. It results from fluctuating effective magnetic fields experienced by charge carriers, which receive important contributions from uniform and random spin-orbit interactions [21].

The control over spin relaxation mechanisms is crucial for applications because it ultimately sets the spin-transfer capabilities of a spintronic device. For example, graphene allows spin transmission over micrometer lengths [97, 98, 99, 100, 101], making it an ideal spin channel [102, 103, 104], and high-fidelity spin propagation is crucial to develop spin-logic devices, like spin field-effect transistors [105, 106, 107]. Such apparatuses have the same general structure of modern MOSFETs, i.e. a source and drain contacts, a gate designed for electrical control of the signal, and a transport channel. The information is carried by a spin current, injected into the system from the ferromagnetic source, then travelling along the channel, where the electrons are subject to a gate-tunable spin-orbit interaction. Large SOC induced by the gate potential favours rotations of spins of electrons allowing for the electrical control of the information. The presence of spin-relaxation mechanisms is therefore detrimental, limiting the range of operation of such devices randomizing the electrons spin [108].

The effective fluctuating magnetic fields, at the origin of spin relaxation of the conduction electron's spin, can be qualitatively described in terms of two parameters: the correlation time τ_c,i.e., the time in which the magnetic field is considered to be constant, and the characteristic spin precession frequency ω. A spin of a travelling electron starts

precessing with frequency ω around the direction of the effective field during a time τ_c. After this time, the effective field direction changes, in a random fashion, and the spin starts its precession along a new direction. After enough time steps, the initial spin information is lost. How fast this happens depends on the dimensionless parameter $\omega\tau_c$, which is the precession angle during the correlation time, and we can distinguish two extreme cases: $\omega\tau_c \ll 1$ and $\omega\tau_c \gg 1$.

In the first limit, the precession angle is very small during each correlation time. Like the one-dimensional symmetric random walk, with a variance $\langle x^2 \rangle = L^2\, N$ with L being the step (average) length and N the number of steps [109], the spin precession variance is $\langle \phi^2 \rangle = (\omega\tau_c)^2\, 1/\tau_c\, t$, where t/τ_c is the number of uncorrelated random steps. The spin relaxation time τ_s is defined as the characteristic time in which this angle becomes ~ 1, obtaining

$$\frac{1}{\tau_s} = \omega^2 \tau_c, \tag{2.11}$$

where we notice that $\tau_s \gg \tau_c$. In the opposite limit, the spin precesses many times during the correlation time. During a time $\sim 1/\omega$, the original spin projection transverse to the random field is completely destroyed while its projection along the field is conserved. After a further time $\sim \tau_c$ passes, the direction of the field changes and the initial spin configuration disappears, obtaining

$$\tau_s \sim \tau_c. \tag{2.12}$$

The considerations made above are general and we can now relate the quantities ω and τ_c to microscopic scattering processes in disordered systems induced by the SOC.

The case of a weak uniform spin-orbit interaction, originating from the lack of an inversion centre in the system, induces the so-called Dyakonov-Perel (DP) relaxation mechanism in systems with randomly distributed impurities [7] and follows Eq.(2.11). In this scenario, the electrons are subject to a Zeeman field of the general form

$$H_{\mathrm{SOC}} = \frac{\hbar}{2} \mathbf{s} \cdot \boldsymbol{\Omega}_{\boldsymbol{p}}, \tag{2.13}$$

where $\boldsymbol{\Omega}_{\boldsymbol{p}}$ is the precession frequency of the momentum-space effective magnetic field. The direction of the precession axis is determined both the type of inversion asymmetry and the electrons' momentum. This means that a scattering event with an impurity induces a change in the direction of the effective magnetic field, leading to spin dephasing after enough collisions. The correlation time is then of the order of the scattering time τ_p, and we finally get

$$\frac{1}{\tau_s} \sim \Omega^2\, \tau_p, \tag{2.14}$$

with $\Omega = (\langle \boldsymbol{\Omega}_{\boldsymbol{p}}^2 \rangle)^{1/2}$ the characteristic precession frequency averaged over the Fermi surface. Since in the dilute regime τ_p is inversely proportional to the concentration of impurities n_i, we find $\tau_s \sim n_i$. The strength of the constant Ω depends on the type of broken inversion symmetry. A structure inversion asymmetry (SIA) generates a Rashba type interaction and $\boldsymbol{\Omega}_{\mathrm{SIA}} = \alpha(p_y, -p_x)$, while bulk inversion asymmetry (BIA) induces

a Dresselhaus coupling. For example, in (001)-grown A_3B_5 2D semiconductors, we find $\mathbf{\Omega}_{\mathrm{BIA}} = \beta(p_y, p_x)$ in the coordinate system of $x \parallel [1\,\bar{1}\,0]$, $y \parallel [1\,1\,0]$, obtaining $\Omega^2 = \langle|p|\rangle^2 (\alpha^2 + \beta^2 - 2\alpha\beta\cos 2\theta)$, where θ is the angle between $\mathbf{p}$ and the direction $[1\,\bar{1}\,0]$. Eq.(2.14) is only valid for weak Ω, while the opposite limit, expressed by Eq.(2.11) is valid for $\Omega\tau_{\mathrm{p}} \gg 1$, and $\tau_s \sim 1/n_i$ (Fig.(2.7)).

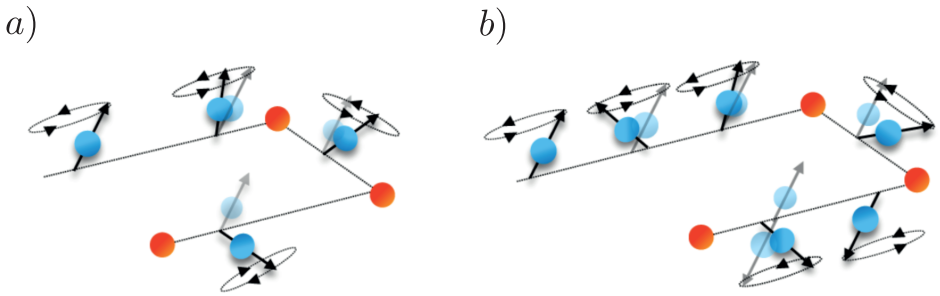

Figure 2.7: Spin-relaxation mechanisms in systems with symmetry-breaking SOC [51]. In (a) the SOC is weak, $\Omega\tau_{\mathrm{p}} \ll 1$, and the spin precesses slowly between collisions, while (b) illustrates the opposite limit with $\Omega\tau_{\mathrm{p}} \gg 1$.

The second type of spin dephasing mechanism, called Elliott-Yafet (EY) spin-relaxation [6], is mediated by local SOC due to lattice vibrations, charged impurities, and pinpointed inversion symmetry breaking [110]. It results from local spin-flips upon interaction with local spin-orbit fields. The spin rotates of a small angle φ in each scattering event. Following the angle-random walk argument developed before, we find

$$\frac{1}{\tau_{\mathrm{s}}} \sim \frac{\langle\varphi^2\rangle}{\tau_{\mathrm{p}}}. \tag{2.15}$$

The equation above is a linear relation between the spin relaxation time and the momentum scattering time, i.e, the rate $1/\tau_{\mathrm{s}} \sim n_i$, and we can interpret the term $\langle\varphi^2\rangle$ as the spin-flip probability during a momentum relaxation event [111]. Graphene provides an excellent example for materials with spin relaxation induced by extrinsic sources, according to the EY mechanism [112], while DP relaxation can be induced by substrates or periodic adatom insertion [35]. Besides, as shall be discussed in detail in Chap.(5), randomly distributed impurities produce spin-dependent self energies that activate a DP-like spin relaxation mechanism on top of the usual EY-relaxation contribution [38].

2.2.6 Current-induced spin-current

As the transport of information is carried by the electric current in charge-based devices, spin currents, i.e., flow of spin densities [21], play a crucial role in spintronics [107, 113, 114]. Three major approaches are currently adopted for practical spin injection in nonmagnetic materials. The first method induces the alignment of the electrons' spin orientation from a charge current flowing through a magnetic medium [115]. Nevertheless, it requires large magnetic fields in paramagnetic II-VI semiconductor spin aligners [116] and may result in low injection efficiency, e.g. due to a dead layer at the FM/semiconductor interface [117]. The second method exploits the diffusion of a spin

density generated by a circularly polarized light beam [118], which, however, can be cumbersome in everyday spin-related nano-technologies. The third option consists in a purely electrically-generated spin current, via spin-Hall effect (SHE) in nommagnetic conductors or anomalous Hall effect (AHE) in ferromagnets. The SHE is a central focus of investigation in this thesis as a charge-spin conversion effect.

The first experimental studies of SHE in semiconductors and metals [119, 15, 120, 121] sparked interest in this phenomenon, which currently represents an evolving front in spintronics research due to its ability to convert charge currents directly into a transverse spin current via spin-orbit interaction (Fig.(2.8a)). We also note that the Onsager reciprocity [122] guarantees the existence of the reversed effect, called inverse SHE (ISHE), that enables the transformation of pure spin currents into electric currents [123]. Different experimental works proposed various set-ups to capture both phenomena experimentally. A common approach is currently used to observe the ISHE [124] and consists of the injection of a spin current through an adjacent ferromagnet and the detection of the spin Hall-induced electric potential difference V between the electrodes attached to the nonmagnetic layer (Figs.(2.8b)). First observations of direct SHE [119], which induces the spin accumulation at the sample, are based on detection and imaging using Kerr rotation microscopy, as shown in Fig.(2.8c). Finally, a significant advancement in generating and detecting spin-to-charge intercorversion effects is represented by the recent fabrication of lateral (cross-shaped) spin valve devices made from 2D materials [125] (Fig.(2.8d)) which require the only use of purely electric currents.

The charge-spin current intercorversion at the heart of all these experiments can be described by the simple phenomenological equations

$$j_i(\gamma) = j_i(0) + \gamma \epsilon_{ilk} j_l^k(0), \tag{2.16a}$$

$$j_i^l(\gamma) = j_i^l(0) - \gamma \epsilon_{ilk} j_k(0), \tag{2.16b}$$

where $j_i(\gamma)$ and $j_{il}(\gamma)$ ($j_i(0)$ and $j_{il}(0)$) are charge and spin currents respectively, the index i is the direction of the flow and l is the component of the spin that is flowing. The change in sign between Eqs.(2.16a) and (b) is due to the Onsager relations. The spin-Hall conversion is expressed by γ, while ϵ_{ilk} is the unit antisymmetric tensor. SOC dictates the spin-charge conversion parameter γ and receives contributions from intrinsic and extrinsic mechanisms.

The intrinsic mechanism is driven by the band structure, does not require local sources of SOC, such as heavy impurities [126] , and is rooted in the topological nature of the system, manifesting itself in a nonzero momentum-space Berry phase [127]. In very simple terms, we can imagine that the electrons with opposite-oriented spins interact with the uniform SOC, resulting in spin-dependent forces that separate the spin carriers. To better understand the physical intuition behind the system's intrinsic response, we consider the AHE, where the unbalance between particles with opposite-oriented spin induces a net voltage at the edge of the sample. In this case, the Berry phase adjusts the semiclassical theory of wavepackets dynamics by establishing an "anomalous velocity" [128, 129]. The equation of motion for the centroid of the wavepacket $\mathbf{r}_c$ then becomes

$$\partial \mathbf{r}_c / \partial t = \partial E_n(\mathbf{k}) / \hbar \partial \mathbf{k} - (\mathbf{E}/\hbar) \times \mathbf{b}_n(\mathbf{k}), \tag{2.17}$$

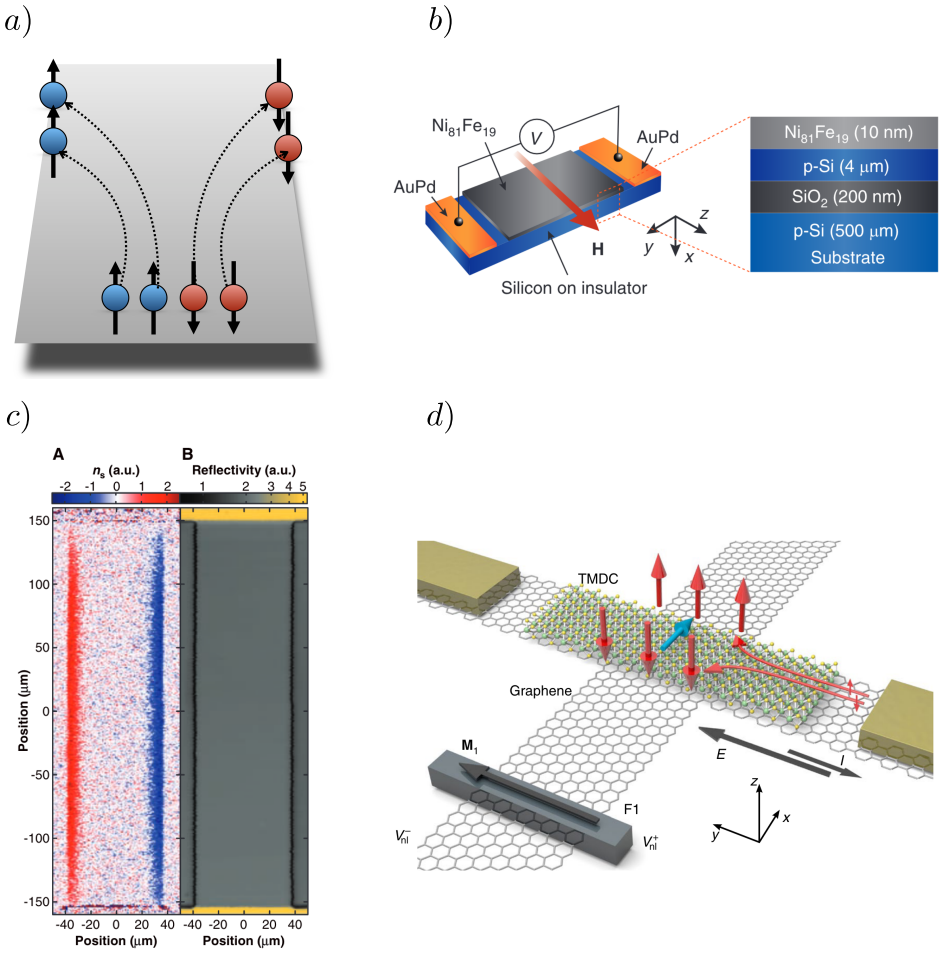

Figure 2.8: Spin Hall effect and related experiments. A charge current, initially unpolarized, is disentangled into its spin components, leading to a bulid-up of spin accumulation at the boundaries of the sample (a). The inverse effect, i.e., ISHE, can be detected by the apparatus in (b), where the spin current pumped from the ferromagnetic film is converted into an electrical signal [124]. The traditional observation of CISC uses optical detection techniques, including Kerr-microscopy (c) [119]. In particular, A and B show two-dimensional images of spin density and reflectivity for the GaAs sample. (d) presents a schematic illustration of a graphene Hall cross-device able to inject and detect the (I)SHE [125]. An electric field **E** produces an electric current **I**, which is then converted into a spin current by the SOC, enhanced in the transition metal dichalcogenide (TMDC) stripe. The ferromagnet F1 than detects the spin current via non-local electric-potential measurement ($V_{\mathrm{nl}}^{+} - V_{\mathrm{nl}}^{-}$). The reciprocal effect is realized by injecting a spin current polarized by the ferromagnet and then exploiting the ISHE to measure the ensuing charge current.

with $\mathbf{b}_n(\mathbf{k}) = \mathrm{i}\boldsymbol{\nabla}_k \times \langle n, \mathbf{k}|\boldsymbol{\nabla}_k|n, \mathbf{k}\rangle$ being the Berry curvature, and n is the band index. The additional term in Eq.(2.17), linear in the electric field, produces an Hall current contribution coming from the Fermi sea, $j_{int} \sim \sum_{n,\mathbf{k}} \mathbf{b}_n(\mathbf{k})$.

The purely extrinsic mechanisms contributing to the SHE, on the other hand, rely entirely on random fluctuations of spin-orbit fields and on the presence of randomly distributed impurities. These are the skew scattering, described in details in Sec.(2.2.3), and the side jump. The former intuitively gives rise to a spin current, deviating spin up and down electrons in opposite directions, while the latter builds up the effect by inducing a displacement of the incident wavepacket transverse to its momentum [130, 131]. In the clean limit ($\varepsilon\tau_c \gg 1$), where ε is the Fermi energy, mainly under investigation in this thesis, the skew scattering dominates over quantum side jump and intrinsic response. In this limit, the response functions are proportional to the transport lifetime $\tau \sim 1/n_i$, while the other two effects are independent on the concentration of impurities. In the way of conclusion, hybrid intrinsic–extrinsic SHE mechanisms are also operative in nonmagnetic materials with non-coplanar **k**-space spin textures. An elegant example is the universal skew scattering mechanism supported by proximitised graphene, first predicted in Ref. [36], and explored in detail in Chap. 6. This spin-orbit scattering mechanism is activated by the out-of-plane tilting of Rashba spin textures induced by spin-valley coupling, and does not require a specific type of impurity (hence, 'universal').

2.2.7 Spin-orbit torque

One of the most promising applications of CISP and CISC is the possibility of manipulating the magnetization dynamics of ferromagnets, antiferromagnets, and interfaces of magnetic insulating materials [132, 133]. This offers the prospect of replacing magnetic fields with current-induced spin torques to control bit states in nanomagnets and write/store information. In fact, the magnetization direction can represent a bit of information in binary language (for example, magnetization up = 1 and down = 0) [134], and the application of an electric current controls such orientation by inducing magnetization switching [135, 136]. Since the origin of this type of torque is traced back to the spin-orbit interaction, it is called *spin-orbit torque* (SOT). It represents a novel, efficient, and versatile way to control the magnetization states and dynamics in different classes of materials.

Compared to the spin-transfer torque (STT) [137], already exploited in MRAM devices, the SOT paves the way toward faster, more reliable, and less energy-consuming storage devices. It enables [138] room temperature magnetization switching with two orders of magnitude smaller current densities[137], reducing the size of current driving transistor and achieves high-density of SOT-MRAM. Also, the switching time is an order of magnitude smaller in the case of SOT when compared to STT; read and write current paths are orthogonal to each other and can be independently optimized [139, 140] without the presence of the tunnel barrier in the write path; SOT-MRAM requires much smaller total number of layers than complicated stacks in STT-MRAM maintaining noncollinearity of two FM layers [2]; and SOT-MRAM evades asymmetric magnetization switching issue with STT-MRAM [139].

The primary picture describing the SOT, at the origin of more sophisticated devices, involves nonmagnetic materials coupled with (anti)ferromagnets (Fig.(2.9a,b,c)). Two main microscopic mechanisms, that can act in parallel, play an active role. In one scenario (Fig.(2.9a)), the electric current flowing through a nonmagnetic bulk generates a spin current via SHE, which induces an accumulation of spin at the interface next to the FM partner, then absorbed as a magnetization torque [132]. In the second picture (Fig.(2.9b)), the unpolarized charge current travels parallel to an interface with broken inversion symmetry in FM/nonmagnetic bilayers yielding a spin density $\mathbf{S}$ and the corresponding torque $\mathbf{T}$.

A commonly employed SOT decomposition in the unit magnetization is

$$\mathbf{T} = \tau_{\mathrm{FL}}\, \mathbf{m} \times \boldsymbol{\xi} + \tau_{\mathrm{DL}}\, \mathbf{m} \times (\mathbf{m} \times \boldsymbol{\xi}), \tag{2.18}$$

where $\mathbf{m}$ is the magnetization unit vector and $\tau_{\mathrm{FL,DL}}$ are coefficients that can be functions of the magnetization angle [142]. The unit vector $\boldsymbol{\xi}$ depends on the mechanism at the origin of the torque, the CISC or CISP. For example, two-dimensional interfaces lacking inversion symmetry develop a macroscopic spin accumulation via Edelstein effect, leading to a torque of the form $\mathbf{T} \sim \Delta_{\mathrm{xc}}(\hat{K} \cdot \mathbf{E}) \times \mathbf{m}$, with Δ_{xc} being the exchange coupling between the classical magnetic moments in the ferromagnet and the spin of the conduction electrons in the nonmagnetic material.

To better understand the physics behind Eq.(2.18), we put it in the more general context of the Landau-Lifshits-Gilbert (LLG) equation

$$\frac{\partial \mathbf{m}}{\partial t} = -\gamma \mathbf{m} \times \mathbf{H}_{\mathrm{eff}} + \alpha_{\mathrm{G}} \mathbf{m} \times \frac{\partial \mathbf{m}}{\partial t} + \mathbf{T}, \tag{2.19}$$

which controls the magnetization dynamics of the magnetic layer. The first term on the right-hand side describes the precession of $\mathbf{m}$ around the effective magnetic field $\mathbf{H}_{\mathrm{eff}}$, created by localized moments in the ferromagnet [75]. This contribution is renormalized by the first torque factor $\tau_{\mathrm{FL}}\, \mathbf{m} \times \boldsymbol{\xi}$, which for this reason, is traditionally called *field-like torque* (FLT). The second term in the LLG equation accounts for the relaxation of the magnetization toward its equilibrium state, mediated by the Gilbert damping parameter α_{G}. This contribution is renormalized by the second term in Eq.(2.18), $\tau_{\mathrm{DL}}\, \mathbf{m} \times (\mathbf{m} \times \boldsymbol{\xi})$, that is known as *damping-like torque* (DLT) (Fig.(2.10)). The magnetization switching is enabled by the DLT, which in ferromagnet/heavy-metal (FM/HM) bilayers is attributed to the spin Hall current flowing in the bulk of the HM layer [136, 143]. Conversely, the FLT triggers the precession of $\mathbf{m}$ around a current-induced effective field. This contribution is attributed to the Edelstein Effect produced at the surface of the HM and is usually considered detrimental [144].

The traditional link between torque components and bulk/surface effect has been questioned by replacing the HM with topological insulators in FM/TI bilayers. In fact, efficient SOT was achieved in the regime where the charge current flows only on the TI surface [145, 138]. As we will show in Chaps.(7), our studies try to understand this phenomenon by accounting for purely interfacial effects, as discussed in Sec.(2.2.4). We find that a giant damping-like torque can indeed be generated at the surface of topological insulators (via skew scattering), leading to a fast magnetization switching.

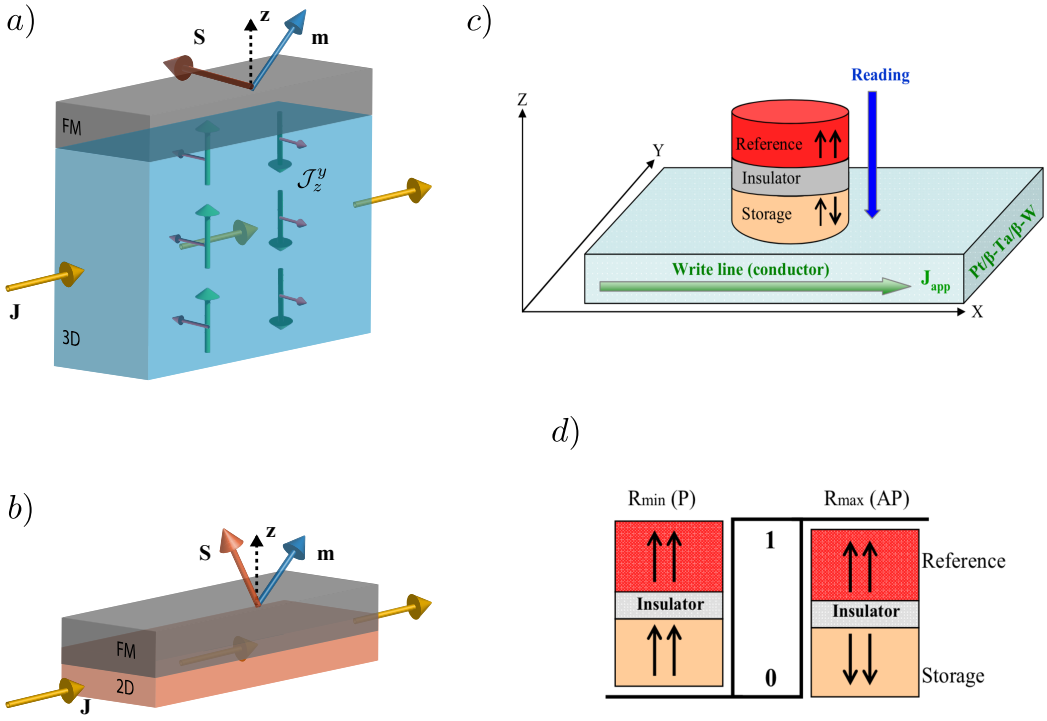

Figure 2.9: Spin-orbit torque. In three-dimensional systems (a), an electric current **J** generates a CISC $\mathcal{J}_z^y$ that propagates toward the surface. The accumulated spin density exerts a torque on the ferromagnet magnetization. This type of SOT is traditionally identified as damping-like and is responsible for the switching of **m**. On the other hand, the SOT in two-dimensional interfaces (b) is driven by the CISP originating in the Rashba SOC. It is usually identified as field-like, leading to the precession of **m**. (c) Three-terminal SOT device proposed as building-block for SOT-MRAMs [141]. The spin density established at the surface of the nonmagnetic material (writing line) controls the magnetization in the magnetic layer (storage) that favors or suppresses the flowing of charge current through the magnetic tunnel junction (MTJ,reading channel), via giant magnetoresistance (GMR). If the magnetization of the storage and reference layers is parallel (P) or atiparallel (AP), the resistance of the MTJ is low or high. These two configurations can be used two identify two logic states, 0 and 1 (d).

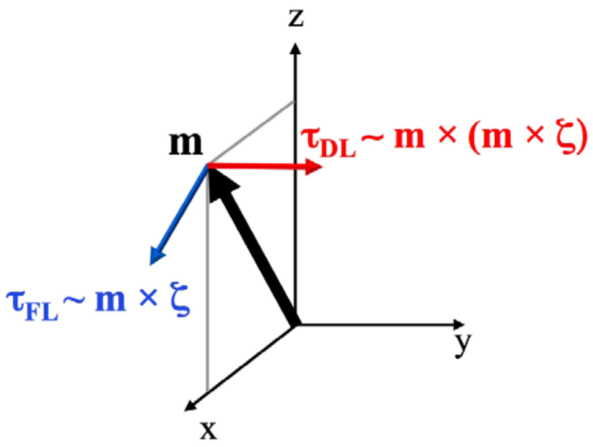

Figure 2.10: Vector decomposition of the SOT acting on the magnetization $\mathbf{m}$. In the present example $\boldsymbol{\xi} = y$ [142].

2.3 Summary and outline

This thesis aims to expand the current theoretical knowledge of coupled spin-charge transport phenomena at interfaces. As representative model systems in this respect, we focus on 2DEGs, surface states of topological insulators, adatom-decorated graphene and proximitised graphene systems. As we navigate through these systems, we consider the effects of SOC and impurity scattering non-perturbatively. That is, we make no expansions in the spin-orbit coupling constants or the impurity potentials at the level of the propagators' self-energy and response functions. Such a *tour de force* will be required for self-consistency,i.e., the achievement of results that are internally consistent and coherent based on the principles of the theory itself, and that don't rely on external assumptions [19], and to be able to probe new spin-orbit scattering mechanisms. This thesis is organized as follows.

- Chapter 3 presents the low-energy models that will provide the foundation for addressing the spin transport physics. We first briefly present the general features of 2DEGs and, in particular, the impact of the SOC on the band structure. We then analyze the 2D Dirac model for surface states of 3D topological insulators in FM/TI bilayers. Finally, we review the low-energy properties of graphene materials, focusing on the effect of twisting and adatoms.

- Chapter 4 outlines the techniques used to tackle the non-equilibrium properties, essential for the structure of Chaps.(5), (6), and (7). Firstly, we present the kinetic theory. It includes the *semiclassical Boltzmann equation*, designed to handle single impurity scattering events at all orders in perturbation theory, and then its quantum extension, i.e., the *quantum Boltzmann equation* (QBE), able to include conduction-valence band transitions. Finally, we present our fully quantum mechanically self-consistent formalism based on the Kubo-Streda formula in the linear response theory. It enables the evaluation of the system's response to external perturbations by employing Feynman diagrammatics and can treat the

intrinsic and extrinsic contributions to transport coefficients on equal footing, encompassing the skew scattering mechanism. Moreover, based on this method, we develop a formalism to derive a set of spin drift-diffusion equations that provide a complete description of the system dynamics the Diffuson Hamiltonian method.

- In chapter 5, our focus is on monolayer graphene with random and local sources of SOC. This scenario includes adatom absorption in the hollow honeycomb lattice position and random fluctuation of uniform spin-orbit fields, both cases relevant in realistic systems [53, 146, 54]. Using the QBE and the extended Kubo formalism, we unveil a direct coupling between charge and spin currents, activated by the quantum interference between distintic random-SOC-field components, which competes with skew scattering-induced spin-Hall effect. This new type of extrinsic SHE is mediated by an anomalous *interband spin-orbit scattering mechanism* involving virtual transitions between conduction and valence electrons. It is robust in the weak impurity potential regime and is already present in FBA. We include this new effect in a more general landscape by deriving a set of equations that explains charge-spin drift-diffusive transport in a wide range of relevant experimental situations, including scenarios where spin-polarized carriers are created optically [147, 148, 149] and injected from other systems [117, 150].

- Chapter 6 examines coupled spin-charge transport phenomena in graphene-based twisted van der Waals heterostructures. These systems experience sizable and tuneable spin-orbit fields, leading to an unique phenomenology [8, 151, 152]. In particular, we inspect the impact of off-setting proximity-coupled vdW layers by some (non trivial) twist angle θ. Drawing inspiration from recent works that have unveiled enhanced proximity-induced SOC in these systems [153, 154], we develop a microscopic theory of CISP and CISC that is valid for arbitrary twist angle in graphene/TMD heterostructures and fully captures the interplay of symmetry-breaking SOC and impurity scattering. Our findings predict that twisted vdW heterostructures exhibit highly anisotropic spin-density-current responses, in which the orientation of non-equilibrium electron spins is extremely sensitive to the twist angle. At critical twist angles, the non-equilibrium spin density is parallel to the applied current, i.e. a *collinear Edelstein effect* (CEE) is realized. Finally, we present an exhaustive theoretical description of the emerging intrinsic and extrinsic SHE.

- Chapter 7 discusses the appearance of purely interfacial giant antidamping SOTs in FM/TI(HM) bilayers induced by skew scattering. Employing the generalized Kubo-Streda formalism, we can treat disorder and band structure effects on equal footing. This level of theory allows us to include skew scattering at all orders in perturbation theory (ideal for considering strong impurities) as well as to analyze the effect of generic magnetization direction in the magnetic layer (inaccessible to previous treatments of disordered normal-metal/ferromagnetic-metal heterostructures). Furthermore, we deepen our analysis of SOTs induced by TIs, which are of great importance for technological applications, by extending the formalism to

magnetic disorder [155, 156]. Here, we consider both the clean limit and in the dirty regime, where the concentration of impurities is relatively high.

Chapter 3

Two-dimensional materials-based spintronics

3.1 Overview

This chapter examines the main spin-related properties of various two-dimensional systems investigated in this thesis and central in spintronics. We will establish the theoretical foundations required to develop effective spin-charge transport theories, including the Hamiltonian and the quantum observable operators.

We first present the honeycomb crystal structure of bare graphene, which gives rise to its unusual linear dispersion relation in the low-energy theory, at the origin of the high mobility of the charge carriers. The result is an electron gas of massless relativistic-like (Dirac) particles, characterized by the spin degree of freedom and the *pseudospin*, both 2×2 representations of the SU(2) Lie algebra. Next, we thoroughly examine the symmetries of honeycomb lattice materials, highlighting the connection between broken symmetries and the emergence of spin-orbit interactions, such as Rashba, Kane-Mele and spin-valley SOC. This analysis is crucial for describing Van der Waals graphene-based heterostructures (also applicable to adatom-decorated graphene, as we will see), where the combination of different two-dimensional systems lowers graphene's original C_{6h} point group symmetry. We also briefly discuss the emergence of local spin-orbit interactions originating in physisorbed atomic species on graphene.

We conclude the chapter by discussing the electronic properties of 3D topological insulators. These materials have a distinct property where the bulk is insulating, while the surface is conducting, resulting in purely two-dimensional particles' transport at the surface. The corresponding time-reversal invariant low-energy Hamiltonian is linear in momentum and takes the form of the standard Rashba interaction. Consequently, the kinetic term presents a robust spin-orbital coupling with unprecedented strength, yielding sizable charge-spin interrelated effects.

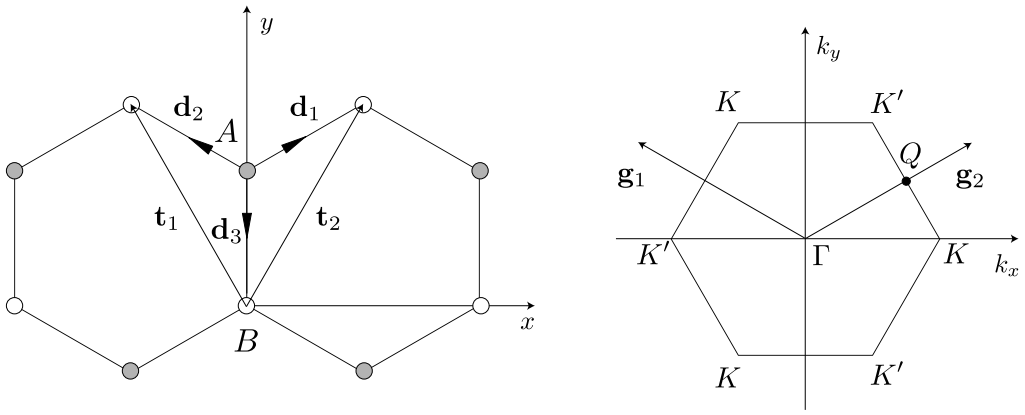

Figure 3.1: Graphene's honeycomb lattice (left panel) described by the primitive translational vector, $\mathbf{t}_{1,2} = a\left(\pm 1/2, \sqrt{3}/2\right)$, where $a = 2.46\mathring{A}$ is the lattice constant. The two inequivalent sublattices, A and B (both carbon atoms), are portrayed with different colours. They are translated into two inequivalent high symmetry points K and K' in the hexagonal first Brillouin zone (right panel).

3.2 Graphene

3.2.1 Crystal structure, electronic bands and Hamiltonian

We commented in the Introduction on the reasons behind the growing interest in condensed matter, and charge-spin transport in particular, for graphene. Here we can understand more in detail some of its basic electronic properties by employing a simple tight-binding model [157]. To start, the monolayer structure of graphene has an honeycomb shape shown in Fig.(3.1) (left panel), consequence of the sp^2 hybridization of the $2s$, $2p_x$, and $2p_y$ carbon orbitals. Being the primitive unit cell composed of two carbon atoms, we expect eight bands when excluding the $1s$ core atomic orbitals, strongly localized near the nuclei. The bonding and anti-bonding σ-bands, six in total, built from the s, p_x, and p_y orbitals, are separated by a large energy gap of $\sim 5.6\,\text{eV}$ and are inert in terms of charge transport. To our ends, the π-bands originating in the p_z orbitals are the most relevant. In fact, they give rise to the highest (completely filled) valance band and lowest (completely empty) conduction band, degenerate at the corner of the Brillouin zone, called *Dirac points* (see Fig.(3.2)). This semimetal behaviour occurs in correspondence of the high symmetry point K and K', called inequivalent *valleys*, because not connected by a reciprocal lattice vector $\mathbf{g}_{1,2}$. Notably, the dispersion relation turns out to be linear in the proximity of the two valleys. This "regime" is the most significant since the Fermi energy lies precisely at Dirac points in bare graphene. Therefore, we briefly derive the tight-binding Hamiltonian near these regions, the *low-energy theory*.

The usual form of the second quantized Hamiltonian, excluding any spin-orbital

interaction, is

$$H = -t \sum_{\langle i,j \rangle} \left(a_i^\dagger b_j + h.c. \right), \tag{3.1}$$

where we restricted our discussion to nearest-neighbour electrons hopping. The operators $a[b]_i^{(\dagger)}$ annihilates (creates) a p_z-electron on site i belonging to the sublattice A [B] and $t \sim 3\,\mathrm{eV}$ is the hopping parameter. The translation of Eq.(3.1) from real to momentum space is readily performed by defining the unitary transformation, i.e., the discrete Fourier transform,

$$a(b)_i = \frac{1}{\sqrt{N_{A(B)}}} \sum_{\mathbf{k}} e^{-\mathrm{i}\mathbf{k}\cdot\mathbf{r}_i} a(b)_{\mathbf{k}}, \tag{3.2}$$

with $N_A + N_B = N$ being to total number of carbon atoms in the lattice. Inserting this relation inside the tight-binding Hamiltonian, we obtain terms $\sim \mathbf{k} \cdot (\mathbf{r}_i - \mathbf{r}_j)$, which become $\sim \mathbf{k} \cdot \boldsymbol{\delta}_i$ in the nearest-neighbour approximation, being $\boldsymbol{\delta}_{1(2)} = a/2\left(\pm\sqrt{3}, 1\right)$ and $\boldsymbol{\delta}_3 = a\,(0, -1)$ the three nearest-neighbour vectors (see Fig.(3.1)). The resulting momentum-space Hamiltonian has the form

$$H = \sum_{\mathbf{k}} \begin{pmatrix} a_{\mathbf{k}}^\dagger & b_{\mathbf{k}}^\dagger \end{pmatrix} \begin{pmatrix} 0 & \phi^*(\mathbf{k}) \\ \phi(\mathbf{k}) & 0 \end{pmatrix} \begin{pmatrix} a_{\mathbf{k}} \\ b_{\mathbf{k}}, \end{pmatrix}, \tag{3.3}$$

where the function $\phi(\mathbf{k}) = -t \sum_{a=1,2,3} e^{\mathrm{i}\mathbf{k}\cdot\boldsymbol{\delta}_a}$ contains all the information about the crystal geometry. This Hamiltonian reproduces the complete p_z-dispersion relation in Fig.(3.2) (dotted line).

We now expand Eq.(3.3) around two inequivalent valleys K and $K' = -K$ by setting $\mathbf{k} = \pm\mathbf{K} + \mathbf{q}$ and choosing, for instance, $\mathbf{K} = (4\pi/3a\sqrt{e})\hat{x}$. Retaining only the linear terms in momentum, the final result is the 8×8 Dirac Hamiltonian

$$H = \hbar \mathrm{v} \tau_z \boldsymbol{\sigma} \cdot \mathbf{q}, \tag{3.4}$$

describing six Dirac cones grouped into two valleys (see Fig.(3.3)). $\mathrm{v} = 3at/2\hbar \sim 10^6$ is the Fermi velocity of electronic excitations around the Dirac valleys and we wrote Eq.(3.4) in the *magic basis*, i.e., swapping the K' components of the relative spinorial Bloch wavefunction, $\Psi_{\mathbf{q}} = \left(\Psi_A^K, \Psi_B^K, \Psi_B^{K'}, \Psi_A^{K'}\right)$. The transformation from the standard basis to the magic basic and vice-versa is readily performed by the unitary transformation $U_\mathrm{M} = \frac{1}{2}\tau_0(\sigma_0 s_0 + \sigma_x s_0) + \frac{1}{2}\tau_z(\sigma_0 s_0 - \sigma_x s_0)$, with $U_\mathrm{M} U_\mathrm{M}^\dagger = 1$ and $U_\mathrm{M} = U_\mathrm{M}^\dagger$. The vector of Pauli matrices $\boldsymbol{\sigma}$ acts in the *pseudospin* space, stemming from the presence of the two graphene's sublattices. Similarly, the Pauli matrix τ_z is defined in the valley space, where the relative factor $(\tau_z)_{11(22)} = 1(-1)$ describes the valley $K(K')$. The four eigenfunctions of Eq.(3.4) can be written as

$$\Psi_{\mathbf{q},s}^{\tau=1} = 1/\sqrt{2}\left(1, s\, e^{\mathrm{i}\phi_{\mathbf{q}}}, 0, 0\right), \tag{3.5}$$

$$\Psi_{\mathbf{q},s}^{\tau=-1} = 1/\sqrt{2}\left(0, 0, 1, -s\, e^{\mathrm{i}\phi_{\mathbf{q}}}\right), \tag{3.6}$$

where the band index $s = \pm 1$ refers to the pseudospin space, $\tau = \pm$ is the valley index, and $\phi_{\mathbf{q}} = \arctan\left(q_y/q_x\right)$.

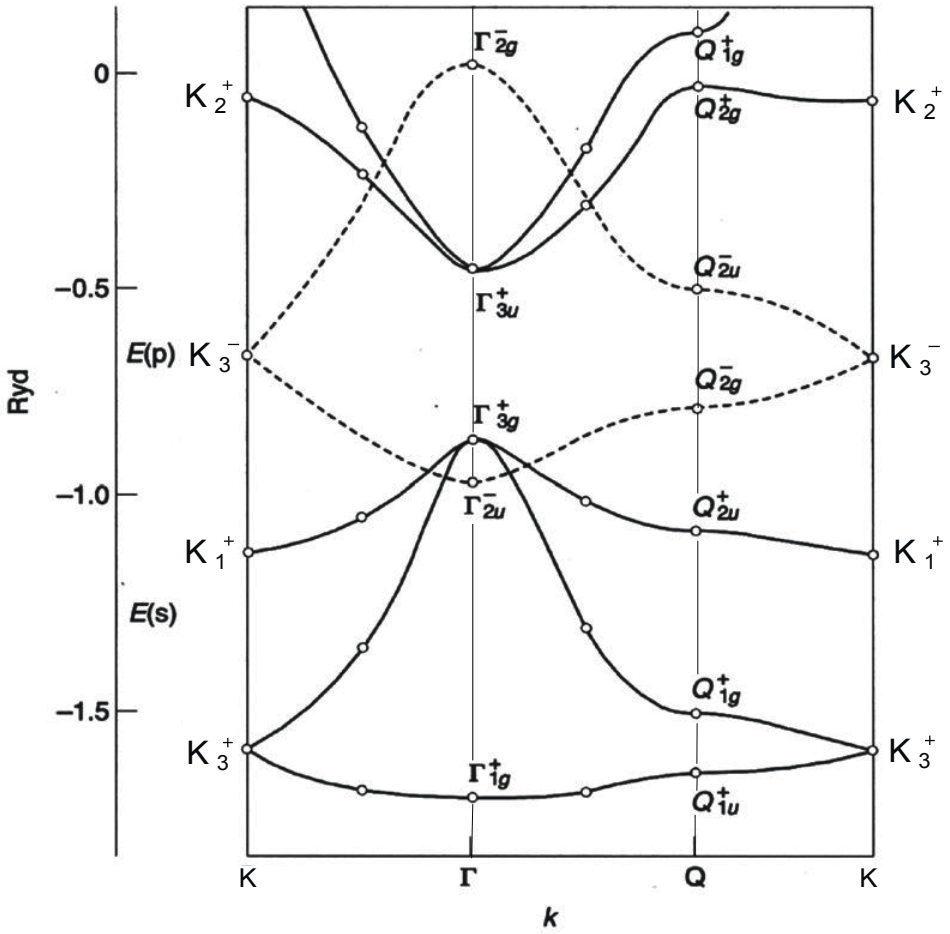

Figure 3.2: Band structure of graphene emerging from the s, $p_{x,y,z}$ carbon orbitals with the tight-binding model [157]. The solid lines represent the bonding and anti-bonding σ-bands, while the dashed lines show the π-band, relevant for transport. The dispersion relation is divergent at the corner of the Brillouin zone, realizing the Dirac cones and becoming linear in the proximity of the K high symmetry point.

3.2.2 Properties of the linear graphene's Hamiltonian

In this chapter we have seen that the low-energy Hamiltonian of graphene is linear in momentum and, as we stated in the Introduction, possesses many noteworthy properties. To begin with, graphene's relativistic carriers have a definite *chirality* (or helicity for massless particles): they are "right(left)-handed" if their pseudospin is (anti)collinear to their momentum. In fact, the chirality operator is defined as

$$h(\mathbf{q}) = \frac{\boldsymbol{\sigma} \cdot \mathbf{q}}{|q|}, \tag{3.7}$$

that is the usual definition employed in QED where the spin is substituted with the pseudospin. The corresponding eigenvalues are ± 1 (right-left handed) and $h(\mathbf{q})$ commutes with H, so the helicity is *conserved*.

This feature of graphene has two significant consequences. In the first place, it

implies that each cone of the graphene dispersion relation has a definite chirality, as shown in Fig.(3.3). Second, it prevents graphene backscattering associated with the antilocalization of electrons in this material [158]. To show that, we notice that the diffusion of particles in the system includes closed-path trajectories, which become relevant when two particles counter-propagate and yield an interference between the wavefunctions of the electrons. Since the pseudospin always follows the direction of the particles' momentum, the two carriers will possess a phase difference of π, which is a *destructive* interference, suppressing backscattering. This property of graphene contributes to the ultra-high mobility of chiral carriers, making graphene an excellent candidate for transport of information.

Chirality manifests in a large number of quantum electrodynamics effects, from the Klein tunnelling to the chiral quantum Hall effect [159, 160, 161], and has consequences on the topological properties of graphene. In fact, the adiabatic evolution of the wavefunction around a closed loop $\mathcal{C}$ produces a nonzero Berry-phase (see Fig.(3.3))

$$\gamma = \oint_{\mathcal{C}} \mathbf{A}_{n,\mathbf{k}} dl = \pi, \tag{3.8}$$

where $\mathbf{A}_{n,\mathbf{k}} = \langle n, \mathbf{k} | \boldsymbol{\nabla}_k | n, \mathbf{k} \rangle$ is the Berry curvature. Because of this property, breaking the chiral symmetry, i.e., the inclusion of a mass term, means driving graphene into topological insulating phases, like the quantum Hall one [162].

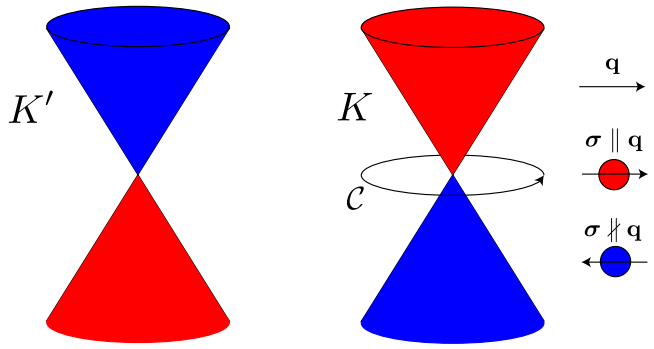

Figure 3.3: Bipartite low-energy dispersion of graphene: the K and K' Dirac cones. The red (blue) color indicates positive (negative) chirality, opposite in the two valleys.

Another crucial product of Eq.(3.4), more related to transport problems, is the favoured appearance of strong short-range scattering centers [80]. In graphene, in fact, the resonant effect, represented by an effective scattering potential V_{eff}, takes the form $V_{\text{eff}} = V_{\text{ad}}^2/(E - \epsilon_{\text{ad}})$, where E is the energy, V_{ad} is the hopping parameter between a carbon site and the impurity, and ϵ_{ad} is the onsite adatom energy (relative to carbon). Using typical values of $\epsilon_{\text{ad}} \sim -0.2\,\text{eV}$ and $V_{\text{ad}} \sim 5\,\text{eV}$, we find $V_{\text{eff}} \sim 100\,\text{eV}$ at the Dirac point ($E = 0$), which is a resonant impurity potential. For this reason, the skew scattering plays a major role graphene and cannot be ignored in transport problems in general.

In conclusion, graphene's Hamiltonian has consequences on the observable of interest in spin-transport problems. To show that and align with the literature, we introduce the SO(5) Clifford algebra of the spin and pseudospin space and focus on one valley only. Hence the full Hamiltonian becomes $\sim \mathrm{v}\gamma_{i0}p_i$, and we consider local observable operators that admit the decomposition $\mathcal{O} = \sum_{\alpha\beta}\mathcal{O}_{\alpha\beta}\gamma_{\alpha\beta}$, where $\gamma_{ij} = \sigma_i \otimes s_j$ are Dirac matrices defined on spin and pseudospin space. The density and charge- (spin-) current operators are

$$\hat{\gamma}_{\mu\nu} = \psi^\dagger(\mathbf{x})\,\gamma_{\mu\nu}\,\psi(\mathbf{x}) \tag{3.9}$$

$$\hat{\mathcal{J}}^{\nu}_{\mu} = \psi^\dagger(\mathbf{x})\,\frac{1}{2}\{J_\mu, \gamma_{0\nu}\}\,\psi(\mathbf{x}) \tag{3.10}$$

where $J_\mu = e\partial\mathcal{H}/\partial p_\mu$ is the first-quantized charge-current operator, $\{\cdot,\cdot\}$ denotes the anticommutator, and $e < 0$ is the electron's charge. In Dirac systems, $J_\mu = e\mathrm{v}\gamma_{\mu 0}$, implying that the charge (spin) current operator is related to the density one as $\hat{\mathcal{J}}^{\nu}_{\mu} = \hbar\mathrm{v}\hat{\gamma}_{\mu 0}$. This means that the current observables averaged over the system's statistics, i.e., the *current-response* to external perturbations, are automatically evaluated once the density-response is known, in particular

$$\begin{pmatrix} S_a \\ N \\ \mathcal{J}^a_i \\ J_i \end{pmatrix} = \begin{pmatrix} \frac{\hbar}{2}\langle\gamma_{0a}\rangle \\ e\langle\gamma_{00}\rangle \\ \frac{\mathrm{v}\hbar}{2}\langle\gamma_{ia}\rangle \\ e\mathrm{v}\langle\gamma_{i0}\rangle \end{pmatrix}, \tag{3.11}$$

where $\langle ...\rangle$ stands for the statistical average; see Chap.(4) for further details.

3.2.3 The intrinsic spin-orbit interaction

Settled the basics of the Dirac minimal model of graphene, we can now deepen our analysis by including spin-orbital effects. The most direct way to derive the corresponding Hamiltonian is to encompass symmetry arguments. The most general interaction in graphene has the form

$$H_{int} = \sum_{\alpha,\beta,\gamma=0}^{3} \lambda_{\alpha\beta\gamma}\tau_\alpha\sigma_\beta s_\gamma, \tag{3.12}$$

where $\lambda_{\alpha\beta\gamma}$ are coupling constants. The spin-orbit coupling ignores intervalley processes, usually allowed by electrons' scattering with small impurities [163]. As a result, the terms proportional to τ_x and τ_y can be omitted because connecting the two valleys. Also, we clearly look for spin-active interactions, thus for terms in the SOC Hamiltonian $\sim s_x$, s_y, and s_z.

To begin with, the SOC preserves the time-reversal symmetry, where the corresponding operator, in the normal basis, has the form

$$T = \mathrm{i}\tau_x\sigma_0 s_y\Theta, \tag{3.13}$$

with Θ being the usual complex-conjugate operator. The term σ_0 reflects the conservation of the sublattice structure: operators $\sim \sigma_{x,y}$ transform Eq.(3.3) such that

$\phi \leftrightarrow \phi^*$, obtainable from the tight-binding theory by replacing $A \leftrightarrow B$. The term $\sim s_y$ represents the spin-inversion under time-reversal and τ_x the momentum-inversion, i.e., $\mathrm{K} \leftrightarrow \mathrm{K}'$.

Together with time-reversal symmetry, the ideal honeycomb lattice structure contains 24 group symmetry elements of the D_{6h} point group, that can be expressed in terms of the identity E and the three generators

$$\Sigma_h^{xy} = \sigma_0 \tau_0 s_z, \tag{3.14}$$
$$\Sigma_v^{yz} = \sigma_0 \tau_x s_x, \tag{3.15}$$
$$\Sigma_d^{xz} = \sigma_x \tau_0 s_y, \tag{3.16}$$

namely the horizontal reflections on the xy plane, the vertical on the yz plane, and the dihedral on the rotated xz plane [41], all depicted in Fig.(3.5). The remaining elements of the D_{6h} symmetry (such as the space inversion, sixfold, threefold, and twofold rotations) are combinations of those four operators. By applying them to Eq.(3.12), we obtain

$$H_{\mathrm{KM}} = \lambda_{\mathrm{I}} \tau_0 \sigma_z s_z, \tag{3.17}$$

traditionally called *Kane-Mele* SOC [45], presented now in the magic basis for convenience. As shown in Ref.[47], it is mediated by two consecutive electron's nearest neighbour's hopping between carbon atoms, as well as the atomic spin-valley coupling, as already described in the Introduction. However, this term is usually neglected in bare graphene because it solely contributes to opening a gap as small as tens of μeV [71], i.e., $\lambda_{\mathrm{I}} \sim 4.6\,\mathrm{eV}$. As a consequence, spin relaxation is marginal, making graphene an ideal channel for transporting spin information. However, we emphasize that the strength of the Kane-Mele interaction can be modulated by coupling graphene with other crystals in Van der Waals heterostructures or by adatom decoration, as we will discuss in the following sections.

3.3 Graphene-based heterostructures

This thesis' Introduction revealed that graphene's potential in spintronics goes far beyond its topological properties and the singular high mobility of the spin carriers. In particular, the vertical stacking with other 2D materials, the already mentioned Van der Waals heterostructures (see Fig.(3.4)), can enhance and induce spin-orbital interactions in graphene, resulting in unusual, mineable charge-spin coupled dynamics. This field of research has been initiated by combining graphene with hexagonal boron nitride (hBN) [165], presenting the fundamental technique for vdW reassembly and showing the exceptional advance in the resulting electronic quality. Inspired by these early works, further developments in vdW heterostructures shifted the attention to transition metal dichalcogenides (TMD) monolayers, recognized as ideal substrates for graphene [164] and capable to induce sizable spin-orbit interactions.

To fully understand that and derive the effective Hamiltonians, we present a symmetry analysis of graphene/TMD heterostructures initiated in the former section, showing that the proximity-induced SOC results from breaking symmetries in graphene-based

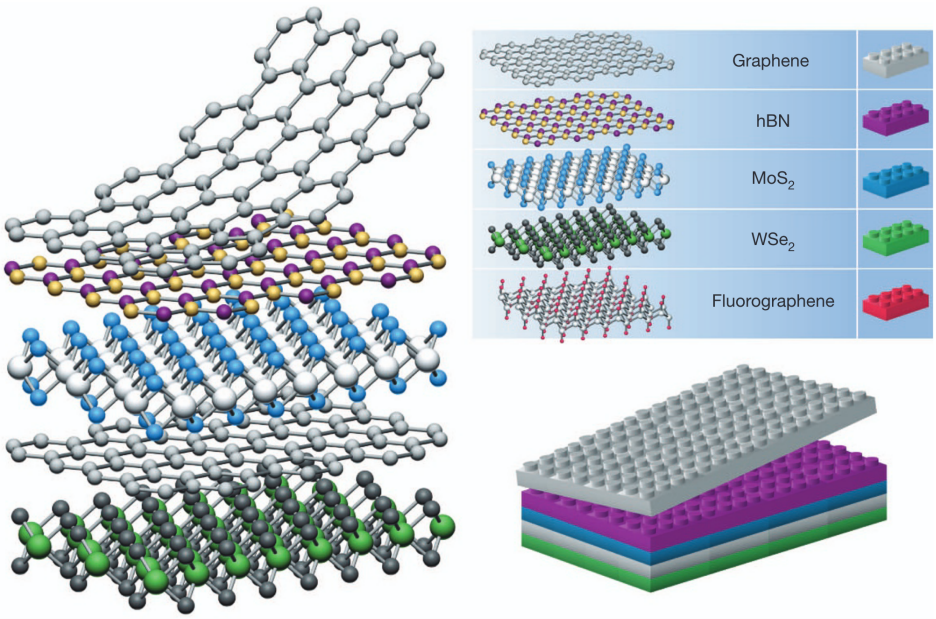

Figure 3.4: Illustration of multilayered Van der Waals heterostructures Lego-like approach [164]. Ideal partner materials belong to the graphene family (hBN, fluorographene, etc.) and 2D dichalcogenides (MoS_2, WSe_2, etc.).

systems. To begin with, the effect of the graphene's deposition on a substrate or the presence of a transverse electric field is to break the inversion symmetry along the $\hat{z}$ direction, hence reducing the system's symmetry from $D_{6h} \to C_{6v}$. Eq.(3.12) is no longer invariant under reflection about the xy plane, Σ_h^{xy}, and the resulting interaction is the Rashba-Bychkov SOC (in magic basis),

$$H_R = \lambda_{\mathrm{R}} \tau_z \left(\boldsymbol{\sigma} \times \boldsymbol{s} \right) \cdot \hat{z}. \tag{3.18}$$

We notice that the momentum operator, present in 2DEGs, Eq.(2.7), is replaced by the pseudospin Pauli matrix, leaving the velocity operator unperturbed. The energy dispersion relation of a single valley is represented in Fig.(3.6b) (green line). It displays the spin splitting of the conduction and valance bands that, even though it differs from the standard 2DEG picture, leads to the same spin-momentum locking. However, unlike 2DEGs, we can identify two different regions depending on the position of the Fermi energy ϵ. For $\epsilon > 2\lambda_{\mathrm{R}}$, graphene's *nonchiral* quasiparticles are in region II, and two counter-rotating Fermi rings are present, similar to the 2DEG case (Fig.(3.6a), top panel) [37]. However, with $\epsilon < 2\lambda_{\mathrm{R}}$, the Fermi energy intersects only one band, resulting in a single Fermi ring (Fig.(3.6a), bottom panel). In this case, graphene's carriers have a well-defined helicity and resemble the surface states of 3D topological insulators. The result is an unusually strong charge-current to spin-density conversion, being absent the opposite contribution from two counter-rotating Fermi rings.

TMD substrates are also responsible for breaking the sublattice symmetry, hence the two atomic sites A and B become inequivalent. Under this condition, the reflection about the xz plane and the sixfold rotation symmetries are absent, and the system is described by the $C_{6v} \to C_{3v}$ point group. The Hamiltonian is supplemented with an

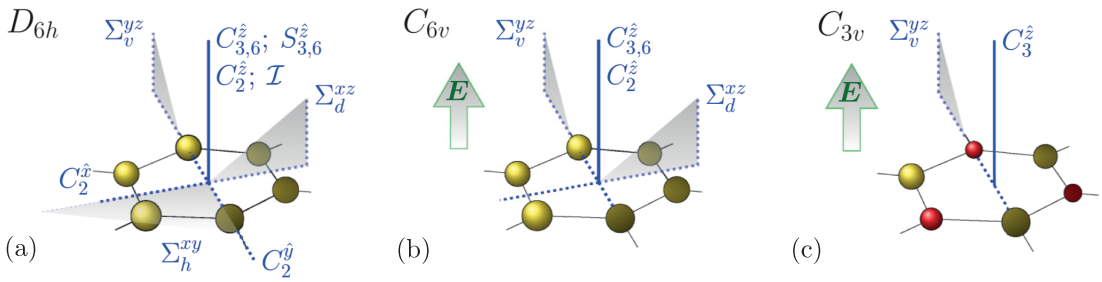

Figure 3.5: Point group selected symmetries of graphene and graphene with substrate. The operator shown are the reflections $\Sigma_{h,v,d}^{\hat{x},\hat{y},\hat{z}}$, the n-fold rotations $C_n^{\hat{x},\hat{y},\hat{z}}$, the space inversion $\mathcal{I}$, and the improper rotations $S_n^{\hat{z}}$. The time-reversal symmetry is always included. Panel (a) shows the D_{6h} symmetry of monolayer graphene. The resulting Hamiltonian is the Dirac minimal model with Kane-Mele SOC. Panel (b) shows the broken inversion symmetry along the stacking direction $\hat{z}$, i.e., $D_{6h} \to C_{6v}$, resulting in the Rashba-Bychkov SOC. Panel (c) presents the broken sixfold rotation symmetry, due to the nonequivalent A and B sublattices. The system's symmetry is further lowered, $C_{6v} \to C_{3v}$, resulting in a mass term and inducing the spin-valley coupling. Figure adapted from Ref.[41].

orbital mass term Δ and the spin-valley spin-orbit coupling. The full graphene/TMD Hamiltonian reads

$$H = \int d\mathbf{x}\psi^\dagger(\mathbf{x})\tau_z(\mathrm{v}\boldsymbol{\sigma}\cdot\mathbf{p} + \lambda_\mathrm{R}(\boldsymbol{\sigma}\times\mathbf{s})\cdot\hat{z} + \Delta\sigma_z + \lambda_\mathrm{sv}s_z)\psi(\mathbf{x}), \tag{3.19}$$

where we neglect the intrinsic-like SOC $\sim \sigma_z s_z$, typically tiny in graphene based heterostructures [33]. The spectrum associated to Eq.(3.19) is represented in Fig.(3.6). The rich structure of the graphene/TMD Hamiltonian dramatically impacts the spin-texture, which possesses an in-plane spin winding generated by the RSOC and an out-of-plane tilting controlled by the spin-valley coupling. It acts as a Zeeman interaction with an effective magnetic field $\sim \lambda_\mathrm{sv}$. However, the time-reversal symmetry, still preserved, forces the spin splitting to be opposite in the two valleys.

In Chap.(6), we will adapt Eq.(3.19) for describing twisted graphene/TMD bilayers. While most terms remain unchanged, even though their magnitude depends on the twist angle, the resulting RSOC is altered, with consequences in the related charge-spin conversion effects.

3.4 Spin-orbit active adatoms on graphene

An exciting feature of two-dimensional materials, and graphene in particular, is the possibility to vary the spatial extent of the induced symmetry-dependent spin-orbit interactions. Beyond the uniform SOC generated by suitable substrates, as discussed in the former section, it is possible to access the subnanometer range using adatoms. The impurity configuration can be periodic, affecting the band structure like substrates, or

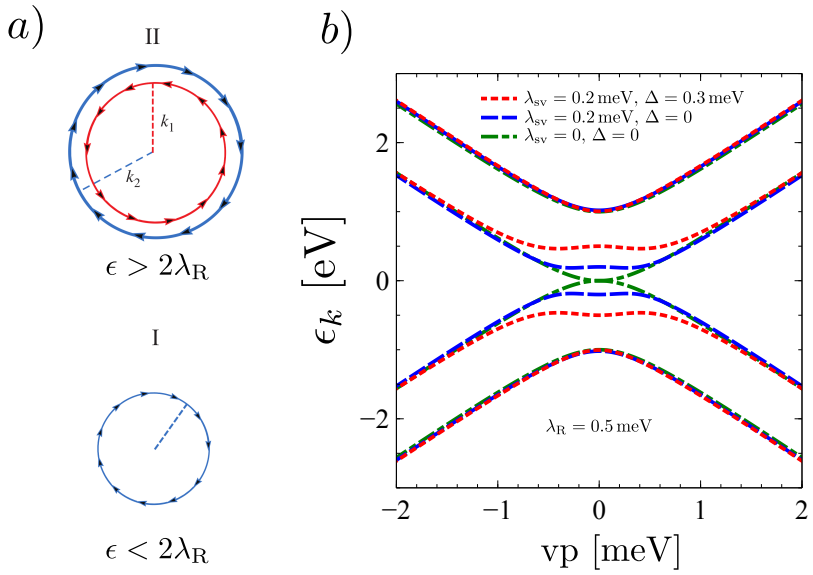

Figure 3.6: Effects of broken symmetries on the electronic band structure of graphene-based vdW heterostructures. Panel (a) shows the spin-momentum locking in the presence of Bychkov-Rashba SOC. On top, the two Fermi rings wind in opposite directions, similar to the 2DEG case (regime II), while on the bottom, a single Fermi ring is present (regime I). This figure is adapted from Ref.[37]. Panel (b) presents the dispersion relation in the presence of spin-orbit interactions. The RSOC spin-splits the valance and conduction bands (green line). The spin-valley coupling produces the Mexican-hat shaped bands, and the mass term rigidly shifts the electrons (holes) bands upward (downward).

random, yielding a broadening of the spectral lines. The idea behind adatom-engineered graphene is rather simple: graphene's carriers tunnel onto an impurity, experience a robust spin-orbit interaction, and then return to the graphene sheet [53]. Depending on the high-symmetry position of the adatom, the "bridge", "hollow", or "top", schematically represented in Fig.(3.7), the effective SOCs generated take many exotic and nontrivial forms [110]. However, this thesis will mainly focus on chemically modified graphene with adatoms in the hollow position, because of particular interest in spintronics. In fact, they most effectively mediate the electrons' next-nearest neighbour hopping, hence the intrinsic-like Kane-Mele SOC $\sim \sigma_z s_z$, as discussed previously.

The combination of scalar electrostatic and Kane-Mele impurities is responsible for a rich phenomenology that includes the extrinsic SHE [19]. It is enabled by the skew scattering mechanism, particularly efficient because of the impurity resonances favoured in graphene. Moreover, the local break of the mirror symmetry also generates local Rashba-like "anomalous" coupling that competes with the intrinsic-like. Recent works developed related theories, discovering the novel semiclassical "anisotropic spin precession" (ASP) mechanism [38, 166]. It is responsible for a substantial enrichment of the phenomenology, which includes and expands the graphene-based heterostructures predictions [35, 19, 31].

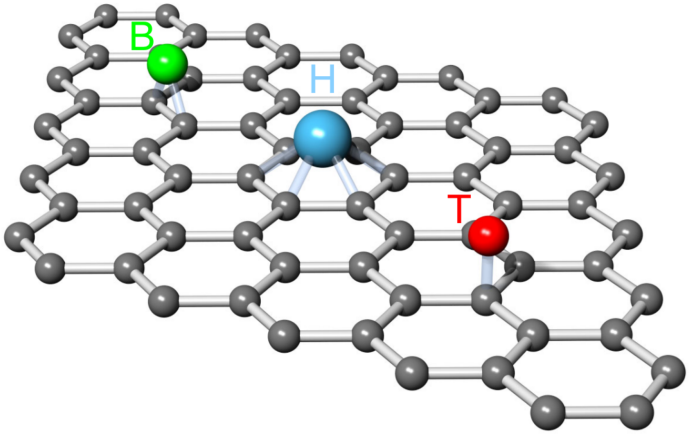

Figure 3.7: Schematics of adatom-decorated graphene with impurities absorbed in the bridge (B), hollow (H), and top (T) position [53]

For instance, the ASP contributes to the production of the CISP in the diffusive regime [38]. While the traditional Edelstein effect is a two-step process governed by the spin-Hall angle and the Rashba scattering rate [17, 167], this new mechanism couples directly spin densities and charge currents, resulting in a sizable CISP. It also renormalises the standard SHE and the spin relaxation processes.

The adatom-decorated graphene Hamiltonian has the form

$$\mathcal{H} = \int d\mathbf{x}\, \psi^{\dagger}(\mathbf{x}) \left[H_0 + V(\mathbf{x})\right] \psi(\mathbf{x}), \tag{3.20}$$

where H_0 is the Dirac minimal model + possible uniform interactions expressed by Eq.(3.19). $V(\mathbf{x})$ denotes the disorder potential,

$$V(\mathbf{x}) = \sum_{i=1}^{N} M R^2 \delta(\mathbf{x} - \mathbf{x}_i) = \sum_{i=1}^{N} W(\mathbf{x} - \mathbf{x}_i), \tag{3.21}$$

where R is the radius of the scatterer, and $R \gg a$. The intervalley scattering is therefore neglected, allowing us to focus on a single valley. M is a 4×4 matrix acting on the sublattice and spin degrees of freedom and it has information about the adatoms potentials, $M = H_R + H_{KM} + H_V$, with

$$\begin{aligned} H_R &= u_R(\gamma_{12} \mp \gamma_{21}), \\ H_{KM} &= u_{KM}\gamma_{33}, \\ H_V &= u_0\gamma_{00}. \end{aligned} \tag{3.22}$$

Λ_i is the impurity coupling and the sign $\mp$ considers both the standard and anomalous Rashba SOC. While the latter describes the hollow impurity insertion, the former accounts for random fluctuations of the uniform Rashba field, always present in realistic settings. We remark that next-order terms in the momentum, which the adatoms produce, can be neglected in the vicinity of the Dirac points [110].

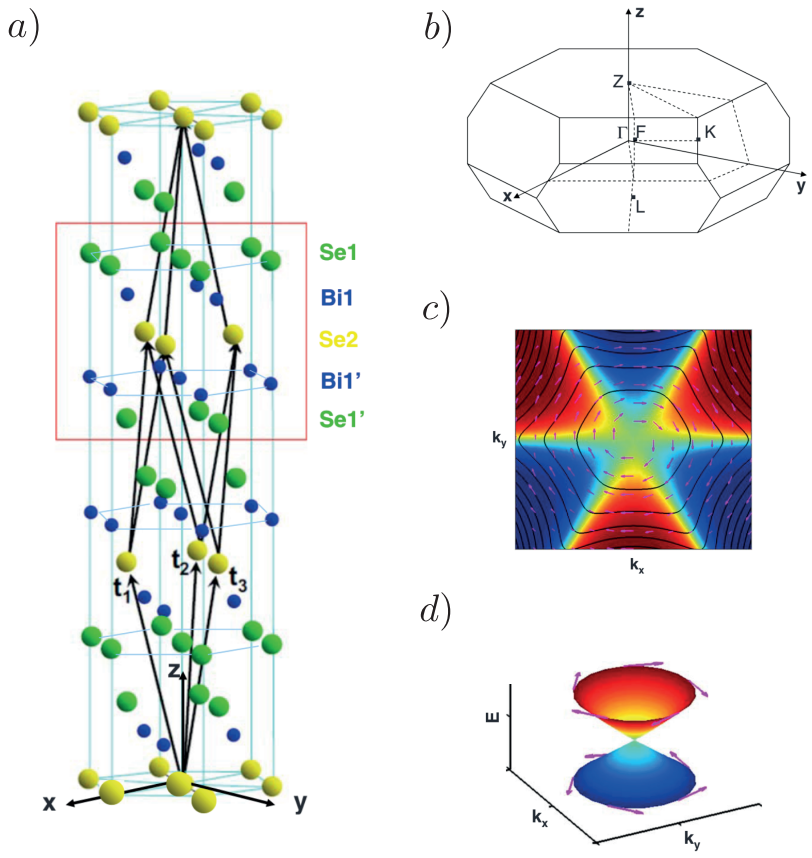

Figure 3.8: Crystal structure of Bi_2Se_3 (a) and corresponding first Brillouin zone (b). In the proximity of the high-symmetry point Γ the dispersion relation becomes linear, and the Fermi surface, initially described by hexagonal warping effects (c), becomes isotropic for $k \to 0$ (d). Figure adapted from Ref.[168].

3.5 Surface states of topological insulators

It is well-known that some phases of matter can be described by topological invariants, similar to the geometrical Gauss-Bonnet theorem [61]. In fact, this theorem states that the surface integral of the Gaussian curvature of an object, which defines the geometrical properties of that object, is quantized, and is a topological invariant. Such states of matter are called *topological phases*. They are traditionally identified by a nontrivial Berry curvature, representing the type of topological order, i.e., the "Gaussian curvature" of the "surface", that is the first Brillouin zone [16]. Historically, topological order was observed and theorized in materials with broken time-reversal symmetry, like 2DEGs with strong magnetic fields and low temperatures, and honeycomb lattice materials within the Haldane model [162], leading to the discovery of the integer quantum Hall effect in terms of the invariant Chern numbers.

A great deal of excitement accompanied the advent of topological $\mathcal{Z}_2$ time-reversal phases in 2D materials, such as graphene, and the focus of this section, 3D solids. In fact, in these media, the topological order is already present with zero magnetic fields,

stemming from the spin-orbit coupling [60], thus leaving the time-reversal symmetry unbroken. While in regular topological systems the topology manifests in the quantized Hall conductivity, in time-reversal topological insulators it generates a quantized spin Hall conductivity, enabling the possibility to generate current-induced spin currents. Here we briefly introduce 3D time-reversal topological insulators, with particular focus on the Bi_2Se_3 family of materials, efficient in terms of charge-spin interconversion mechanisms [169].

The related crystal structure is shown in Fig.(3.8a), and the D^5_{3d} point group symmetry identifies it. In particular, it is invariant under time-reversal symmetry, threefold rotations along the $\hat{z}$-direction, twofold rotations along the $\hat{x}$ direction, and inversion (Se2 $\rightarrow$ Se2, Bi1 $\rightarrow$ Bi1′, Se1 $\rightarrow$ Se1′; $(x, y, z) \rightarrow (-x, -y, -z)$). Ref.[168] elegantly derives the full Hamiltonian by using these symmetries similarly to our graphene section and, most importantly, the corresponding *surface states*. The theoretical establishment for such states has been motivated by angle-resolved photoemission spectroscopy (ARPES) measurements, showing the presence of Dirac cones surface states around the high-symmetry Γ-point [170]. This is, in fact, an important aspect of topological phases; they are gapped in bulk but gapless at the edges, so the carriers mostly travel at the TI surface. In the limit of $k \rightarrow 0$, the resulting low-energy Hamiltonian is expressed by the minimal Dirac model

$$H_{TI} = \mathrm{v}\,(\boldsymbol{p} \times \boldsymbol{s}) \cdot \hat{z}, \tag{3.23}$$

resulting in a linear dispersion relation with helical spin-texture (see Fig.(3.8d)), coming from the atomic SOC in these media. Alike graphene, the eigenstates are labeled by helicity, reason why this systems are also called helical metals. In particular, in the conduction band the helicity is left-handed, while for the valance band is right handed.

Eq.(3.23) has the same form as the standard Rashba SOC in two-dimensional gases, with the difference that in topological insulators, it is promoted from weak perturbation of the quadratic kinetic energy to the sole term. The main physical consequence is the strong spin-momentum locking, yielding sizable charge-spin conversion phenomena, as new magnetoresistance effects [62] and highly efficient SOTs (see Chap.(7)).

As a consequence of the form of the Hamiltonian, the observables of interest in spintronics become directly related to the 2×2 Pauli algebra similarly to what happens in graphene-based systems with the Clifford algebra,

$$\hat{s}_\mu = \psi^\dagger(\mathbf{x})\, s_\mu\, \psi(\mathbf{x}), \tag{3.24}$$

$$\hat{\mathcal{J}}^\nu_\mu = \psi^\dagger(\mathbf{x})\, \frac{1}{2}\{J_\mu, s_\nu\}\, \psi(\mathbf{x}), \tag{3.25}$$

where the current operator is proportional to the spin operator, $J_\mu = e\mathrm{v}\,(\hat{\mu} \times \mathbf{s})$.

Chapter 4

The quantum theory of transport

4.1 Overview

This chapter presents the main methods used in the literature, and this thesis projects, to study transport phenomena in solid-state media. To begin with, we derive the kinetic theory of disordered Fermi systems based on the classical Boltzmann equation (CBE) [171]. This method approximates the electrons' dynamics as classical between scattering events but treats the collisions quantum-mechanically through the Fermi golden rule. For that reason, beyond the traditional disorder Gaussian approximation describing weak uncorrelated impurities, this method effectively incorporates the role of skew scattering and quantum side jump [172] at low impurity concentrations, being able to identify, among other things, the spin Hall effect [19]. The advantage of this formalism over other techniques is the more transparent interpretation of the studied phenomenon, which can therefore be used to establish the mechanisms at the origin of a given effect.

However, not surprisingly, the CBE fails to describe general scenarios in which purely quantum effects play a significant role; a better description of the system's dynamical properties is therefore needed. To this end, we introduce the formalism of the density matrix, which completely defines a many-particle quantum system and replaces the role of the distribution function in classical statistical mechanics. Its first application is the so-called Quantum Boltzmann Equation (QBE) [38] for disordered graphene systems, able to capture quantum effects such as the interference between spin-active impurities and conduction-valence band transitions. In addition, this method offers easy interpretations of the investigated phenomenon and successfully uncovers the ASP mechanism and the Interband Spin-Orbit Scattering, both missed by the CBE. Unfortunately, this technique suffers from two critical downsides: it is based on the projection of the system's Hamiltonian to the conduction states, possibly missing other quantum effects, and is generally not self-consistent, as solving the associated integro-differential closure problem needs the formulation of an ansatz. While this external assumption facilitates problem closure, it may inadvertently neglect crucial contributions to the final result.

The density matrix-based linear response theory overcomes these drawbacks, offering a complete self-consistent, fully-quantum mechanical system description. In par-

ticular, this chapter derives the widely-used Kubo formula with an emphasis on the diagrammatic handling of the theory and focusing on Feynman's diagrams related to non-interacting disordered fermionic systems. In this context, we present the nonperturbative treatment of stochastic disorder potentials referred to as T-matrix approximation, which requires the inclusion of a new class of diagrams previously neglected in the traditional First Born Approximation [19, 51]. In conclusion, we rearrange the Kubo formula in a way to find the kinetic equation of the system, able to derive the spin-charge coupled dynamics, spin relaxation mechanisms, and drift-diffusion equations. This technique, commonly used in Gaussian approximation, is further developed here. We call it Diffuson Hamiltonian formalism, fully self-consistent and able to treat the disorder at the T-matrix level.

4.2 Kinetic theory

The foundation of the classical kinetic theory of gases, valid in quantum systems as well with due differences, is the idea of relating macroscopic thermodynamic quantities to the statistical average of microscopic observables $O(\mathbf{p}, \mathbf{q})$, defined as

$$\langle O \rangle (\mathbf{q}, t) = \int_{\mathbf{p}} O(\mathbf{p}, \mathbf{q}) \; f(\mathbf{p}, \mathbf{q}, t) \; , \tag{4.1}$$

where $f(\mathbf{p}, \mathbf{q}, t)$ is the distribution function, representing the probability of finding a particle with momentum $\mathbf{p}$ and position $\mathbf{q}$ at a given time t. Among others, the equation above can be used to find the average velocity of a fluid, its density, pressure, and temperature. In the most simple case of a dilute gas in the absence of external fields, the distribution function becomes independent of the position $\mathbf{q}$ and, as an extraordinary result of Boltzmann's H theorem [171], is also constant in time. The resulting *equilibrium* distribution function, $f_0(\mathbf{p})$, corresponds to the Maxwell-Boltzmann distribution for non-interacting classical gases, and the Fermi-Dirac or the Bose-Einstein statistics in quantum systems. On the other hand, in the presence of external perturbations, scattering effects, gradients of temperature, and particles' concentration, $f(\mathbf{p}, \mathbf{q}, t)$ differs from the equilibrium distribution function and produces observables otherwise equals to zero, like charge and spin currents [19] or nonequilibrium charge and spin macroscopic accumulations [52].

In short, the knowledge of the distribution function provides a complete understanding of the macroscopic properties of a many-body system based on the microscopic interactions and dynamical properties of the particles that compose it. A general and relatively simple way to derive the form of $f(\mathbf{p}, \mathbf{q}, t)$ is to solve the so-called Boltzmann equation, presented in the next section.

4.2.1 The Boltzmann equation

At a specific time t, the mechanical state of a dilute gas of N classical particles is defined by the position $\mathbf{q}$ and the momentum $\mathbf{p}$ of all the particles. Their dynamics are commonly represented in the so-called μ phase-space, where the six components of

$\mathbf{q}$ and $\mathbf{p}$ play the role of coordinates. According to the definition of the distribution function, the number of particles $\mathrm{d}N\left(\mathbf{q},\mathbf{p},t\right)$, contained in a volume element $\mathrm{d}^3p\mathrm{d}^3q$, is determined by

$$\mathrm{d}N\left(\mathbf{q},\mathbf{p},t\right)=f\left(\mathbf{q},\mathbf{p},t\right)\mathrm{d}^3p\mathrm{d}^3q, \tag{4.2}$$

which relates the statistical properties of the system, represented by f, to the particles' microscopic dynamics, included in $\mathrm{d}N$. After a time interval $\mathrm{d}t$ the system evolved, and the particles will be moved into another phase-space element $\mathrm{d}^3p'\mathrm{d}^3q'$ of same volume, according to the Liouville theorem. Moreover, if we neglect the interactions among the particles, their number $\mathrm{d}N$ is also preserved, thus the following relation must hold,

$$f\left(\mathbf{q}',\mathbf{p}',t+\mathrm{d}t\right)=f\left(\mathbf{q},\mathbf{p},t\right), \tag{4.3}$$

where $\mathbf{q}'=\mathbf{q}+\dot{\mathbf{q}}\mathrm{d}t$ and $\mathbf{p}'=\mathbf{p}+\dot{\mathbf{p}}\mathrm{d}t$ according to the classical equations of motions. By expanding to linear order in $\mathrm{d}t$, we obtain

$$\frac{\mathrm{d}N}{\mathrm{d}t}=\frac{\partial f}{\partial t}+\mathbf{v}\cdot\frac{\partial f}{\partial\mathbf{q}}+\mathbf{F}\cdot\frac{\partial f}{\partial\mathbf{p}}=0, \tag{4.4}$$

where $\mathbf{v}=\dot{\mathbf{q}}$ is the velocity of the particles and $\mathbf{F}=\dot{\mathbf{p}}$ is the external force. Eq.(4.4) must be integrated with the collision processes occurring during the motion of the particles, leading to a net rate of change in the number of elements inside the phase-space volume. We then introduce a function comprising these information, the *collisional integral* I, defined as

$$\frac{\mathrm{d}N}{\mathrm{d}t}=I\mathrm{d}^3p\mathrm{d}^3q, \tag{4.5}$$

where $\mathrm{d}N/\mathrm{d}t$ is the number of collisions inside the volume element. The particles that enter (leave) the volume element as a result of particle-particle interactions, are described by the scatter-in (out) component of the collisional integral, $I=I_{\mathrm{in}}-I_{\mathrm{out}}$. Assuming binary collisions, valid for sufficiently high diluted systems, and molecular chaos, in which two interacting particles are statistically independent [173], the collisional integral becomes

$$I=\int_{\mathbf{p}_2}\int_{\mathbf{p}_{1'}}\int_{\mathbf{p}_{2'}}\frac{1}{2m^2}\frac{\mathrm{d}\sigma}{\mathrm{d}\Omega}\left[f(\mathbf{p'}_1)f(\mathbf{p'}_2)-f(\mathbf{p}_1)f(\mathbf{p}_2)\right]\delta_\epsilon\,\delta_p, \tag{4.6}$$

describing two particles entering in the volume element with initial momenta $\mathbf{p'}_1$ and $\mathbf{p'}_2$, colliding, and leaving with new momenta $\mathbf{p}_1$ and $\mathbf{p}_2$. $\frac{\mathrm{d}\sigma}{\mathrm{d}\Omega}$ is the classical differential cross-section, m is the mass of the particles and $\delta_{\epsilon(p)}$ is the Dirac delta expressing the conservation of the energy (momentum), i.e., $\delta_\epsilon=\delta\left(\epsilon_1^{'}+\epsilon_2^{'}-\epsilon_1-\epsilon_2\right)$ and $\delta_p=\delta\left(\mathbf{p}_1^{'}+\mathbf{p}_2^{'}-\mathbf{p}_1-\mathbf{p}_2\right)$. Putting together Eqs.(4.4) and (4.5), we finally obtain a closed relation for the distribution function,

$$\frac{\partial f}{\partial t}+\mathbf{v}\cdot\frac{\partial f}{\partial\mathbf{q}}+\mathbf{F}\cdot\frac{\partial f}{\partial\mathbf{p}}=I, \tag{4.7}$$

that is the Classical Boltzmann Equation (CBE). The system is driven out of equilibrium by the joint effects of external fields ($\mathbf{F}$) and collisions (I) and the resulting statistics can be derived from Eq.(4.7).

Clearly, this formalism is strictly valid only for classical systems since the distribution function requires simultaneous knowledge of the position and momentum arguments, contradicting Heisenberg's uncertainty principle. Moreover, the derivation of the Boltzmann equation avails particles' classical trajectories within Newtonian dynamics, again far from the quantum mechanical picture. Nevertheless, Eq.(4.7) can be extended to study non-classical gases, in which quantum mechanical effects become relevant when particles collide and their wave functions overlap. This semiclassical picture encapsulates all the quantum information inside the collisional integral and approximates the particles' motions as classical between scattering events, allowing the usage of momentum-distribution functions at each point in space. To ascertain the validity of such approximation, the average distance between particles d, defined as the ratio between the number of particles and the volume, is compared with the *thermal wavelength*, $\lambda_{\mathrm{T}} = h/\sqrt{2\pi m k_{\mathrm{B}} \mathrm{T}}$, which estimates the size of the particles' wave functions. If $d \gg \lambda_{\mathrm{T}}$, the particles are non-interacting, and the fluid can be treated as semiclassical.

4.2.2 The semiclassical

Boltzmann equation

Being interested in electronic transport processes in solids, here we examine how the CBE formalism can be applied to solid-state non-interacting (or weakly-interacting) systems, primarily defined by the relative electronic band structures and the single-particle Hamiltonian. At thermodynamic equilibrium, the probability of occupation of an electronic energy band $\epsilon_\chi(\mathbf{k})$, is given by the Fermi-Dirac distribution function

$$g_{0\chi}\left(\mathbf{k}\right) = \frac{1}{e^{(\epsilon_\chi(\mathbf{k})-\varepsilon)/k_B T}+1}, \tag{4.8}$$

where $\mathbf{k} = \mathbf{p}/\hbar$ is the wave vector, χ is the band index distinguishing between different branches of the dispersion relation, and ε is the Fermi energy. When external perturbations are applied to the system, the disturbed distribution function $g_\chi\left(\mathbf{k}\right)$ follows Eq.(4.7), assuming semiclassical dynamics of the electrons between two collisions. We adapt the left-hand side of the Boltzmann equation by replacing the particles' velocity with the electrons' group velocity

$$\mathbf{v}_{\mathbf{k},\chi} = \frac{1}{\hbar}\frac{\partial \epsilon_\chi(\mathbf{k})}{\partial \mathbf{k}}, \tag{4.9}$$

while the collisional integral takes the form

$$I[g_\chi] = -\sum_{\chi'}\int_{\mathbf{k}'}\left[g_\chi\left(\mathbf{k}\right)\left(1-g_{\chi'}\left(\mathbf{k}'\right)\right)W_{\mathbf{k}\chi,\mathbf{k}'\chi'} - g_{\chi'}\left(\mathbf{k}'\right)\left(1-g_\chi\left(\mathbf{k}\right)\right)W_{\mathbf{k}',\chi' k\chi}\right], \tag{4.10}$$

with $W_{\mathbf{k}\chi,\mathbf{k}'\chi'}$ being the probability per unit time that an electron, defined by the quantum numbers $\mathbf{k}$ and χ, is scattered into a state $|\mathbf{k}',\chi'\rangle$. The terms of the form

$g_\chi(\mathbf{k})(1-g_{\chi'}(\mathbf{k}'))$ take into account the Pauli exclusion principle, allowing transitions from occupied initial states to non-occupied final states. At equilibrium, the collisional integral must vanish and, for elastic interactions ($\epsilon_\chi(\mathbf{k}) = \epsilon_{\chi'}(\mathbf{k}')$), a scattering event is balanced by its reverse process, implying $W_{\mathbf{k}\chi,\mathbf{k}'\chi'} = W_{\mathbf{k}'\chi',\mathbf{k}\chi}$. From Eq.(4.10), we extract the condition

$$\log\left(g_\chi(\mathbf{k})\right) = \log(g_{\chi'}(\mathbf{k}')), \tag{4.11}$$

that is satisfied by the Fermi-Dirac statistics, i.e: $I[g_{0\chi}] = 0$. To make the quantum version of Eq.(4.7) more treatable, we assume small deviations of the distribution function from its equilibrium state due to weak perturbations [157], defining

$$g_\chi(\mathbf{k}) = g_{0\chi}(\mathbf{k}) + \delta g_\chi(\mathbf{k}), \tag{4.12}$$

where $\delta g_\chi(\mathbf{k})$ linearly depends on the applied perturbation. Focusing our interest on the response of homogeneous systems to an external electric field $\mathbf{E}$, we can write a linearized Boltzmann equation in the first order in the perturbation as

$$\frac{\partial \delta g_\chi(\mathbf{k})}{\partial t} - \mathrm{e}\lambda_{\mathbf{k},\chi}\mathbf{E}\cdot\mathbf{v}_{\mathbf{k},\chi}\frac{\partial g_{0\chi}(\mathbf{k})}{\partial \epsilon_\chi(\mathbf{k})} = -\sum_{\chi'}\int_{\mathbf{k}'}[\delta g_\chi(\mathbf{k})W_{\mathbf{k}\chi,\mathbf{k}'\chi'} - \delta g_{\chi'}(\mathbf{k}')W_{\mathbf{k}',\chi'k\chi}], \tag{4.13}$$

where $\lambda_{\mathbf{k},\chi} \equiv \mathrm{sign}(\epsilon_\chi(\mathbf{k}))$.

Eq.(4.13) is the main result of this section and the first tool we developed to study semiclassical transport effects in solids. We term this generalization of the CBE, which encompasses quantum effects during particle collisions *semiclassical Boltzmann equation* [174, 175]. It can be solved by formulating a suitable *ansatz* for the distribution function in terms of the scattering times $\sum_i\{\tau_i\}$, which in the best-case scenario closes the equation, but in general provides non-self-consistent solutions for τ_i. Moreover, the CBE requires the microscopic description of the scattering processes encoded in $W_{\mathbf{k}\chi,\mathbf{k}'\chi'}$, which, in our case, includes only the effect of randomly distributed impurities, regarded here as the only scatterers, neglecting electron-electron and electron-phonon interactions. The physics of scattering processes is then described by the Lippmann-Schwinger equation, yielding a generalized Fermi golden rule for the transition rates $W_{\mathbf{k}\chi,\mathbf{k}'\chi'}$.

4.2.3 The Golden Rule

To evaluate the scattering probability $W_{\mathbf{k}\chi,\mathbf{k}'\chi'}$ in disordered systems we use the so-called golden rule [176], defined as

$$W_{\mathbf{k}\chi,\mathbf{k}'\chi'} = \frac{2\pi}{\hbar}\left|T_{\mathbf{k}\chi,\mathbf{k}'\chi'}\right|^2\delta(\epsilon_{\mathbf{k}\chi} - \epsilon_{\mathbf{k}'\chi'}), \tag{4.14}$$

where

$$T_{\mathbf{k}'\chi',\mathbf{k}\chi} = \langle\mathbf{k}',\chi'|\hat{U}|\psi_{\mathbf{k},\chi}\rangle \tag{4.15}$$

is the T-matrix operator and $\hat{U}$ is the impurity potential. $|\mathbf{k}', \chi'\rangle$ is an eigenstate of the system's Hamiltonian $\hat{H}_0$, while $|\psi_{\mathbf{k},\chi}\rangle$ is solution of the Lippmann-Schwinger equation

$$|\psi_{\mathbf{k},\chi}\rangle = |\mathbf{k}, \chi\rangle + \frac{\hat{U}}{\epsilon_\chi(\mathbf{k}) - \hat{H}_0 + \mathrm{i}\eta}|\psi_{\mathbf{k},\chi}\rangle, \tag{4.16}$$

and eigenstate of the full Hamiltonian $\hat{H} = \hat{H}_0 + \hat{U}$. For weak impurity interactions, one can truncate the series in Eq.(4.16) in powers of $\hat{U}$. The first order expansion, $|\psi_{\mathbf{k},\chi}\rangle = |\mathbf{k}, \chi\rangle$, is called First Born approximation (FBA) and Eq.(4.17) becomes the conventional Fermi golden rule

$$W^{\mathrm{Born}}_{\mathbf{k}\chi,\mathbf{k}'\chi'} = \frac{2\pi}{\hbar}\left|\langle\mathbf{k}', \chi'|\hat{U}|\mathbf{k}, \chi\rangle\right|^2 \delta(\epsilon_\chi(\mathbf{k}) - \epsilon_{\chi'}(\mathbf{k}')), \tag{4.17}$$

that is traditionally implemented in the semiclassical Boltzmann formalism. A further assumption, which we refer to as the Gaussian approximation (GA) in this thesis, disregards the matrix structure of $|\hat{U}|^2$ as well as the interaction between different types of SOC-active disorder, including only the scalar component of the impurity potential.

Must be noticed that the weak FBA and GA miss next order effects triggered by the spin-orbit interaction. To show that in a general way, we notice that the scattering amplitude, proportional to the second term on the right-hand side of Eq.(4.16), takes the general form

$$f(\vartheta) = A(\vartheta) + B(\vartheta)\,\mathbf{s}\cdot\mathbf{n}, \tag{4.18}$$

where ϑ is the scattering angle and $\mathbf{n} = \mathbf{p}' \times \mathbf{p}/\left|\mathbf{p}' \times \mathbf{p}\right|$ is the unit vector normal to the scattering plane [18, 7, 21]. In general, four cross-sections describe the depolarization of an electron beam in a scattering event,

$$\sigma_1 = |A|^2 + |B|^2, \tag{4.19}$$
$$\sigma_2 = 2\mathrm{Re}(AB^*), \tag{4.20}$$
$$\sigma_3 = 2\mathrm{Im}(AB^*), \tag{4.21}$$
$$\sigma_4 = 2|B|^4, \tag{4.22}$$

related, respectively, to the transport cross-section, skew scattering, spin-current swapping, and Elliot-Yafet spin-relaxation. In FBA, the scattering amplitude becomes

$$f \sim \langle\mathbf{p}'|V_0(\mathbf{x}) + H_{\mathrm{SOC}}(\mathbf{x})|\mathbf{p}\rangle, \tag{4.23}$$

where V_0 is a scalar impurity potential and $H_{\mathrm{SOC}} = \lambda_{\mathrm{SOC}}\,\mathbf{s}\times\nabla(V(\mathbf{x}))(-\mathrm{i}\nabla)$ the spin-orbit interaction. In FBA we obtain

$$\langle\mathbf{p}'|H_{\mathrm{SOC}}(\mathbf{x})|\mathbf{p}\rangle = \int d\mathbf{x} e^{-\mathrm{i}\mathbf{p}'\cdot\mathbf{x}} H_{\mathrm{SOC}} e^{\mathrm{i}\mathbf{p}\cdot\mathbf{x}} = -\mathrm{i}\lambda_{\mathrm{SOC}} V(\mathbf{p}-\mathbf{p}')\mathbf{p}\times\mathbf{p}'\cdot\mathbf{s}, \tag{4.24}$$

meaning that $A = V(\mathbf{q})$ and $B = -\mathrm{i}\lambda_{\mathrm{SOC}}|\mathbf{p}|^2 A$ for elastic scattering. As a consequence, $\sigma_2 = 0$, and no skew scattering contribution is established.

Shifting our attention to a more specific example of relevance for this thesis, we examine pristine graphene with scalar and intrinsic-like impurities. The scattering

potential is expressed by $\hat{U} = \sum_{i=0}^{N} V\delta(\mathbf{x} - \mathbf{x}_i)$, where $V = u_0\,\gamma_{00} + u_{\mathrm{KM}}\,\gamma_{33}$ and $u_{0(\mathrm{KM})}$ is the impurity potential strength. The spin-orbit interaction $\sim u_{\mathrm{KM}}$ preserves the spin of the scattered electrons and provides a way to activate skew scattering [19, 177]. Since the impurities are randomly distributed in the system, we define a distribution for $\hat{U}$ such that the disorder average $\langle U_{\mathbf{k}'\chi',\mathbf{k}\chi} U_{\mathbf{k}\chi,\mathbf{k}'\chi'}\rangle_{\mathrm{dis}} = n_i V^2$ (or equivalently $\langle U_{\chi',\chi}(\mathbf{x}) U_{\chi,\chi'}(\mathbf{x}')\rangle_{\mathrm{dis}} = n_i V^2 \delta(\mathbf{x} - \mathbf{x}')$) and the next moments are zero, where $U_{i,j} = \langle i|\hat{U}|j\rangle$ and n_i is the impurity concentration. This ansatz assumes a Gaussian or box distribution of the stochastic impurity potential. More in general, it adopts a *symmetric* distribution, where the odd irreducible cumulants of $\hat{U}$ are absent, and also disregards higher even orders of $\hat{U}$, assuming their irrelevance in the renormalization group sense [178]. In Born approximation we finally find

$$W^{\mathrm{Born}}_{\mathbf{k}\chi,\mathbf{k}'\chi} \sim \cos(\theta - \phi) = \cos\varphi, \tag{4.25}$$

where θ (ϕ) is the angle associated to the momentum $\mathbf{k}$ ($\mathbf{k}'$). Eq.(4.25) is symmetrical in φ, meaning that the electrons are scattered with same probability in opposite directions.

To capture skew scattering we need to include at minimum order U^3 terms [19, 176] by expanding Eq.(4.16) up to the second order

$$|\psi_{\mathbf{k},\chi}\rangle \approx |\mathbf{k},\chi\rangle + \sum_{\mathbf{k}'',\chi''} \frac{U_{\mathbf{k}''\chi'',\mathbf{k}\chi}}{\epsilon_\chi(\mathbf{k}) - \epsilon_{\chi''}(\mathbf{k}'') + \mathrm{i}\eta} |\mathbf{k}'',\chi''\rangle, \tag{4.26}$$

and allow a "non-Gaussian" disorder average of the form $\langle U_{\mathbf{k}'\chi',\mathbf{k}\chi} U_{\mathbf{k}'\chi',\mathbf{k}''\chi''} U_{\mathbf{k}''\chi'',\mathbf{k}\chi}\rangle_{\mathrm{dis}} = n_i V^3$. In this case, we are adopting an *asymmetric* distribution of the impurity potential that allows a third order moment called, not by chance, "skewness". The scattering rate up to the third order becomes

$$W^{\mathrm{Skew}}_{\mathbf{k}\chi,\mathbf{k}'\chi'} = \frac{2\pi}{\hbar} \left(\sum_{\mathbf{k}'',\chi''} \frac{\langle U_{\mathbf{k}'\chi',\mathbf{k}\chi} U_{\mathbf{k}'\chi',\mathbf{k}''\chi''} U_{\mathbf{k}''\chi'',\mathbf{k}\chi}\rangle_{\mathrm{dis}}}{\epsilon_\chi(\mathbf{k}) - \epsilon_{\chi''}(\mathbf{k}'') - \mathrm{i}\eta} + \mathrm{c.c.} \right) \delta(\epsilon_{\mathbf{k}\chi} - \epsilon_{\mathbf{k}'\chi'}), \tag{4.27}$$

that in our example translates to

$$W^{\mathrm{Skew}}_{\mathbf{k}\chi,\mathbf{k}'\chi} \sim A_\chi + B_\chi \cos\varphi + C_\chi \sin\varphi + D_\chi \cos\varphi^2, \tag{4.28}$$

where A_χ, B_χ, C_χ, and D_χ are functions of the microscopic parameters. This solution is asymmetric in φ, inducing spin up and down electrons to be preferably scattered in opposite directions.

The formalism of the golden rule, based on the Lippmann-Schwinger equation, is particularly beneficial to understand the physics behind collisions and the statistical treatment of the scattering probabilities. However, it turns out to be cumbersome at higher orders in perturbation theory, and it is incapable of describing the disorder's nonperturbative approach. Therefore, Sec. (4.4) offers a convenient solution, where the scattering rates are formulated in terms of Feynman propagators in the context of the Kubo formula and adopted in the semiclassical Boltzmann formalism.

4.2.4 Exact solution of linearized Bolzmann equation for isotropic Fermi surfaces

We now briefly discuss how the linearized Boltzmann equation can be employed in systems with isotropic Fermi surfaces in the presence of intrinsic and extrinsic SOC, offering a valuable example of this method's application. The outcome is a simple relation connecting the out-of-equilibrium distribution function $g_\chi(\mathbf{k})$ to the probability rates $W_{\mathbf{k}\chi,\mathbf{k}'\chi'}$, and this result has proven relevant in graphene with intrinsic-like impurities [36] and graphene-based heterostructure with uniform Rashba spin-orbit interaction [8]. In our projects, it is successfully applied in twisted graphene/TMD (Chap.(6)), where we account for the effect of the spin-valley coupling, and adapted with extra care in graphene with scalar and Rashba-like impurities (Chap.(5)).

Our interest lies on the stationary state of the system, which implies $\frac{\partial \delta g_\chi(\mathbf{k})}{\partial t} = 0$, and, without loss of generality, we consider an electric field oriented along the x-axis. We implement the following ansatz,

$$\delta g_\chi(\mathbf{k}) = A_\chi(k)\mathrm{v}_{k,\chi}\cos\beta_{\mathbf{k}} + B_\chi(k)\mathrm{v}_{k,\chi}\sin\beta_{\mathbf{k}}, \tag{4.29}$$

where $A(B)_\chi$ are called *transport coefficients*. For isotropic Fermi surfaces, Eq.(4.29) closes the linearized Boltzmann equation, meaning that Eq.(4.13) can be solved to find the transport coefficients and the final form of the distribution function. Feeding the LBE with our ansatz for the distribution function we find a set of $N = 2\chi$ transport equations

$$eE\,\delta(\epsilon_\chi(\mathbf{k}) - \varepsilon) = \sum_{\chi'}\left\{\frac{\mathrm{v}_{k',\chi'}}{\mathrm{v}_{k,\chi}}A_{\chi'}(k')\Gamma^{[\chi',\chi]}_{\cos} + \frac{\mathrm{v}_{k',\chi'}}{\mathrm{v}_{k,\chi}}B_{\chi'}(k')\Gamma^{[\chi',\chi]}_{\sin} - A_\chi(k)\Gamma^{[\chi,\chi']}_{\mathrm{iden}}\right\}, \tag{4.30}$$

$$0 = \sum_{\chi'}\left\{\frac{\mathrm{v}_{k',\chi'}}{\mathrm{v}_{k,\chi}}B_{\chi'}(k')\Gamma^{[\chi',\chi]}_{\cos} - \frac{\mathrm{v}_{k',\chi'}}{\mathrm{v}_{k,\chi}}A_{\chi'}(k')\Gamma^{[\chi',\chi]}_{\sin} - B_\chi(k)\Gamma^{[\chi,\chi']}_{\mathrm{iden}}\right\}, \tag{4.31}$$

where we defined the quantities

$$\int_{\mathbf{k}'}\cos(\phi_{\mathbf{k}'\mathbf{k}})W_{\mathbf{k}'\chi',\mathbf{k}\chi} = \Gamma^{[\chi',\chi]}_{\cos}, \tag{4.32}$$

$$\int_{\mathbf{k}'}W_{\mathbf{k}'\chi',\mathbf{k}\chi} = \Gamma^{[\chi',\chi]}_{\mathrm{iden}}, \tag{4.33}$$

$$\int_{\mathbf{k}'}\sin(\phi_{\mathbf{k}'\mathbf{k}})W_{\mathbf{k}'\chi',\mathbf{k}\chi} = \Gamma^{[\chi',\chi]}_{\sin}, \tag{4.34}$$

and $\phi_{\mathbf{k}'\mathbf{k}} = \beta_{\mathbf{k}'} - \beta_{\mathbf{k}}$. Eq.(4.30–4.34) are simple ready-to-use relations linking the microscopic scattering processes described by the collisional golden rule and the macroscopic deviation of the system from its equilibrium state, resulting in an out-of-equilibrium response expressed by Eq.(4.1).

We now take a step forward and leverage this method further by reducing the problem's generality and focusing on the particular case of graphene with uniform Rashba

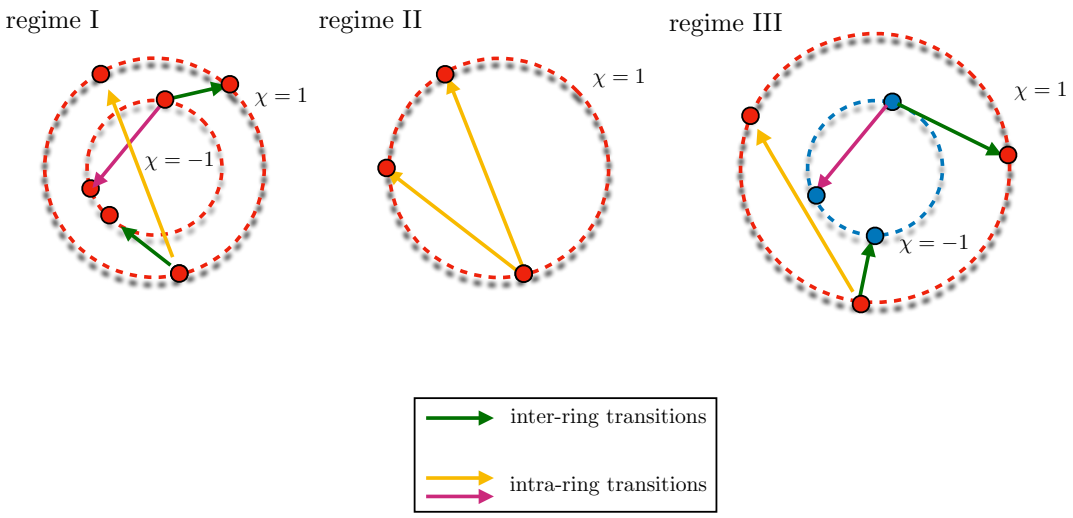

Figure 4.1: Graphical visualization of the impurity scattering processes in the 2D Dirac model with intrinsic SOC. In regime II the electrons are confined in a single Fermi ring, and consequently, only intra-ring transitions occur. Regime I and III describe the two Fermi ring-case, and inter-ring transitions are also allowed.

and interface-induced magnetic exchange coupling (MEC) or spin-valley SOC. Moreover, we consider only the electrons' conduction (valance) states for positive (negative) Fermi energy, $\varepsilon \gtrless 0$, implying that the band index $\chi = \pm$ defines the upper (lower) energy band. The related band structure describes electronic states lying on a single band or two bands depending on the value of the Fermi energy [8]. In the first case, the quasi-particles can only undergo intra-ring scattering transitions, while inter-ring and intra-ring transitions are allowed in the latter (see Fig.(4.1)). This information is entirely encoded in the scattering golden rule that involves overlapping states belonging to the same energy band ($W_{\mathbf{k}+,\mathbf{k}'+}, W_{\mathbf{k}-,\mathbf{k}'-}$) or two different bands ($W_{\mathbf{k}+,\mathbf{k}'-}, W_{\mathbf{k}-,\mathbf{k}'+}$). Having this in mind, we can now solve the system of four equations defined by Eqs.(4.30) and (4.31) with no need for explicit expressions for the probability rates $W_{\mathbf{k}\chi,\mathbf{k}'\chi'}$. Moreover, the scattering coefficients $\{A_+(k), A_-(k), B_+(k), B_-(k)\}$ are related to the so-called *scattering rates* $\{\tau_\parallel, \tau_\parallel^*, \tau_\perp, \tau_\perp^*\}$ so that the charge conductivity and the spin-Hall conductivity admit an exact closed-form

$$\sigma_{xx} = \frac{g_v e^2 \mathrm{v}^2 \rho(\epsilon_\mathrm{F})}{2\pi} \frac{\tau_\parallel}{1 + \frac{\tau_\parallel \tau_\parallel^*}{\tau_\perp \tau_\perp^*}}, \tag{4.35}$$

$$\sigma_{xy}^z = \frac{g_v e^2 \mathrm{v}^2 \rho(\epsilon_\mathrm{F})}{2\pi} \frac{\tau_\perp}{1 + \frac{\tau_\perp \tau_\perp^*}{\tau_\parallel \tau_\parallel^*}}, \tag{4.36}$$

where v is the Fermi velocity, $g_v = 2$ is the valley degeneracy, and $\rho(\epsilon_\mathrm{F})$ is the density of states of graphene. We have defined the scattering rates as

$$\frac{1}{\tau_{\parallel}} = \Gamma_{\text{iden}} - \Gamma_{\text{cos}} + \Gamma^{\text{flip}}_{\text{iden}} - \frac{v_{\pm}}{v_{\mp}}\Gamma^{\text{flip}}_{\text{cos}}, \tag{4.37}$$

$$\frac{1}{\tau^{*}_{\parallel}} = \Gamma_{\text{iden}} - \Gamma_{\text{cos}} + \Gamma^{\text{flip}}_{\text{iden}} + \frac{v_{\pm}}{v_{\mp}}\Gamma^{\text{flip}}_{\text{cos}}, \tag{4.38}$$

$$\frac{1}{\tau_{\perp}} = \Gamma_{\text{sin}} + \frac{v_{\pm}}{v_{\mp}}\Gamma^{\text{flip}}_{\text{sin}}, \tag{4.39}$$

$$\frac{1}{\tau^{*}_{\perp}} = \Gamma_{\text{sin}} - \frac{v_{\pm}}{v_{\mp}}\Gamma^{\text{flip}}_{\text{sin}}, \tag{4.40}$$

$$\tag{4.41}$$

where $v_{\pm}$ is the electrons' group velocity at the Fermi level in the outer (inner) Fermi ring. $\tau_{\parallel}$ is the standard longitudinal transport time responsible for the emergence of the charge conductivity (Eq.(4.35)), while $\tau_{\perp}$ is the skew scattering antisymmetric term at the origin of a net transverse spin current (Eq.(4.36)). Eqs.(4.35–4.40) are the main result of this section, relating directly the observable of interest to us to the microscopic processes involved in the system. This method can also be easily applied to systems described by a single band, identical to the regime II case in the presence of SOC, in which $v_{+} = v_{-}$ and $\tau_{\parallel(\perp)} = \tau^{*}_{\parallel(\perp)}$.

In Ref.[19], the spin-Hall conductivity in pristine graphene with intrinsic-like SOC and scalar impurities is successfully evaluated with this method. The result of Milletari and Ferreira [19] is virtually indistinguishable from the outcome of a more sophisticated self-consistent diagrammatic approach. However, this work points out that the two analytic expressions for the response do not coincide for strong impurity potential due to the semiclassical approximation required in the Boltzmann approach, as we also stressed in Sec.(4.2.1). Mathematically, this is realized by the sole implication of the clean system's eigenstates in the golden rule (Eq.(4.17)), which disregards the effect of the background disorder field in the electrons' trajectory [179]. Therefore, this method is no longer valid when the propagators cannot be treated as classical objects and Eq.(4.17) breaks down, as we will show in Chap.(5). Another limitation is represented by non-isotropic band structures, realized, for example, by the presence of in-plane MEC (see Chaps.(7) or the retention of higher order terms in the Hamiltonian of TIs [180], in which Eq.(4.29) fails to close the system of equations and a more general ansatz is needed.

4.3 The Liouville equation

The extension of the Boltzmann equation to quantum gases, derived in the former section and widely used to study weakly disordered systems [31, 8, 181], is an incomplete description of the quantum particles' dynamics. The reason lies in the semiclassical nature of the Boltzmann formalism, in which the quantum mechanical cross-section is employed to describe scattering events, but the particles are treated as classical objects between collisions [179].

Even though this formalism has been successfully extended to include single-impurity semiclassical skew-scattering [19, 176] and the side jump [182, 172], it fails to predict other quantum effects, such as the contribution of randomly distributed extrinsic SOC [166]. For that reason, this section presents a fully quantum approach to evaluate the observable of interest to us, in particular spin-currents and densities . We introduce the density matrix formalism and the Liouville equation, in the context of the Boltzmann-Gibbs theory. In this context, we offer an intelligible and tractable equation to derive the out-of-equilibrium distribution function in bare graphene with general SOC impurities: the quantum Boltzmann equation, first formulated in Ref.[38] to uncover the ASP mechanism and capable to predict other exotic spin-conversion effects such as the interband skew-scattering. The theoretical framework introduced here will serve as the foundation for introducing the Kubo-Streda formula in the upcoming chapter

4.3.1 The Boltzmann-Gibbs theory

Alternatively to Eq.(4.1), the connection between a thermodynamic macroscopic observable O_{TH} and its microscopic counterpart $O(\{q(t)\},\{p(t)\})$ is defined as

$$O_{TH}(t) = \langle O \rangle (t) = \frac{1}{t}\int_0^t dt' O(\{q(t')\},\{p(t')\}), \tag{4.42}$$

where $\{q(t)\}$ and $\{p(t)\}$ are sets of time-evolving particle positions and momenta in the 6N-dimensional phase space $\Gamma_{q,p} = \{p\}\{q\}$. Eq.(4.42) represents the temporal average of O along the trajectory in $\Gamma_{q,p}$ outlined by the Hamiltonian H, called energy surface. Even though this description is relatively intuitive, it is not ideal for operative purposes. J.W. Gibbs overcame this difficulty by replacing Eq.(4.42) with an average over many virtual microscopic copies of the system (micro-states) at $t = 0$, called an *ensemble* (ergodic hypothesis) [171]. The idea behind that is to translate the time spent by the system's particles in the phase space into a density of virtual copies of the system, represented by the distribution function $\rho(\{q\},\{p\},t)$. Using this picture, we may write Eq.(4.42) as

$$\langle O \rangle (t) = \int d\Gamma_{q,p}\, \rho(\{q\},\{p\},t)\, O(\{q\},\{p\}), \tag{4.43}$$

where the distribution function $\rho(\{q\},\{p\},t)$ in general evolves over time according to the Liouville theorem

$$\partial_t \rho = -\{\rho, H\}, \tag{4.44}$$

where {...} are the Poisson brackets. The Gibbs postulate [171] asserts that for an isolated macro-system (microcanonical ensemble) the micro-states on the energy surface are all equally accessible or probable, implying an uniform distribution

$$\rho = \frac{\delta(H-E)}{\int \mathrm{d}\Gamma_{q,p}\,\delta(H-E)}, \tag{4.45}$$

where E is the energy of the system. The resulting thermodynamics is at macroscopic equilibrium. In fact, this state of the system corresponds to the largest region in the

phase space Σ_{eq} and, during the evolution of the system, the time spent in Σ_{eq} is proportional to its measure. Thus, the non-equilibrium states, represented by regions $\Sigma_{\text{neq}} \ll \Sigma_{\text{eq}}$, are only small deviations due to fluctuations. Eqs.(4.43), (4.44), and (4.45) form the foundations of classical statistical mechanics and are the main tools to predict the behavior systems in the thermodynamic limit.

We conclude the presentation of classical gases by indicating that, in the rest of this thesis, we will work with open systems exchanging energy and particles with a *reservoir* or thermostat (grand canonical ensemble). In this case, the thermodynamic variables are temperature T and chemical potential μ. The distribution function takes the form

$$\rho_{\text{gc}} = \frac{e^{-\beta(H-\mu N)}}{h^{3N}\, N!\, \mathcal{Z}} \tag{4.46}$$

where

$$\mathcal{Z} = \sum_{N=0}^{\infty} \int \mathrm{d}\Gamma_{q,p} \frac{e^{-\beta(H-\mu N)}}{h^{3N}\, N!} \tag{4.47}$$

is the partition function, h the Planck's constant, $\beta^{-1} = k_B T$, and N is the number of particles. In quantum mechanics, the formalism of the distribution function $\rho(\{q\}, \{p\}, t)$ and what follows is preserved with due differences.

4.3.2 Quantum statistical mechanics

A many-particle quantum system described by a single wave function $\psi = \langle \{\mathbf{x}\} | \, \psi \rangle$, called *pure* ensemble, can also be completely represented by the density matrix (or density operator) $\hat{\rho}$, defined as the outer product between the "pure" state of the system $|\psi\rangle$ and the corresponding bra

$$\hat{\rho} = |\psi\rangle \langle\psi| \tag{4.48}$$

where $|\{\mathbf{x}\}\rangle$ is the set of coordinates of the particles. $\hat{\rho}$ can be used to evaluate the average of an observable O over the ensemble according to

$$\langle O \rangle = tr\, \{\hat{\rho}\, O\}, \tag{4.49}$$

where we used that $\langle\psi| \, O \, |\psi\rangle = \int \int d\,\{\mathbf{x}\}\, d\,\{\mathbf{x}'\} \, \langle \{\mathbf{x}'\} | \, \psi \rangle \, \langle \psi | \, \{\mathbf{x}\} \rangle \, \langle \{\mathbf{x}\} | \, O \, | \{\mathbf{x}\} \rangle$, proving Eq.(4.49). We notice from Eq.(4.48) that the density matrix is Hermitian

$$\rho_{ij} = \rho^*_{ji} \tag{4.50}$$

and normalized

$$tr\, \{\hat{\rho}\} = 1. \tag{4.51}$$

At this stage, the density matrix and wavefunction description of the quantum system are equivalent, which only occurs in pure ensembles. We notice that in this particular case, governed by Eq.(4.48), the density operator is idempotent, i.e: $\hat{\rho}^2 = \hat{\rho}$.

The relevance of the density matrix formalism kicks in when we examine *mixtures* of pure states $\{|\psi_i\rangle\}$, where a state $|\psi_i\rangle$ occurs with probability p_i. In this case, the traditional wavefunction analysis of the system is insufficient to make statistical predictions about an ensemble. We then introduce the more general definition of the density matrix

$$\hat{\rho} = \sum_{i=1}^{N} p_i \left|\psi_i\right\rangle \left\langle\psi_i\right| \tag{4.52}$$

where $0 < p_i \leq 1$ and $\sum_{i=1}^{N} p_i = 1$, and Eqs.(4.50) and (4.51) are preserved. The idempotence of the density matrix fails in a mixed ensemble, in particular

$$\begin{cases} Tr\left\{\hat{\rho}^2\right\} = 1 & pure\ state \\ Tr\left\{\hat{\rho}^2\right\} < 1 & mixed\ state \end{cases}, \tag{4.53}$$

where the last expression reflects the fact that diagonal terms in a pure state are either 0 or 1, but lie between these two numbers in a mixed state.

The states involved in Eq.(4.52) naturally evolve according to the Schrodinger equation, while the probabilities p_i don't change if the mixed ensemble in unperturbed. Consequently, the time-evolution of Eq.(4.52) is

$$\partial_t \hat{\rho} = -\mathrm{i}\left[\hat{\rho}, \hat{H}\right], \tag{4.54}$$

that is called "Liouville equation". We considered $\hbar = 1$ to lighten the derivations. Alike Eq.(4.46), the equilibrium condition implies, in a grand canonical ensemble,

$$\hat{\rho}_{\mathrm{Eq}} = \frac{e^{-\beta(\hat{H}-\mu\hat{N})}}{\mathcal{Z}} \tag{4.55}$$

where $\hat{H}$ and $\hat{N}$ are the Hamiltonian and number operator and $\mathcal{Z} = tr\{e^{-\beta(\hat{H}-\mu\hat{N})}\}$ is the quantum partition function. Eqs.(4.49), (4.54), and (4.55) are the quantum translation of Eqs.(4.43), (4.44), and (4.46), where $tr\{...\} \to \int d\Gamma_{q,p}$ and $\{...\} \to [.,.]$.

The formalism of the density matrix is widely used in physics and can be applied to a plethora of problems in many different ways, like in quantum information theory, quantum decoherence, and statistical mechanics. In this particular work, we implement it to study transport problems, where the Liouville equation becomes a generalization of the Boltzmann equation. To see that, rather than using the density matrix, we avail the occupation number operator for fermions, which is the quantum analogous to the Boltzmann distribution function (BDF). In this case, we neglect any electron-electron interactions and, therefore, we specialize in single-particle states that can eventually be described by the Fermi-Dirac distribution. The first step is to derive the averaged number of particles at equilibrium, given by

$$N = tr\left\{\hat{\rho}_{\mathrm{Eq}}\hat{N}\right\} = \frac{\sum_{n_1,..,n_N} e^{-\beta(\epsilon_1-\mu)n_1}...e^{-\beta(\epsilon_N-\mu)n_N}(n_1+...+n_N)}{\prod_{i=1}^{N}(1+e^{-\beta(\epsilon_i-\mu)})} \tag{4.56}$$

where we used that $\left\langle\psi_i\right| \hat{H} \left|\psi_i\right\rangle = E_i = n_i\epsilon_i$, valid in non-interacting systems, and $\left\langle\psi_i\right| \hat{N} \left|\psi_i\right\rangle = n_i$ where n_i is the number of particles in that state (for fermions it is

either 0 or 1) and ϵ_i the energy of a single particle in the state $|\psi_i\rangle$. The j^{th} term of Eq.(4.56) can be rewritten as

$$\frac{e^{-\beta(\epsilon_j-\mu)}\prod_{i=1..j-1,j+1}^{N}(1+e^{-\beta(\epsilon_i-\mu)})}{\prod_{i=1}^{N}(1+e^{-\beta(\epsilon_i-\mu)})}=\frac{e^{-\beta(\epsilon_j-\mu)}}{(1+e^{-\beta(\epsilon_j-\mu)})}=\frac{1}{e^{\beta(\epsilon_j-\mu)}+1}$$

that survives only if $n_j=1$. We finally have

$$N=\sum_i \frac{1}{e^{\beta(\epsilon_i-\mu)}+1} \tag{4.57}$$

and we can define the occupation number operator as

$$\tilde{\rho}_{\mathrm{Eq}}=\frac{1}{N}\,\hat{\rho}\cdot\hat{N}=\frac{1}{N}\,\frac{1}{e^{\beta(\hat{H}-\mu)}+1}=\frac{1}{N}\sum_{i=1}^{N}\frac{1}{e^{\beta(\epsilon_i-\mu)}+1}\,|\psi_i\rangle\,\langle\psi_i|\,, \tag{4.58}$$

where in the last passage we wrote $\tilde{\rho}_{\mathrm{Eq}}$ in terms of the eigenstates of the Hamiltonian. The probability

$$P_i=\frac{1}{e^{\beta(\epsilon_i-\mu)}+1}, \tag{4.59}$$

which represents the averaged occupation number, is the Fermi-Dirac distribution. Eq.(4.58) trivially respects Eqs.(4.51) and (4.54) (the number operator and the Hamiltonian commute) and

$$\langle O\rangle=tr\,\{\tilde{\rho}\,O\}\,, \tag{4.60}$$

which means that we can use $\tilde{\rho}$ to evaluate averages of observables over the ensemble.

4.3.3 The projected Liouville equation in graphene: the quantum Boltzmann equation

This paragraph is devoted to deriving an operative form of the Liouville equation suitable for extracting the spin-electronic transport properties in disordered graphene.

The outcome of this derivation yields a comprehensive extension of the semiclassical Boltzmann equation presented in this chapter, and we call it *quantum Boltzmann equation* (QBE), following the nomenclature used in the literature [38]. This generalized equation takes into account quantum effects more accurately, making it particularly relevant for investigating extrinsic spin-dependent scattering potentials.

We focus on the case of a weak external perturbation of the system that deviates linearly the quantum distribution function from its equilibrium state, thus writing

$$\tilde{\rho}=\tilde{\rho}_{\mathrm{Eq}}+\delta\tilde{\rho}, \tag{4.61}$$

where

$$\delta\tilde{\rho}=\sum_{\mathbf{k}\mathbf{k}'}p_{\mathbf{k}\mathbf{k}'}\,|\psi_{\mathbf{k}}\rangle\,\langle\psi_{\mathbf{k}'}|\sim\mathbf{E} \tag{4.62}$$

and $\mathbf{E}$ is the electric field. The modified $\tilde{\rho}$ is then employed to evaluate observable otherwise equal to zero at equilibrium, in particular

$$\langle \gamma_{ij} \rangle = tr\left\{\tilde{\rho}\,\gamma_{ij}\right\} = tr\left\{\delta\tilde{\rho}\,\gamma_{ij}\right\} \sim \mathbf{E} \tag{4.63}$$

where $\gamma_{ij} = \sigma_i \otimes s_j$ are Dirac matrices defined on pseudo-spin space. They are related to the observables of interest to us as

$$\begin{pmatrix} S_a \\ N \\ \mathcal{J}_i^a \\ J_i \end{pmatrix} = \begin{pmatrix} \frac{1}{2}\langle \gamma_{0a} \rangle \\ -\langle \gamma_{00} \rangle \\ \frac{\mathrm{v}}{2}\langle \gamma_{ia} \rangle \\ -\mathrm{v}\langle \gamma_{i0} \rangle \end{pmatrix}, \tag{4.64}$$

where N is the charge density, S_a is the spin density, J_i is the charge current and $\mathcal{J}_i^a$ is the spin current, as shown in Chap.(3), and made use of natural units. The index $i = (x, y)$ and $a = (x, y, z)$.

The full Hamiltonian $\mathcal{H}$ describing our system is made up of three terms,

$$\hat{\mathcal{H}} = \hat{H} + \hat{H}^E + \hat{U} \tag{4.65}$$

where $\hat{H}$ is the pristine graphene Hamiltonian, $\hat{U}$ is the impurity potential of the adatoms shown earlier in this chapter, and $\hat{H}^E = \mathrm{i}e\mathbf{E}\cdot\mathbf{r}$ is the coupling with the constant electric field. The relation that correlates the Hamiltonian and the distribution function is Eq.(4.54), so the time evolution of $\tilde{\rho}$ is described by

$$\frac{\partial\tilde{\rho}}{\partial t} + \mathrm{i}[\hat{H} + \hat{H}^E + \hat{U}, \tilde{\rho}] = 0 \tag{4.66}$$

that we use to find the out-of-equilibrium distribution function. We now project Eq.(4.66) in momentum space [183] by using a complete set of states $\{|\mathbf{k}\sigma\rangle\}$ with definite momentum $\mathbf{k}$ and pseudo-spin σ, defining the matrix elements of the distribution function as $\langle \mathbf{k}\sigma|\,\tilde{\rho}\,|\mathbf{k}'\sigma'\rangle = \rho_{\mathbf{k}\mathbf{k}'}^{\sigma\sigma'}$, thus writing its matrix form in pseudo-spin space as $\rho_{\mathbf{k}\mathbf{k}'}$. The states introduced are not eigenstates of the Hamiltonian $\hat{H}^{(E)}$, which becomes diagonal in momentum space but keeps its (pseudo-)spin matrix form; $\hat{H}^{(E)} \to H_{\mathbf{k}\mathbf{k}'}^{(E)} = H_{\mathbf{k}}^{(E)}\delta_{\mathbf{k},\mathbf{k}'}$. We can identify diagonal and off-diagonal components of the operators involved in Eq.(4.66), in particular, the density operator and the impurity potential become

$$\rho_{\mathbf{k}\mathbf{k}'} = f_{\mathbf{k}}\delta_{\mathbf{k},\mathbf{k}'} + g_{\mathbf{k}\mathbf{k}'}(1 - \delta_{\mathbf{k},\mathbf{k}'}) \tag{4.67}$$

and

$$U_{\mathbf{k}\mathbf{k}'} = U_{\mathbf{k}\mathbf{k}} + U_{\mathbf{k}-\mathbf{k}'} = V\delta_{\mathbf{k},\mathbf{k}'} + V\sum_i e^{\mathrm{i}(\mathbf{k}-\mathbf{k}')\cdot\mathbf{x}_i}(1 - \delta_{\mathbf{k},\mathbf{k}'}), \tag{4.68}$$

where $\mathbf{x}_i$ is the position of the impurities. The advantage of the projection in the momentum space is to break down Eq.(4.66) into two interrelated relations for $g_{\mathbf{k}\mathbf{k}'}$ and $f_{\mathbf{k}}$, which can be reduced to a single equation for the diagonal component of the distribution function in the momentum [183].

After performing the disorder average in momentum space, i.e: $\langle U_q + U_q O U_{q'} \rangle_{\text{dis}} = n_i V + n_i (VOV)\delta_{q+q',0}$ [1], we obtain

$$\frac{\partial f_{\mathbf{k}}}{\partial t} + \mathrm{i}[(H_{\mathbf{k}} + n_i V) + H^E_{\mathbf{k}}, f_{\mathbf{k}}] = I_{\text{out}}[f_{\mathbf{k}}] + I_{\text{in}}[f_{\mathbf{k}}] \tag{4.69}$$

where

$$I_{\text{out}}[f_{\mathbf{k}}] = -n_i \int_{\mathbf{p}} \int_0^\infty d\tau e^{-\eta\tau} [V e^{-\mathrm{i}H_{\mathbf{p}}\tau} V f_{\mathbf{k}} e^{\mathrm{i}H_{\mathbf{k}}\tau} + e^{-\mathrm{i}H_{\mathbf{k}}\tau} f_{\mathbf{k}} V e^{\mathrm{i}H_{\mathbf{p}}\tau} V] \tag{4.70}$$

and

$$I_{\text{in}}[f_{\mathbf{k}}] \;=\; n_i \int_{\mathbf{p}} \int_0^\infty d\tau e^{-\eta\tau} [V e^{-\mathrm{i}H_{\mathbf{p}}\tau} f_{\mathbf{p}} V e^{\mathrm{i}H_{\mathbf{k}}\tau} + e^{-\mathrm{i}H_{\mathbf{k}}\tau} V f_{\mathbf{p}} e^{\mathrm{i}H_{\mathbf{p}}\tau} V] \tag{4.71}$$

identify the scatter-out and scatter-in processes and n_i is the impurity concentration. Eq.(4.69) is the generalization of the Boltzmann equation that envisages quantum effects, where $f_{\mathbf{k}}$ is identified as the out-of-equilibrium quantum BDF and $I[f_{\mathbf{k}}] = I_{\text{out}}[f_{\mathbf{k}}] + I_{\text{in}}[f_{\mathbf{k}}]$ is the quantum collisional integral.

For a linear displacement of the distribution function from its equilibrium state, described in Eq.(4.61), the coupling with the electric field in Eq.(4.69) becomes also linear in the external perturbation. The commutator between the the distribution function and the electric Hamiltonian is then approximated as

$$\mathrm{i}e[H^E_{\mathbf{k}}, f_{\mathbf{k}}] \sim \mathrm{i}e[H^E_{\mathbf{k}}, f^{\text{Eq}}_{\mathbf{k}}] = \mathrm{i}e\mathbf{E}\cdot[\mathbf{r}, f^{\text{Eq}}_{\mathbf{k}}] = e\mathbf{E}\frac{\partial f^{\text{Eq}}_{\mathbf{k}}}{\partial \mathbf{k}}, \tag{4.72}$$

where $f^{\text{Eq}}_{\mathbf{k}}(\hat{H}) = \sum_\lambda f^{\text{Eq}}_{\mathbf{k}}(\epsilon_\lambda) \left|\mathbf{k}, \lambda\right\rangle\!\left\langle \mathbf{k}, \lambda\right|$ is the equilibrium distribution function, that at zero temperature becomes [183]

$$f^{\text{Eq}}_{\mathbf{k}} = \frac{\Theta(\varepsilon - \epsilon_+) + \Theta(\varepsilon - \epsilon_-)}{2}\gamma_{00} + \frac{\Theta(\varepsilon - \epsilon_+) - \Theta(\varepsilon - \epsilon_-)}{2}(\gamma_{10}k_x + \gamma_{20}k_y), \tag{4.73}$$

$\Theta(x)$ is the Heaviside step function, $\epsilon_\pm = \pm \mathrm{v}k$ is the conduction (valance) dispersion relation and v is the Fermi velocity. We target our interest in the response of the conduction electrons of our system for positive Fermi energy, which justifies the projection of $f_{\mathbf{k}}$ in the Bloch eigenstates chiral basis of graphene. In particular, the average value of an observable after the projection becomes

$$\langle O^{cc} \rangle = \sum_k tr\{f^{cc}_{\mathbf{k}} O^{cc}\} \tag{4.74}$$

where $\left(f^{cc(vv)}_{\mathbf{k}}, O^{cc(vv)}\right) = \left\langle \mathbf{k}\sigma, c(v)\right| (f_{\mathbf{k}}, O_k) \left|\mathbf{k}\sigma, c(v)\right\rangle$ and $\left|\mathbf{k}\sigma, c(v)\right\rangle$ is the conduction(valence) graphene's eigenstate with spin σ. Our aim is now to project Eq.(4.69) in graphene's eigenstates, that becomes a relation for the time-evolution of $f^{cc}_{\mathbf{k}}$.

[1] It is the Fourier transform of the standard expression $\langle V(\mathbf{x})V(\mathbf{x}')\rangle_{\text{dis}} = V^2\delta(\mathbf{x} - \mathbf{x}') \rightarrow \langle V(\mathbf{q})V(\mathbf{q}')\rangle_{\text{dis}} = V^2 \int d\mathbf{x}d\mathbf{x}' e^{-\mathrm{i}\mathbf{q}\cdot\mathbf{x}} e^{-\mathrm{i}\mathbf{q}'\cdot\mathbf{x}'} \delta(\mathbf{x} - \mathbf{x}')$.

We first examine the form of the projected collisional integral $(I[f_{\mathbf{k}}])_{cc} = I[f^{cc}_{\mathbf{k}}]$. For illustrative purposes we start considering the first term in I_{out}: we project it in the conduction band and we insert the resolution of identity between each operator [2], where χ is the spin. We find

$$Ve^{-iH_{\mathbf{p}}\tau}Vf^{cc}_{\mathbf{k}}e^{iH_{\mathbf{k}}\tau} \rightarrow V^{cc}_{\mathbf{kp}}e^{-\mathrm{i}\epsilon_p\tau}V^{cc}_{\mathbf{pk}}f^{cc}_{\mathbf{k}}e^{\mathrm{i}\epsilon_k\tau} + V^{cv}_{\mathbf{kp}}e^{\mathrm{i}\epsilon_p\tau}V^{vc}_{\mathbf{pk}}f^{cc}_{\mathbf{k}}e^{\mathrm{i}\epsilon_k\tau} + V^{cv}_{\mathbf{kp}}e^{\mathrm{i}\epsilon_p\tau}V^{vv}_{\mathbf{pk}}f^{vc}_{\mathbf{k}}e^{\mathrm{i}\epsilon_k\tau}$$

where $V_{\mathbf{kp}} = \langle \mathbf{k}| V |\mathbf{p}\rangle$. The first and second terms describe the electrons' dynamics in the conduction band, while the third piece determines the statistical behavior of electron-hole pairs. Being interested in the conduction dynamics, we consider only the first two terms, i.e: $f^{vc}_{\mathbf{k}} \rightarrow 0$, where, importantly, the cross-terms $V^{vc(cv)}$ are still preserved. They represent the amplitude of probability of electrons to jump from the conduction to the valence band and vice-versa after a scattering event. Their meaning becomes clearer by looking at the collisional integral in its entirety; the scatter-out component becomes

$$\begin{aligned} I_{\text{out}} = &- n_i \int_{\mathbf{p}} \left(\frac{\mathrm{i}}{\epsilon_k - \epsilon_p + \mathrm{i}\eta}\right)\left(V^{cc}_{\mathbf{kp}}V^{cc}_{\mathbf{pk}}f^{cc}_{\mathbf{k}}\right) + \left(f^{cc}_{\mathbf{k}}V^{cc}_{\mathbf{kp}}V^{cc}_{\mathbf{pk}}\right)\left(\frac{-\mathrm{i}}{\epsilon_k - \epsilon_p - \mathrm{i}\eta}\right) - \\ & n_i \int_{\mathbf{p}} \left(\frac{\mathrm{i}}{\epsilon_k + \epsilon_p + \mathrm{i}\eta}\right)\left(V^{cv}_{\mathbf{kp}}V^{vc}_{\mathbf{pk}}f^{cc}_{\mathbf{k}}\right) + \left(f^{cc}_{\mathbf{k}}V^{cv}_{\mathbf{kp}}V^{vc}_{\mathbf{pk}}\right)\left(\frac{-\mathrm{i}}{\epsilon_k + \epsilon_p - \mathrm{i}\eta}\right), \end{aligned} \tag{4.75}$$

and following the same procedure

$$I_{\text{in}} = n_i \int_{p} \left(\frac{\mathrm{i}}{\epsilon_k - \epsilon_p + \mathrm{i}\eta}\right)\left(V^{cc}_{\mathbf{kp}}f^{cc}_{\mathbf{p}}V^{cc}_{\mathbf{pk}}\right) + \left(\frac{-\mathrm{i}}{\epsilon_k - \epsilon_p - \mathrm{i}\eta}\right)\left(V^{cc}_{\mathbf{kp}}f^{cc}_{\mathbf{p}}V^{cc}_{\mathbf{pk}}\right) \tag{4.76}$$

where in the last expression all the crossed terms $V^{vc(cv)}$ disappear under the approximation of $f^{cv}_{\mathbf{p}} \rightarrow 0$. The terms $\sim V^{cc}_{\mathbf{kp}}V^{cc}_{\mathbf{pk}} + V^{cv}_{\mathbf{kp}}V^{vc}_{\mathbf{pk}}$ in Eq.(4.75) can be then understood as a generalization of the standard Fermi golden rule traditionally used in the Boltzmann theory, where only conduction states are involved, and quantum transition effects are entirely disregarded.

The projected collisional integral can be further manipulated to obtain a more operative form. According to the Sokhotski–Plemelj theorem,

$$\lim_{\eta\rightarrow 0}\frac{\mathrm{i}}{\epsilon_k \mp \epsilon_p - \mathrm{i}\eta} = \mathrm{i}P\left(\frac{1}{\epsilon_k \mp \epsilon_p}\right) + \pi\delta(\epsilon_k \mp \epsilon_p) \tag{4.77}$$

which helps us to decompose the scatter-in and scatter-out components of the collisional integral into the real and imaginary part

$$I_{\text{in}} = 2\pi n_i \int_{\mathbf{p}} \delta(\epsilon_k - \epsilon_p) V^{cc}_{\mathbf{kp}}f^{cc}_{\mathbf{p}}V^{cc}_{\mathbf{pk}} \tag{4.78}$$

$$\begin{aligned} I_{\text{out}} = & \, n_i \mathrm{i}P \int_{\mathbf{p}} \left[f^{cc}_{\mathbf{k}}, V^{cc}_{\mathbf{kp}}V^{cc}_{\mathbf{pk}}\frac{1}{\epsilon_k - \epsilon_p}\right] - n_i\pi \int_{\mathbf{p}} \delta(\epsilon_k - \epsilon_p)\left\{f^{cc}_{\mathbf{k}}, V^{cc}_{\mathbf{kp}}V^{cc}_{\mathbf{pk}}\right\} \\ & n_i \mathrm{i}P \int_{\mathbf{p}} \left[f^{cc}_{\mathbf{k}}, V^{cv}_{\mathbf{kp}}V^{vc}_{\mathbf{pk}}\frac{1}{\epsilon_k + \epsilon_p}\right] - n_i\pi \int_{\mathbf{p}} \delta(\epsilon_k + \epsilon_p)\left\{f^{cc}_{\mathbf{k}}, V^{cv}_{\mathbf{kp}}V^{vc}_{\mathbf{pk}}\right\}. \end{aligned} \tag{4.79}$$

[2] i.e., $\sum_{i=c,v}\sum_{\chi} |\mathbf{p}(\mathbf{k})\chi, i\rangle \langle \mathbf{p}(\mathbf{k})\chi, i| = 1$

The principal value contribution of Eq.(4.79) is related to the hermitian part of the second order electrons' self-energy as

$$P[I_{\text{out}}] = \mathrm{i}n_i \langle \mathbf{k}\sigma, c| \, [f^{cc}_{\mathbf{k}}, P\int_{\mathbf{p}} V \frac{1}{\epsilon - H_{\mathbf{p}} + \mathrm{i}\eta} V] \, |\mathbf{k}\sigma, c\rangle = \mathrm{i}\left[f^{cc}_{\mathbf{k}}, \left(\Sigma^{\prime(2)}_R\right)_{cc}\right], \tag{4.80}$$

readily proven by noticing that

$$\sum_{i,j=c,v}\sum_{\chi\rho}\int_{\mathbf{p}} \langle \mathbf{k}\sigma, c| \, V \, |\mathbf{p}\chi, i\rangle \langle \mathbf{p}\chi, i| \, \frac{1}{\epsilon - H_{\mathbf{p}} + i\eta} \, |\mathbf{p}\rho, j\rangle \langle \mathbf{p}\rho, j| \, V \, |\mathbf{k}\sigma, c\rangle$$
$$= \int_{\mathbf{p}} V^{cc}_{\mathbf{kp}} \frac{1}{\epsilon_k - \epsilon_p + i\eta} V^{cc}_{\mathbf{pk}} + \int_{\mathbf{p}} V^{cv}_{\mathbf{kp}} \frac{1}{\epsilon_k + \epsilon_p + i\eta} V^{vc}_{\mathbf{pk}},$$

where we specified the (anti-)hermitian component of Σ_R as $\mathrm{i}\left(\Sigma^{\prime(\prime\prime)}_R\right)_{cc}$. Analogously, the imaginary part of I_{out} becomes

$$I''_{\text{out}} = n_i \langle \mathbf{k}\sigma, c| \, \{f^{cc}_{\mathbf{k}}, (lim_{\eta\to 0}\int_p V \frac{1}{\epsilon - H_{\mathbf{p}} + i\eta} V)''\} \, |\mathbf{k}\sigma, c\rangle = \left(\Sigma''_R\right)_{cc}. \tag{4.81}$$

Putting the term $\mathrm{i}[n_i V, f_{\mathbf{k}}]$ on the right-hand side of Eq.(4.69), the collisional integral takes the final form

$$I\left[f^{cc}_{\mathbf{k}}\right] = -\mathrm{i}[\left(\Sigma'_R\right)_{cc}, f^{cc}_{\mathbf{k}}] + \{\left(\Sigma''_R\right)_{cc}, f^{cc}_{\mathbf{k}}\} + 2\pi n_i \int_{\mathbf{p}} \delta(\epsilon_k - \epsilon_p) V_{\mathbf{kp}} f^{cc}_{\mathbf{p}} V_{\mathbf{pk}}, \tag{4.82}$$

where $\left(\Sigma_R\right)_{cc} = n_i V + \left(\Sigma^{(2)}_R\right)_{cc}$ is identified as the electrons' self-energy in first Born approximation (FBA).

We complete the analysis of the projected Liouville equation by looking at the coupling with the electric field. For $\varepsilon > 0$, Eq.(4.72) becomes

$$\mathrm{i}[H^E_{\mathbf{k}}, f_{\mathbf{k}}] = -\frac{e\mathrm{v}}{2}\mathbf{E}\cdot\hat{\mathbf{k}}\delta(\varepsilon - \epsilon_k)(\gamma_{00}\cos\theta_{\mathbf{k}} + \gamma_{10}\cos^2\theta_{\mathbf{k}} + \gamma_{20}\cos\theta_{\mathbf{k}}\sin\theta_{\mathbf{k}}),$$

[3] where we neglected Fermi sea contributions proportional to $\Theta(\varepsilon - \epsilon_k)$. By projecting it in the chiral basis states of graphene, it reads

$$\mathrm{i}[H^{cc}_E, f^{cc}_{\mathbf{k}}] = -e\mathrm{v}\mathbf{E}\cdot\hat{\mathbf{k}}\,\delta(\varepsilon - \epsilon_k), \tag{4.83}$$

that is the traditional driving term appearing in the calssical Boltzmann equation (CBE).

[3] We used that $\partial_{\mathbf{k}} = \hat{k}_x\partial_{k_x} + \hat{k}_y\partial_{k_y} = \hat{\mathbf{k}}\partial_k + \frac{\hat{\boldsymbol{\theta}}_k}{k}\partial_{\theta_k}$, with $\hat{\boldsymbol{\theta}}_k = (-\sin\theta_{\mathbf{k}}, \cos\theta_{\mathbf{k}})$

Putting together Eq.(4.82) and Eq.(4.83), we finally write the projected Liouville equation, or quantum Boltzmann equation, as

$$\partial_t \delta f_{\mathbf{k}} - e\mathrm{v}\mathbf{E}\cdot\hat{\mathbf{k}}\,\delta(\epsilon-\epsilon_k) = -\mathrm{i}[\Sigma_R^{'}, \delta f_{\mathbf{k}}] + \{\Sigma_R^{''}, \delta f_{\mathbf{k}}\} + 2\pi n_i \int_{\mathbf{p}} \delta(\epsilon_k - \epsilon_p) V_{\mathbf{kp}} \delta f_{\mathbf{p}} V_{\mathbf{pk}}, \quad (4.84)$$

where we dropped the "cc" subscript and used that only $\delta f_{\mathbf{k}}$ contributes. A comparison between the classical and quantum Boltzmann equations can shed light upon the importance of the new terms derived in in Eq.(4.84). The classical collisional integral of the CBL reads

$$I_{\text{classical}}\left[\delta f_{\mathbf{k}}\right] = 2\pi n_i \int_{\mathbf{p}} \delta(\epsilon_k - \epsilon_p)(\delta f_{\mathbf{p}} - \delta f_{\mathbf{k}}) \left|V_{\mathbf{kp}}\right|^2 \quad (4.85)$$

that matches the right-hand side of the QBE only by considering scalar impurities $(V_{\mathbf{pk}}, \Sigma_R) \sim \gamma_{00}$, and no conduction-valance crossed terms. In fact, we emphasis that the impurity potential $V_{\mathbf{pk}}$ and the distribution function $f_{\mathbf{k}}$ are matrices in the spin space, so $[\Sigma_R^{'}, \delta f_{\mathbf{k}}] \neq 0$ and the order of factors in the collisional integral cannot be altered in general. This means that the CBE cannot tackle disordered systems with spin-dependent impurities, like extrinsic spin-orbit interactions or magnetic moments, but a full quantum Liouville equation approach is required. In addiction, Eq.(4.85) has no information about the Hermitian part of the self-energy, which behaves as an effective magnetic field [38]. In fact, by writing $\delta f_{\mathbf{k}} = \delta f_{\mathbf{k}}^0 s_0 + \mathbf{m}_{\mathbf{k}} \cdot \mathbf{s}$ and $\Sigma_R^{'} = \Sigma_{R,0}^{'} s_0 + \mathbf{B}_{\mathbf{k}} \cdot \mathbf{s}$, we find a QBE for $\mathbf{m}_{\mathbf{k}}$ of the form

$$\partial_t \mathbf{m}_{\mathbf{k}} \sim \mathbf{B}_{\mathbf{k}} \times \mathbf{m}_{\mathbf{k}} \quad (4.86)$$

the information of which is lost in the classical Boltzmann formalism. As we show in pristine graphene with spatially inhomogeneous Rashba-type SOC, $\mathbf{B}_{\mathbf{k}}$ generates a robust spin Hall current in the weak impurity potential regime. This new effect is unrelated to the traditional spin Hall effect, which requires skew scattering activated by strong impurities. The Hermitian part of the self-energy then manifests the presence of a novel semiclassical mechanism, the interband spin-orbit scattering mechanism, which stems from conduction-valance virtual band transitions, specified by the cross-scattering amplitude probabilities $V_{\mathbf{pk}}^{vc}$.

4.4 Fully quantum mechanical response theory

In the previous sections, we introduced the Boltzmann technique for the evaluation of out-of-equilibrium responses of the system, pointing out its limitations due to simple quantum adjustments to classical statistical mechanics. We showed that an accurate quantum mechanical description is rather offered by quantum statistical mechanics, where observables are evaluated with the assistance of the density matrix through Eq.(4.49). Thanks to this formalism, and in particular the quantum version of the Liouville equation, we developed an extension of the semiclassical method, the quantum Boltzmann equation. However, even though it can capture quantum effects disregarded

by the classical counterpart, this method offers only a partial description of the system due to the projection of the Liouville equation in the conduction (or valance) states of the Hamiltonian. The Kubo formula solves all the shortcomings of the semiclassical and quantum Boltzmann equation, providing a fully quantum mechanical evaluation of the observables. This section aims to present a short derivation for clean and disordered systems, where we also illustrate the related diagrammatic technique for evaluation in momentum and frequency space. In particular, we show the diagrams of interest for including the skew scattering mechanism in the strong impurity potential regime and their exact re-summation, the T-matrix approximation. In this context, we also develop a technique based on the Kubo formula for deriving drift-diffusion spin-charge equations, called Diffuson Hamiltonian method.

4.4.1 Linear response theory

Let us consider a generic fermionic system described by the bare Hamiltonian H_0 and perturbed by an external field $F(\mathbf{r},t)$. The full Hamiltonian reads

$$H = H_0 + H_{\text{ext}}, \tag{4.87}$$

with $H_{\text{ext}} = \int d\mathbf{r}\, B(\mathbf{r})F(\mathbf{r},t)$ and B($\mathbf{r}$) being the physical observable coupled to the external field. From Eq.(4.49), the average of an observable $A(\mathbf{r})$ in the grand canonical ensemble is

$$\langle A(\mathbf{r})\rangle(t) = tr\{\hat{\rho}_{\text{Eq}}(t)\, A(\mathbf{r})\}, \tag{4.88}$$

where the time dependency of $\hat{\rho}_{\text{Eq}}$ comes from H_{ext}. Sufficiently weak external fields allow an expansion of the density matrix in the perturbation strength, that we carry out with the assistance of the Liouville equation (Eq.(4.54)). Particularly, the first order expansion of $\hat{\rho}_{\text{Eq}}(t)$ is of interest in experimental setups, and establishes the so-called *linear response theory* (to point out its importance, we notice that the renowned Ohm's law, at the basis of modern electronics, is valid within the linear response theory). The density matrix translates into

$$\hat{\rho}_{\text{Eq}}(t) \sim \hat{\rho}^{(0)}_{\text{Eq}} + \hat{\rho}^{(1)}_{\text{Eq}}(t), \tag{4.89}$$

where the first order contribution is described by

$$\mathrm{i}\,\partial_t \rho^{(1)}_{\text{Eq}}(t) = \left[H_0, \rho^{(1)}_{\text{Eq}}\right] + \left[H_{\text{ext}}, \rho^{(0)}_{\text{Eq}}\right], \tag{4.90}$$

and the solution is [171]

$$\rho^{(1)}_{\text{Eq}}(t) = -\mathrm{i}\int_{-\infty}^{t} dt'\, e^{-\mathrm{i}\,H_0(t-t')}\left[H_{\text{ext}}(t'), \rho^{(0)}_{\text{Eq}}\right] e^{\mathrm{i}\,H_0(t-t')}, \tag{4.91}$$

valid under the assumption of no external fields at $t = -\infty$. We finally obtain an expression for the linear deviation of the observable A($\mathbf{r}$) from its equilibrium average $\delta\langle A(\mathbf{r})\rangle(t) = \langle A(\mathbf{r})\rangle_{(1)}(t) - \langle A(\mathbf{r})\rangle_0$,

$$\delta\langle A(\mathbf{r})\rangle(t) = -\mathrm{i}\int_{-\infty}^{t} dt' \int d\mathbf{r}'\, tr\{\rho^{(0)}_{\text{Eq}}\,[A(\mathbf{r},t), B(\mathbf{r}',t')]\}F(\mathbf{r}',t'), \tag{4.92}$$

where $\langle ... \rangle_{0(1)} = tr\{\rho_{\text{Eq}}^{0(1)} ...\}$. The operators A and B are written in the Interaction picture, i.e., $O(t) = e^{\mathrm{i}\, H_0 t} O e^{-\mathrm{i}\, H_0 t}$, and have been obtained using the cyclicality of the trace. The core of Eq.(7.25) is the trace piece, usually called *response function*, which expression is

$$R^{AB}(\mathbf{r}, \mathbf{r}'; t, t') = -\mathrm{i}\theta(t - t') tr\{\rho_{\text{Eq}}^{(0)} [A(\mathbf{r}, t), B(\mathbf{r}', t')]\}. \tag{4.93}$$

Notably, $R^{AB}(\mathbf{r}, \mathbf{r}'; t, t')$ depends on the properties of the unperturbed system only. Accordingly, if the unperturbed system is translational invariant in space, the response function depends only on the difference of the space arguments, $R^{AB}(\mathbf{r} - \mathbf{r}'; t - t')$. This allows a rewriting of Eq.(7.25) in Fourier space, acquiring a frequency-momentum description of the perturbed system, i.e., $R^{AB}(\mathbf{q}, \omega)$. Eq.(4.93) allows us to write Eq.(7.25) in a more compact way,

$$\delta\langle A(\mathbf{r})\rangle(t) = \int_{-\infty}^{\infty} dt' \int d\mathbf{r}' R^{AB}(\mathbf{r} - \mathbf{r}'; t - t') F(\mathbf{r}', t'), \tag{4.94}$$

that has now a more explicit physical interpretation: the variation of an observable at a given space-time point $(\mathbf{r}, t)$ is the result of counting all the system's configurations in time and space transmitted via the response function, which controls causality [171].

A more operative form of Eq.(4.93) is realized by writing explicitly the trace in terms of eigenstates $\{|m\rangle\}$ of H_0 and performing a Fourier transformation $\mathcal{F} = \int_{-\infty}^{\infty} dt e^{\mathrm{i}(\omega + \mathrm{i}0^+)t}$, the so-called Lehmann representation [171],

$$R^{AB}(\mathbf{r}, \mathbf{r}'; \omega) = \frac{1}{\mathcal{Z}} \sum_{n,m} \frac{\langle n|A(\mathbf{r})|m\rangle\langle m|B(\mathbf{r}')|n\rangle}{\omega + E_n - E_m + \mathrm{i}0^+} (e^{-\beta E_n} - e^{-\beta E_m}), \tag{4.95}$$

that is the main result presented in this section. We remind that $R^{AB}(\mathbf{r}, \mathbf{r}'; \omega)$ is a property of the system at equilibrium without the effect of any external perturbation.

The relation above offers a general procedure to evaluate the variation of an observable A to an external field F coupled to B. For example, it can be used to evaluate the spin susceptibility for a magnetic field, the electrical conductivity for an applied electric potential (Ohm's law), the specific heat for a temperature gradient, and much more. In this thesis, we will apply the linear response formalism to charge-spin conversion phenomena, thus mostly caring about spin-charge responses of crystals to electric fields. Some algebraic simplifications make the problem more tractable and lead to the Kubo formula. In the next section, we show its original form [184] and a more transparent formulation involving single-particle Green's function, commonly referred to as the Kubo-Streda formula [185].

4.4.2 The Kubo formula

We now focus on the perturbation originating from an applied electric field, $E = -\partial_t F$, which can be inserted in Eq.(7.25) by using the identity

$$\int_{-\infty}^{t} dt' A(t') e^{\mathrm{i}a(t-t')} = \frac{\mathrm{i}}{a} \int_{-\infty}^{t} dt' \left[1 - e^{\mathrm{i}a(t-t')}\right] \partial_{t'} A(t'), \tag{4.96}$$

where $a \neq 0$. After simple algebraic manipulations, we finally obtain a new form of the linear response in terms of E,

$$\delta\langle A(\mathbf{r})\rangle(t) = \int_{-\infty}^{\infty} dt' \int d\mathbf{r}' \tilde{R}^{AB}(\mathbf{r},\mathbf{r}';t-t')E(\mathbf{r}',t'), \tag{4.97}$$

where

$$\tilde{R}^{AB}(\mathbf{r},\mathbf{r}';\omega) = \frac{1}{\mathcal{Z}}\sum_{n,m}\frac{\langle n|A(\mathbf{r})|m\rangle\langle m|B(\mathbf{r}')|n\rangle}{E_n - E_m}\frac{\mathrm{i}(e^{-\beta E_n} - e^{-\beta E_m})}{\omega + E_n - E_m + \mathrm{i}0^+} \tag{4.98}$$

is the celebrated Kubo formula. We neglected a similar contribution $\sim 1/(E_n - E_m)(\omega + \mathrm{i}0^+)$ divergent in the DC limit, i.e., $\omega \to 0$. In fact, in the cases of interest to us, it is equal to zero on general grounds. For example, the calculation for longitudinal electrical conductivity involves $A(\mathbf{r}) \to \tilde{\mathbf{j}}$ and $B(\mathbf{r}) \to \mathbf{j}$, where the latter is the standard current operator coupled to the external vector potential, $\mathbf{j} = e\mathbf{p}/m$, and the former is the total current operator comprising the diamagnetic term, $\tilde{\mathbf{j}} = e(\mathbf{p} + e\mathbf{F})/m$ which cancels against the divergent contribution. The same result holds for the (spin) Hall conductivity and spin density-current response by expanding the divergent contribution and using that $A \to v_i = \mathrm{i}\,[x_i, H]$ and $[x_i, v_{j\neq i}] = 0$ in the former case, $\{s_i, s_{j\neq i}\} = 0$ in the latter [19, 52].

In the single-electron picture, the density matrix is replaced by the occupation number operator at the first step of our derivation, and the Kubo formula is readily seen to be

$$\tilde{R}^{AB}(\mathbf{r},\mathbf{r}';\omega) = \mathrm{i}\sum_{n,m}\frac{\langle n|A(\mathbf{r})|m\rangle\langle m|B(\mathbf{r}')|n\rangle}{E_n - E_m}\frac{f(E_m) - f(E_n)}{\omega + E_n - E_m + \mathrm{i}0^+}, \tag{4.99}$$

where $f(E) = \left(e^{(E-\varepsilon)/k_{\mathrm{B}}T} + 1\right)^{-1}$ is the Fermi-Dirac distribution, and the states $|n\rangle$ are single-particle states. The advantage of this recasting is the possibility to introduce the single-particle propagators or Green's functions (GF)

$$G^{R(A)}(\epsilon + \omega) = \frac{1}{\epsilon + \omega - H_0 \pm \mathrm{i}0^+} = \sum_n \frac{|n\rangle\langle n|}{\epsilon + \omega - E_n \pm \mathrm{i}0^+}, \tag{4.100}$$

which, in a continuous model, is interpreted as the amplitude of probability of a particle to move from a space-time point $(\mathbf{x}, t)$ to $(\mathbf{x}', t')$. $G^{R(A)}$ are referred to as *retarded* (*advanced*) GF, depending on the position of the corresponding energy poles in the complex plane. The response function, that we now show in momentum-frequency space, is then split into two halves,

$$\begin{aligned}\tilde{R}^{\mathrm{I}}_{AB} = \frac{1}{4\pi}\int d\mathbf{k}\int d\epsilon \frac{df(\epsilon)}{d\epsilon} tr\{&A(\mathbf{k})\,G^R\,B(\mathbf{k})\,(G^R - G^A) \\ &- A(\mathbf{k})\,(G^R - G^A)\,B(\mathbf{k})\,G^A)\},\end{aligned} \tag{4.101}$$

and

$$\begin{aligned}\tilde{R}^{\mathrm{II}}_{AB} = \frac{1}{4\pi}\int d\mathbf{k}\int d\epsilon f(\epsilon) tr\{&A(\mathbf{k})\,G^R\,B(\mathbf{k})\frac{dG^R(\epsilon)}{d\epsilon} + A(\mathbf{k})\,\frac{dG^A(\epsilon)}{d\epsilon}\,B(\mathbf{k})G^A \\ &- \frac{dG^R(\epsilon)}{d\epsilon}\,B(\mathbf{k})G^R - A(\mathbf{k})\,G^A\,B(\mathbf{k})\frac{dG^A(\epsilon)}{d\epsilon}\},\end{aligned} \tag{4.102}$$

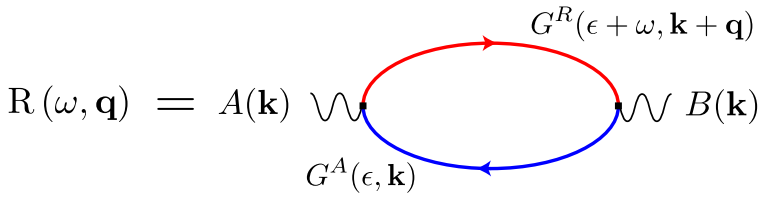

Figure 4.2: This schematic shows the diagrammatic representation of the Kubo formula, Eq.(4.103). The vertices are the observables connected by the retarded GR (in red) and the advanced GF (in blue). The wavy lines correspond to external perturbation carrying the momentum and frequency $\mathbf{q}$ and ω.

called *type-I* and *type-II* responses respectively, where for simplicity we presented the case with zero external frequency and momentum, i.e., $\omega = 0$ and $\mathbf{q} = 0$. The first term, which includes the derivative of the distribution function, is interpreted as a *surface* contribution to the response, meaning that only the states close to the Fermi energy are counted. On the contrary, the second term describes the effect of the *Fermi sea*, being proportional to $f(\epsilon)$ [186].

As anticipated in the introduction, this thesis' goal is to study disordered systems in the clean limit, i.e., low concentration of impurities n_i. In this regime, $\tilde{R}^{\mathrm{I}}_{AB} \sim 1/n_i$, while the type-II response contributes to the next order and can therefore be disregarded for our porpoises. The type-I response can be further simplified by realizing that the product of GF of the same sector contributes only at order $\sim n_i$ and then can be safely neglected [19]. The final elegant expression, relevant in disordered systems, is

$$\mathrm{R}(\omega, \mathbf{k}) = \frac{1}{2\pi} \int d\mathbf{k}\, tr\{A(\mathbf{k})\, G^R(\epsilon+\omega, \mathbf{k}+\mathbf{q})\, B(\mathbf{k})\, G^A(\epsilon, \mathbf{k})\, B(\mathbf{k})\}, \tag{4.103}$$

where we assumed the zero temperature limit $T = 0$ and restored finite external frequency and momentum. The presence of disorder renormalizes this expression and requires some extra care to write an explicit form readable for calculation.

4.4.3 The diagrammatic treatment of the Kubo Formula

The presence of interactions in the system makes the task of solving Eq.(4.103) far from trivial, and a more explicit representation of the Kubo formula is therefore desirable. The *diagrammatic* technique can fulfil this task by reinterpreting the GFs, interactions, and response functions as Feynman's diagrams (the connection between the Kubo formula and the diagrammatic technique is more formally shown in App.(A)). In this language, Eq.(4.103) is depicted as an empty "bubble" in the absence of interactions, as shown in Fig.(4.2). In our case, the full equilibrium Hamiltonian is the sum of a bare term and a disorder contribution,

$$H = \sum_{\sigma,\sigma'} \int d\mathbf{r}\, \psi^+_\sigma(\mathbf{r})(H^0_{\sigma\sigma'} + U_{\sigma\sigma'}(\mathbf{r}))\psi_{\sigma'}(\mathbf{r}), \tag{4.104}$$

where $H_0 = \sum_{\sigma,\sigma'} H^0_{\sigma\sigma'}$ describes the clean crystal, $\psi^{(+)}_\sigma$ is the annihilation (creation) operator with defined spin σ, and $U_{\sigma\sigma'}(\mathbf{r}) = \sum_{i=0}^{N} V_{\sigma\sigma'}\delta(\mathbf{x}-\mathbf{x}_i)$ the stochastic field coming from defects in the system. The form of $U_{\sigma\sigma'}(\mathbf{r})$ is generally unknown; therefore, a statistical average over disorder that considers all possible configurations is commonly adopted in momentum-space LRT [178]. It is worth anticipating that this procedure has the same meaning of the Lippmann-Schwinger expansion shown in Sec. 4.2.2, as we will shortly discuss.

One effect of including disorder is the renormalization of the propagators [178]. Diagrammatically, it is represented by the insertion, in the GF, of an arbitrary number of interaction vertices averaged over the disorder statistics, as shown in Fig.(4.3d). The first diagram is the *mean* value of the impurity potential, $\langle U_{\sigma\sigma'}\rangle_{\text{dis}} = n_i V_{\sigma\sigma'}$, the second one is the *variance*, $\langle U_{\sigma\sigma'}U_{\sigma'\sigma}\rangle_{\text{dis}} = n_i V_{\sigma\sigma'}V_{\sigma'\sigma}$, and the third contribution is the *skewness*, $\langle U_{\sigma\sigma'}U_{\sigma'\sigma''}U_{\sigma''\sigma}\rangle_{\text{dis}} = n_i V_{\sigma\sigma'}V_{\sigma'\sigma''}V_{\sigma''\sigma}$. The sum of all the scattering diagrams of this type, with a single density dot, is called $T-matrix$,

$$\mathcal{T}^{R(A)} \equiv \langle T^{R(A)}\rangle_{\text{dis}} = V + V\, g^{R(A)}\, V + ... = \frac{V}{1 - g^{R(A)}\, V}, \tag{4.105}$$

where $g^{R(A)} = \int d\mathbf{p}\, G^{R(A)}(\epsilon, \mathbf{p})$ is the momentum-integrated GF. $\mathcal{T}$ describes the scattering off a single impurity at all orders in perturbation theory and is proportional to the concentration of impurities. We neglected irreducible multi-dot diagrams proportional to powers of the impurity concentrations. These terms are next-order quantum corrections that, with our current knowledge, cannot be re-summed exactly. The renormalized GF, $\mathcal{G}^{R(A)} \equiv \langle G^{R(A)}\rangle_{\text{dis}}$, is a Dyson series involving the T-matrix, that mathematically has the form

$$\mathcal{G}^{R(A)} = G^{R(A)} + G^{R(A)}\,\Sigma_{R(A)}\,G^{R(A)} + ... = G^{R(A)}\,\Sigma_{R(A)}\,\mathcal{G}^{R(A)}, \tag{4.106}$$

which leads to

$$\mathcal{G}^{R(A)} = \frac{1}{\epsilon - H_0 - \Sigma^{R(A)}}, \tag{4.107}$$

with $\Sigma_{R(A)} = n_i \mathcal{T}^{R(A)}$ being the propagator's *self-energy*. The real (hermitian) part of the self-energy, $\Sigma'_{R(A)}$, renormalizes the particle's Hamiltonian H_0, meaning that now $\epsilon - H_0 - \Sigma'_{R(A)} = 0$ solves the dispersion relation. On the other hand, the imaginary (anti-hermitian) component $\Sigma''_{R(A)}$ is interpreted as the inverse of the lifetime a particle spends in a renormalized state $\mathbf{k}$ [178], leading to a broadening of spectral lines.

Interestingly, the self-energy is directly connected to the collisional integral of the kinetic theory. This is shown in Refs.[178] and [179], and in the previously presented quantum Boltzmann equation. The T-matrix treatment of the disorder is then understood as the Lippmann-Schwinger expansion in scattering theory. The truncation of the T-matrix series at the second order, $\mathcal{T} \sim n_i V^2$, is, therefore, the standard FBA, and the third order starts capturing the skew scattering mechanism.

The disorder average also renormalizes the bubble through a procedure called *vertex renormalization*. The role of T-matrix is now to connect the retarded and the advanced sectors of the response function as shown in Fig.(4.3a) and (4.3b). The mathematical

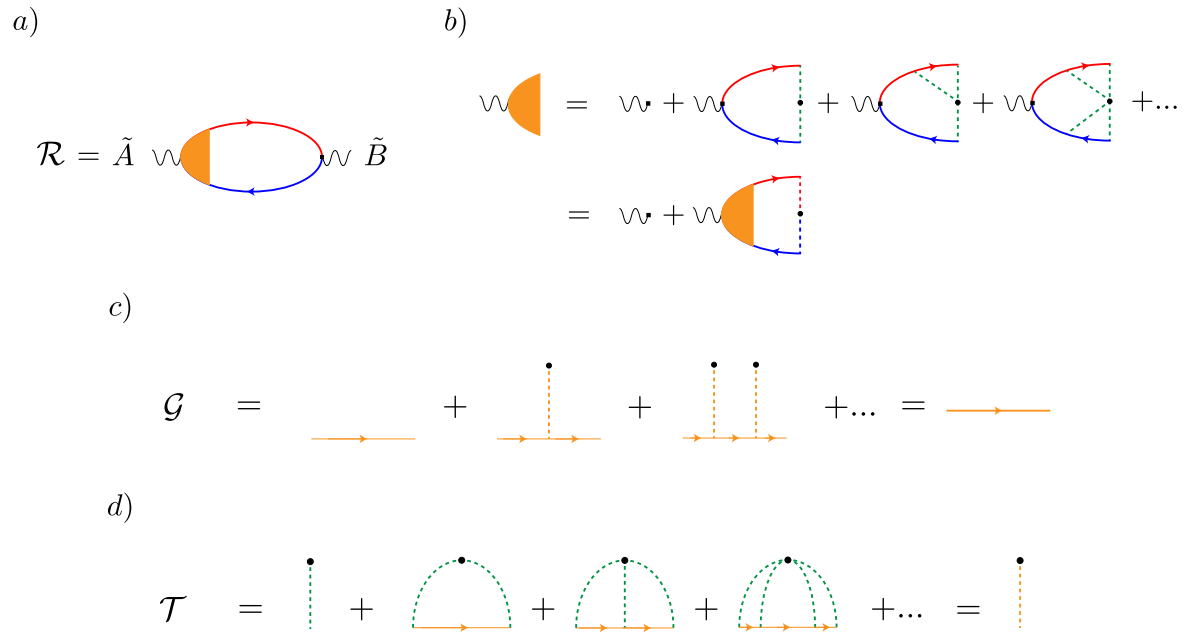

Figure 4.3: Here we present the diagrammatic representations of the disordered averaged response function (a), the renormalized vertex (b), the disorder-averaged Green's function (c), and the T-matrix (d). (a): The red/blue solid lines denote $\mathcal{G}^{R/A}$, and the orange shaded region represents the renormalized density vertex. (b): The green dashed lines indicate scatting events with the impurity represented by the black dot. The red/blue dashed lines signify the retarded/advanced T-matrix associated to the the impurity at the black dot. (c): Orange lines denote a Green's function that is retarded or advanced. The thin lines in this case denote $G^{R/A}$, whilst the thick line represents $\mathcal{G}^{R/A}$. (d): Here solid lines correspond to $\mathcal{G}^{R/A}$, the green dashed lines have the same meaning as in panel (b), and the orange dashed line represents $\mathcal{T}^{R/A}$.

translation for the vertex renormalization procedure, depicted in Fig.((4.3b)), is the Bethe-Salpeter equation [52]

$$\tilde{A} = A + n_i \sum_{\mathbf{k}} \mathcal{T}^A \, \mathcal{G}^A_{\mathbf{k}} \, \tilde{A} \, \mathcal{G}^R_{\mathbf{k}} \, \mathcal{T}^R, \tag{4.108}$$

that is a self-consistent equation to find the renormalized vertex $\tilde{A}$. A traditional way to solve it requires formulating an ansatz for $\tilde{A}$, which validity is checked a posteriori [19]. A second route, relevant in spin-current responses, rewrites Eq.(4.108) in terms of the *Diffuson* operator and finds the renormalized vertex with no need for ansatzes. This procedure will be presented in detail in the next section.

Restoring $\hbar$, we finally obtain the disorder-averaged Kubo formula

$$\mathcal{R}(\omega, \mathbf{q}) = \langle \mathrm{R}(\omega, \mathbf{q}) \rangle_{\mathrm{dis}} = \frac{\hbar}{2\pi} \int d\mathbf{k} \, tr\{ \tilde{A}(\mathbf{k}) \, \mathcal{G}^R(\epsilon + \omega, \mathbf{k} + \mathbf{q}) \, B(\mathbf{k}) \, \mathcal{G}^A(\epsilon, \mathbf{k}) \}, \tag{4.109}$$

which is the primary tool we use in this thesis' projects to evaluate the spin-current and current-current response of various disordered systems, like bare graphene, graphene

heterostructures, topological insulators, and two-dimensional gases. Beyond its use as a method to find the responses to an electrical field, a manipulation of Eq.(4.109) leads to a technique to derive the drift-diffusion equations controlling the system's spin and charge dynamics [187, 35]. We dub it the *Diffuson Hamiltonian method*.

4.4.4 Vertex renormalization

We first consider the case of a *density vertex* on the left of the bubble, renormalized by random disorder. This example has the advantage of working with an observable independent from the momentum, which leads to significant simplification. The density vertex generally has a matrix structure and is represented by a generator of the considered algebra, $A \to \gamma_i$. For instance, γ_i is SU(2) if describing the spin or SO(5) if the graphene's pseudospin is included. For convenience we consider again $\hbar = 1$. To begin with, we project Eq.(4.108) onto the corresponding algebra, obtaining

$$\tilde{\gamma}_{(i)\mu} = \delta_{i\mu} + \frac{n_i}{D}\sum_{\mathbf{k}} tr\{\mathcal{T}^R\mathcal{G}^R\tilde{\gamma}_i\mathcal{G}^A\mathcal{T}^A\gamma_\mu\}, \tag{4.110}$$

where $\tilde{\gamma}_{(i)\mu} = \frac{1}{D}tr\{\tilde{\gamma}_i\gamma_\mu\}$ and D is the dimension of the algebra. We now notice that the trace piece of Eq.(4.110) can be split into two contributions,

$$\frac{1}{D}tr\{\mathcal{T}^R\mathcal{G}^R\tilde{\gamma}_i\mathcal{G}^A\mathcal{T}^A\gamma_\mu\} = \frac{1}{D}tr\{\mathcal{T}^R\mathcal{G}^R\gamma_\nu\mathcal{G}^A\mathcal{T}^A\gamma_\mu\}\frac{1}{D}tr\{\tilde{\gamma}_i\gamma_\nu\} = I_{\mu\nu}\tilde{\gamma}_{(i)\nu}, \tag{4.111}$$

where we adopted the Einstein summation and used that $(\gamma_\nu)_{ij}(\gamma_\nu)_{lm} = \delta_{im}\delta_{jl}$. By decomposing $I_{\mu\nu}$ in a similar way, we obtain the compact relation

$$\tilde{\gamma}_{(i)\mu} = \delta_{i\mu} + \Upsilon_{\mu\xi}\mathcal{N}_{\xi\nu}\tilde{\gamma}_{(i)\nu} \longleftrightarrow \tilde{\gamma}_i = \gamma_i + \Upsilon\mathcal{N}\tilde{\gamma}_i, \tag{4.112}$$

that can now be rearranged to attain an open equation for the renormalized vertex,

$$\tilde{\gamma}_{(i)\nu} = \mathcal{D}_{\nu\mu}\gamma_{(i)\mu} = \mathcal{D}_{\nu i} \longleftrightarrow \tilde{\gamma}_i = \sum_\nu \mathcal{D}_{\nu i}, \tag{4.113}$$

that is the main result of this section. The operator $\mathcal{D}^{-1}_{\mu\nu} = \delta_{\mu\nu} - \Upsilon_{\mu\xi}\mathcal{N}_{\xi\nu}$ is called "Diffuson" [187], where

$$\begin{aligned}\Upsilon_{ij} &= \frac{1}{D}\mathrm{tr}[\gamma_i\mathcal{T}^R\gamma_j\mathcal{T}^A],\\ \mathcal{N}_{ij} &= \frac{n_i}{D}\sum_{\mathbf{k}}\mathrm{tr}[\gamma_i\mathcal{G}^R\gamma_j\mathcal{G}^A],\end{aligned} \tag{4.114}$$

where the momentum integration has been absorbed by the $\mathcal{N}$ matrix, exploiting the independence of the density vertex from the momentum. This operator encodes information about the disorder-averaged Green's functions forming a response bubble in the absence of interference, whilst the Υ matrix describes the insertion of impurities connecting the two sides of the response bubble. The density-current response function in the static limit, $K_{\alpha\beta}$, finally becomes

$$K_{\alpha\beta} = \frac{1}{2\pi}\sum_\nu \int d\mathbf{k}\, tr\{\mathcal{D}_{\nu\alpha}\,\mathcal{G}^R(\epsilon+\omega,\mathbf{k}+\mathbf{q})\,\mathbf{J}_\beta(\mathbf{k})\,\mathcal{G}^A(\epsilon,\mathbf{k})\}, \tag{4.115}$$

with $J_\beta = e\partial\mathcal{H}/\partial p_\beta$ being the electrical current operator [188] ($e < 0$). The technique shown here offers a general and transparent algorithm to evaluate the density-current response with no needs for ansatzes. However, further simplifications can be adopted if the current vertex is independent on the momentum as well, that is the case of Dirac systems. Before delving into that, we question how to apply a similar method to momentum-dependent vertices, relevant in current-current response function, the conductivity.

Self-consistent vertex renormalization in current-current responses

The inversion of the Diffuson operator that we used between Eqs.(4.112) and (4.113) is the critical passage to derive a transparent formula for the renormalized density vertex $\tilde{\gamma}_i$. Such operation is, however, forbidden if the renormalized vertex is momentum-dependent, since it would be impossible to dissociate the $\mathcal{N}$ matrix from the vertex operator. Nevertheless, we can overcome this obstacle in non-interacting systems. To show that, we consider the current operator $\tilde{J}_\beta$ (right vertex), where the related Bethe-Salpeter equation is

$$\tilde{J}_\beta = J_\beta + n_i \sum_{\mathbf{k}} \mathrm{tr}[T^A \mathcal{G}^A \tilde{J}_\beta \mathcal{G}^R T^R]. \tag{4.116}$$

We can understand it as the sum of two components, the bare current operator and the renormalized counterpart, $\tilde{J}_\beta = J_\beta + \delta J_\beta$. While J_β and $\tilde{J}_\beta$ are momentum-dependent, the last term is an integration over the renormalized vertex, and is therefore *independent* on the momentum. Moreover, it follows in turn another Bethe-Salpeter equation,

$$\delta J_\beta = \delta \bar{J}_\beta + n_i \sum_{\mathbf{k}} \mathrm{tr}[T^A \mathcal{G}^A \delta J_\beta \mathcal{G}^R T^R], \tag{4.117}$$

where

$$\delta \bar{J}_\beta = n_i \sum_{\mathbf{k}} \mathrm{tr}[T^A \mathcal{G}^A J_\beta \mathcal{G}^R T^R], \tag{4.118}$$

meaning that we can follow the same passages presented in the former section, and obtain an open equation for δJ_β. We derive an analogous formula to Eq.(4.113), where the Kronecker delta $\gamma_{(i)\nu}$ is replaced by the projection of the first-order renormalized vertex in the algebra, $\delta\bar{J}_{(i)\nu}$. We finally reach

$$\delta J_\beta = \widetilde{\mathcal{D}}_{\beta\nu} \delta \bar{J}_\nu, \tag{4.119}$$

and the diffuson operator becomes

$$\widetilde{\mathcal{D}}^{-1} = \mathbb{1} - \mathcal{N}^{\mathrm{T}} \Upsilon^{\mathrm{T}}, \tag{4.120}$$

where the transpose of the $\mathcal{N}$ and Υ matrices is due to the different position of the renormalized vertex. The current-current response tensor is thus given by

$$\sigma_{\alpha\beta} = \frac{1}{2\pi} \sum_{\mathbf{p}} \mathrm{tr}[J_\alpha \mathcal{G}^R_{\mathbf{p}} \left(J_\nu + \widetilde{\mathcal{D}}_{\beta\nu} \delta \bar{J}_\nu \right) \mathcal{G}^A_{\mathbf{p}}]. \tag{4.121}$$

Response function in Dirac systems

In this particular case, relevant in graphene and surface states of 3D topological insulators, the current operator is proportional to the density vertex, i.e., $J_\beta \sim \gamma_\beta$. The density-current, density-density, and current-current responses have therefore all the same form. Excluding prefactors, the response function becomes

$$\mathcal{R}_{\mu\nu} \sim \sum_{\mathbf{k}} tr\{\mathcal{G}^A \gamma_\mu \mathcal{G}^R \tilde{\gamma}_\nu\}, \tag{4.122}$$

that is similar to the Bethe-Salpeter equation and can therefore be treated in an analogous way. We can split the expression above as

$$\mathcal{R}_{\mu\nu} \sim \sum_{\mathbf{k}} tr\{\mathcal{G}^A \gamma_\mu \mathcal{G}^R \gamma_\alpha\} \tilde{\gamma}_{(\nu)\alpha} = \frac{D}{n_i} \mathcal{N}_{\mu\alpha} \tilde{\gamma}_{(\nu)\alpha}, \tag{4.123}$$

which using Eq.(4.112) and (4.113), takes the form

$$\mathcal{R}_{\mu\nu} = c_{\mu\nu} \frac{D}{n_i} \Upsilon^{-1}_{\mu\alpha} (\mathcal{D}_{\alpha\nu} - \gamma_{(\nu)\alpha}), \tag{4.124}$$

elegantly introduced in Ref. [52]. The coefficient $c_{\mu\nu}$ comprises the factors identifying the type of response desired. Beyond the Dirac system case, this approach can be adopted in the density-density response of generic systems, included 2DEGs. Its significant advantage is the possibility to avoid the momentum integration in Eq.(4.115), which is computationally convenient and allows the formulation of the "Diffusion Hamiltonian", presented in the next chapter.

It can be helpful to clarify the notation we adopt with the SO(5) Clifford algebra, used to describe graphene and graphene-based heterostructures. As shown in Chap.(3), the generator of the algebra, hence the density/current operator, is $\gamma_{ij} = \sigma_i \otimes s_j$, which implies a response function of the form

$$\mathcal{R}_{\alpha\beta\rho\sigma} = \frac{1}{2\pi} tr\left\{\gamma_{\alpha\beta} \mathcal{G}^R \tilde{\gamma}_{\rho\sigma} \mathcal{G}^A\right\} \longrightarrow \frac{2}{\pi n} \Upsilon^{-1}_{\mu\alpha ab} (\mathcal{D}_{ab\sigma\beta} - \gamma_{\sigma\beta ab}), \tag{4.125}$$

where we neglected the prefactors coming from the observable operators for simplicity. We also used

$$\tilde{\gamma}_{\alpha\beta} = \gamma_{\alpha\beta} + n_i \sum_{\mathbf{k}} \mathcal{T}^A \mathcal{G}^A \tilde{\gamma}_{\alpha\beta} \mathcal{G}^R \mathcal{T}^R, \tag{4.126}$$

directly obtained from Eq.(4.110), the projection of the generator on the algebra, $\tilde{\gamma}_{\alpha\beta ab} = \frac{1}{4} tr\{\tilde{\gamma}_{\alpha\beta} \gamma_{ab}\}$, and $\tilde{\gamma}_{\alpha\beta ab} = \mathcal{D}_{abcd} \gamma_{\alpha\beta cd} = \mathcal{D}_{ab\alpha\beta}$.

4.4.5 The Diffuson method

The Diffuson method, widely used in the condensed matter literature [187, 62, 35], is a way to derive the spin and charge-coupled dynamics under very general space-time perturbations. It can treat the effect of electric and magnetic fields and provides a detailed description of diffusion effects arising from initial non-equilibrium charge and spin density accumulations. The resulting equations can also describe a number of interrelated effects such as the SHE, EE and much more. The idea behind this method is particularly simple.

For a start, the density-density linear response theory in frequency-momentum space, which extends to density-current and current-current responses in Dirac systems, is adopted (see Eq.(4.94) and (4.115)),

$$\delta\mathbf{A}(\omega,\mathbf{q}) = K(\omega,\mathbf{q})\cdot\mathbf{F}(\omega,\mathbf{q}), \tag{4.127}$$

where we dropped the average symbol $\langle ...\rangle$ to lighten the notation. In this form, $\delta\mathbf{A}(\omega,\mathbf{q})$ is a vector of perturbed observable of interest to us (densities in 2DEGs, also currents in 3D-TI and graphene-based systems) and $\mathbf{F}(\omega,\mathbf{q})$ is a vector listing all the relevant external fields coupled to the system. Consequently, $K(\omega,\mathbf{q})$ is a matrix describing all the possible couplings between $\mathbf{F}$ and $\delta\mathbf{A}$. For example, systems characterized by the SU(2) algebra have $\delta\mathbf{A} = (N,\mathbf{S})$ and $F = (V,\mathbf{A}_{\rm v})$, where V is the scalar potential and $\mathbf{A}_{\rm v}$ is the vector potential. Clearly, the inversion of Eq.(4.127) generates a set of coupled-observables equations connected to the external fields

$$K^{-1}(\omega,\mathbf{q})\cdot\delta\mathbf{A}(\omega,\mathbf{q}) = \mathbf{F}(\omega,\mathbf{q}). \tag{4.128}$$

The next step [35] is to compute a series expansion in $\mathbf{q}$ and ω and perform an inverse Fourier transform, i.e., $-\mathrm{i}\omega\to\partial_t$ and $\mathrm{i}q_i\to\nabla_i$. The result is a partial differential set of kinetic equations

$$(-Q\partial_t - Y_i\nabla_i^2 - P_i\nabla_i + L)\cdot\delta\mathbf{A}(t,\mathbf{r}) = F(t,\mathbf{r}), \tag{4.129}$$

where $Q = -\mathrm{i}(\partial_\omega K^{-1})_{\omega=0}$, $(\mathbf{P},\mathbf{Y}) = \mathrm{i}(\partial^{(2)}_{\mathbf{q}}K^{-1})_{\mathbf{q}=0}$, and $L = K^{-1})_{\omega=0,\mathbf{q}=0}$. The evaluation of Eq.(4.129) is, however, computationally costly and cannot be applied in general. Our aim is then to write a more explicit form.

Gaussian approximation

For illustrative porpoises, we first present the standard expression for Eq.(4.128) in Gaussian approximation, wherein $\Upsilon\to u$ and u is the diagonal component of the impurity potential. From Eq.(4.123), the density-density linear response can be written as

$$\delta\mathbf{A}(\omega,\mathbf{q}) = \frac{D}{2\pi\, n_i}\mathcal{N}\cdot\mathcal{D}\cdot\mathbf{F}(\omega,\mathbf{q}), \tag{4.130}$$

where $\mathcal{D}^{-1} = \mathbb{1} - u^{-1}\mathcal{N}$. Once we invert the relation above to obtain Eq.(4.128), we realize that the most relevant modes of the inverse Diffuson operator $\mathcal{D}$ are identified by

the condition $\mathcal{N} \sim u$. If we apply it, Eq.(4.130) can then be redesigned in the simplified form

$$\mathcal{D}^{-1} \cdot \delta\mathbf{A}(\omega, \mathbf{q}) = 0. \tag{4.131}$$

The inverse density fluctuation propagator $\mathcal{D}^{-1}$ becomes the kernel of the kinetic equations and we set the external fields to zero. This formulation of the Diffuson method has been successfully applied to two-dimensional gases and topological insulators with scalar impurities [187, 62], where the coefficient linear in the momentum $\mathrm{i}(\partial_{\mathbf{q}}\mathcal{D}^{-1})_{\mathbf{q}=0} = 0$, and the kinetic equation take the form of diffusion relations. Nevertheless, Eq.(4.131) leads, in general, to wrong results due to assumption on the $\mathcal{N}$-matrix used above and the resulting loss of information, crucial in other systems such as graphene. Moreover, it has no access to a self-consistent treatment of the external potentials, which are usually added by hand.

Self-consistent treatment and the Diffuson Hamiltonian

A general self-consistent procedure to find the kinetic equations is desirable to tackle a wider variety of systems, like Dirac materials and solids with some generic disorder. The expression for the generalized kernel of the kinetic equations is surprisingly simple and significantly impactful to finding the related equation and is called *Diffuson Hamiltonian*, $\mathcal{H}_{\mathrm{D}}$. To find its expression, we start by combining Eq.(4.124) and (4.128), finding

$$\left(\Upsilon^{-1}(\mathcal{D} - \mathbb{1})\right)^{-1} \cdot \delta\mathbf{A}(\omega, \mathbf{q}) = \frac{D}{n_i}\, \hat{c} \cdot \mathbf{F}(\omega, \mathbf{q}), \tag{4.132}$$

where $(\hat{c})_{\mu\nu} = c_{\mu\nu}$. We now use the matrix identity $(A - B)^{-1} = A^{-1} + A^{-1}(B^{-1} - A^{-1})^{-1}A^{-1}$, and identifying $A = -\mathbb{1}$ and $B = -\mathcal{D}$, we easily obtain

$$\mathcal{H}_{\mathrm{D}} \cdot \delta\mathbf{A}(\omega, \mathbf{q}) = \frac{D}{n_i}\, \hat{c} \cdot \mathbf{F}(\omega, \mathbf{q}), \tag{4.133}$$

where

$$\mathcal{H}_{\mathrm{D}} = -\Upsilon + \mathcal{N}^{-1}. \tag{4.134}$$

This expression elegantly simplifies the difficult task of inverting the response function by disentangling different disorder contributions. In fact, the Diffuson Hamiltonian separates the vertex renormalization in the bubble (Υ) from the propagators ($\mathcal{N}$). In contrast to the approximated Eq.(4.131), the Diffuson Hamiltonian is an exact inversion of the response function, encapsulating all the information it encodes. Firstly, it does not approximate the contribution of the $\mathcal{N}$ matrix for the identification of the most relevant modes. Secondly, it can effectively deal with the T-matrix treatment of the disorder. Lastly it self-consistently incorporates the external fields.

The Diffuson Hamiltonian method is accurately applied in Ref. [35] and in Chap.(5), where it results to be particularly convenient due to the large Clifford space of Dirac materials. In these cases, $\mathcal{H}_{\mathrm{D}}$ is linear in $\mathbf{q}$ and the resulting transport relations incorporate continuity-like and Fick-like equations.

Chapter 5

Anomalous Spin-Charge Conversion in Graphene with Random Spin-Orbit Coupling

5.1 Overview

This chapter starts our analysis of coupled spin and charge dynamics in graphene with random sources of spin-orbit interactions. These may stem from adatom decoration of graphene sheets or from fluctuations of uniform spin-orbit fields. Our interest in these systems is fueled by the recent attention on their transport properties, since the current experimental and theoretical viewpoint [110, 53, 189, 190] emphasizes the crucial role of such impurities on spin-transport phenomena, being able to generate a sizable spin Hall [31] and current-induced spin-accumulation effect [38]. Previous theoretical works attempted to study the resulting transport properties by employing both the semiclassical [31] and quantum Boltzmann equations [38]. The value of these early works was to unveil the crucial importance of the skew scattering mechanism to producing current-induced spin-currents [19] and the unconventional anisotropic spin-precession to inducing nonequilibrium spin densities [191].

The goal of this project is to extend the current understanding of the system by fully characterizing its transport properties using our established Diffusion Hamiltonian formalism. In this context, we derive a complete set of space and time-dependent charge-spin transport relations, divided into continuity-like equations for charge/spin densities and drift-diffusion equations for charge/spin currents. This unified theory can model a large number of transport experiments that include electric and optical charge/spin injection and detection. It captures rich opto-spintronic phenomena, such as the spin galvanic-effect, Dyakonov-Perel and Elliott-Yafet spin-relaxations, the spin-Hall effect, and the ASP. In particular, we will demonstrate that the interference between scalar and SOC parts of the scattering potentials gives rise to an unusual interband spin-orbit scattering (ISOS) mechanism that has not been reported to date. The result is a robust extrinsic spin current that dominates over the semiclassical skew-scattering-induced spin Hall effect at low electronic density in and weak impurity po-

tential regime. In order to better interpret the results, we also implement the QBE with an extended ansatz, enabling it to better describe the system and reproduce the ISOS results.

5.2 The Diffuson approach

The minimal model for adatom-decorated graphene is captured by the low-energy Dirac Hamiltonian and a short-range disorder potential $V(\mathbf{x})$ including Rashba-type, Kane-Mele and scalar impurity interactions (Eq.(3.22)). Our theory neglects the uniform intrinsic SOC and intervalley scattering, which requires a tiny impurity range of the order of the lattice constant. As a consequence, we can restrict our analysis to the Hamiltonian of a single Dirac cone

$$\mathcal{H} = \int d\mathbf{x}\, \psi^{\dagger}(\mathbf{x}) \left[\mathrm{v}\gamma_{i0} p_i - \gamma_{00}\epsilon + V(\mathbf{x}) \right] \psi(\mathbf{x}), \tag{5.1}$$

where we make use of natural units $\hbar \equiv 1$ and $e \equiv 1$, and ϵ is the Fermi energy. The matrix structure of the disorder potential is the most unusual attribute of Eq.(5.1) and the crucial feature that enables the emergence of the rich phenomenology distinguishing this system from other 2D materials. To show that, we investigate the linear response to a weak external space and time-dependent perturbation $\boldsymbol{\mathcal{A}}(\mathbf{x}, t)$, and we limit our examination to diffusive disordered systems, where $k_f l \ll 1$, with k_f and l being the Fermi momentum and mean free path respectively, and coherent multiple scattering corrections can be neglected [51]. Furthermore, we focus on the dilute limit, where the renormalized response function becomes inversely proportional to the concentration of impurities, i.e., $\mathcal{R}_{\alpha\beta\rho\sigma}(\mathbf{q}, \omega) \sim 1/n_i$. The linear response takes the form

$$\langle \gamma_{\alpha\beta} \rangle (\mathbf{q}, \omega) = -i\omega \mathcal{R}_{\alpha\beta\rho\sigma}(\mathbf{q}, \omega) \mathcal{A}_{\rho\sigma}(\mathbf{q}, \omega), \tag{5.2}$$

where the external field $\mathcal{A}_{\rho\sigma}(\mathbf{q}, \omega)$ spans the whole Clifford algebra; it describes spin and charge densities and vector fields. We recall that Eq.(7.25) underlies any type of linear response up to additive constants, being all the macroscopic observables expressed in terms of γ-matrices (see Eq.(4.64)). Following the diagrammatic Kubo-Streda formulation of the linear response theory, the disorder averaged response can be expressed as

$$\mathcal{R}_{\alpha\beta\rho\sigma}(\mathbf{q}, \omega) = \frac{1}{4\pi} \int d\mathbf{k} tr \left\{ \gamma_{\alpha\beta} \mathcal{G}^{R}_{\epsilon+\omega}(\mathbf{k}+\mathbf{q}) \tilde{\gamma}_{\rho\sigma}(\mathbf{q}, \omega) \mathcal{G}^{A}_{\epsilon}(\mathbf{k}) \right\}, \tag{5.3}$$

where

$$\mathcal{G}^{R(A)} = \frac{1}{(G^{R(A)})^{-1} - \Sigma^{R(A)}} \tag{5.4}$$

is the renormalized retarded (advanced) Green's function (GF), $\Sigma^{R,A} = \langle V + V G^{R,A} V + ... \rangle_{\mathrm{dis}}$ the self-energy, and

$$\tilde{\gamma}_{\alpha\beta}(\mathbf{q}, \omega) = \gamma_{\alpha\beta} + n_i \sum_{\mathbf{k}} \mathcal{T}^{A} \mathcal{G}^{A}_{\epsilon}(\mathbf{k}) \tilde{\gamma}_{\alpha\beta}(\mathbf{q}, \omega) \mathcal{G}^{R}_{\epsilon+\omega}(\mathbf{k}+\mathbf{q}) \mathcal{T}^{R}, \tag{5.5}$$

the dressed density vertex (see Eq.(4.110)). The form of the disorder potential implies a non-trivial matrix structure of the self-energy, which also involves mixed products of impurity couplings. This suggests, and will be shown along the chapter, that some phenomenological effects are direct consequence of the interplay between different types of extrinsic couplings. Clearly, the commonly used Gaussian approximation (GA), i.e: $\langle V(\mathbf{x})V(\mathbf{x}')\rangle_{\text{dis}} \sim \sum_{i=R,KM,V} u_l^2\delta(\mathbf{x}-\mathbf{x}')\gamma_{00}$, loses this information, producing solely an imaginary scalar self-energy. Our disordered system provides an example of such mixture, where the evaluation of low-order diagrams in the weak impurity potential regime, the first Born approximation (FBA), produces a self-energy of the form

$$\Sigma = \Sigma_0 + \Sigma_{12} + \Sigma_{33} \sim \gamma_{00} \sum_{i=R,KM,V} u_i^2 + u_R(\gamma_{12}-\gamma_{21})(u_0-u_{KM}) + \gamma_{33}(u_R^2 - u_{KM}u_0) \quad (5.6)$$

where we showed only the second order expression in the impurity coupling (the first order is trivially the impurity potential itself).

The intricated coupled dynamics of spin and charge, enclosed in Eq.(5.3), can be displayed by evaluating the inverse of $\mathcal{R}(\mathbf{q},\omega)$, the Diffuson Hamiltonian $\mathcal{H}_D$. The corresponding inverse Fourier transform in real space and time leads to a system of 12 coupled kinetic equations, one for each observable of interest to us. At first, we simplify the problem by evaluating $\mathcal{H}_D$, i.e., Eq.(4.134), in FBA, thus focusing our interest on quantum interference effects between the different impurities and excluding the role of skew scattering. Our findings are summarized by the following three compact relations:

$$\partial_t S_\mu + \mathcal{T}^{0\mu} S_\mu - (\mathbf{\Psi}^\mu \times \boldsymbol{\mathcal{J}})_z + \mathbf{H}^{\mu a}\cdot\mathcal{J}^a = \frac{\nu_0}{4}(1-\delta_{u0})\mathcal{B}_\mu \quad (5.7)$$

$$\partial_t \mathcal{J}_l^\nu + \mathcal{T}^{l\nu}(\mathcal{J}_l^\nu + \epsilon_{zlj}\Lambda_l^{\nu a}\mathcal{J}_j^a + D_{l\nu}\partial_l S_\nu + D_A^{\nu lj}\epsilon_{zik}\partial_i\mathcal{J}_j^k + D_B^{\nu li}\partial_j\mathcal{J}_i^j - \epsilon_{zlj}I_l^\nu S_j + \delta_{\nu z}\alpha_{\text{xyR}}S_l) = \nu_0 \text{D}\mathcal{T}^{l\nu}\delta_{\nu 0}\text{E}_l \quad (5.8)$$

$$\partial_t \mathcal{J}_l^m + \mathcal{T}^{lm}(\mathcal{J}_l^m + \epsilon_{zlj}\Lambda_l^{mk}\mathcal{J}_j^k + D_{lm}\partial_l S_m + D_C^{mlai}\epsilon_{zij}\partial_i\mathcal{J}_j^a + D_D^{mlai}\partial_i\mathcal{J}_i^a - \delta_{lm}\alpha_{\text{zR}}S_z) = 0 \quad (5.9)$$

where $\nu_0 = \epsilon/\pi \text{v}^2$ is the density of states, $\text{E}_\mu = -\partial_t\mathcal{A}_{\mu 0}(\mathbf{x},t)$ is the external electric field, and $\mathcal{B}_\mu = \frac{1}{\text{v}}\partial_t\mathcal{A}_{0\mu}(\mathbf{x},t)$ is the Zeeman field. The coefficients $D_{A,B,C,D}$ represent the spin and charge density transfer via diffusion mechanisms and the $\mathcal{T}$s are relaxation times. $\mathbf{H}^{\mu\nu} = \delta_{\mu\nu}\boldsymbol{\nabla} + \mathbf{R}^{\mu\nu}$, with $\mathbf{R}$ describing the spin density precession mediated by the Rashba impurities [192], and $\mathbf{\Lambda}^{\nu\sigma} = \mathbf{\Gamma}^{\nu\sigma} + \mathbf{\Omega}^{\nu\sigma}\partial_t$ expresses the time-dependent spin current swapping and the spin-charge current conversion. The index $\mu = (0,x,y,z)$, $\nu = (0,z)$, $(m,l,a,i,j,k) = (x,y)$, and all the coefficients are listed in Appendix B. Eq.(5.7) encompasses the continuity equation for the charge density N and three continuity-like equations for $S_{x,y,z}$. Eqs.(5.8) and (5.9) are generalized

drift-diffusion relations for charge and spin currents, where the former addresses the charge-spin current conversions, i.e., the (inverse) spin Hall effect, and the latter captures spin-current swappings.

We can notice how the phenomenology described by the transport equations shown above strongly resembles the spin-charge dynamics in graphene monolayers with uniform Rashba SOC as shown in Ref. [35]. As we will better discuss in the chapter, such similarity is a consequence of the effective homogeneous spin-orbit field produced by the Rashba-type disorder, where the product between the impurity concentration and the local SOC strength plays the role of the uniform Rashba coupling acting on the band structure. For this reason, the system of equations derived for our system more generally describes, phenomenologically, disordered graphene with intrinsic and extrinsic Rashba and Kane-Mele SOC, where all the coefficients must be adapted accordingly.

A more transparent interpretation of the spin-charge drift-diffusion equations is attainable by neglecting diffusion processes in the limit of $\mathbf{q} \to 0$, i.e., no gradients, and showing all the coupling constants in the weak SOC regime, defined as $u_{KM} < u_R < u_0 < 1$ [31]. Within these approximations, we first present the simplified version of Eq.(5.7)

$$\begin{cases} \partial_t S_{x(y)} + \frac{1}{\tau_\parallel} S_{x(y)} \mp [-]\alpha_{\mathrm{ASP}} J_{y(x)} - [\mp]\alpha_{\mathrm{R}} \mathcal{J}^z_{x(y)} = \frac{\nu_0}{2} \mathcal{B}_{x(y)} \\ \\ \partial_t S_z + \frac{1}{\tau_\perp} S_z + \alpha_{\mathrm{R}} (\mathcal{J}^{\mathrm{x}}_{\mathrm{x}} + [-]\mathcal{J}^{\mathrm{y}}_{\mathrm{y}}) = \frac{\nu_0}{2} \mathcal{B}_z \end{cases} , \tag{5.10}$$

where the sign change inside the squared brackets refers to the anomalous Rashba case. We omitted the ubiquitous continuity equation for the charge density, which guarantees the conservation of mass. On the contrary, $S_{x(y)}$ and S_z are not conserved quantities, dephasing with characteristic relaxation times proportional to $\tau_\parallel$ and $\tau_\perp$ respectively.

The Rashba constant α_R mediates the interplay between spin densities and currents, also displaying the first similarity between graphene with active adatoms and graphene with uniform Rashba SOC; such coupling is, in fact, present in both systems. In particular, our theory finds $\alpha_{\mathrm{R}} = 2 n_i u_R / \mathrm{v}$, which also describes the homogeneous scenario by mapping

$$n_i u_R \longleftrightarrow \lambda, \tag{5.11}$$

with λ being the Rashba interaction in the band structure [35]. Eq.(5.11) shows that the Rashba impurities also play the role of an uniform interaction in our system which strength is proportional to the impurity potential u_R and concentration n_i.

Finally, the coupling constant $\alpha_{\mathrm{ASP}} = n_i u_{KM} u_R \epsilon / \mathrm{v}^3$, which entangles the spin density with the charge current, entirely arises from the ASP mechanism, requiring the presence of both u_{KM} and u_R.

The spin-flip scattering off nonmagnetic impurities in the presence of local spin-orbit interaction leads to the Elliott-Yafet (EY) type spin relaxation mechanism [193], where the spin relaxation is proportional to the scattering time $\tau = 2\mathrm{v}^2 / n\epsilon u_0^2$, i.e. $\tau_s \sim \tau$. This term is encoded in $\tau_\parallel$ and $\tau_\perp$ that take the form $\tau_\parallel = 2\tau_\perp = \mathrm{v}^2 / 2 n_i u_R^2 \epsilon$ in the weak SOC limit. On the other hand, the homogeneous behaviour of the Rashba-type

impurities, identified by Eq.(5.11), would suggest the contribution of the D'yakonov-Perel' (DP) spin relaxation mechanism $\tau_s \sim \tau^{-1}$. Indeed, solving Eqs.(5.7) and (5.8) self-consistently, we find a closed form for the relaxation times

$$\begin{cases} \frac{1}{\tau_{sx(sy)}} = \frac{1}{\tau_\parallel} + D_z\alpha_{\mathrm{R}}^2 - 4D\alpha_{\mathrm{ASP}}^2 \\ \frac{1}{\tau_{sz}} = \frac{1}{\tau_\perp} + 2D_{xx}\alpha_{\mathrm{R}}^2 \end{cases} \tag{5.12}$$

where D_{xx} is the diffusion constant related to $J^{x(y)}_{x(y)}$ ($D_{xx} = D$ in the weak SOC limit). The purely Rashba-type contribution to the relaxation times, $2D_{xx}\alpha_{\mathrm{R}}^2 = 2D_z\alpha_{\mathrm{R}}^2 = 4\mathrm{v}\tau(nu_R)^2$, is the DP mechanism, also present in graphene heterostructures, and mediated by the coupling constant $\lambda^2\tau$ [51]. Once again, this result is contained in our theory and displayed by Eq.(5.11).

We can now proceed with the analysis of charge-spin current conversion mechanisms by unfolding Eq.(5.8). This is the main result of the chapter, revealing the presence of the ISOS-induced spin Hall effect that the theory uncovers:

$$\begin{cases} \mathrm{J_{x(y)}} + \tau_{\mathrm{J}_\parallel}\partial_\mathrm{t}\mathrm{J_{x(y)}} \pm [-]\alpha_{\mathrm{IASP}}\mathrm{S_{y(x)}} \pm [\mp]\beta^{\mathrm{ISOS}}_{\mathrm{IsH}}\mathcal{J}^z_{y(x)} = \nu_0 D E_x \\ \\ \mathcal{J}^\mathrm{z}_{\mathrm{x(y)}} + \tau_{\mathrm{J}_\perp}\partial_\mathrm{t}\mathcal{J}^\mathrm{z}_{\mathrm{x(y)}} + [\pm]\alpha_{\mathrm{xyR}}\mathrm{S_{x(y)}} \pm [\mp]\beta^{\mathrm{ISOS}}_{\mathrm{sH}} J_{y(x)} = 0 \end{cases}, \tag{5.13}$$

where $D = \mathrm{v}^2\tau$ is the diffusion constant. The time evolution of the currents is controlled by the relaxation times $\tau_{J_\parallel}$ and $\tau_{J_\perp}$, that in the weak SOC limit become proportional to the scattering time, $\tau_{J_\parallel} = \tau_{J_\perp} = 2\tau$. The inverse coupling between the charge-current and the spin-density, absent in the uniform Rashba case, is allowed by the ASP mechanism via $\alpha_{\mathrm{IASP}} = 8u_{KM}u_R\mathrm{v}/u_0^2$, while $J^z_{x(y)}$ and the in-plane spin-densities are paired via α_{xyR}, where $\alpha_{\mathrm{xyR}}/\tau_{J_\perp} = \mathrm{v}nu_R \to \mathrm{v}\lambda$.

The leading contribution in the impurity potential strength to the (inverse) spin Hall effect is determined by the coupling constant $\beta^{\mathrm{ISOS}}_{\mathrm{(I)sH}} = (4\times)4u_R^2\mathrm{v}^2/u_0^3\epsilon$, which entirely originates from the ISOS mechanism. Surprisingly, this term is still present in the absence of skew scattering, currently considered the crucial ingredient to generate current-induced spin-currents in the dilute (weak disorder) regime [19, 8]. Similar to the ASP mechanism, which results from the interference between Rashba and Kane-Mele impurities, the ISOS emerges from the simultaneous presence of scalar and Rashba potentials. This term is obtained by an accurate renormalization of the particles' propagators, where the hermitian part of the self-energy, usually irrelevant in transport problems, plays a crucial role. As such, its omission would lead to the absence of the ISOS mechanism. Even though this coupling is present in graphene with uniform Rashba SOC, the resulting constitutive relations, obtained by solving the system of drift-diffusion equations exhibit zero spin Hall effect in FBA [35].

To better understand the role of this novel mechanism, we now include strong impurities, which presence requires the truncation of the T-matrix series at the third order in the impurity potential strength. This procedure activates the skew scattering mechanism, which contributes to generating current-induced spin currents. As a result, the total coupling becomes $\beta_{\mathrm{sH}} \simeq \beta^{\mathrm{ISOS}}_{\mathrm{sH}} - \beta^{\mathrm{skew}}_{\mathrm{sH}}$, where $\beta^{\mathrm{skew}}_{\mathrm{sH}} = u_{KM}\epsilon/4\mathrm{v}^2$ is the classic

result in the weak SOC limit and defines the conventional spin Hall angle. Moreover, we notice that the two terms have opposite signs, reducing the magnitude of the spin-current response for weak impurities, as identified in previous works [38, 31]. Restoring $\hbar$, we plot $\beta_{\rm sH}$ in Fig(5.1) at T-matrix approximation as a function of the Fermi energy (left panel) and the impurity potential strength (right panel). The total coupling has been decomposed into two terms,

$$\beta_{\rm sH} = \beta_{\rm sH}^{\rm ISOS} - \beta_{\rm sH}^{\rm skew}, \tag{5.14}$$

where both contributions on the right-hand side depend on the two mechanisms, but $\beta_{\rm sH}^{\rm ISOS}$ disappears in the absence of ISOS and $\beta_{\rm sH}^{\rm skew}$ returns a null result in FBA. Fig(5.1)

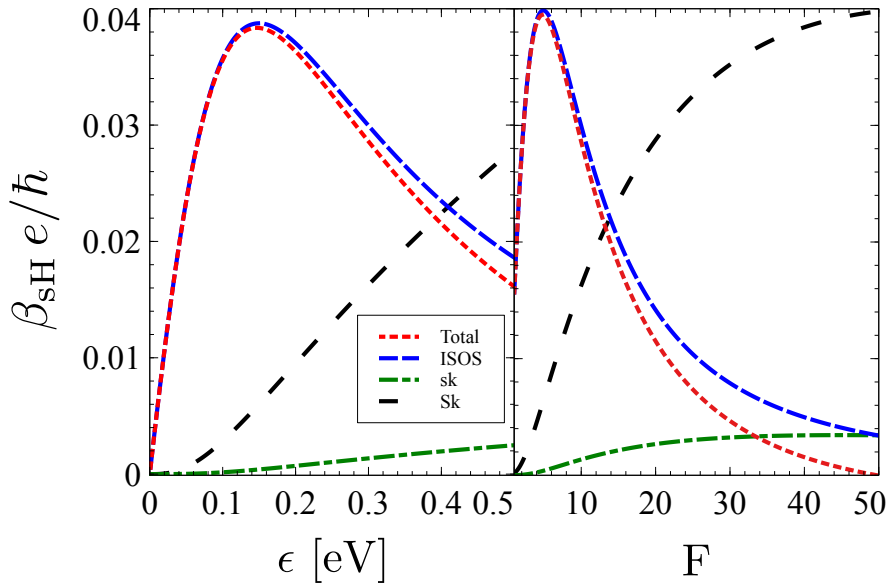

Figure 5.1: Spin Hall angle plotted versus the Fermi energy (a) and the scaling factor F (impurity strength) (b), defined as $u_{0,KM,R}^{new} = {\rm F} \times u_{0,KM,R}^{old}$. The total response (Total) is the sum of the skew scattering contribution (sk) and ISOS one. The results are compared with a strong skew scattering contribution (Sk) induced by large Kane-Mele impurities, $u_R < u_{KM} < u_0$, where the ISOS mechanism becomes negligible. Parameters: $u_0 = 100 \times {\rm F\,meV}$, $u_{\rm KM} = 3 \times {\rm F\,meV}$, $u_R = 10 \times {\rm F\,meV}$, and $u_{\rm KM} = 50 \times {\rm F\,meV}$ for the black curve. ${\rm F} = 10$ on the left panel.

reveals that the ISOS mechanism is dominant for low Fermi energy and weak impurity potential, and rapidly decreases, $\beta_{\rm sH}^{\rm ISOS} \to 0$ for $(\epsilon, u_{0,KM,R}) \to \infty$. The opposite holds for the skew scattering contribution.

The complete expression for the current-induced spin current,i.e., the spin Hall conductivity $\sigma_{\rm sH}$, is finally derived by solving Eq.(5.10) and (5.13), where this time we can compare the contributions from the ISOS and the ASP mechanism in the absence of skew scattering. Fig.(5.2a) plots the figure of merit for the spin Hall effect, expressed as the adimensional ratio $\frac{2e}{\hbar}\sigma_{\rm sH}/\sigma_{\rm D}$, where $\sigma_{\rm D}$ is the charge conductivity. This is plotted against the Fermi energy in the context of the weak SOC limit. In this regime, we

observe a similar contribution coming from the ASP and ISOS mechanism, and together they give rise to a sizable charge-to-spin conversion even in first Born approximation.

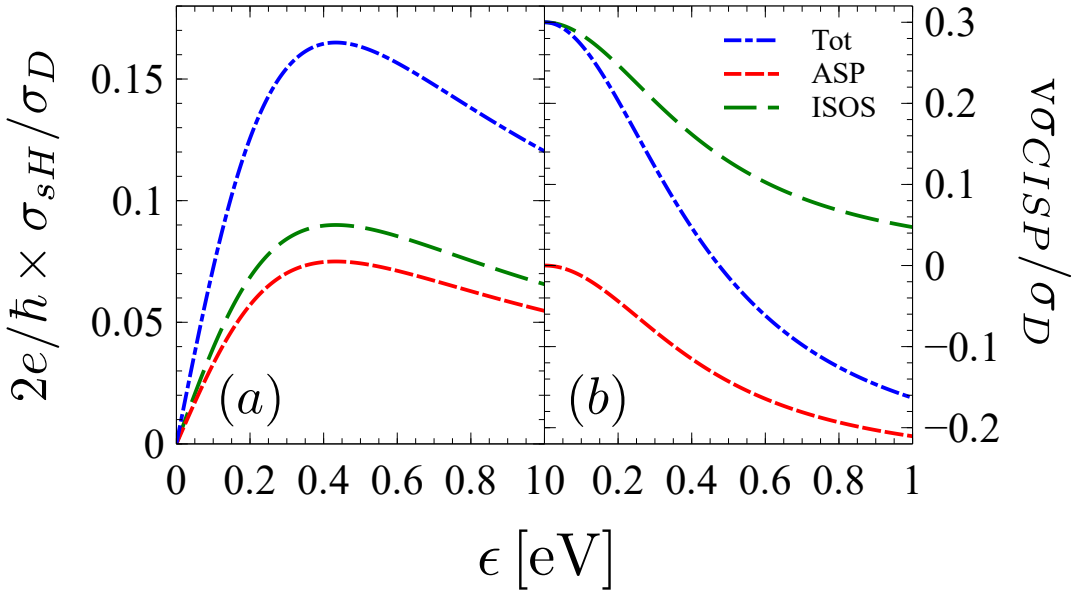

Figure 5.2: Adimensional ratio of the spin Hall (a) and current-induced spin polarization (b) conductivities to the charge conductivity, plotted against the Fermi energy. These quantities are evaluated using the first Born approximation in the absence of skew scattering and under the weak SOC limit, i.e., $u_{KM} < u_R < u_0$. In this regime, the two dominant mechanisms, ASP and ISOS, contribute equally, leading to a significant current-induced spin-current and polarization.

An expansion of the spin Hall conductivity for small α_{ASP} and $\beta_{\mathrm{sH}}^{\mathrm{ISOS}}$ allows us to write a simple expression for σ_{sH},

$$\sigma_{\mathrm{sH}} = \frac{\nu_0([-]\beta_{\mathrm{sH}}^{\mathrm{ISOS}} + D\alpha_{\mathrm{ASP}}\alpha_{\mathrm{R}}\tau_{\parallel})}{\alpha_{\mathrm{R}}^2\tau_{\parallel}}, \tag{5.15}$$

where we used $\alpha_{\mathrm{IASP}} = 4\alpha_{\mathrm{ASP}}D$, $\beta_{\mathrm{IsH}}^{\mathrm{ISOS}} = 4\beta_{\mathrm{sH}}^{\mathrm{ISOS}}$, and $\alpha_{\mathrm{xyR}} = \alpha_{\mathrm{R}}D$. The first dominant contribution is the direct ISOS-induced spin Hall coupling, while the second term is a two-step process allowed by the ASP mechanism, controlled by the interference between Kane-Mele and Rashba-type impurities, and evaluating to zero for $u_{KM} \to 0$. This second component can also generate CISC without skew scattering and has already been identified in the literature [38]. In the absence of Kane-Mele and scalar impurities, both contributions vanish and $\sigma_{\mathrm{sH}} = 0$.

Following the same procedure, the expression for the current-induced spin-polarization is

$$\sigma_{\mathrm{CISP}} = \frac{\nu_0(-[+]\alpha_{\mathrm{ASP}} + \alpha_R\beta_{\mathrm{sH}}^{\mathrm{ISOS}})}{\alpha_R^2}, \tag{5.16}$$

where the role of $\beta_{\mathrm{sH}}^{\mathrm{ISOS}}$ and α_{ASP} is now inverted. The ASP is the dominant direct mechanism, while the second order contribution is a two-step process that requires

a conversion from charge to spin current, via $\beta_{\mathrm{sH}}^{\mathrm{ISOS}}$, and a second conversion from spin current to spin density through α_R. This chain of couplings identifies the typical Edelstein effect [194], with the difference that the impurities entirely produce it in our system. Fig.(5.2b) shows $\mathrm{v}\sigma_{\mathrm{CISP}}/\sigma_{\mathrm{D}}$ against the Fermi energy. Interestingly, we observe that the competition between the ASP and the ISOS mechanisms, which are equal in magnitude but opposite in sign, yields an interpolation between the two contributions resulting in a change of the CISP's sign dependent on the Fermi energy's position.

Our transport analysis of the perturbed system, relying on the self-consistent Kubo-Streda formalism, offers an extensive insight into the spin-related effects in play but fails to provide a semiclassical intuition of the ISOS mechanism. For this reason, we aim to complement our findings by implementing the quantum Boltzmann equation technique developed in Sec.(4.3.3). The advantage of this method over the Kubo-Streda approach is the direct evaluation of the scattering processes (the golden rule), providing a clearer understanding of the underlying mechanisms [19].

5.3 The QBE approach to graphene with random SOC

The former section revealed how the ISOS mechanism contributes to the spin Hall effect in FBA, and this section aims to recover the same results by employing the quantum extension of the Boltzmann equation formalism, the QBE. This technique considers the response of conduction electrons for positive Fermi energy, thus disregarding Fermi sea contributions and projecting the operators on the conduction band. However, it preserves knowledge of purely quantum conduction-valence band transitions, which are crucial in our model, as we will shortly see. For a start, we define the spin Hall current as

$$\mathcal{J}_y^z = \sum_{\mathbf{k}} \mathrm{tr}\{(\frac{\mathrm{v}}{2}\gamma_{23}^{cc})\delta f_{\mathbf{k}}\}, \tag{5.17}$$

where $\frac{\mathrm{v}}{2}\gamma_{23}^{cc}$ is spin-current operator projected in the conduction Bloch eigenstates of pristine graphene, and $\delta f_{\mathbf{k}}$ is the deviation from the equilibrium Fermi-Dirac distribution function. As the most general ansatz for $\delta f_{\mathbf{k}}$ we avail the Fourier series

$$\delta f_{\mathbf{k}} = E \sum_j \sum_{n=-\infty}^{\infty} (\tau_{j,n} e^{in\theta_{\mathbf{k}}} s_j), \tag{5.18}$$

where $\tau_{j,n}$ are coefficients that we identify as transport times and $\mathbf{E} = (E, 0)$ is the electric field in the x-direction. The equation above captures the right ISOS physics if it can reproduce the same results as the previous section when combined with Eq.(5.17). Since we need to employ a closed solution for δf, we need to single out a subsets of harmonics from Eq.(5.18). The commonly adopted [8] first order expansion in n produces a zero spin Hall current; thus an unusual second-order is needed,

$$\delta f_{\mathbf{k}} = \mathrm{v}E \sum_{i=0}^{3} (\tau_{\parallel,i}^{(1)} \cos\theta_{\mathbf{k}} + \tau_{\perp,i}^{(1)} \sin\theta_{\mathbf{k}} + \tau_{\parallel,i}^{(2)} \cos 2\theta_{\mathbf{k}} + \tau_{\perp,i}^{(2)} \sin 2\theta_{\mathbf{k}}) s_i, \tag{5.19}$$

where we excluded θ-independent terms, responsible for the nonequilibrium density responses of the system. For simplicity, we also neglect the local Kane-Mele contribution to the disorder and, in the limit of weak extrinsic Rashba coupling, $u_R < u_0 < 1$, the scattering times read

$$\tau^{(1)}_{\parallel,0} = \frac{4e\mathrm{v}^2}{n_i u_0^2 \epsilon}, \tag{5.20}$$

$$\tau^{(1)}_{\perp,3} = \tau^{(2)}_{\parallel,2} = -\tau^{(2)}_{\perp,1} = -\frac{4eu_R\mathrm{v}^2}{n_i u_0^3 \epsilon}, \tag{5.21}$$

which are solutions of the steady-state version of Eq.(4.84). Alike the Kubo formalism, these results depend on the hermitian part of the electrons' self-energy, and $\tau^{(1)}_{\perp,3}$ evaluates to zero for $\left(\Sigma^{'}_R\right)_{cc} = 0$. Eq.(5.20) is the standard longitudinal transport time at the origin of charge conductivity

$$J_x = \sum_{\mathbf{k}} \mathrm{tr}\{(e\mathrm{v}\gamma^{cc}_{10})\delta f_{\mathbf{k}}\} = -\frac{2\mathrm{v}^2 e^2}{n_i \pi u_0^2} E, \tag{5.22}$$

while $\tau^{(1)}_{\perp,3}$ establishes a net transverse spin current

$$\mathcal{J}^z_y = -\frac{eu_R^2 \epsilon}{n_i \pi u_0^3} E, \tag{5.23}$$

which is the main result of this section. Counting for the graphene's valley degeneracy $g_v = 2$, it matches Eq.(5.15) in the absence of ASP, i.e., $u_{KM} = 0$. The relation above shows that, in the weak impurity potential limit, the extrinsic spin Hall effect appears at leading order in the impurity concentration n_i, increases linearly with the Fermi energy ϵ, and is inversely proportional to the impurity potential, mimicking the leading-order skew scattering scaling $\sim 1/u_0$.

From a technical perspective, we emphasize that even though the scattering times $\tau^{(2)}_{\parallel,2}$ and $\tau^{(2)}_{\perp,1}$ are absent in the expression for the spin current response, the crucial role of the second-order expansion of the general ansatz is to renormalize the first order antisymmetric term $\tau^{(1)}_{\perp,3}$, otherwise equals to zero. Ultimately, we point out that the antisymmetric contribution $\tau^{(1)}_{\perp,0} \sim \sin(\theta_{\mathbf{k}})$, that traditionally generates the skew scattering-activated SHE, is missing here, thus not contributing to Eq.(5.23).

For completeness, we also investigate the effect of Gaussian disorder, which is more frequently used in the literature to study disordered systems [187]. This model better describes uncorrelated weak impurities, which do not possess a collective preferred intensity of the potential. As a consequence, the random impurity field follows a white-noise distribution, implying that the first-order disorder average is equal to zero, i.e., $\langle V \rangle_{\mathrm{dis}} = 0$. The Gaussian statistics modifies the hermitian part of the self-energy, where only the second order contribution in the impurity potential is retained, $\left(\Sigma^{'}_R\right)_{cc} \to \left(\Sigma^{'(2)}_R\right)_{cc}$. A nonzero SHE of the form

$$\mathcal{J}^z_y = \frac{4u_R^2 \mathrm{v}^2 \ln(\frac{\Lambda^2}{\epsilon^2}) e}{n_i u_0^4 (\pi^2 + 2\ln(\frac{\Lambda^2}{\epsilon^2})^2)} E \tag{5.24}$$

is still produced, where Λ is the momentum cutoff. The interplay between spin-transparent and spin-flipping impurities is still at the foundation of the spin Hall effect, except that the scaling of the local electrostatic potential is now inversely proportional to its squared value. In addition, the Spin Hall current becomes less sensitive to the variation of Fermi energy with Gaussian impurities than the FBA counterpart.

5.3.1 Discussion

The cross-scattering amplitude probabilities $V^{vc}_{\mathbf{pk}}$, embedded in the hermitian part of the self-energy (see Eq.(4.84)), are the main ingredients yielding to the result shown in Eqs.(5.23) and (5.24). Their importance suggests that the SHE is activated by a mechanism that involves virtual conduction-valence band transitions and can distinguish between the spin up and down electrons; for this reason the effect is called interband spin-orbit scattering.

In order to build up a better intuition for the ISOS mechanism, we simplify the QBE using the relaxation time approximation, where the imaginary part of the collisional integral (Eq.(4.82)) is replaced by a matrix in the SO(5) Clifford space, $1/\hat{\tau}_{\parallel,\mathbf{k}}$. Any projection in graphene's conduction states is avoided here and the random distributed impurity potential is treated with the Gaussian white-noise statistics. The simplified Boltzmann equation reads

$$\mathrm{i}[\Sigma^{'}_{R}, \delta f_{\mathbf{k}}] - \frac{\mathrm{v}}{2} E(\cos\theta_{\mathbf{k}}\gamma_{00} + \cos^2\theta_{\mathbf{k}}\gamma_{10} + \cos\theta_{\mathbf{k}}\sin\theta_{\mathbf{k}}\gamma_{20})\,\delta(\epsilon - \epsilon_k) = \frac{1}{\hat{\tau}_{\parallel,\mathbf{k}}}\,\delta f_{\mathbf{k}}, \quad (5.25)$$

where the contribution $\mathrm{i}[\Sigma^{'}_{R}, \delta f_{\mathbf{k}}]$ is treated as a small perturbation of the semiclassical description of the system without which no spin Hall effect is produced. This term is the one making the quantum Liouville approach indispensable in capturing more physics in play, as against the classical Boltzmann technique. Expanding Eq.(5.25) in $\Sigma^{'}_{R}$, the displacement of the distribution function from its equilibrium form becomes

$$\delta f_{\mathbf{k}} \approx \delta f^{Boltz}_{\mathbf{k}} + i\hat{\tau}_{\parallel,\mathbf{k}} \cdot [\Sigma^{'}_{R}, \delta f^{Boltz}_{\mathbf{k}}], \quad (5.26)$$

where

$$\delta f^{Boltz}_{\mathbf{k}} = -\frac{\mathrm{v}}{2} E\,\hat{\tau}_{\parallel,\mathbf{k}} \cdot (\cos\theta_{\mathbf{k}}\gamma_{00} + \cos^2\theta_{\mathbf{k}}\gamma_{10} + \cos\theta_{\mathbf{k}}\sin\theta_{\mathbf{k}}\gamma_{20})\,\delta(\epsilon - \epsilon_k) \quad (5.27)$$

must match the standard solution from the classical Boltzmann equation [31] for a given choice of $\hat{\tau}_{\parallel,\mathbf{k}}$. In particular, we impose that the projection of Eq.(5.27) onto the conduction band must return the same values for the transport times produced in the QBE without $\Sigma^{'}_{R}$,

$$\delta f^{\mathrm{QBE}}_{\mathbf{k}} \sim \tau^{cc}_0 s_0 \cos\theta_{\mathbf{k}} + \tau^{cc}_1 s_1 \sin 2\theta_{\mathbf{k}} + \tau^{cc}_2 s_2 \cos 2\theta_{\mathbf{k}}, \quad (5.28)$$

which is the solution presented in Eqs.(5.19) and (5.21) with $\tau^{(1)}_{\perp,3} = 0$. The relaxation time $\hat{\tau}_{\parallel,\mathbf{k}}$ cannot be uniquely determined by equating $\delta f^{\mathrm{QBE}}_{\mathbf{k}}$ and $\delta f^{Boltz}_{\mathbf{k}}$, since, in general, it is a function of the momentum angle $\theta_{\mathbf{k}}$. We therefore assume $\hat{\tau}_{\parallel,\mathbf{k}}$ to be

independent on the angle to close the system of equations and establish the structure of the transport times, finally obtaining

$$\hat{\tau}_{\parallel,\mathbf{k}} \to \hat{\tau}_{\parallel} = \tau_{00}\gamma_{00} + \tau_{12}\gamma_{12} + \tau_{12}\gamma_{21}. \tag{5.29}$$

This assumption leads to a potential loss of information about the scattering processes, enclosed in $\hat{\tau}_{\parallel}$, and its relevance can be checked a posteriori by comparing the resulting expression for the spin Hall current with the rigorous result obtained with the QBE formalisms. The adopted decomposition for the relaxation time allows a simplified recast of Eq.(5.26) since $\hat{\tau}_{\parallel}$ and $\Sigma_R^{'}$ now commute, having the same matrix structure. As a result, the distribution function can be rearranged as

$$\delta f_{\mathbf{k}} \approx \delta f_{\mathbf{k}}^{Boltz} + \delta f_{\mathbf{k}}^{\mathrm{II}}, \tag{5.30}$$

where

$$\delta f_{\mathbf{k}}^{\mathrm{II}} = -i\frac{\mathrm{v}}{2}E[\Sigma_R^{'}, \left(\cos\theta_{\mathbf{k}}\hat{\tau}_{\parallel}\cdot\hat{\tau}_{\parallel}\cdot\gamma_{00} + \cos^2\theta_{\mathbf{k}}\hat{\tau}_{\parallel}\cdot\hat{\tau}_{\parallel}\cdot\gamma_{10} + \cos\theta_{\mathbf{k}}\sin\theta_{\mathbf{k}}\hat{\tau}_{\parallel}\cdot\hat{\tau}_{\parallel}\cdot\gamma_{20}\right)]\,\delta(\epsilon-\epsilon_k) \tag{5.31}$$

is the contribution to the distribution function that generates the SHE. The nonequilibrium spin Hall current is then expressed by

$$\mathcal{J}_y^z(\hat{\tau}_{\parallel}) = \sum_{\mathbf{k}} \mathrm{tr}[\delta f_{\mathbf{k}}^{\mathrm{II}}\cdot\gamma_{23}] \sim -i\frac{\mathrm{v}}{2}E\int_{\mathbf{k}}\cos^2\theta_{\mathbf{k}}\mathrm{tr}\left\{[\gamma_{12}-\gamma_{21},\hat{\tau}_{\parallel}\cdot\hat{\tau}_{\parallel}\cdot\gamma_{10}]\cdot\gamma_{23}\right\}, \tag{5.32}$$

where the terms proportional to $\cos\theta_{\mathbf{k}}\sin\theta_{\mathbf{k}}$ and $\cos\theta_{\mathbf{k}}$ disappear upon angular integration. Only the first two terms in Eq.(5.29) survive after the trace operation, and simple manipulations yield

$$\mathcal{J}_y^z = \frac{e}{\pi}\epsilon\Sigma_{12}\tau_{00}\tau_{12}E = \frac{4u_R^2\mathrm{v}^2\ln(\frac{\Lambda^2}{\epsilon^2})e}{n_i u_0^4\pi^2}E \tag{5.33}$$

where $\Sigma_{12} = -n_i\frac{u_0u_R\ln(\frac{\Lambda^2}{\epsilon^2})\epsilon}{2\pi\mathrm{v}^2}$ and we used $\tau_{00} = \frac{4\mathrm{v}^2}{n_i u_0^2\epsilon}$, $\tau_{12} = -\frac{2u_R\mathrm{v}^2}{n_i u_0^3\epsilon}$. This expression, produced by a simplified quantum Liouville equation, agrees with the rigorous results presented previously in the chapter, where a linear expansion in the hermitian part of the self-energy must be employed, according to our assumptions.

Eq.(5.33) benchmarks the validity of the relaxation time approximation, which can now be used to understand the physics behind the ISOS. To begin with, the simplified treatment of the Boltzmann equation clarifies the role of the unusual second-order harmonic expansion employed in the former section. In fact, Eq.(5.32) requires relaxation times proportional to γ_{12} to produce a non-zero spin Hall current. The relative effect on the conduction band is found by projecting such contribution onto the appropriate states, obtaining $\left(\delta f_{\mathbf{k}}^{Boltz}\right)_{cc} \sim (\tau_{12})_{cc} \sim \cos^2\theta_{\mathbf{k}}s_2$, which is the term appearing in the ansatz for the QBE. Therefore, the inclusion of second harmonics is an artefact of the projection procedure that keeps track of the non-diagonal Rashba-like contribution of the relaxation time.

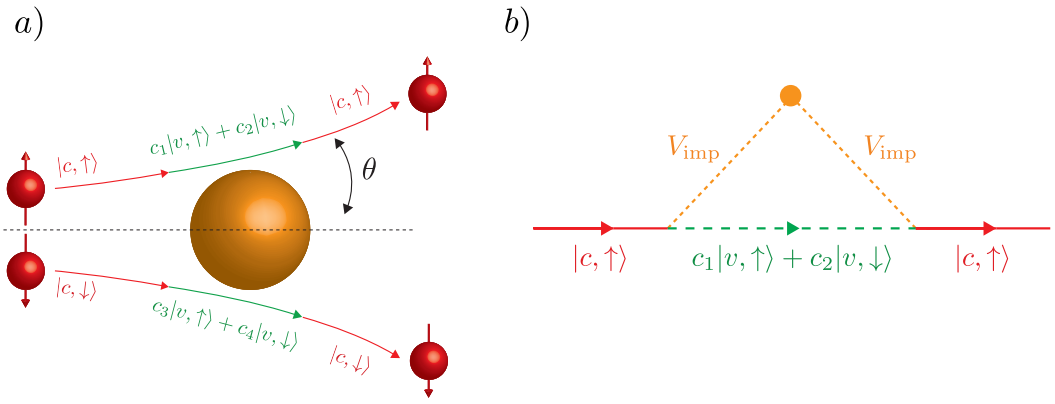

Figure 5.3: ISOS mechanism at the single-impurity level. a) A conduction quasiparticle with spin up (down) undergoes a virtual transition to a combination of valence states, mediated by the interference between scalar and Rashba-type impurities. After the collision, the particle returns to its initial state, likely deviated to the left (right). b) Impurity self-energy in the presence of ISOS mechanism.

Moreover, the complete decomposition of the distribution function in the Clifford algebra explicitly shows the role of the conduction-valence band transitions in generating spin-currents. To see that, we first note that Eq.(5.26) can be understood as the linear expansion of an unitary transformation of $\delta f_{\mathbf{k}}^{Boltz}$,

$$\delta f_{\mathbf{k}} = U \delta f_{\mathbf{k}}^{Boltz} U^{-1}, \tag{5.34}$$

where $U = e^{i\hat{\tau}_{\parallel}\cdot\Sigma_R^{'}}$. Since the linear displacement of the distribution function is defined as the outer product of the Hamiltonian's eigenstates, Eq.(5.34) can be translated into an unitary transformation of such states

$$|\mathbf{k}\sigma, i\rangle \rightarrow U\,|\mathbf{k}\sigma, i\rangle\,, \tag{5.35}$$

that is the effect of the ISOS mechanism on an electron after a scattering event: a single conduction state is transformed into a linear combination of conduction–valence spin up–down states as

$$|\mathbf{k}'\sigma', c(v)\rangle \rightarrow u_0\,|\mathbf{k}'\sigma', c(v)\rangle + u_1\,|\mathbf{k}'\sigma', v(c)\rangle + u_2\,|\mathbf{k}'\sigma, c(v)\rangle + u_3\,|\mathbf{k}'\sigma, v(c)\rangle\,,$$

where u_0, u_1, u_2, u_3 are coefficients that depend on $\Sigma_R^{'}$ and $\hat{\tau}_{\parallel}$. This idea is illustrated in the scattering diagram of Fig.(5.3), where a conduction state with spin "up" undergoes an impurity-induced transition to the valence band and then again to the conduction band. This intuitive argument is converted into a generalized Fermi golden rule

$$W_{\mathbf{k}\rightarrow\mathbf{k}'} = 2\pi n_i \left|\langle \mathbf{k}'\sigma', c(v)|\, U^{-1}V\,|\mathbf{k}\sigma, c(v)\rangle\right|^2 \delta(\epsilon_k - \epsilon_{k'}), \tag{5.36}$$

that expands the standard description widely used in the semiclassical Boltzmann equation approach. Notably, the impurity potential is substituted by an effective interaction $\sim U^{-1}V$ which acquires a *complex* part, mimicking the effect of higher order corrections

to the FBA in Eq.(4.105). In other words, the inclusion of the phase factor generates a spin-active scattering amplitude with real coefficients, allowing for spin asymmetry in scattering processes [18]. In first approximation,

$$U^{-1}V \sim \tilde{u}_0\gamma_{00} + \tilde{u}_R(\gamma_{12} - \gamma_{21}) + \tilde{u}_{KM}\gamma_{33}, \tag{5.37}$$

where we considered $V \sim u_0$. We are now able to include the information carried by $\Sigma_R^{'}$ in the classical collisional integral via the generalized Fermi golden rule, and use the traditional Boltzmann transport equations to evaluate the spin Hall current [8] (see Sec.(4.2.4)). We find

$$\mathcal{J}_y^z = \frac{4u_R^2 \mathrm{v}^2 \ln(\frac{\Lambda^2}{\epsilon^2})e}{n_i u_0^4 \pi^2} E, \tag{5.38}$$

which matches the expressions derived in Eqs.(5.24) and (5.33). This result only depends on coefficients u_1^2 and u_3^2, confirming the origin of the ISOS mechanism in the purely quantum conduction-valence band transitions.

5.4 Conclusions

In conclusion, this chapter unveils a novel purely quantum mechanism in graphene with random fluctuations of the spin-orbit field, called interband spin-orbit scattering (ISOS). It can asymmetrically deviate particles possessing opposite spin moments, resulting in a robust extrinsic spin Hall effect that dominates over the conventional skew scattering contribution at low electronic density. This result has been obtained by employing the self-consistent Diffuson Hamiltonian formalism based on the diagrammatic elaboration of the Kubo-Streda formula, whereby we also derive space-time dependent generalized drift-diffusion equations. Such an extensive description of the system models many possible experimental setups and presents several charge-spin conversion mechanisms along with drift, diffusion and spin-precession processes.

An accurate application of the quantum Boltzmann equation technique offers better intuition about the ISOS mechanism. In detail, we propose an adequate ansatz for the distribution function that quantitatively describes the system and predicts the correct ISOS-induced spin Hall effect. Even though the method is limited to account only for the conduction band dynamics, it preserves information about the virtual conduction-valence band transitions, neglected in previous semiclassical frameworks and revealed to be critical to induce the ISOS mechanism. In particular, the hermitian part of the quasiparticles' self-energy mediates such transitions, and the quantum interference between scalar and spin-flip Rashba-type induces its relevant attributes.

Beyond the graphene context, the ISOS mechanism might be present in any disordered system described by the conduction-valence band duality with locally broken inversion symmetry, like, most notably, Weyl semimetals. The last requirement is essential to produce SOC disorder and can occur in coupled systems with interfacial roughness or randomly distributed spin-active impurities.

Chapter 6

Twist-Angle Controlled Collinear Edelstein Effect and spin Hall effect in van der Waals Heterostructures

6.1 Overview

In this chapter, we shift our attention to graphene/TMD Van der Waals (vdW) heterostructures, paradigmatic in spintronics due to their distinctive suitability to engender charge-spin coupled effects. In fact, these media host enhanced spin-orbit and exchange interactions induced by proximity effects (see Chap.(3)), yielding robust current-driven spin polarization and spin-relaxation processes. Going beyond this framework, the current possibility to offset vdW layers by some twist angle θ gave birth to moiré systems and the field of *twistronics* [195], which studies the electrical properties of models with band structure tuned on demand through an interlayer angle rotation. Such tailoring of the system's electronic structure also affects the spin texture, as demonstrated in recent theoretical works [154], making twisted-vdW of great interest in spintronics. Specifically, these systems host a twist-enhanced Rashba and spin-valley coupling, wherein the in-plane Rashba spin-momentum locking evolves by varying the angle θ and acquires a hedgehog component (see Fig.(6.1)). This peculiarity of twist-controlled spin textures motivates our interest in the possible consequences on the related spin-dependent phenomena.

For this reason, here we develop a microscopic theory of coupled spin-charge transport in twisted graphene/TMD bilayers that is valid for arbitrary twist angle and captures the interplay of symmetry-breaking SOC effects in the band structure and impurity scattering.

We first focus our interest in current-induced spin-accumulations, i.e., the generation of macroscopic spin densities upon application of a charge current. In particular, we predict that twisted vdW heterostructures support highly anisotropic spin-density-current responses that allow full control over the in-plane orientation of non-equilibrium electron spins. At critical twist angles, the non-equilibrium spin density is parallel to the applied current, i.e., a *collinear Edelstein effect* (CEE) is realized. Importantly, the anisotropic

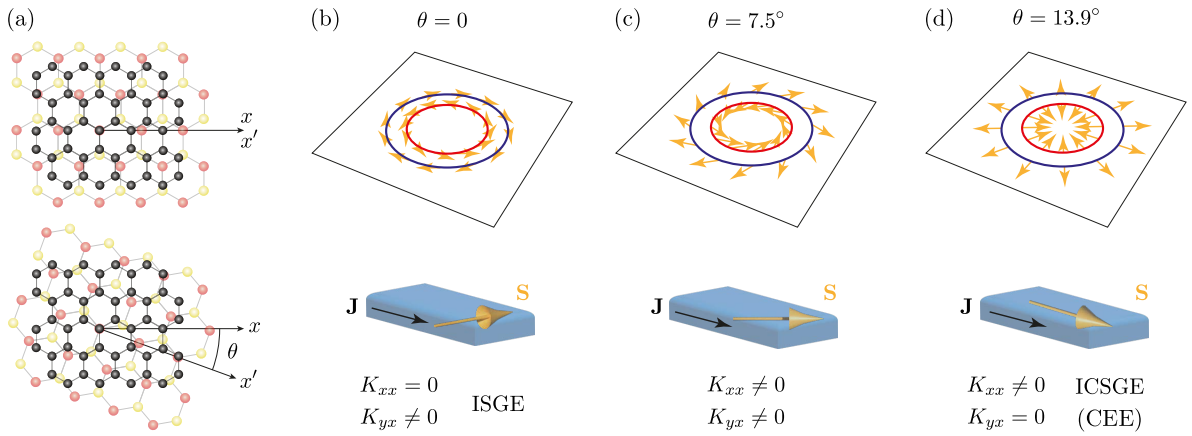

Figure 6.1: (a): Black spheres denote carbon atoms, faded red and yellow spheres represent metal and chalcogen atoms. The x axis belongs to graphene, whilst the x' axis is associated to the TMD. Top: Aligned bilayer. Bottom: Twisted bilayer, with twist angle θ. (b)-(d): Spin texture evolution with twist angle. Below each spin-texture is a visulatization of the non-equilibrium spin-polarization (orange arrow) induced by an applied electrical current (black arrow) through graphene/TMD (blue box).

inverse spin galvanic effect unveiled in this work is robust against *twist-disorder* and can be detected seamlessly via Hanle-type spin precession measurements [196]. To better understand the emergence of this generalized current-induced spin density, we employ simple symmetry arguments, inspired by Ref. [75]. The presence of inversion symmetries along the perpendicular mirror planes in conventional Rashba-coupled systems (which includes untwisted vdW heterostructures), enforces diagonal components of the spin-current response tensor K (Eq.(4.109), with $\tilde{A} = S_i$ and $B = J_i$) , to be vanishing. In fact, the charge current and spin polarization, $J_{x(y)}$ and $S_{x(y)}$, transform differently under $x(y) \to -x(y)$ reflection, i.e., $J_{x(y)} \to -J_{x(y)}$ and $S_{x(y)} \to S_{x(y)}$. As a result, $K = -K$ under reflections, which implies $K = 0$. Only the off-diagonal components survive, and the spin polarization is locked to be perpendicular to the applied electric current, which is the Edelstein effect. The twist of the two layers by non-trivial angles, breaks all σ_v mirror symmetries possessed by aligned bilayers, opening up the possibility for more exotic types of spin-charge conversion phenomena without the need for magnetic impurities, skew scattering, and proximity-induced exchange interactions [20].

We then continue our analysis of bilayer heterostructure by focusing on another crucial phenomenon in spintronics, the spin Hall effect. Traditionally, it has been studied in graphene-TMD bilayers in several limits, including within the Rashba spin gap, without disorder and in the absence of spin-valley coupling [36, 8, 197]. However, the regime of the diffusive limit with a Fermi energy located well above the Rashba spin gap is the most relevant to spin valve experiments [198, 125] and will be explored in this chapter. In particular, we present analytic results within the Kubo-Streda formalism at any twist angle in both the clean and diffusive limit. In the last case, the SHE requires the presence of skew scattering activated by the spin-valley coupling since the sole Rashba SOC is unable to generate spin Hall currents in the diffusive

limit [199], in contrast to the (collinear) Edelstein effect, already present in the first Born approximation for the disorder average. The skew scattering mechanism will be captured by performing a non-Gaussian disorder average to the third order in the impurity potential, the *Y-diagram* approximation, a subclass of the T-matrix expansion.

6.2 Model

Being interested in the spin-electronic properties of the graphene sheet, we use its reference frame to define the axes, as shown in Fig.(6.1a). Thus, our starting point is the low-energy Hamiltonian for graphene/TMD bilayers (Eq.(3.19)), wherein the mass term is negligible and the coupling constants λ_R and $\lambda_{\rm sv}$ become θ-dependent,

$$H_{\mathbf{k}} = \mathrm{v}\left(\tau_z k_x \gamma_{10} + k_y \gamma_{20}\right) + \lambda_{\rm sv}(\theta)\tau_z\gamma_{03} + H_R. \tag{6.1}$$

More interestingly, according to Ref. [77], the Rashba SOC, H_R, is rotated by a *Rashba phase* $\alpha_R(\theta)$ in spin-space, obtaining

$$H_R = \lambda_R(\theta) e^{i s_z \frac{\alpha_R(\theta)}{2}} (\tau_z \sigma_x s_y - \sigma_y s_x) e^{-i s_z \frac{\alpha_R(\theta)}{2}}. \tag{6.2}$$

The corresponding in-plane spin texture is illustrated in Fig.(6.1b), and displays the standard spin winding for $\theta = 0$ and a complete hedgehog configuration at the critical twist-angle. The functions $\alpha_R(\theta)$, $\lambda_R(\theta)$, and $\lambda_{\rm sv}(\theta)$ are given in Ref. [77] and shown in Fig.(6.2), plotted versus the twist angle in WSe_2/graphene bilayers. It reveals that the Rashba term possesses 6-fold twist symmetry [154, 77] whilst the spin valley interaction possesses the same 3-fold symmetry as the bilayer system. This is in agreement with previous theoretical studies on graphene with transition metal adatoms above the A and B sublattices [200, 110], which qualitatively describe the same system. The results of Ref. [200] show that the Rashba coupling is unaffected by the exchanging of the metal atom positions, and hence predicts a twist periodicity of $\pi/3$ for H_R. This is in contrast to the spin-valley coupling, where the swapping of metal atom positions introduces a minus sign and thus implies anti-periodicity for $H_{\rm sv}$ upon a $\pi/3$ twist.

Before we investigate coupled spin-charge transport phenomena in the presence of impurity scattering, it is instructive to consider the spin texture of clean eigenstates at different twist angles. Specifically, we use parameters based on DFT simulations of graphene/WSe_2 [77] in conjunction with the TMD tight-binding model of Ref. [201]. For ease of visualization, we neglect the spin-valley coupling in Fig.(6.1) as it mainly acts to tilt the spin texture out-of-plane. For no twist, $\theta = 0$, the spin polarization of eigenstates is locked in-plane and perpendicular to the momentum as shown in Fig.(6.1b). Thus, the untwisted system supports a conventional ISGE ($\mathbf{S} \perp \mathbf{J}$). As the system is twisted, the spin begins to rotate clockwise, remaining in-plane but no longer perpendicular to the momentum, see Fig.(6.1c). At a critical twist angle of $\theta \simeq 14°$, the system exhibits a hedgehog (Weyl-type) spin texture, Fig.(6.1d). Intuitively, this spin helicity of eigenstates at the critical twist angle should allow a purely collinear spin–current response ($\mathbf{S} \parallel \mathbf{J}$) with efficiency akin to the ISGE. Motivated by this, in what follows we investigate the spin–current response evolution with the twist angle.

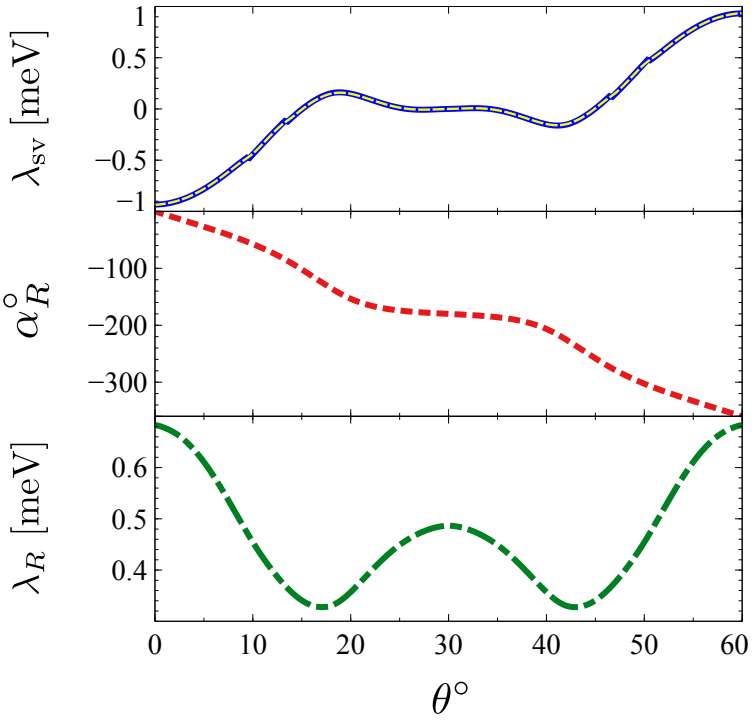

Figure 6.2: Numerical data from Ref. [77] for the spin-valley, Rashba angle, and Rashba coupling. The original data for $\lambda_{\rm sv}$ (blue curve, top panel) suffers spurious discontinuities at $\theta = \pm 9.6^\circ, \pm 13.4^\circ$, which is an artifact of the applied model [196]. We smoothly interpolated the data over the affected regions by applying a Gaussian average with a standard deviation of $\sigma = 0.5^\circ$, obtaining a smoother plot (yellow curve). No significant changes can be seen in the Rashba SOC and angle upon the application of this smoothing process. Hence we do not present the data for $\lambda_{\rm R}$ and α_R before and after smoothing here.

6.3 Current-induced spin-densities

The collinear ($j = x$) and perpendicular ($j = y$) spin response functions to an electric field applied along the x-axis (E_x) are given by Eq.(4.109), particularly

$$K_{jx} = \frac{1}{4\pi} \int d\mathbf{k}\, tr\{s_j \left\langle G^R J_x\, G^A \right\rangle_{\rm dis}\}, \tag{6.3}$$

where $J_i = ev\gamma_{i0}$ is the charge current operator and we set $\hbar \equiv 1$. The effect of the Rashba angle on Eq.(6.3), at the origin of the novel charge-to-spin density conversion, can be easily understood by noting that the Hamiltonian of the twisted bilayer system can be obtained by applying the rotation $U = e^{-is_z\alpha_R(\theta)/2}$ on the 2D Dirac Hamiltonian,

$$H_{\mathbf{k}} = U^{-1}\left(H_{0\mathbf{k}} + H_R(\theta, \alpha_R = 0) + H_{\rm sv}\right) U = H_{0\mathbf{k}} + H_R(\theta) + H_{\rm sv}. \tag{6.4}$$

This operation allows us to rewrite the Green's functions in terms of the rotation operator,

$$G^{R(A)}(\alpha_{\rm R}) = U^{-1} G^{R(A)}(0) U, \tag{6.5}$$

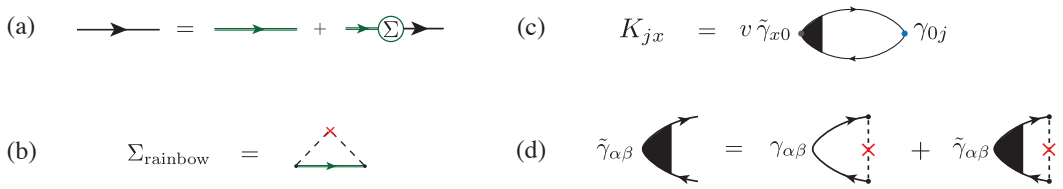

Figure 6.3: *Diagrammatic technique* – Green (black) solid line with an arrow denotes the free (disorder-averaged) Green's function. Dashed lines depict scattering potential insertions (u_0) and the cross represents the impurity density (n).

where we note that the coupling coefficients λ_{R} and λ_{sv} appearing in $G^{R(A)}(0)$ still have a remaining θ dependence. Substituting Eq.(6.5) into the Kubo-Streda formula we obtain

$$K_{jx} \sim tr\{(Us_jU^{-1})G^R(0)J_xG^A(0)\}, \tag{6.6}$$

which implies a simple recasting in relation to the response function of the untwisted system

$$K_{xx}(\theta) = \cos\alpha_R(\theta)\, K_{xx}(\theta;\alpha_R=0) + \sin\alpha_R(\theta)\, K_{yx}(\theta;\alpha_R=0)\,, \tag{6.7a}$$

$$K_{yx}(\theta) = \cos\alpha_R(\theta)\, K_{yx}(\theta;\alpha_R=0) - \sin\alpha_R(\theta) K_{xx}(\theta;\alpha_R=0)\,. \tag{6.7b}$$

Owing to the C_{3v} point-group symmetry of the regular 2D Dirac Hamiltonian, $K_{xx}(\theta;\alpha_R = 0) = 0$, and thus the calculation of $K_{jx}(\theta)$ boils down to evaluating the yx-response function for an untwisted system with θ-dependent Rashba-type and spin-valley couplings.

Our next step is to implement the disorder-averaging procedure, where we employ the first Born approximation for weak, short-range impurities to rule out the skew scattering mechanism and focus only on the contribution coming from the band structure. In this work, we avoid including random fluctuations of the spin-orbit field and consider only electrostatic scalar impurities, u_0. Nevertheless, the anti-hermitian part of self-energy acquires a matrix structure induced by the uniform spin valley SOC, $\Sigma'' \sim \epsilon\gamma_{00} + \lambda_{\text{sv}}\gamma_{03}$, that must be included in the Kubo-Streda formula for consistency.

According to Eq.(4.124), the expression for the leading order disorder-averaged density-current response function is

$$K_{jx} = \frac{2e\text{v}}{\pi n_i u_0^2}\mathcal{D}_{0jx0} = \frac{e\text{v}}{2\pi n_i u_0^2} tr\{\tilde{\gamma}_{x0}\gamma_{0y}\}, \tag{6.8}$$

evaluated diagrammatically as schematically shown in Fig.(6.3)

For typical charge carrier density with both spin-split subbands occupied at the Fermi level (i.e., $|\epsilon| > \sqrt{4\lambda_{\text{R}}^2 + \lambda_{\text{sv}}}$, traditionally called "Regime II" [37]) Eq.(6.8) evaluates to

$$K_{xx}(\theta) = f(\theta)\sin(\alpha_{\text{R}}), \tag{6.9a}$$

$$K_{yx}(\theta) = f(\theta)\cos(\alpha_{\text{R}}), \tag{6.9b}$$

where

$$f(\theta) = -\frac{4ev\epsilon}{\pi n_i u_0^2} \frac{\lambda_R^3(\epsilon^2 + \lambda_{sv}^2)}{\epsilon^4(\lambda_R^2 + \lambda_{sv}^2) - \epsilon^2\lambda_{sv}^4 + 3\lambda_R^2\lambda_{sv}^4}, \tag{6.10}$$

and we have suppressed the θ arguments of λ_R, α_R, and λ_{sv} for notational convenience. The charge-to-spin conversion is entirely driven by the Rashba SOC, the only interaction responsible for our model's nontrivial in-plane spin texture, unbalanced by the applied electric field. The contribution of the spin helicities controls the magnitude of the CISP; it is maximized for Fermi energies close to the spin gap, encouraged by strong spin-valley coupling, and decays for large Fermi energies, most likely for $|\lambda_{sv}| \ll |\lambda_R|$ [37]. The role of λ_{sv} in FBA is then to tune the strength of the conversion mechanism. On the other hand, the interplay between skew scattering and the spin-valley interaction leads to a particularly efficient spin Hall effect [36], concurrent with the CEE predicted in this work. We also remark that in the limit of $\alpha_R = \lambda_{sv} = 0$, we recover the spin-charge susceptibility of the minimal Dirac-Rashba model for 2D vdW heterostructures with intact C_{3v} symmetry i.e., $K_{xx} = 0$ and $K_{yx} \propto \lambda/\epsilon$ [37]. The most crucial feature of

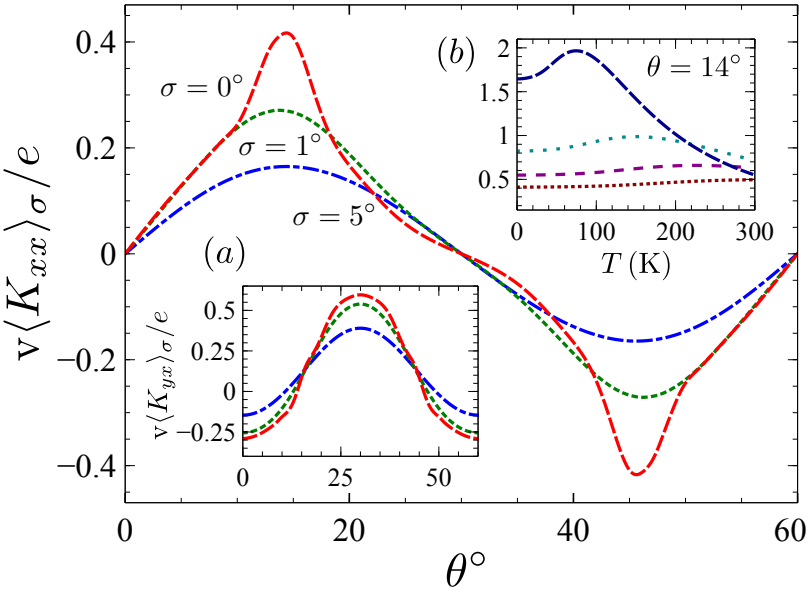

Figure 6.4: Collinear spin-charge response of graphene/WSe_2 for various degrees of twist-angle disorder, represented by different standard deviations at 0 K. Inset (a): Conventional (ISGE) spin–current response for $\epsilon = 0.1$ eV. Inset (b): Temperature dependence of K_{xx} for critical twist angle and $\sigma = 0$ at selected chemical potentials (25 meV, 50 meV, 75 meV, and 0.1 eV from top to bottom). DFT-parameterized SOCs vary in the range $|\lambda_{sv}| < 1$ meV and 0.3 meV $\lesssim \lambda_R \lesssim$ 0.7 meV [77]. Other parameters: $n_i = 5 \times 10^{-16}\text{m}^{-2}$ and $u_0 = 10^{-19}$ eV m^2.

Eq.(6.9) is the possibility of realizing the CEE, where the nonequilibrium spin density is pinned parallel to the applied electric field. The Rashba angle controls the effect, occurring for $\alpha_R(\theta_c) = \pi/2$ (modulo π) at critical twist angles θ_c, which value depends on the examined system.

Fig.(6.4) provides us with a better insight into the behaviour of the collinear and regular EE as a function of the twist angle. In particular, we study graphene/WSe_2 bilayers, where the values of the spin-orbit coupling coefficients are based on Ref. [77] and shown in Fig.(6.2). The plot exhibits a sizeable charge-spin conversion robust against twist-angle disorder, ubiquitous in realistic smearing up to room temperature (inset (b)), where the finite-temperature result is simply obtained from Eq.(6.3) by computing

$$K_{jx}(\mu, T) = \int d\varepsilon \frac{df(\varepsilon - \mu, T)}{d\varepsilon} K_{jx}(\varepsilon, 0), \tag{6.11}$$

according to Eq.(4.101). It also reveals that in this particular system, a pure collinear Edelstein response is achieved for $|\theta_c| \simeq 14^\circ$ (modulo $\pi/3$). The large related efficiency, defined as $\varrho = 2\mathrm{v}e(K_{xx}/\sigma_{xx})_{\theta=\theta_c}$ is evaluated to be in the range of 0.23–0.03 and 0.01–0.004 at zero and room temperature, depending on the charge carrier density, i.e. $3 < \epsilon < 25\,\mathrm{meV}$. We used the analytic expression for the leading-order charge conductivity

$$\sigma_{xx} = \frac{2e^2(8\lambda_{\mathrm{R}}^4\lambda_{\mathrm{sv}}^2 + 3\lambda_{\mathrm{R}}^2\lambda_{\mathrm{sv}}^4 + \epsilon^4(\lambda_{\mathrm{R}}^2 + \lambda_{\mathrm{sv}}^2) - \epsilon^2(4\lambda_{\mathrm{R}}^2\lambda_{\mathrm{sv}}^2 + \lambda_{\mathrm{sv}}^4))}{n_i u_0^2 \pi(\epsilon^4(\lambda_{\mathrm{R}}^2 + \lambda_{\mathrm{sv}}^2) - \epsilon^2\lambda_{\mathrm{sv}}^4 + 3\lambda_{\mathrm{R}}^2\lambda_{\mathrm{sv}}^4)}, \tag{6.12}$$

which, we note, is independent from the Rashba angle α_{R}.

Finally, we qualitatively assess the CEE's robustness against twist-angle disorder [202]. Our idea is to model the effect of the twist-inhomogeneity as a Gaussian average of the response function over the full range of twist angles, i.e.,

$$\langle K_{jx}(\theta)\rangle_\sigma = \int_{\theta-\frac{\pi}{6}}^{\theta+\frac{\pi}{6}} d\phi\, f_\sigma(\phi - \theta) K_{jx}(\phi), \tag{6.13}$$

where

$$f_\sigma(\phi - \theta) = \frac{1}{\mathcal{N}} e^{-\frac{(\phi-\theta)^2}{2\sigma^2}} \tag{6.14}$$

is the normal distribution with standard deviation σ. As a result, the value of K_{xx} at a given θ will be affected by its value at other twist angles, depending on σ. The results are summarized in Fig.(6.4). For small twist disorder, where the standard deviation $\sigma \lesssim 1^\circ$, the linear response of the system is virtually indistinguishable from its well-aligned counterpart. Continuing to increase the twist disorder into the strong limit, up to $\sigma = 10^\circ$, we see that the CEE remains significant at twists away from $\theta = m\pi/6$ ($m \in \mathbb{Z}$), and hence proves to be extremely robust against twist disorder. We note that the mean value of twist angle θ_c at which the pure CEE is realized depends upon the twist disorder present within the system, as can be seen by the moving zeros of K_{yx} in inset (a) of Fig.(6.4). At $\theta = m\pi/6$, $x \to -x$ symmetry is restored and hence K_{xx} must vanish at these points. Thus, the results shown in Fig.(6.4) are consistent with the symmetries of a twisted graphene/TMD bilayer.

6.4 The spin Hall effect

Our starting point is again the Kubo formula, where, now, the observable of interest to us is the z-spin current operator in the y-direction, $\hat{\mathcal{J}}_y^z = (\mathrm{v}/2)\gamma_{23}$, in response to an

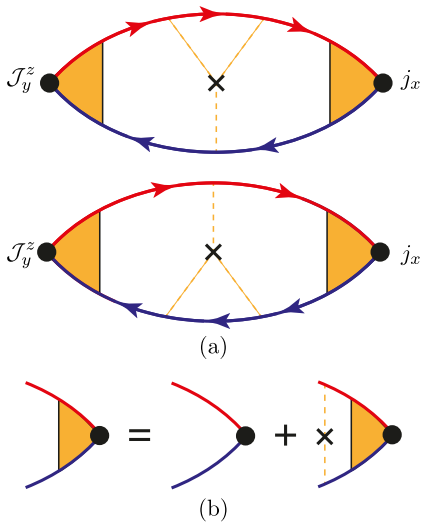

Figure 6.5: (a): Y-type diagrams encoding skew-scattering mechanisms that generate the SHE. The red/blue lines denote retarded/advanced disorder-averaged Green's function, orange dashed lines represent scattering events, the cross equates to an insertion of the impurity density, the black circles on either side denote the spin current and current vertices, and the orange shaded regions indicate vertex renormalization. (b): Vertex renormalization within the Born approximation.

electric field along the x-axis,

$$\sigma_{yx}^{z} = \frac{e^2 \mathrm{v}^2}{4\pi} \int d\mathbf{k}\, tr\left[\gamma_{23} G_{\mathbf{k}}^{R} \gamma_{10} G_{\mathbf{k}}^{A}\right], \tag{6.15}$$

which describes the clean system, i.e., without disorder. In principle, the extrinsic contribution to the spin Hall effect requires the renormalization of the vertices and propagators, as shown in the former section, with the extra difficulty of considering contributions beyond the FBA. However, the self-consistent treatment of the disorder yields too cumbersome analytic results. For that reason, we only investigate the leading order to the extrinsic response in the weak scattering limit obtained by handling the disorder-averaged Green's functions and vertices with the assumption that the scattering events obey a Gaussian white-noise distribution. Then, the renormalized bubble diagram includes the non-Gaussian average prescription $\langle U(\mathbf{r})U(\mathbf{r}')U(\mathbf{r}'')\rangle_{\mathrm{dis}} = n_i u_0^3$, as shown in Fig.(7.5), and the Kubo formula becomes

$$\widetilde{\sigma}_{yx}^{z} = \frac{\mathrm{v}^2 e^2}{2\pi} \int d\mathbf{k}\, d\mathbf{p}\, \mathrm{Re}\left\{tr\left[\mathcal{G}_{\mathbf{k}}^{A} \tilde{\gamma}_{23} \mathcal{G}_{\mathbf{k}}^{R} Y^{R} \mathcal{G}_{\mathbf{p}}^{R} \tilde{\gamma}_{10} \mathcal{G}_{\mathbf{p}}^{A}\right]\right\}. \tag{6.16}$$

Here, $Y^R = n_i u_0^3 \int d\mathbf{q}\, G_{\mathbf{q}}^{R}$ is the retarded skew-scattering insertion that allows for the manifestation of the extrinsic SHE, $\tilde{\gamma}_{23}$ and $\tilde{\gamma}_{10}$ are the disorder-renormalized spin current and charge current vertices respectively (see Fig.(7.5b)).

The evaluation of Eqs.(6.15) and (6.16) for a Fermi energy above the spin gap, i.e., $\varepsilon > \sqrt{4\lambda_{\mathrm{R}}^2 + \lambda_{\mathrm{sv}}^2}$, leads to the results

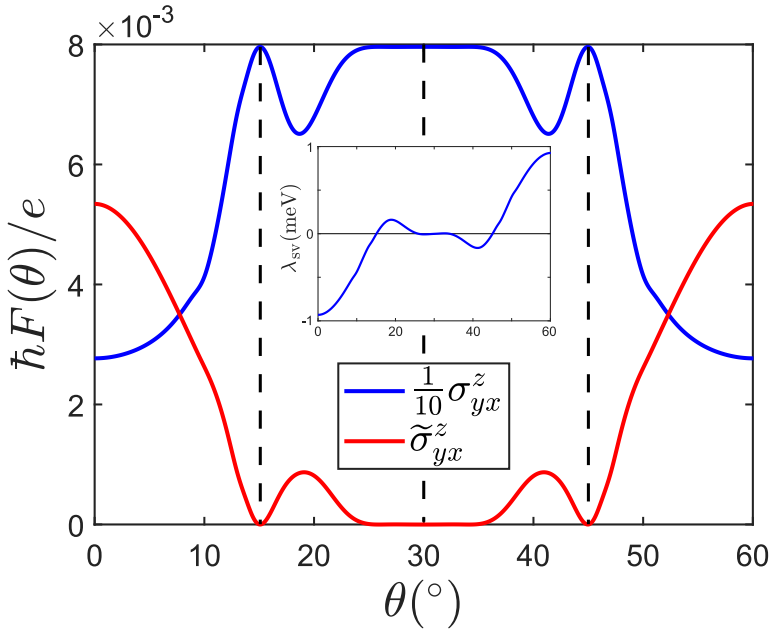

Figure 6.6: Twist angle dependence for the extrinsic and intrinsic spin Hall conductivities for a graphene/WSe_2 bilayer. The extrinsic response vanishes at $\theta \simeq \pi/12, \pi/6, \pi/4$ (dashed lines), which coincides with $\lambda_{\rm sv}(\theta) = 0$. We use the data of Ref. [77] for the twist dependence of the SOCs. Furthermore, we have taken $\varepsilon = 0.1$ eV, $u_0 = 10^{-19}$ eVm^2, and $n_i = 5 \times 10^{15}$ m^{-2}. Inset: Spin-valley coupling twist angle dependence data for a WSe_2 TMD partner from Ref. [77].

$$\sigma^z_{yx} = \frac{e}{4\pi}\frac{\lambda_{\rm R}^2(\varepsilon^2+\lambda_{\rm sv}^2)}{\varepsilon^2(\lambda_{\rm R}^2+\lambda_{\rm sv}^2)-3\lambda_{\rm R}^2\lambda_{\rm sv}^2-\lambda_{\rm R}^4-\lambda_{\rm sv}^4}, \tag{6.17a}$$

$$\widetilde{\sigma}^z_{yx} = \frac{8e\varepsilon}{n_i\pi u_0}\frac{\lambda_{\rm R}^4\lambda_{\rm sv}^2(\varepsilon^2-\lambda_{\rm sv}^2)(\varepsilon^2+\lambda_{\rm sv}^2)^2}{(\varepsilon^4(\lambda_{\rm R}^2+\lambda_{\rm sv}^2)+3\lambda_{\rm R}^2\lambda_{\rm sv}^4-\varepsilon^2\lambda_{\rm sv}^4)^2}, \tag{6.17b}$$

where, in the limit $\lambda_{\rm sv} \to 0$, we recover the results of Ref. [36]. We notice that the spin Hall conductivity is independent on the Rashba phase, simply because the current operators commute with the rotation operator U. However, it still varies by modulating theta, as shown in Fig.(6.6), because of the coupling coefficients' dependence on the twist angle. We also notice that the behaviour of the clean and extrinsic contributions differs significantly; while $\widetilde{\sigma}^z_{yx}$ vanishes at $\theta = \pi/6$, concurrently with a zero spin-valley coupling, guaranteed by symmetries, the intrinsic contribution reaches its maximum. Similarly, in the case of WSe_2, $\lambda_{\rm sv}$ can be seen to vanish at $\theta \simeq \pi/12, \pi/4$ and hence the same behavior can be seen at these angles as is observed at $\theta = \pi/6$. However, these additional angles of vanishing $\widetilde{\sigma}^z_{yx}$ are extremely sensitive to the TMD considered and the material parameters associated to them [154, 77]. Hence, there is no guarantee that $\lambda_{\rm sv}$, and thus the extrinsic response, will vanish at any twist angle other than $\pi/6$.

In the way of conclusion, we stress that the clean and extrinsic spin Hall responses do not contribute simultaneously. As explicitly shown by Ref. [199], as soon as the system becomes disordered, the clean contribution is cancelled by the renormalized

spin Hall conductivity in FBA. More generally, the evolution of the spin operator is $\dot{s}^\mu = i[H, s^\mu] \sim \mathcal{J}^z_\mu$, and since a *static* spin accumulation is generated by an electric field, i.e. the Edelstein effect, the spin Hall conductivity must be zero. However, in the presence of inelastic scattering mediated by lattice vibrations, the Hamiltonian acquires additional terms coupling the sublattice and the spin degree of freedom, $\sim \sigma_\mu \sigma_\nu$. The evolution of the spin operator then becomes $\sim \mathcal{J}^z_\mu$+new terms: the cancellation reported in Ref. [199] is not guaranteed by general principles, and the intrinsic contribution may indeed manifest in disordered systems and also dominate. In fact, the associated spin-lattice relaxation rate is expected to be of the order 1 neV in freestanding graphene [203, 204] which is much smaller than any other energy scale appearing in these systems. Consequently, by treating the effects of inelastic scattering as a simple broadening in the density of states – this is equivalent to replacing δ with some finite, albeit small, value – as a naive first approximation, σ^z_{yx} will remain largely unchanged from Eq. 6.17a due to the small characteristic energy scale of this scattering channel, but survives the effect of weak disorder.

6.5 Conclusion

In this Chapter, we investigated charge-spin conversion phenomena in graphene/TMD bilayers, where the proximity-induced spin-orbit interactions can be tuned on demand by interlayer twisting. In particular, we studied current-induced spin accumulations and the spin Hall effect.

In the former case, we found that an anomalous twist-angle-dependent Rashba-type SOC in the band structure allows for an anisotropic spin-density accumulation whose orientation depends on the twisting. Furthermore, at a critical twist angle, whose value depends on the examined system, the bilayer's spin texture acquires a hedgehog configuration, which generates a purely collinear Edelstein effect parallel to the applied electric current. Such response is robust again twist angle disorder and temperature fluctuations and is independent of skew scattering, thus already appearing in the weak impurity potential regime, the Gaussian approximation particularly.

However, the skew scattering mechanism can play a significant role in the presence of resonances, allowed by the linearly vanishing density of states of graphene. As a result, different charge-spin conversion effects are concurrent in these systems; the collinear Edelstein effect, the regular spin-galvanic effect and the spin Hall effect. The isolation of each component is allowed by a recently developed detection scheme called X-protocol [196], where the manipulation of an external magnetic field's direction filters out the individual contributions.

For that reason, we obtain analytic results for the spin Hall effect in both the intrinsic and extrinsic case, which magnitude depends on the twist angle, i.e., the strength of the Rashba and spin-valley coupling terms. While the first scenario is relevant in clean systems and reaches its maximum at zero spin-valley interaction, the second manifests in disordered systems. It relies entirely on the skew scattering mechanism, allowing for the asymmetric scattering of the quasi-particles, which in turn needs the spin-valley coupling to be activated and distinguishes between up and down electrons' spin. Then,

for zero spin-valley coupling, realized at specific twist angles, the spin Hall conductivity evaluates to zero.

Chapter 7

Nonperturbative approach to interfacial spin-orbit torques induced by Rashba effect: from normal metals to topological insulator surface states

7.1 Overview

In this chapter, we study the spin-orbit torque, a critical application of current-induced spin observables to next-generation technologies. This phenomenon describes the interaction between a macroscopic spin density $\mathbf{S}$, traditionally induced at the surface of a normal metal (NM) or a 3D topological insulator (TI), and the magnetization $\mathbf{M}$ of a ferromagnet (FM) in FM/NM(TI) bilayer systems. Such spin density can be generated by applying an external electric field, which allows total electrical control of the magnetization dynamics. Specifically, the field-like (FL) SOT is responsible for the precession of the magnetization, while the damping-like (DL) torque induces the magnetization switching.

There is currently a debate about the physical origin of the SOT because of the discrepancy between experiments and theoretical models. According to the latter, two main mechanisms drive SOTs at FM/NM(TI) bilayers: the spin Hall effect (SHE) appearing in the bulk of the NM(TI), inducing a spin accumulation at the edge of the NM(TI), and the Rashba-Edelstein effect (EE) at the interface. [205], The corresponding results are summarized in Fig.(7.1). Firstly, it shows that the contribution of the SHE to the DL and FL torques goes to zero as the system thickness w decreases, concurrently with a spin diffusion length much larger than the NM(TI) thickness, $\mu^{\uparrow} - \mu^{\downarrow} \sim J_x w$, with $u^{\uparrow(\downarrow)}$ being the spin-dependent chemical potential at the edges of the sample [13, 206]. Secondly, it evidences that interfacial scattering, allowing vertical transport of surface-SOC-induced spin currents which applies a DL torque to the magnetic layer via the spin-transfer process [207], becomes negligible in the ultra-thin limit. Meanwhile, the EE's FL torque remains approximately constant.

However, these microscopic theories [181, 75, 208] have failed to capture DL torques

large enough to explain experimental observation [209], as well as the anisotropy of the DL torque [210]. Furthermore, these theories predict the *complete absence of DL torques* in the two-dimensional Rashba-coupled ferromagnet model, inconsistently with an experimental study on ultra-thin metallic bilayers which reported non-negligible DL torques responsible for the magnetic switching of the FM whose origin must be the interface [209].

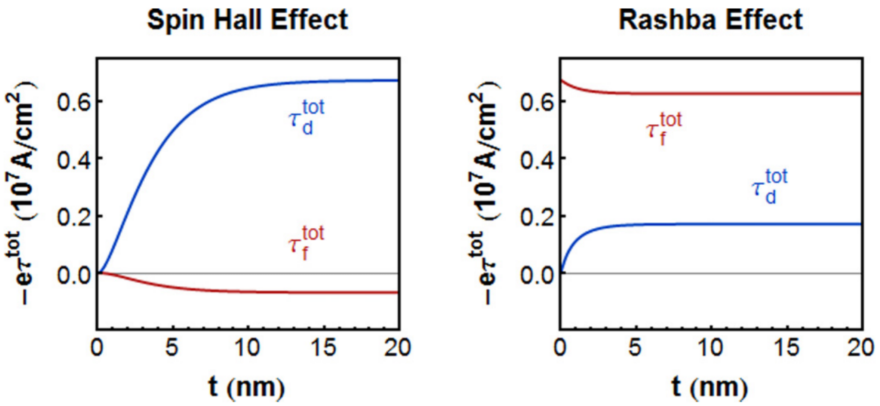

Figure 7.1: Contributions of the spin Hall effect and Rashba effect to the DL, $\tau_{\mathrm{d}}^{\mathrm{tot}}$ and FL, $\tau_{\mathrm{f}}^{\mathrm{tot}}$ spin-orbit torque. The SHE, stemming from the bulk, is mostly responsible for the magnetization switching, while the opposite holds for the purely interfacial Rashba effect. This model predicts a vanishingly small DL torque with decreasing the system thickness. Figure taken from Ref. [207]

.

We believe that such an incomplete description of the problem derives from a perturbative treatment of the disorder scattering potential within the Gaussian (white-noise) approximation and similar handling of the magnetic exchange interaction. In fact, the use of perturbative methods has been questioned in a recent study [20], where strong impurity scattering and the rich evolution of equilibrium spin textures with the Fermi level were seen to play a crucial role in the build up of nonequilibrium spin polarization and associated SOTs in van der Waals heterostructures. Motivated by these questions in the field and developments in the theory, this chapter aims to shed light on surface-generated spin densities' contribution to the spin-orbit torques' damping-like component. To this end, we formulate a microscopic theory based on the Kubo-Streda formalism able to treat nonperturbatively both the impurity scattering strength and spin interactions (magnetic exchange and Rashba SOC) to calculate the current-induced spin polarization in the system. In particular, we employ a generalized self-consistent diagrammatic technique that handles disorder at the complete T-matrix level to calculate the spin-density-charge-current response functions, whilst allowing for the FM's magnetization to lie at an arbitrary angle.

The method is applied to two paradigmatic systems in the literature. First, we tackle the standard FM/NM problem, where the normal metal is modelled as a conventional two-dimensional electron gas (2DEG). Then, we analyze the SOT in FM/TI systems, which drew much attention recently due to their unprecedented SOT efficiency, meeting

the demand to optimize the effect [138]. In both cases, we demonstrate that *DL torques with nontrivial angular dependence* can be generated purely at the interface due to the interplay of Rashba SOC, magnetic proximity effect and impurity scattering. In practice, the anisotropic spin texture of 2DEG and TI's Fermi rings can be seen to enrich the possible current-induced spin polarizations and hence we predict new types of interfacial SOT with extrinsic origin.

In two-dimensional gases, the skew scattering mechanism activated by a scalar electrostatic impurity potential and uniform exchange interaction, generates macroscopic spin accumulations with non-zero components pointing at any direction in three-dimensional space, resulting in rich SOT dynamics. On the contrary, the spin-texture of TIs in the low-energy theory forbids out-of-plane components of the susceptibility tensor. To overcome this limitation, we explore the effect of *magnetic adatoms*, proven to retain their magnetic moment when absorbed by surface layers of 3D topological insulators [211, 212]. In particular, they are usually polarized along the out-of-plane direction [155], strongly enhancing skew scattering, but a strong in-plane anisotropy can also characterize them [156]. This rich impurity landscape leads to a fully-populated spin susceptibility tensor, and out-of-plane spin accumulations are now allowed. In this context, aiming at improving the SOT efficiency, we go beyond the traditional diffusive regime, where the concentration of impurities is sufficiently low, and investigate the effect of the quantum side-jump mechanism, relevant in the so-called *dirty regime*.

We present analytical results in the weak impurity potential regime (incorporating skew scattering) for both 2DEGs and TIs, and in the resonant regime for TI bilayers. Also, we use a numerical procedure to extract the full angular dependence of the SOTs and present the spin susceptibility tensor elements as a function of the impurity concentration.

7.2 Models and methods

7.2.1 SOT components and notation

The spin-orbit torque's dynamics enters in the Landau-Lifshits-Gilbert equation, presented in the Introduction, via the additive term

$$\mathbf{T} = \frac{\gamma}{d\, M_s} \mathbf{H}_{\mathrm{SOT}} \times \mathbf{m}, \tag{7.1}$$

where d is the FM's thickness, $\mathbf{m} = \frac{\mathbf{M}}{|\mathbf{M}|}$, γ is the gyromagnetic ratio, M_s the saturation magnetization of the magnetic layer, and $\mathbf{H}_{\mathrm{SOT}}$ is the effective magnetic field generated by the nonequilibrium spin polarization of conduction electrons. The analysis of the SOT then boils down to determine the charge to spin conversion taking place in the NM(TI) layer via the symmetry-breaking SOC (RSOC). We then relate $\mathbf{H}_{\mathrm{SOT}}$ to the density-current linear response as

$$\mathbf{H}_{\mathrm{SOT}} = \Delta_{\mathrm{xc}} \hat{K}\, \mathbf{E}, \tag{7.2}$$

where Δ_{xc} is the interfacial exchange coupling, $\hat{K}$ is the spin susceptibility tensor, and $\mathbf{E}$ is the external electric field. It is convenient to establish some basic properties

of the response function based on symmetry transformations, in order to simplify the separation between DL and FL torques. Following Ref. [75], the $\hat{K}$-tensor's components are established to be even or odd in the magnetization vector,

$$\hat{K} = \begin{pmatrix} m_z\kappa_{xx} & \kappa_{xy} \\ \kappa_{yx} & m_z\kappa_{yy} \\ m_x\kappa_{zx} & m_x m_z \kappa_{zy} \end{pmatrix}, \tag{7.3}$$

where we chose for convenience a reference frame where $\mathbf{m}$ lies on the zx-plane. From Eqs.(7.1), (7.2), and (7.3), we obtain a simple decomposition of the SOT into damping-like (even in $\mathbf{m}$) and field-like (odd in $\mathbf{m}$) parts, $\mathbf{T}^{\mathrm{e}}$ and $\mathbf{T}^{\mathrm{o}}$ respectively, which derivation is presented in Appendix C,

$$\mathbf{T}^{\mathrm{e}} = \frac{\Delta_{\mathrm{xc}}\gamma}{d\, M_s}(t_1^{\mathrm{e}}\mathbf{m} \times (\mathbf{m} \times (\hat{z} \times \mathbf{E})) + t_2^{\mathrm{e}}\mathbf{m} \times \hat{z}(\mathbf{m} \cdot \mathbf{E})), \tag{7.4a}$$

$$\mathbf{T}^{\mathrm{o}} = \frac{\Delta_{\mathrm{xc}}\gamma}{d\, M_s}(t_1^{\mathrm{o}}\mathbf{m} \times (\hat{z} \times \mathbf{E}) + t_2^{\mathrm{o}}\mathbf{m} \times (\mathbf{m} \times \hat{z})(\mathbf{m} \cdot \mathbf{E})), \tag{7.4b}$$

which assumes an interface with continuous rotational symmetry about the z-axis [213, 214, 215, 216]. The torque coefficients, t_i^j, are the controlling parameters of the SOT and hence are the primary focus of our work. They may be written in terms of the magnetization and spin susceptibility tensor components as

$$t_1^{\mathrm{e}} = \frac{K_{yy}}{m_z} = \kappa_{yy}, \tag{7.5a}$$

$$t_2^{\mathrm{e}} = \frac{K_{xx} - K_{yy}}{m_x^2 m_z} - \frac{K_{xx}}{m_z} - \frac{K_{zx}}{m_x} = \frac{\kappa_{xx} - \kappa_{yy}}{m_x^2} - \kappa_{zx} - \kappa_{xx}, \tag{7.5b}$$

$$t_1^{\mathrm{o}} = K_{xy} - \frac{m_x}{m_z}K_{zy} = \kappa_{xy} - m_x^2\kappa_{zy}, \tag{7.5c}$$

$$t_2^{\mathrm{o}} = \frac{1}{m_x}\left(\frac{K_{xy} + K_{yx}}{m_x} - \frac{K_{zy}}{m_z}\right) = \frac{\kappa_{xy} + \kappa_{yx}}{m_x^2} - \kappa_{zy}. \tag{7.5d}$$

From these expressions, we clearly see that K_{xx}, K_{yy}, and K_{zx} contribute solely to the damping-like torque, whilst K_{xy}, K_{yx}, and K_{zy} generate the field-like torque.

7.3 The Hamiltonian

Being interested in the charge-spin conversion phenomena of the FM partner, we only consider its Hamiltonian, which comprises a term describing the clean isolated 2DEG or TI, $\mathcal{H}_0$, the proximity effects due to the interaction with the FM, $\mathcal{H}_{\mathrm{PE}}$, and the impurity landscape, $\mathcal{H}_{\mathrm{dis}}$,

$$\mathcal{H} = \mathcal{H}_0 + \mathcal{H}_{\mathrm{PE}} + \mathcal{H}_{\mathrm{dis}}. \tag{7.6}$$

The breaking of the inversion symmetry along the stacking direction $\hat{z}$ yields the ubiquitous Rashba spin-orbit coupling (RSOC), $\mathcal{H}_{\mathrm{BR}}$, which guarantees the generation of

current-induced spin-accumulations. On the other hand, localized electrons in the ferromagnet provide their spins, which interact with the conduction electrons of the HM/TI layer. The model Hamiltonian is borrowed from the s-d(f) model [217, 218], emerging from the exchange interaction of anti-symmetrized many-body electronic states, and takes the Zeeman-like form

$$\mathcal{H}_{\rm xc} = \Delta_{\rm xc}\, \mathbf{m}\cdot\mathbf{s}, \tag{7.7}$$

with $\mathbf{s}$ being the vector of Pauli matrices acting in spin space. The interplay between the exchange and Rashba interactions enriches the structure of the spin texture, which, in general, acquires an out-of-plane and $\hat{x}$-in-plane ingredient on top of the helical component. Intuitively, this leads to a current-induced spin density that generalises the Edelstein spin accumulation, pointing in any direction of the 3D space. The full proximity-induced Hamiltonian may be written as the sum of the two terms, $\mathcal{H}_{\rm PE} = \mathcal{H}_{\rm BR} + \mathcal{H}_{\rm xc}$, which can be added to $\mathcal{H}_0$ by introducing the non-Abelian SU(2) gauge field [219]

$$\mathcal{A}^{\mu} = \mathcal{A}^{\mu}_{i} s_i, \qquad (i = 0, x, y, z) \tag{7.8}$$

where the exact expressions for the $\mathcal{A}^{\mu}_{i}$ elements are system dependent, and so we later provide the non-zero elements for the HM and TI cases. This field is then inserted into the bare Hamiltonian in an analogous manner to minimal coupling as a generalized vector potential. In the absence of disorder, the Hamiltonians describing the HM and TI systems may be written, respectively, as

$$\mathcal{H}^{\rm 2DEG} = \int d\mathbf{x}\, \psi^{\dagger}(\mathbf{x}) \left[\frac{(\mathbf{p}+\boldsymbol{\mathcal{A}})^2 - \boldsymbol{\mathcal{A}}^2}{2m^*} - \varepsilon - \mathcal{A}^0 \right] \psi(\mathbf{x}), \tag{7.9a}$$

$$\mathcal{H}^{\rm Dirac} = \int d\mathbf{x}\, \psi^{\dagger}(\mathbf{x}) \left[\mathrm{v}\, \Sigma_{\mu} (p^{\mu} + \mathcal{A}^{\mu}) \right] \psi(\mathbf{x}). \tag{7.9b}$$

Here m^* is the effective electron mass, ε is the Fermi energy, and $p^{\mu} = (-\varepsilon/v, \mathbf{p})$ is the 3-momentum operator. In the 2DEG, v is simply the Fermi velocity of the electrons, whilst in Dirac materials it is the Fermi velocity of the massless Dirac fermions. Finally, Σ_{μ} is an operator comprised of Pauli matrices acting in spin space, or, in the case of van der Waals hetetrostructures such as graphene and transition metal dichalogenides, pseudospin space. We account for disorder via the $\mathcal{H}_{\rm dis}$ term in the Hamiltonian, which has the form

$$\mathcal{H}_{\rm dis} = \int d\mathbf{x}\, \psi^{\dagger}(\mathbf{x})\, V(\mathbf{x})\, \psi(\mathbf{x}), \tag{7.10a}$$

$$V(\mathbf{x}) = \sum_i W(\mathbf{x} - \mathbf{x}_i), \tag{7.10b}$$

where $V(\mathbf{x})$ is the total impurity potential, and $W(\mathbf{x}-\mathbf{x}_i)$ is the potential of a single impurity located at $\mathbf{x}_i$. As we have seen in Chap.(5), $V(\mathbf{x})$ generally has a matrix structure and can include effects such as local SOC and magnetic impurities [38]. In 2DEGs, however, these are not necessary for generating FL and DL SOTs, as we shall see later and for that reason, we first focus on short-range scalar impurities of form $W_0(\mathbf{r}) = u_0 R^2 \delta(\mathbf{r})$. On the contrary, the SOT is greatly enriched by strong correlated in-plane magnetic disorder in topological insulators [156], which we will model

as $W_{mag}(\mathbf{r}) = (u_0 + u_x s_x + u_y s_y)R^2\delta(\mathbf{r})$. To recover macroscopic results, we average over all possible impurity distributions beyond the first Born approximation, in order to include skew scattering and activate different type of spin-orbit torques previously neglected in traditional microscopic theories. To this end, we apply the self-consistent T-matrix formalism in the dilute regime presented in Chap.(4).

Having set up the Hamiltonian describing the partner materials, our focus now turns to calculating the generalized spin-density–charge-current response tensor. The following sections detail our results in 2DEGs and TIs, including the $\hat{K}$-tensor in the weak and resonant impurity potential regime, the corresponding torque coefficients, and the fully-numerical evaluation of the response for arbitrary magnetization angle.

7.4 2D electron gas

We begin our analysis by applying the Kubo-Streda formalism, developed in Chap.(4), to the FM/HM bilayer system, wherein we may treat the HM as a 2DEG described by the Hamiltonian in Eq.(7.9a) in the presence of scalar impurities, $W_0(\mathbf{r})$. The gauge field has the following non-zero components,

$$\mathcal{A}_x^y = -\mathcal{A}_y^x = \alpha m^*, \qquad \mathcal{A}^0 = -\Delta_{\text{xc}}\mathbf{m}\cdot\mathbf{s} \equiv -\boldsymbol{\Delta}\cdot\mathbf{s}, \tag{7.11}$$

where the first two components describe the Rashba SOC (α is the coupling strength), and the final term accounts for the exchange interaction. Starting from the free electron picture of a 2DEG, the Rashba SOC causes spin-splitting of the parabolic dispersion into two bands, with the spin being locked in-plane and perpendicular to the momentum. The upper band spins wind in an clockwise manner around their Fermi ring, whilst the lower band spins wind anti-clockwise around their Fermi ring. We label these bands by the index ν. Next, the out-of-plane exchange interaction due to m_z opens up a gap between the two bands, and leads to an out-of-plane tilting in each band's spin texture: the upper band spins rotate to align with $m_z\hat{z}$, and the lower band spins rotate to align with $-m_z\hat{z}$. Finally, the in-plane magnetization deforms the shape of the bands, whilst also shifting them in opposite directions along the axis perpendicular to the in-plane component. This generates a highly anisotropic dispersion relation

$$\epsilon_{\mathbf{k}\uparrow\downarrow} = \frac{k^2}{2m^*} - \sqrt{m_x^2 - 2\alpha m_x k\sin(\phi) + m_z^2 + \alpha^2 k^2}, \tag{7.12}$$

see Fig.(7.2), where $p_y = 0$, and so requires expansion in m_x and m_y to allow for analytic evaluation. For ease of analysis, we write the magnetization as

$$\mathbf{m} = \sin\theta\,\hat{x} + \cos\theta\,\hat{z}, \tag{7.13}$$

where we have assumed $m_y = 0$ and θ is the magnetization angle, defined with respect to the z-axis in the x-z plane.

7.4.1 Semiclassical approach

Before delving into the fully quantum-mechanical results, it is convenient to frame the problem from a semiclassical perspective via the Boltzmann formalism elaborated in

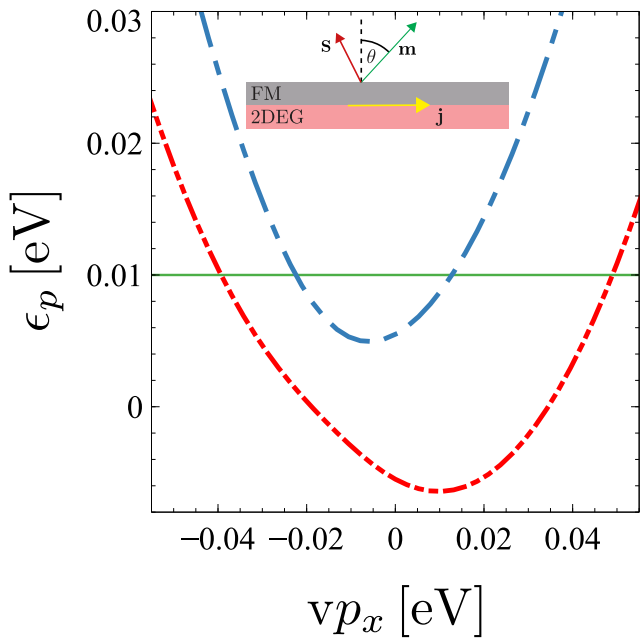

Figure 7.2: Band structure of a 2DEG with Rashba SOC and an exchange interaction, where we have assumed $m_y = 0$ without loss of generality, which shifts the Fermi rings along the y-axis by the m_x component. Parameters: $\alpha = 1.7 \times 10^{-11}$ eVm, $\Delta_{\text{xc}} = 5.5$ meV, v $= 10^5$ ms^{-1}, $\theta = \pi/4$, and $p_y = 0$. The green line represents the Fermi energy $\varepsilon = 0.01$ eV. Inset: NM/FM bilayer schematic, with electric current, $\mathbf{j}$, aligned with the x-axis, and FM magnetization at angle θ to the z-axis.

Chap.(4). As we previously discussed, applying an electric field, $\mathbf{E}$, to the system shifts the Fermi rings in the direction of $-\mathbf{E}$, leading to a non-zero centre-of-mass momentum and hence an electrical current. In other words, the distribution function of the electrons undergoes a small perturbation due to the electric field, $f_{\mathbf{k}\nu} + \delta f_{\mathbf{k}\nu}$, where $f_{\mathbf{k}\nu}$ is the Fermi function for the band ν, and the electronic states with momentum antiparallel to $\mathbf{E}$ are occupied more likely than parallel ones. Thus, the statistical-averaged electric current reads

$$\mathbf{J} = \sum_{\mathbf{k},\nu} \mathbf{v}_{\mathbf{k}\nu}\, \delta f_{\mathbf{k}\nu}, \tag{7.14}$$

where $\mathbf{v}_{\mathbf{k}\nu}$ is the expectation value of the velocity operator with respect to states with momentum $\mathbf{k}$ and band index ν. Analogously, the spin response is the statistical average of the spin texture, given by

$$\mathbf{S} = \sum_{\mathbf{k},\nu} \mathbf{s}_{\mathbf{k}\nu}\, \delta f_{\mathbf{k}\nu}, \tag{7.15}$$

where the momentum-dependence of $\mathbf{s}_{\mathbf{k}\nu}$ is a fundamental ingredient in generating a nonzero out-of-equilibrium spin density. Varying the occupation probability of a constant spin texture fails to produce a change in the density response relative to the equilibrium case, yielding $\mathbf{S} = 0$. However, in our system the spin texture depends on the azimuthal angle of the momentum, ϕ, and for a small in-plane magnetization the

2DEG's spin texture may be written as

$$\mathbf{s}_{\mathbf{k}\nu} = \nu(\mathbf{s}^0_{\mathbf{k}} + m_x\,\delta\mathbf{s}_{\mathbf{k}}), \tag{7.16a}$$

$$\mathbf{s}^0_{\mathbf{k}} = \rho_{\parallel}\hat{\mathbf{k}} \times \hat{z} + \rho_{\perp}\hat{z}, \tag{7.16b}$$

$$\begin{aligned}\delta\mathbf{s}_{\mathbf{k}} = [\omega_{\parallel} + \xi_{\parallel}\cos(2\phi)]\hat{x} \\ + \xi_{\parallel}\,\sin(2\phi)\,\hat{y} - \omega_{\perp}m_z\sin\phi\hat{z},\end{aligned} \tag{7.16c}$$

where $\omega(\rho)_{\parallel}$, $\omega(\rho)_{\perp}$, and $\xi_{\parallel}$ are also functions of α, m_z^2, and $|\mathbf{k}|$. The structure of Eq.(7.16) is preserved at zero temperature,

$$\mathbf{s}_{\phi\nu} = \mathbf{s}^0_{\phi\nu} + m_x\,\delta\mathbf{s}_{\phi\nu}, \tag{7.17a}$$

$$\mathbf{s}^0_{\phi\nu} = \nu\,\tilde{\rho}_{\parallel}\hat{\mathbf{k}}_{\mathrm{f}} \times \hat{z} + \tilde{\rho}_{\perp\nu}\,\hat{z}, \tag{7.17b}$$

$$\begin{aligned}\delta\mathbf{s}_{\phi\nu} = [\tilde{\omega}_{\parallel\nu} + \tilde{\xi}_{\parallel\nu}\cos(2\phi)]\hat{x} \\ + \tilde{\xi}_{\parallel\nu}\,\sin(2\phi)\,\hat{y} + \nu\,\tilde{\omega}_{\perp}m_z\sin\phi\hat{z},\end{aligned} \tag{7.17c}$$

where the momentum is substituted by the Fermi momentum due to the form of the perturbed distribution function, $\delta f_{\mathbf{k}\nu} \sim \theta(\varepsilon - \epsilon_{k\nu})$. As we will show in the next section, this is not the case of surface states of TI systems, where the angular dependence of the out-of-plane component of the spin texture disappears at the Fermi level. The $\mathbf{s}^0_{\mathbf{k}\nu}$ term is responsible for the spin-helical part of $\mathbf{s}_{\mathbf{k}\nu}$, and therefore produces an imbalance in oppositely aligned spins that is transverse to the applied electric field. Clearly, this term is the origin of the familiar Edelstein effect, depending entirely on Rashba SOC, and generates non-zero contributions to K_{xy} and K_{yx}. These components survive the restrictions enforced by the FBA, where they appear independent of the magnetization. We can easily see from Eqs.(7.16) and (7.17) that the presence of an in-plane magnetization allows for an angle-dependent out-of-plane spin accumulation. Hence, this correction contributes to the K_{zx} and K_{zy} elements. However, under the FBA we find that no such response is seen in the out-of-plane polarization, S_z, when $\varepsilon > \Delta_{\mathrm{xc}}$, suggesting that the physics governing out-of-plane polarization is more sensitive to the scattering strength than Edelstein effect. It turns out that the non-zero spin polarizations of the individual bands cancel out perfectly within the FBA, which explains the vanishing of K_{zy} reported in Ref. [75]. Overall, there are 4 vanishing responses within the FBA, namely, $K_{zx} = K_{zy} = K_{xx} = K_{yy} = 0$.

To see that, we briefly present a Boltzmann treatment of the S_z density-response to an external electric field. The starting point is the Boltzmann equation, Eq.(4.7),

$$-sgn[v]Ev_{\mathbf{k}\nu}\cos\phi\left(\frac{\partial f^0_{\mathbf{k}\nu}}{\partial\epsilon_{\mathbf{k}\nu}}\right) = I[\delta f_{\mathbf{k}\nu}], \tag{7.18}$$

where $v_{\mathbf{k}\nu} = \sqrt{(\partial\epsilon_{\mathbf{k}\nu}/\partial k_x)^2 + (\partial\epsilon_{\mathbf{k}\nu}/\partial k_y)^2}$ is the absolute value of the group velocity with band index ν. The collisional integral is the sum of an inter and intra-ring component, $I[\delta f_{\mathbf{k}\nu}] = I^{intra}[\delta f_{\mathbf{k}\nu}] + I^{inter}[\delta f_{\mathbf{k}\nu}]$, and

$$I[\delta f_{\mathbf{k}\nu}]^{intra} = -\int d\mathbf{k}'(\delta f_{\mathbf{k}\nu}W_{\mathbf{k}\nu,\mathbf{k}'\nu} - \delta f_{\mathbf{k}'\nu}W_{\mathbf{k}'\nu,\mathbf{k}\nu}) \tag{7.19a}$$

$$I[\delta f_{\mathbf{k}\nu}]^{inter} = -\int d\mathbf{k}'(\delta f_{\mathbf{k}\nu}W_{\mathbf{k}\nu,\mathbf{k}'\bar{\nu}} - \delta f_{\mathbf{k}'\bar{\nu}}W_{\mathbf{k}'\bar{\nu}\mathbf{k}\nu}), \tag{7.19b}$$

where the transition probabilities W in FBA take the form

$$W_{\mathbf{k}\nu,\mathbf{k}'\nu} = W_{\mathbf{k}'\nu,\mathbf{k}\nu} = 2\pi n_i \delta(\epsilon_{\mathbf{k}\nu} - \varepsilon_{\mathbf{k}'\nu}) u_0^2 |\langle \mathbf{k}'\nu \,|\mathbf{k}\nu\rangle|^2 \tag{7.20a}$$

$$W_{\mathbf{k}\nu,\mathbf{k}'\bar{\nu}} = W_{\mathbf{k}'\bar{\nu},\mathbf{k}\nu} = 2\pi n_i \delta(\epsilon_{\mathbf{k}\nu} - \epsilon_{\mathbf{k}'\bar{\nu}}) u_0^2 |\langle \mathbf{k}'\bar{\nu} \,|\mathbf{k}\nu\rangle|^2 . \tag{7.20b}$$

The dispersion relation's anisotropy requires an extended ansatz similar to the one employed in Chap.(5). However, in the present case, we need a minimum of three harmonics, obtaining

$$\delta f_{\mathbf{k}\nu} = -sgn[v] E (\frac{\partial f^0_{\mathbf{k}\nu}}{\partial \epsilon_{\mathbf{k}\nu}}) v_{\mathbf{k}\nu} \sum_{n=1}^{3} \left(\tau^{\parallel}_{n\nu} \cos(n\phi) + \tau^{\perp}_{n\nu} \sin(n\phi_k) \right) , \tag{7.21}$$

that we insert into Eq.(7.18). After simple algebraic manipulations, we achieve an operative form for the collisional integral at zero temperature

$$I[\delta f_{\mathbf{k}\nu}]^{intra} = 2\pi n_i sgn[v] E \left(\frac{\partial f^0_k}{\partial \epsilon_{\mathbf{k}\nu}} \right) \sum_n \int \frac{d\phi'}{(2\pi)^2} \frac{T_{\nu\nu}(\phi,\phi')}{|\partial \epsilon_{\mathbf{k}\nu}/\partial k|} k'_{\mathrm{f}\nu} \times$$
$$\Big\{ v_{\mathrm{f}\nu}(\phi)(\tau^{\parallel}_{n\nu} \cos(n\phi) + \tau^{\perp}_{n\nu} \sin(n\phi)) - v_{\mathrm{f}\nu}(\phi')(\tau^{\parallel}_{n\nu} \cos(n\phi') + \tau^{\perp}_{n\nu} \sin(n\phi')) \Big\}, \tag{7.22a}$$

$$I[\delta f_{\mathbf{k}\nu}]^{inter} = 2\pi n_i sgn[v] E \left(\frac{\partial f^0_k}{\partial \epsilon_{\mathbf{k}\nu}} \right) \sum_{n,\bar{\nu}} \int \frac{d\phi'}{(2\pi)^2} \frac{T_{\nu\bar{\nu}}(\phi,\phi')}{|\partial \epsilon_{\mathbf{k}\bar{\nu}}/\partial k|} k'_{\mathrm{f}\bar{\nu}} \times$$
$$\Big\{ v_{\mathrm{f}\nu}(\phi)(\tau^{\parallel}_{n\nu} \cos(n\phi) + \tau^{\perp}_{n\nu} \sin(n\phi)) - v_{\mathrm{f}\bar{\nu}}(\phi')(\tau^{\parallel}_{n\bar{\nu}} \cos(n\phi') + \tau^{\perp}_{n\bar{\nu}} \sin(n\phi')) \Big\}, \tag{7.22b}$$

where $k'_{\mathrm{f}\nu}$ is the Fermi momentum of band ν, $v_{\mathrm{f}\nu}$ the related group velocity, and $T_{\nu\bar{\nu}}(\phi,\phi') = |\langle \mathbf{k}'_{\mathrm{f}\bar{\nu}}\bar{\nu} \,|\mathbf{k}_{\mathrm{f}\nu}\nu\rangle|^2$ is the transition probability. The integrals in Eq.(7.22) produce, for each harmonic, the former and next-order element, meaning, in particular, that the third harmonic generates the fourth term and renormalizes the second. The former prevents a self-consistent evaluation of the scattering times $\tau^{\parallel(\perp)}_{n\nu}$, so we cut it out and close the system of equations. On the other hand, the third harmonic is renormalized by the fourth one, which is absent in our approximation; thus, the third order will also be omitted. As a result, the final system of equations finds eight scattering times. The meaning of the approximations shown above is the perturbative treatment of the system's anisotropy; the inclusion of additional harmonics would fine-tune the effect of such deformation. In the limit of large Fermi energy and expanding the in-plane magnetization to the first we find four nonzero transport times

$$\tau^{\parallel}_{1\uparrow} = \tau^{\parallel}_{1\downarrow} \sim 1/n_i u_0^2 \tag{7.23a}$$

$$\tau^{\perp}_{1\uparrow} = \tau^{\perp}_{1\downarrow} \sim -\alpha m_x / n_i u_0^2 \varepsilon^{3/2}, \tag{7.23b}$$

leading to a density-current response from each band equals to

$$S_{z\uparrow} = -S_{z\downarrow} \sim \frac{m_x m_z}{n_i u_0^2 \alpha^2 \sqrt{\varepsilon}} E_y. \tag{7.24}$$

Clearly, Eq.(7.24) tells us that the two bands contribute equally with an opposite sign, and therefore no out-of-plane response is allowed in FBA.

7.4.2 Kubo-Streda approach

Our investigation of the system's response away from equilibrium continues using the Kubo-Streda approach within the linear response theory. In particular, we assume that **M** and **E** vary slowly in both position and time (i.e. on scales larger than the mean free path and τ), and hence neglect their spatial and temporal dependence. The spin density is then directly related to the electric field via

$$S_\alpha = K_{\alpha\beta} E_\beta, \tag{7.25}$$

where $K_{\alpha\beta}$ ($\alpha = x, y, z$ and $\beta = x, y$) is the spin susceptibility response tensor with a 3×2 matrix structure in our case (c.f. Eq. (7.2)). Therefore, the effect of SOT upon the FM is contained entirely within the object $K_{\alpha\beta}$. As explained in Chap.(4), the spin-current response function can be separated into two contributions,

$$K_{\alpha\beta} = R^0_{\alpha\beta} + R^\varepsilon_{\alpha\beta}, \tag{7.26}$$

where $R^0_{\alpha\beta}$ is the system's Fermi sea (type II) response, and $R^\varepsilon_{\alpha\beta}$ is the Fermi surface (type I) contribution to the total response. By working in the dilute limit (i.e. low impurity concentration) we may neglect the Fermi sea contribution, and ignore terms containing products of the same Green's function,

$$K_{\alpha\beta} \simeq \frac{1}{2\pi} \int d\mathbf{p}\, \mathrm{tr}[\langle s_\alpha G^R j_\beta G^A \rangle_{\mathrm{dis}}]. \tag{7.27}$$

Applying the disorder average we get

$$K_{\alpha\beta} = \frac{1}{2\pi} \int d\mathbf{p}\, \mathrm{tr}[\tilde{s}_\alpha \mathcal{G}^R_{\mathbf{p}} j_\beta \mathcal{G}^A_{\mathbf{p}}], \tag{7.28}$$

where $\tilde{s}_\alpha$ is the renormalized vertex operator defined by the Bethe-Salpeter equation, Eq.(4.108), and $\mathcal{G}^{R(A)}$ is the dressed Green's function defined by the self-energy $\Sigma^{R(A)}$, Eq.(4.107). We perform our calculations using the standard rules of diagrammatics and assume the non-crossing approximation. Again, we see that the FBA fails to produce any out-of-plane spin accumulation, in agreement with the Boltzmann-semiclassical argument discussed before. We overcome the symmetric cancellation between the two bands by including the skew scattering mechanism, well defined by the presence of the out-of-plane magnetization. To this end, we perform a complete T-matrix treatment of the response, where the electrons' self-energy becomes

$$\Sigma^{R(A)} = n_i T^{R(A)} = n_i \frac{u_0}{1 - u_0 g_0^{R(A)}}, \tag{7.29a}$$

$$g_0^{R(A)} = \int \frac{d^2p}{(2\pi)^2} G^{R(A)}_{0,\mathbf{p}}, \tag{7.29b}$$

where $g_0^{R(A)}$ is the momentum integrated clean Green's function, and we omitted the length scale R to lighten the notation. In particular, we obtain

$$\Sigma^{R(A)} = \sum_{\alpha=0}^{3} n_i [g_\alpha(\varepsilon, \alpha, \mathbf{m}) \pm \mathrm{i}\Gamma_\alpha(\varepsilon, \alpha, \mathbf{m})] s_\alpha, \tag{7.30}$$

where we note that the self-energy has now acquired a matrix structure (unlike in the Gaussian approximation), g_α and Γ_α are real functions, and $g_2 = \Gamma_2 = 0$. Now that we have all the elements required, the response function is ready for evaluation.

We begin by presenting the numerical results for the efficiency and the torque efficiencies, which can be defined as $\theta_{\alpha\beta} = -2ev K_{\alpha\beta}/\sigma_{xx}$ and $\tau_i^{\mathrm{e/o}} = t_i^{\mathrm{e/o}}/\sigma_{xx}$ respectively, where σ_{xx} is the longitudinal DC conductivity. Fig.(7.3) plots the efficiency at fixed magnetization angle against the Fermi energy, and Fig.(7.4) shows the behaviour of the torque efficiencies as a function of θ. Panel (a) of the first figure shows a strong damping-like SOT originating from the diagonal terms of the $\hat{K}$-tensor, $\theta_{xx(yy)}$, with zero in-plane magnetization. Here we see a discontinuity in $\theta_{xx(yy)}$, which can be attributed to breaching the upper limit of the spin gap, where-after the magnitude of the current-induced spin-polarization efficiency decreases monotonically and smoothly with increasing ε. This efficiency reduction is explained by noting that the difference in occupation numbers of the two Fermi rings becomes less significant by increasing the Fermi energy. In the limit of $\varepsilon \to \infty$, there is a total overlap of the two Fermi rings that provide opposing contributions to $S_{x(y)}$; the result is a zero diagonal response. For comparison, we present the Edelstein contribution to the field-like SOT, $\theta_{xy,yx}$, dominant in this system. However, we find that the damping-like contribution becomes gigantic inside the spin-gap, approaching a relative magnitude of 7%. Moving away from the

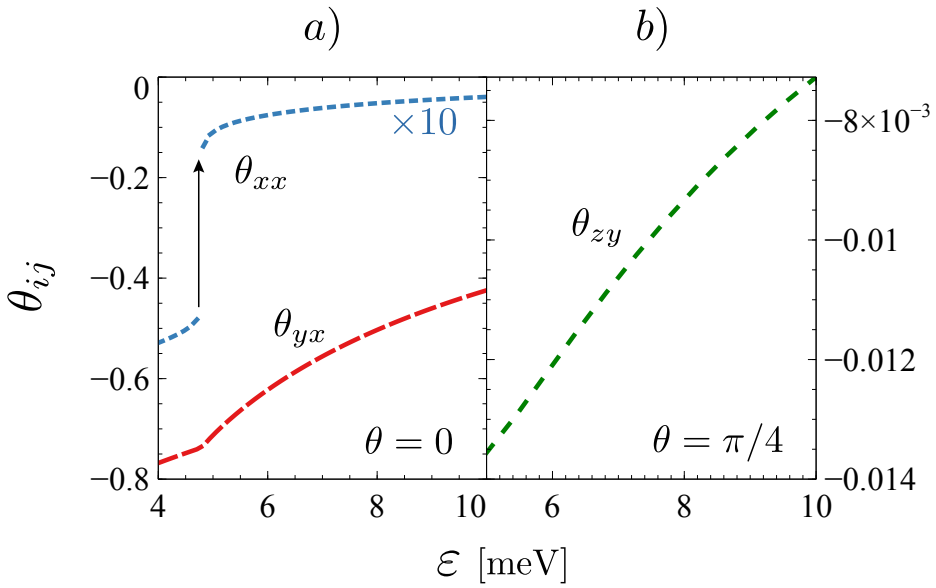

Figure 7.3: Current-induced torque efficiencies as functions of the Fermi energy in the strong scattering limit, with magnetization a): $\theta = 0$ and b): $\theta = \pi/4$. In the former case, the range of Fermi energies covered spans both inside and outside the spin gap, whose upper limit is 4.8 meV, while in the latter only the regime outside the spin gap is resolved. The blue lines portrays the damping-like torque efficiency, while the red and green curves represent the field-like torque efficiencies. Parameters: $m^* = 0.8m_e$ $\alpha = 1.7 \times 10^{-11}$ ms^{-1}, $\Delta_{\mathrm{xc}} m_z = 4.8$ meV, $n_i = 5 \times 10^{14}$ m^{-2}.

in-plane configuration, we find vertical spin accumulations. While the DL component

coming from θ_{zx} remains negligible, θ_{zy} produces small corrections to the FL torque (right panel (b)). It reaches its maximum value of 2% with respect to the EE-FL SOT for $\theta = \pi/4$.

The nonperturbative treatment of the response function in the magnetization angle allows an in-depth analysis of the torque coefficients against θ in the strong disorder regime, illustrated in Fig.(7.4). In particular, we find three nonzero terms, τ_1^o and $\tau_{1,2}^e$. The left panel (Fig.(7.4a)) considers a Fermi energy inside the spin gap for an initial out-of-plane configuration of the magnetization. This is the *strong damping* regime, where the ratio between the DL and FL torques is maximized (see Fig.(7.3)). As the FM's magnetization is shifted from purely out-of-plane to in-plane, the spin gap between the bands, originating in the vertical component of the exchange interaction, begins to shrink and vanishes when $\theta = \pi/2$. Consequently, the fixed Fermi energy will only intersect a single band for smaller angles, before then intersecting both bands at some *critical angle*, $\theta_c(\varepsilon)$ ($\sim \pi/4$ in this case), where the spin gap has shrunk sufficiently to allow this, and hence a discontinuity is observed at this $\theta_c(\varepsilon)$. This corresponds to moving from the strong damping regime to the *weak damping regime*. The angular dependence of the SOT coefficients is clearly symmetric about $\theta = \pi/2$. On the other hand, the right panel (Fig.(7.4b)) illustrates the angular behaviour of the torque coefficients if the Fermi energy is situated outside the spin gap at $\theta = 0$. In this regime, there are no discontinuities since ε always intersects the two bands simultaneously. As a consequence, the torque coefficients will be smooth continuous functions of θ.

In conclusion, we present analytic expressions of the response tensor to relate the microscopic quantities more clearly to macroscopic accumulations. To do that, we need ad-hoc expansion to simplify the term as much as possible. We first consider the regime $\Delta_x \ll \Delta_z \ll \alpha \ll \varepsilon$, and denote the $\hat{K}$-tensor by using a tilde. In this case, we expand the spin susceptibility to first order in m_x to yield

$$\widetilde{K} = -\frac{e}{2\pi n_i}\begin{pmatrix} -\frac{(m^*)^2\Delta_z\alpha}{2\pi\varepsilon} & \frac{\alpha}{u_0^2} \\ -\frac{\alpha}{u_0^2} & -\frac{(m^*)^2\Delta_z\alpha}{2\pi\varepsilon} \\ \frac{m^*\Delta_x\Delta_z^2}{4\pi\alpha\varepsilon^2} & -\frac{\Delta_x\Delta_z}{2\pi u_0\alpha\varepsilon} \end{pmatrix}, \tag{7.31}$$

where we kept the first nonzero elements in the impurity potential expansion. We note that $\sigma_{xx(yy)} = e^2\varepsilon/(\pi n_i m^* u_0^2)$ in the weak scattering limit for a large Fermi energy. The diagonal terms of Eq.(7.31) ,i.e., $\widetilde{K}_{xx}$ and $\widetilde{K}_{yy}$, define the Edelstein effect, and appear in FBA being inversely proportional to u_0^2. The next order in the impurity potential, u_0^{-1}, generates another field-like component, $\widetilde{K}_{zy}$. It requires the prescription of the non-Gaussian average of the form $\langle V(\mathbf{x})V(\mathbf{x}')V(\mathbf{x}'')\rangle = n_i R^6 u_0^3 \delta(\mathbf{x}-\mathbf{x}')\delta(\mathbf{x}'-\mathbf{x}'')$ [19]. The physics of this triple-scattering within the response function is captured by truncating the T-matrix series at the third order in Fig.(7.5b) [19]. Finally, the damping-like elements, $\mathcal{O}(u^0)$, can be found by calculating fourth-order scattering diagrams. Eq.(7.5)

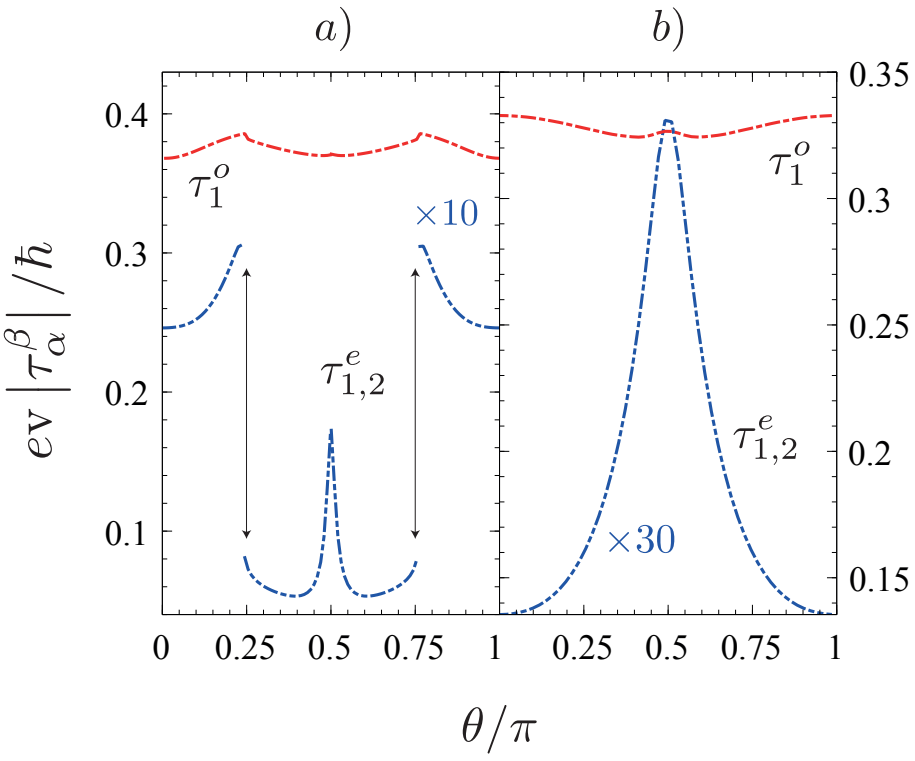

Figure 7.4: Torque efficiencies as a function of magnetization angle, with periodicity π. The field-like torque efficiency $\tau_1^{\rm o}$ is denoted by the red line, whilst the damping-like efficiencies are equal in module, $|\tau_1^{\rm e}| = |\tau_2^{\rm e}|$, and represented by the blue line. In a) the Fermi energy is inside the spin gap for $\theta = 0$, i.e., $\varepsilon = 4.5\,\text{meV}$. The discontinuous behaviour reflects the transition in the electronic band structure from inside to outside the spin gap. In b), the Fermi energy is above the spin gap, $\varepsilon = 5.5\,\text{meV}$, and the torque coefficients are smooth functions of θ. Parameters $m^* = 0.8\,m_e$ (Tantalum), $\text{v} = 5 \times 10^4\,\text{m/s}$, $\Delta_{\rm xc} = 5$ meV, and $n_i = 0.5 \times 10^{15}\,\text{m}^{-1}$.

translates the response tensor to spin-orbit torque coefficients,

$$\begin{aligned}
\tilde{\tau}_1^{\rm o} &= -\frac{m^*}{2e\varepsilon}\left(\alpha + \frac{\Delta_x^2 u_0}{2\pi\alpha\varepsilon}\right), \\
\tilde{\tau}_2^{\rm o} &= -\frac{m^*\Delta_{\rm xc}^2 u}{4\pi e\alpha\varepsilon}, \\
\tilde{\tau}_1^{\rm e} &= \frac{(m^*)^3\Delta_{\rm xc}\alpha u_0^2}{4\pi e\varepsilon^2}, \\
\tilde{\tau}_2^{\rm e} &= -\frac{(m^*)^2\Delta_{\rm xc}u_0^2}{4\pi e\varepsilon^2}\left(m^*\alpha - \frac{\Delta_z^2}{2\alpha\varepsilon}\right).
\end{aligned} \tag{7.32}$$

Alternatively, we can consider a different regime in which the strengths of the Rashba SOC and out-of-plane magnetization are now swapped, $\Delta_x \ll \alpha \ll \Delta_z \ll \varepsilon$. An

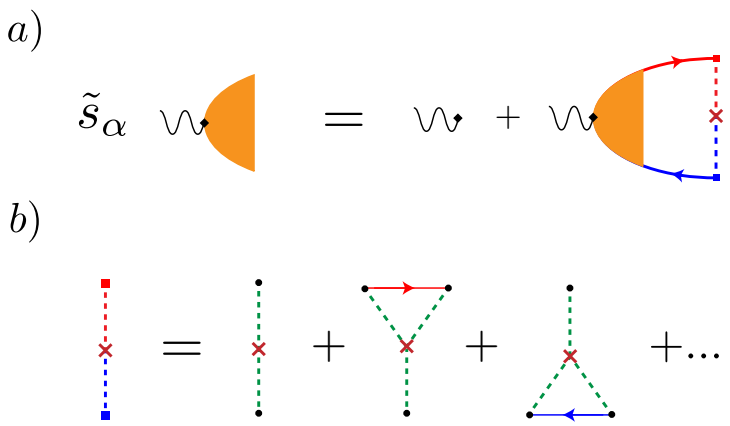

Figure 7.5: Diagrammatic expansion of the zero temperature spin-density–charge-current response function: (a) the disorder-renormalized spin density vertex function and (b) the T-matrix skeleton expansion. Solid lines with arrows denote disorder averaged Green's functions, while green dashed lines represent single impurity potential insertions. Red/blue indicate advanced/retarded sectors.

overline denotes the resulting response in this case. We find

$$\bar{K} = -\frac{e}{2\pi n_i}\begin{pmatrix} -\frac{(m^*)^3\alpha^3}{2\pi\Delta_z} & \frac{\alpha}{u_0^2} \\ -\frac{\alpha}{u_0^2} & -\frac{(m^*)^3\alpha^3}{2\pi\Delta_z} \\ \frac{(m^*)^2\alpha\Delta_x}{4\pi\varepsilon} & -\frac{m^*\alpha\Delta_x}{2\pi u_0\Delta_z}, \end{pmatrix} \tag{7.33}$$

which yields

$$\begin{aligned} \bar{\tau}_1^{\mathrm{o}} &= -\frac{m^*\alpha}{2e\varepsilon}\left(1+\frac{m^*\Delta_x^2 u_0}{2\pi\Delta_z^2}\right), \\ \bar{\tau}_2^{\mathrm{o}} &= -\frac{(m^*)^2\alpha\Delta_{\mathrm{xc}}^2 u}{4\pi e\Delta_z^2\varepsilon}, \\ \bar{\tau}_1^{\mathrm{e}} &= \frac{(m^*)^4\alpha^3\Delta_{\mathrm{xc}}u_0^2}{4\pi e\Delta_z^2\varepsilon}, \\ \bar{\tau}_2^{\mathrm{e}} &= -\frac{\alpha(m^*)^3u_0^2\Delta_{\mathrm{xc}}}{4\pi e\varepsilon}\left(\frac{m^*\alpha^2}{\Delta_z^2}-\frac{1}{2\varepsilon}\right). \end{aligned} \tag{7.34}$$

7.5 Three-dimensional topological insulators

Given the interesting results of the last section, we apply the same methodology to surface states of 3D topological insulators, possessing a much stronger SOC than the 2DEG counterpart. For low energy excitations, the TI's dispersion relation, ignoring bulk states, is well described by Dirac cones shifted and gapped by the magnetic interaction. We therefore use the Hamiltonian in Eq.(7.9b) to describe the TI, in which

we add a scalar impurity potential. Since the system does not possess a pseudospin structure, we use

$$\Sigma_\mu = \xi(s_0, -s_y, s_x, s_z) \tag{7.35}$$

alongside an SU(2) gauge field whose non-zero elements are

$$A_0^x = \varsigma\frac{\Delta_{\text{xc}} m_x}{\text{v}}, \qquad A_0^y = \varsigma\frac{\Delta_{\text{xc}} m_y}{\text{v}}, \qquad A_0^z = \varsigma\frac{\Delta_{\text{xc}} m_z}{\text{v}}, \tag{7.36}$$

where $\xi = \pm$ describes the top (bottom) TI surface ((A)FM/TI – TI/(A)FM configurations) and $\varsigma = \pm$ specifies the ferromagnetic (antiferromagnetic) state of the magnetic layer. The dispersion relation for this model is shown in Fig.(7.6). As in 2DEG/FM

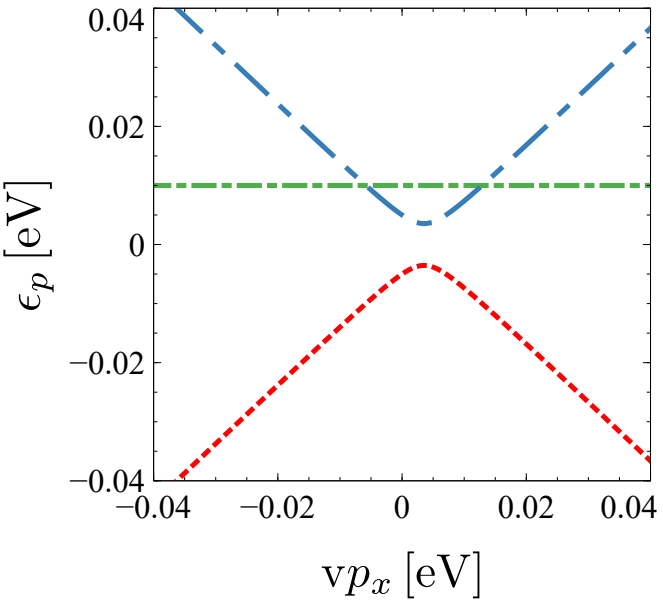

Figure 7.6: Dispersion relation for the linear Dirac Hamiltonian model for a top TI surface with an s-d model exchange interaction with an antiferromagnet and Rashba SOC. Parameters: $\Delta_{\text{xc}} = 5\,\text{meV}$ and $\text{v} = 4.3 \times 10^5\,\text{ms}^{-1}$ (Bi_2Te_3 [208]).

bilayers, the out-of-plane magnetization opens a gap proportional to Δ_{xc} in the TI's band structure, hence we focus on the metallic regime where ε lies above the spin gap. In addition to this, the in-plane magnetization ($m_y = 0$) distorts the spin-texture of the Fermi ring according to

$$\mathbf{s}_\phi = (\mathbf{s}_\phi^0 + m_x\,\delta\mathbf{s}_\phi), \tag{7.37a}$$

$$\mathbf{s}_\phi^0 = \tilde{\rho}_\parallel \hat{\mathbf{k}}_{\text{f}} \times \hat{z} + \tilde{\rho}_\perp \hat{z}, \tag{7.37b}$$

$$\delta\mathbf{s}_\phi = [\tilde{\omega}_\parallel + \xi_\parallel \cos(2\theta)]\hat{x} + \xi_\parallel \sin(2\theta)\,\hat{y}, \tag{7.37c}$$

where, $\omega(\rho)_\parallel$, $\rho_\perp$, and $\xi_\parallel$ are functions of m_z^2 and the Fermi momentum k_{f}, and ϕ is the momentum angle. The in-plane magnetization at the Fermi level does not affect the z-component of the spin texture, meaning that the out-of-plane component of $\mathbf{s}_\phi$ is

independent from the momentum. As a result, no out-of-plane polarization response is observed. The torque coefficients then take the simpler form

$$\tau_1^{\mathrm{e}} = \kappa_{yy}, \tag{7.38a}$$

$$\tau_2^{\mathrm{e}} = \frac{\kappa_{xx} - \kappa_{yy}}{m_x^2} - \kappa_{xx}, \tag{7.38b}$$

$$\tau_1^{\mathrm{o}} = \kappa_{xy}, \tag{7.38c}$$

$$\tau_2^{\mathrm{o}} = \frac{\kappa_{xy} + \kappa_{yx}}{m_x^2}. \tag{7.38d}$$

In the absence of skew-scattering, the observed spin accumulation is produced solely by Edelstein spin accumulation, meaning that only K_{xy} and K_{yx} are the only non-zero elements of the spin susceptibility tensor. Reintroducing skew-scattering generates an imbalance in the number of electrons situated in opposite momentum states and leads to a spin current perpendicular to the electrical current due to $m_z \neq 0$. However, the electron's in-plane spin component is constrained to wind clockwise around the Fermi ring, and so the application of an electric field gives rise to a spin accumulation (anti-)parallel to the field, $S_{x,y} \sim E_{x,y}$. Therefore, we expect the only vanishing elements of $K_{\alpha\beta}$ to be K_{zx} and K_{zy} for this model.

We present the field and damping-like torque efficiencies' dependence on the magnetization angle in Fig.(7.7) in the strong scattering limit (i.e. u_0 is significant but not infinite), treating band structure and scattering strength on the same level. Specifically, the results are valid for the top TI surface configuration and antiferromagnetic state of the magnetic layer. However, we can extend the results for more system configurations. Noting that $\kappa_{yx(xy)} \propto \xi \mathrm{v}$, we realize that $\tau_{1,2}^{o}$ changes the sign by changing the TI surface while remaining unaffected by replacing the antiferromagnet with a ferromagnet. On the other hand, $\kappa_{xx(yy)} \propto (\xi \mathrm{v}) \times (\varsigma \Delta_{\mathrm{xc}})$, so $\tau_{1,2}^{e}$ changes the sign by changing the TI surface and the magnetization state of the magnetic layer. Here we see that τ_1^{o} dominates the field-like torque, with a near constant value ~ 0.5 and varying slowly with ϕ, analogous to the 2DEG case. In comparison, τ_2^{o} experiences notable fluctuations, due to depending on the sum of K_{xy} and K_{yx}, leading to significant corrections as large as 3% of τ_1^{o}. Meanwhile, the damping-like torque coefficients are equal, $\tau_1^{\mathrm{e}} = \tau_2^{\mathrm{e}}$, in agreement with Eq.(7.38b) for $\kappa_{xx} \sim \kappa_{yy}$, and depend strongly upon then magnetization angle. These torques reach up to 9% of their field-like Edelstein counterparts. Let us now analyze the spin susceptibility tensor in the weak scattering and resonant limits. In both cases we may expand in powers of m_x up to first order to obtain

$$K_{\mathrm{Weak}}^{\mathrm{Dirac}} = \frac{e\Gamma_1}{2\pi n_i} \begin{pmatrix} \frac{\Delta_z \Gamma_1}{2u_0 \mathrm{v}} & -\frac{\mathrm{v}}{u_0^2} \\ \frac{\mathrm{v}}{u_0^2} & \frac{\Delta_z \Gamma_1}{2u_0 \mathrm{v}} \\ 0 & 0 \end{pmatrix}, \tag{7.39a}$$

$$K_{\mathrm{Res}}^{\mathrm{Dirac}} = \frac{e}{2\pi n_i \mathrm{v}} \begin{pmatrix} \frac{\Delta_z}{u_0} & -\frac{(\Delta_z^2 - \varepsilon^2)(\pi^2 + 2\Gamma_2)}{8\pi^2 \mathrm{v}^2} \\ \frac{(\Delta_z^2 - \varepsilon^2)(\pi^2 + 2\Gamma_2)}{8\pi^2 \mathrm{v}^2} & \frac{\Delta_z}{u_0} \\ 0 & 0 \end{pmatrix}, \tag{7.39b}$$

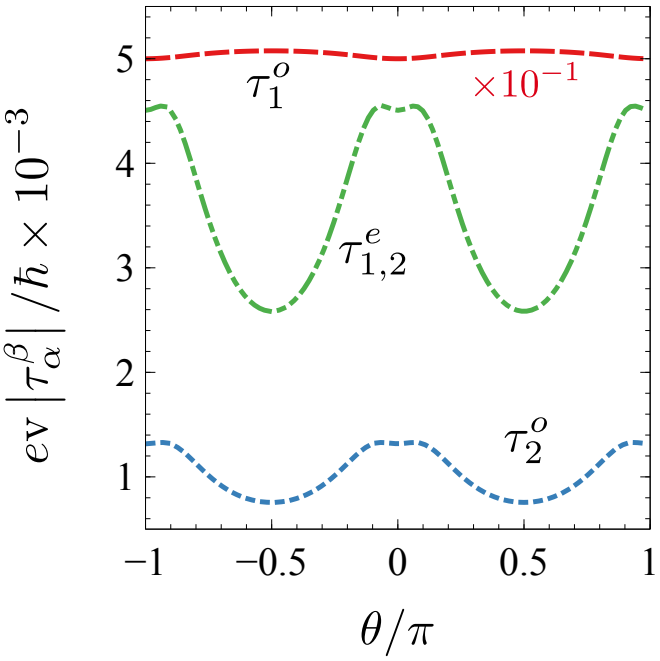

Figure 7.7: Torque efficiencies as a function of magnetization angle. (a): Field-like efficiencies with the blue line denoting $\tau_1^{\rm o}$ and the red line representing $\tau_2^{\rm o}$. (b): Damping-like efficiencies, where $\tau_1^{\rm e} = \tau_2^{\rm e}$. Parameters: $\Delta_{\rm xc} = 0.1\,{\rm eV}$, $\varepsilon = 0.11\,{\rm eV}$, $n_i = 5 \times 10^{12}{\rm m}^{-2}$.

for the weak and resonant limits respectively, where we have defined $\Gamma_1 = (\Delta_z^2 - \varepsilon^2)/(3\Delta_z^2 + \varepsilon^2)$ and $\Gamma_2 = \ln \frac{-\Delta_z^2+\varepsilon^2}{\Lambda^2}$, and Λ is the ultra-violet energy cut-off. In both limits we see that the ESA elements dominate over the damping-like terms; in the resonant limit, $K_{xy(yx)} = \mathcal{O}(u^0)$ and $K_{xx(yy)} = \mathcal{O}(u^0)$, whilst in the weak scattering limit, $K_{xy(yx)} = \mathcal{O}(u^{-2})$ and $K_{xx(yy)} = \mathcal{O}(u^{-1})$. In the limit $\phi \to 0$, the damping-like efficiencies approach

$$\tau_{1,2}^{\rm e} = \mp \frac{\Delta_{\rm xc}\Delta_z u_0 \Gamma_1}{4e{\rm v}^3}, \text{ and } \tau_{1,2}^{\rm e} = \mp \frac{4\pi^2 {\rm v}\Delta_z}{eu_0(\Delta_z^2 - \varepsilon^2)\Gamma_2},$$

in the weak and resonant limits respectively. A different way to look at the results, which is widely used in the experimental literature of the spin-transfer torque [220], involves the definition of the torque conductivity

$$\sigma_{\alpha,\beta}^s = \frac{\mathbf{T}_\alpha^\beta M_s d}{\gamma J}, \tag{7.40}$$

where $\alpha = (1,2)$ and $\beta = ({\rm o},{\rm e})$. The advantage of Eq.(7.40) is to disentangle the efficiency of the SOT from other microscopic characteristic quantities of the system, such as the thickness and the saturation magnetization of the magnetic layer. This facilitates the comparison between the different systems' torque magnitudes and the efficiency of spin-orbit and spin-transfer torque.

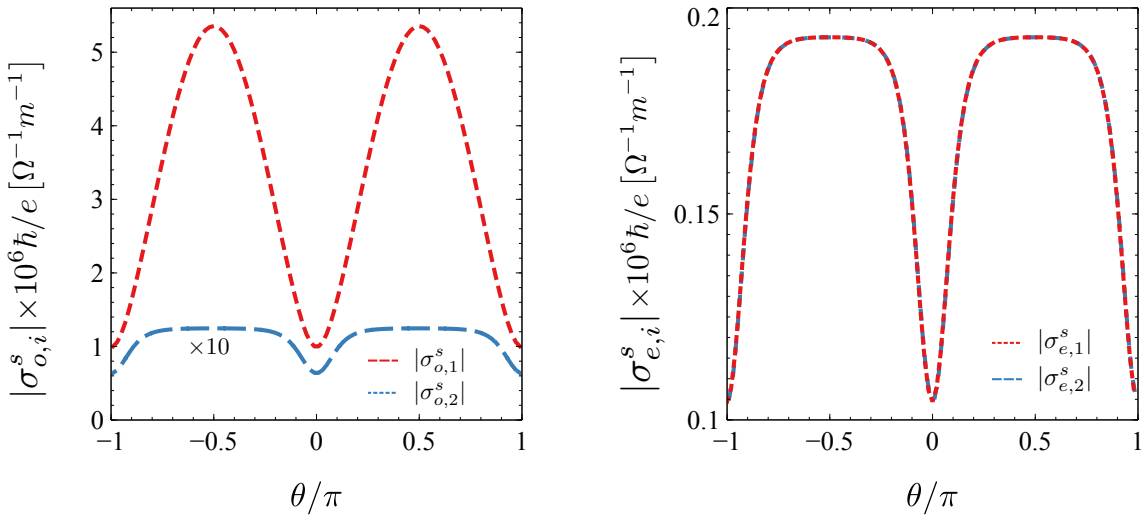

Figure 7.8: Torque conductivity against the magnetization angle. Parameters: $\Delta_{\text{xc}} = 0.2\,\text{eV}$, $\varepsilon = 0.21\,\text{eV}$.

7.5.1 Magnetic disorder

According to our previous findings, only in-plane spin accumulations are generated at the interface of 3D topological insulators, and the field-like torque dominates over the damping-like counterpart, opposite to what generally happens with the spin-transfer torque mechanism [221]. For that reason, even though magnetization switching is still allowed, it is a relatively weak effect. So then, a natural question arises: how can we obtain a more general spin-current response and increase the magnitude of the DL torque? We try to find a solution by considering, along with the scalar electrostatic impurity potential, randomly distributed magnetic defects, modelled as local sources of in-plane exchange interactions. Under this model, the single impurity potential is then represented as $W_{mag}(\mathbf{r}) = (u_0 + u_x s_x + u_y s_y)R^2\delta(\mathbf{r})$. This type of local interactions, intuitively, enhance the effect of skew scattering and break the constraints on the spin response due to the form of the spin texture.

To show that, Fig.(7.9) plots the elements of the $\hat{K}$-tensor against the concentration of impurities with only scalar defects (left panel) and magnetic disorder (right panel). In the former case, only the in-plane components of the spin-current response are generated, while in the latter, magnetic impurities entirely populate the $\hat{K}$-tensor. The increasing n_i smoothly shifts the system from the dilute regime, most commonly adopted in semiclassical theories, to a moderately *dirty regime*, where the side-jump mechanism kicks in, resulting in a stronger damping-like component to the SOT. For purely out-of-plane magnetization and in the presence of scalar impurities, the analyt-

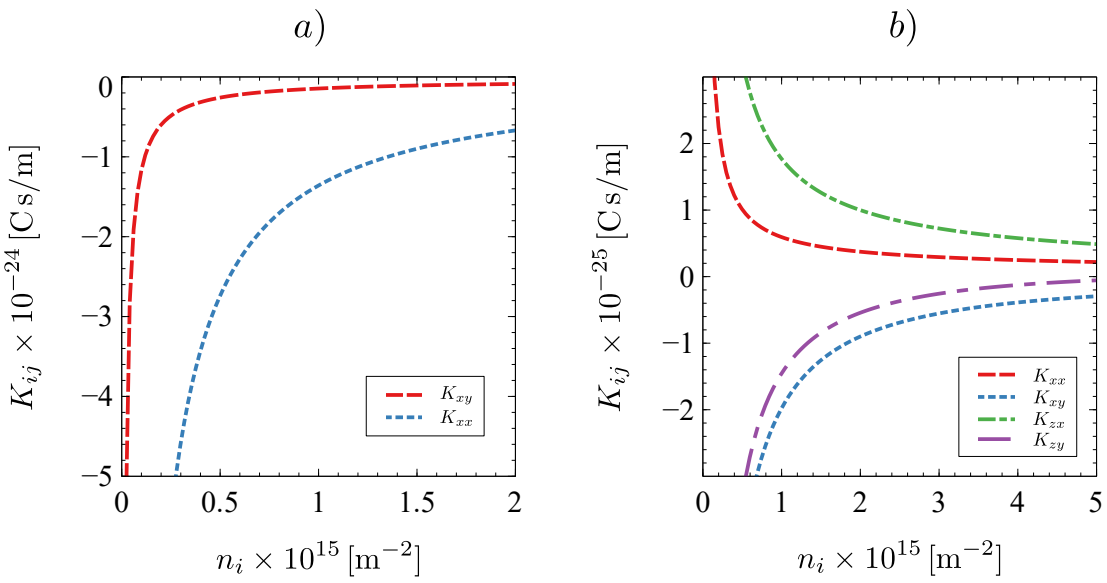

Figure 7.9: Spin susceptibility as a function of the impurity concentration. The graph on the left presents the results for disordered TI with scalar impurities, where only in-plane spin accumulations are generated. On the right, we include strong correlated magnetic disorder, yielding to out-of-plane macroscopic spin densities. The magnetization of the magnetic layer is strictly out-of-plane, whereby $K_{xx} = Kyy$ and $K_{xy} = -Kyx$. Parameters: $\mathrm{v} = 6 \times 10^5\,\mathrm{m/s}$, $R = 10^{-9}\,\mathrm{m}$, $u_0 = 10\,\mathrm{eV}$, $u_x = 20\,\mathrm{eV}$, $\Delta_{xc} = 0.1\,\mathrm{eV}$, $\varepsilon = 0.11\,\mathrm{eV}$.

ical expression of the quantum side-jump contribution to Eq.(7.39b) is,

$$\kappa_{xy} = -\kappa_{yx} = -\frac{e(\Delta_z^2 + \varepsilon^2)^2}{2\pi^2 \mathrm{v}(3\Delta_z^2 + \varepsilon^2)^2}, \tag{7.41a}$$

$$\kappa_{xx} = \kappa_{yy} = \frac{e\varepsilon\Delta_z(\Delta_z^2 + \varepsilon^2)}{\pi \mathrm{v}(3\Delta_z^2 + \varepsilon^2)^2}, \tag{7.41b}$$

obtained by keeping the terms in the Kubo formula which are independent of the concentration of impurities [208], and reproducing the result in Fig.(7.9a).

While with only scalar disorder, the ratio between DL and FL in-plane components reaches the maximum of $K_{yy}/K_{xy} \sim 0.15$, the presence of magnetic impurities leads to $K_{yy}/K_{xy} \sim 0.85$, in addition to obtaining a sizable renormalization to the FL-term, $K_{zy}/K_{xy} \sim 0.18$, and a solid contribution to the DL-term coming from out-of-plane spin accumulations, $K_{zx}/K_{xy} \sim 1.65$, aligning with the efficiency of the STT.

7.6 Conclusions

This chapter provides a better understanding of the interfacial spin-orbit torques by treating the exchange-driven band structure-anisotropy nonperturbatively and includ-

ing the effect of the skew scattering mechanism. Specifically, we find that an efficient damping-like spin-orbit torque can be induced at the interface of normal metal and topological insulator-based bilayer systems, able to induce the magnetization switching in the coupled magnetic layer. These results show that the bulk contribution to the damping-like SOT, driven by the spin Hall effect, is unnecessary, which may shed light on the current unexplained experimental evidence [209]. Furthermore, our exact treatment of the in-plane magnetization reveals a non-trivial angular dependence of the torque coefficients, which shows the limitations in assuming the Zeeman-like coupling in normal metals and topological insulators as purely out-of-plane or mildly tilted toward the horizontal plane. In particular, a strongly angled magnetization in NM/FM bilayers triggers a transition from the strong damping regime, originating from a chemical potential inside the spin gap to the weak counterpart, portrayed by a sharp discontinuity in the system's response. To make magnetization switching more relevant in TI/FM bilayers, we include the effect of randomly distributed magnetic impurities in the system, which turn out to be highly beneficial to enhance the damping-like torque and enrich SOT dynamics, especially in the dirty regime, where the quantum side-jump mechanism plays a significant role.

A careful study of the magnetization dynamics of the magnetic layer, governed by the Landau-Lifshitz-Gilbert equation, would be of crucial interest to understanding the impact of purely-interfacial spin-orbit torques. What remains to be established is, in fact, the efficiency of the SOT-induced damping-like torque in switching the magnetization compared to the bulk companion and the problematic spin-transfer torque. Moreover, other exotic systems can be investigated, like Weyl semimetals or materials decorated with magnetic impurities. These media are promising candidates to find strong out-of-plane spin accumulations due to their strong proximity-induced interactions and can enrich the phenomenology of the SOT.

Chapter 8

Conclusions

Two-dimensional systems are nowadays heavily studied in solid-state physics due to their unique transport properties exploitable in spin-based next-generation devices. Low dimensionality is, in fact, key to acquire optimal control over the strength and symmetry of spin-orbit coupling, and tailor coupled spin-charge phenomena for a specific end. While two-dimensional electron gases have a long history of experimental and theoretical research, there is currently an increased focus on more exotic model systems. The family of three-dimensional topological insulators display metallic surface states that function as 2D systems, with unparalleled strong spin-orbit interaction ideal for exploiting charge-spin conversion phenomena. On the other hand, graphene has gained attention as a high-performance spin channel due to its weak spin-orbit and hyperfine interactions. Moreover, very recent advances in nanofabrication of van der Waals heterostructures have revolutionized the field of graphene spintronics. Specifically, vertical stacks of graphene and atomically thin semiconductors have opened up the possibility of introducing rich symmetry-breaking spin-orbit fields in graphene, opening doors to a myriad of coupled spin-charge transport phenomena.

This thesis aimed to present a unified theoretical framework for analyzing and predicting coupled spin-charge phenomena in two-dimensional systems, including two-dimensional electron gases, surface states of topological insulators (TI) and proximitised graphene. We focused on the effect of proximity-induced spin-dependent interactions and the interplay of scalar (spin-transparent) and spin-orbit-active impurities. A unified treatment of these aspects has allowed us to investigate interesting SOC-related transport phenomena. In the first part, we provided a bird's eye-view of the electronic properties of graphene, engineered graphene, and TI surface states. A detailed study of specific broken symmetries allowed for an extensive understanding of the emergent spin-orbit couplings. For instance, the absence of inversion symmetry along a specific direction leads to the Rashba interaction, central for spin-charge conversion effects and relevant in all model systems studied. Additionally, the breaking of sublattice symmetry in graphene/transition metal dichalcogenides (TMD) heterostructures supplements the Rasbha effect with proximity-induced spin-valley coupling, resulting in a rich SOC phenomenology. We also briefly discussed the topological properties of TI systems yielding to the strong spin-momentum locking present in these materials.

We then introduced the main theoretical techniques used to study spin-charge transport problems in this thesis. To begin, we introduced the semiclassical Boltzmann equation, the simplest quantum extension of the classical kinetic theory. This approach, widely used in the field, treats the electrons as classical objects as they travel through the medium but accounts for quantum effects during collision events using the Fermi golden rule. While simple, this method can predict several effects and offers an excellent understanding of the underlying mechanisms. However, its limitations in handling spin-dependent impurities required the development of a more advanced theory, namely, the quantum Boltzmann equation, able to capture a wider range of quantum effects, like interband spin-orbit transitions. Finally, we extended the fully quantum-mechanical Kubo-Streda approach to the linear response theory to the T-matrix level, able to capture SOC in the band structure and spin-orbit scattering events in a non-perturbative fashion. We formulated the Diffuson Hamiltonian formalism, which allows for the derivation of complete sets of time and space-dependent drift-diffusion equations, spin-charge conversion mechanisms, and relaxation times, providing a unified understanding of the transport properties of the system.

The methods above were first applied to monolayer graphene with randomly-distributed spin-active adatoms and fluctuations of the spin-orbit fields, known to be important in this system. Our findings revealed that the breaking of specific spatial symmetries allows for the interference between different local sources of spin-orbit interactions, resulting in virtual conduction-valence band transitions during scattering events. Such transitions are then able to scatter asymmetrically particles with opposite out-of-plane spin moments and, for this reason, we call the effect *interband spin-orbit scattering*. This mechanism generates a sizable current-induced spin current, which dominates over the traditional skew scattering-driven spin Hall current in the weak impurity potential regime. This new effect is then integrated into a unified theory of space and time-dependent charge-spin coupled dynamics, providing a comprehensive understanding of various opto-spintronic phenomena, including the Edelstein Effect, spin Hall effect, and the anisotropic spin precession.

Next, our focus is shifted to van der Waals heterostructures, specifically graphene/TMD bilayers. These systems show great promise for spintronics due to their enhanced uniform spin-orbit interactions, coupled with the high electronic mobility inherited from graphene. Additionally, the recent ability to offset the two layers by some twist angle adds interesting features to their potential. In fact, the momentum-space spin textures can be tuned by a judicious choice of twist angle, opening doors to a higher level of control over in-plane current-induced spin densities. In this context, we obtained a simple, closed-form expression for the density-current response function in terms of the twist angle. This result reveals a spin accumulation parallel to the applied current at a critical (material-specific) twist angle, which we dubbed *collinear Edelstein effect*.

One of the key areas of pratical application is the spin-orbit torque (SOT), where a macroscopic spin accumulation generated in a non-magnetic layer and induced by an external electric field controls the magnetization of a magnetic material in bilayer systems. The magnetization switching is eventually exploited in storage devices to read/write information. While traditionally such switching is attributed to the spin Hall

effect in a bulk system, our research finds a significant contribution of pure interfacial origin and induced by a skew scattering mechanism. To show this, we calculated the density-current response tensor by treating the Zeeman interaction and other effects non-perturbatively, allowing us to resolve the full angular dependence of SOTs. We have specifically focused on two paradigmatic models: two-dimensional electrons gases formed at the interface between metallic layers and TI surface states, which have the potential to generate giant SOT due to their strong spin-momentum locking.

These discoveries, although small, represent an advance in a field that is far from being exhaustively investigated, and is not yet mature. In fact, there is much room for theoretical understanding to interpret and propose new experiments. For example, we presented a possible theoretical explanation for the appearance of damping-like spin-orbit torques at surfaces of ferromagnetic bilayers, which represents a better understanding of the phenomenon and can lead to improvements in the fabrication of related devices. "In adatom-decorated graphene, the identification of interband spin-orbit scattering and its significance in generating current-induced spin currents can help differentiate between various sources of the same phenomenon - the spin Hall effect - and allow for improved control over it. Furthermore, the discovery of the collinear Edelstein effect and the ability to manipulate current-induced spin densities in twisted heterostructures opens up opportunities for new experiments. These experiments could confirm the phenomenon and apply it to innovative technologies.

Appendix A

Functional approach to the Green's functions method

In this appendix, we briefly present the main principles of the functional Green's functions method to derive some properties of many-particle systems, like the quasi-particle propagators and the response function [178]. We avoid derivations here, aiming for an "hands-on" approach to the technique. We start introducing the *Grassmann algebra*, which defines special numbers representing fermionic fields in the path integral formulation of quantum mechanics. This procedure allows for a representation of quantum mechanics in terms of partition functions by which we can evaluate observables. The advantage of this method is the involvement of Gaussian integrals over the Grassmann numbers, which naturally yields the Wick theorem and the diagrammatic representation of the observables' calculation. We then focus on the effect of external potentials, leading to the Kubo-Streda formula in the specific case of linear response, and impurity interactions, renormalizing the bubble diagrams and the Green's functions.

Grassmann algebra

The main reason for introducing the special Grassmann number is to work with *fermionic coherent states*, that is, eigenfunctions of the annihilation operators. This way, the second quantized system's Hamiltonian can be written in terms of such numbers.

To start with, let us consider a single energy level occupied by spinless fermionic particles. Due to the Pauli exclusion principle, either zero or one particle occupies such state, i.e.,

$$\hat{c}|0\rangle = 0, \quad \hat{c}|1\rangle = |0\rangle, \quad \hat{c}^\dagger|0\rangle = |1\rangle, \quad \hat{c}^\dagger|1\rangle = |0\rangle, \tag{A.1}$$

where $\hat{c}^{(\dagger)}$ is the annihilation (creation) fermionic operator. We notice that no linear combination of states in the Hilbert algebra involving ordinary numbers can be an eigenstate of the annihilation operator, since $\hat{c}(x|0\rangle + y|1\rangle) = y|0\rangle \neq \lambda(x|0\rangle + y|1\rangle)$, unless $y = 0$ or $\lambda = 0$. For that reason, we introduce the Grassmann numbers, denoted by ψ, ψ', ψ'' etc, satisfying

$$\psi\psi' = -\psi'\psi; \quad \psi^2 = 0; \quad f(\psi) = f_0 + f_1\psi, \quad \{\psi, \hat{c}\} = \{\psi, \hat{c}^\dagger\} = 0 \tag{A.2}$$

where $f(\psi)$ is an arbitrary function of the Grassman variable ψ which is *defined* by its first two Taylor expansion coefficients, i.e.,

$$f(\psi,\psi') = f_{00} + f_{10}\psi + f_{01}\psi' + f_{11}\psi\psi'. \tag{A.3}$$

We now have all we need define the fermionic coherent state,

$$|\psi\rangle = |0\rangle - \psi|1\rangle = (1-\psi\hat{c}^\dagger)|0\rangle = e^{-\psi\hat{c}^\dagger}|0\rangle, \tag{A.4}$$

which satisfies the desired relation $\hat{c}|\psi\rangle = \psi|\psi\rangle$ and, analogously, $\langle\psi|\hat{c}^\dagger = \langle\psi|\bar{\psi}$, where we stress that the numbers ψ and $\bar{\psi}$ are completely unrelated.

Lastly, the algebra has special definitions for derivation and integration. In the first case

$$\frac{\partial\psi}{\partial\psi} = 1, \quad \frac{\partial f(\psi)}{\partial\psi} = f_1, \tag{A.5}$$

where double derivatives over two different Grassmann numbers anti-commute,

$$\partial_\psi\partial_{\psi'} f(\psi,\psi') = \partial_\psi(f_{01} - f_{11}\psi) = -f_{11} = -\partial_{\psi'}\partial_\psi f(\psi,\psi'). \tag{A.6}$$

In addition, the integration over Grassmann variables is defined as

$$\int d\psi 1 = 0; \qquad \int d\psi\psi = 1, \tag{A.7}$$

which implies the resolution of identity

$$\hat{1} = \int d\bar{\psi}\int d\psi e^{-\bar{\psi}\psi}|\psi\rangle\langle\psi|. \tag{A.8}$$

We have now set up the necessary basic operations to deal with the path integral partition function and averages over microscopic quantum operators, which we will present in the next section. The general idea is that a statistical average is defined in terms of Gaussian integrals over the Grassmann numbers, which are well-defined in the present algebra. Such integrals have the general form

$$Z\left[\bar{\chi},\chi\right] = \int\prod_{j=1}^{N}\left[d\bar{\psi}_j d\psi_j\right] e^{-\bar{\psi}_i\hat{A}_{ij}\psi_j + \bar{\psi}_j\chi_j + \bar{\chi}_j\psi_j} = \det\hat{A}\, e^{\bar{\chi}_i(\hat{A}^{-1})_{ij}\chi_j}, \tag{A.9}$$

where the sum is implied for any repeated indices, $\chi(\bar{\chi})$ is another Grassmann number, and $\hat{A}$ in any invertible complex matrix. This formula conveniently defines the well-known Wick theorem. In fact, we determine some special averages in the following way,

$$\langle\psi_a\bar{\psi}_b\rangle = \frac{1}{Z\left[0,0\right]}\frac{\delta^2 Z\left[\bar{\chi},\chi\right]}{\delta\chi_b\delta\bar{\chi}_a}\bigg/_{\chi=0} = A^{-1}_{ab} \tag{A.10a}$$

$$\langle\psi_a\psi_b\bar{\psi}_c\bar{\psi}_d\rangle = \frac{1}{Z\left[0,0\right]}\frac{\delta^4 Z\left[\bar{\chi},\chi\right]}{\delta\chi_d\delta\chi_c\delta\bar{\chi}_b\delta\bar{\chi}_a}\bigg/_{\chi=0} = -A^{-1}_{ac}A^{-1}_{bd} + A^{-1}_{ad}A^{-1}_{bc}, \tag{A.10b}$$

which is obtained by the anti-commutativity of the Grassmann numbers, derivation, and integration rules. In particular, we used that, for spinless particles, $a \neq b \neq c \neq$

d, otherwise the related expectation value evaluates to zero, according to the second relation in Eq.(A.2). In general, the Pauli exclusion principle forbids the simultaneous presence of two Grassmann numbers describing the same electron state. As we will see in the next section, the first term defines the propagator, i.e., the Green's function, while next-order terms describe more advanced diagrammatic calculations.

As a rule of thumb, the expectation value obtained through the Wick's theorem is obtained by considering all the permutations of the so-called *contractions* in the following way [222]:

$$\langle \psi_a \psi_b \bar{\psi}_c \bar{\psi}_d \rangle = \langle \psi_a \overbrace{\psi_b \bar{\psi}_c}^{} \bar{\psi}_d \rangle + \langle \overbrace{\psi_a \psi_b}^{} \bar{\psi}_c \bar{\psi}_d \rangle, \tag{A.11}$$

then, we move closer each couple, implying the change of sign due to the Grassmann algebra, and obtaining Eq.(A.10b).

The partition function

As we have shown in this thesis, the objective of any technique in statistical mechanics is to evaluate observables, which can be done by employing the density matrix operator, i.e., Eq.(4.49), and its time evolution is controlled by the Von Neumann equation, Eq.(4.54). As a result, the time-dependent density matrix can be expressed as

$$\hat{\rho}(t) = \hat{U}_{t,-\infty} \hat{\rho}(-\infty) \hat{U}_{-\infty,t}, \tag{A.12}$$

where $\hat{U}_{t,t'}$ is the time-evolution operator which obeys the following relations,

$$\partial_t \hat{U}_{t,t'} = -i\hat{H}(t)\hat{U}_{t,t'} \ , \quad \partial_{t'} \hat{U}_{t,t'} = i\hat{U}_{t,t'}\hat{H}(t'), \tag{A.13}$$

leading to the well-known relation

$$\hat{U}_{t,t'} = \mathbb{T} \exp(-i \int_{t'}^{t} \hat{H}(t) dt), \tag{A.14}$$

where $\mathbb{T}$ is the time-ordered product. The idea is now to rewrite Eq.(4.49) in terms of the time-evolution operator. In this way, the evaluation of an observable is conceptually carried out by letting the system evolve from a time $t = -\infty$, when the system is non-interacting and the density matrix is well-defined, to the time t, when the observable is evaluated, and then back again to $t = -\infty$. Simple manipulations yields

$$\langle \hat{O} \rangle (t) = tr\{\hat{U}_{-\infty,+\infty} \hat{U}_{+\infty,t} \hat{O} \hat{U}_{t,-\infty} \hat{\rho}(-\infty)\}. \tag{A.15}$$

The advantage of this rewriting is the possibility to define the partition function, a convenient object for the functional evaluation of the properties of many-particles systems, and describing the complete evolution in the so-called *closed time contour* $\mathcal{C}$, depicted in Fig.(A.1). The partition function is defined as

$$\mathcal{Z} = Tr\{\hat{U}_C \hat{\rho}(-\infty)\}, \tag{A.16}$$

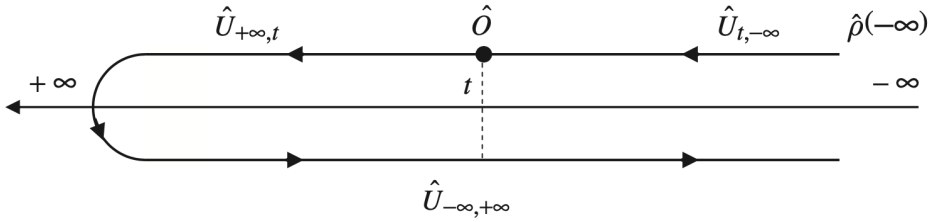

Figure A.1: Graphical visualization of the closed time contour, shown in Ref. [178]. The many-body system evolves from a non-interacting state at $t = -\infty$ to a time t, where the observable O is evaluated, to $t = \infty$ and then back again.

where $\hat{U}_C = \hat{U}_{-\infty,+\infty}\hat{U}_{+\infty,-\infty}$ is the closed time contour operator. We notice that if the Hamiltonian, embedded in $\hat{\rho}(-\infty)$, is the same in the two branches of the $\mathcal{C}$-path, then $\mathcal{Z}$ evaluates to one.

The observable is then inserted in the forward (or backward) branch by including an additional term in the Hamiltonian, i.e., the external field in Eq.(4.87),

$$\hat{H}_V^{\pm}(t) \equiv \hat{H}(t) \pm \hat{O}V(t), \tag{A.17}$$

where $+(-)$ refers to forward (backward) branch. Eq.(A.15) is then re-obtained by performing the functional derivative

$$\langle \hat{O} \rangle(t) = \frac{\mathrm{i}}{2}\frac{\delta \mathcal{Z}[V]}{\delta V(t)}\Big/_{V=0}. \tag{A.18}$$

The general procedure to follow in order to evaluate observable is now much clearer and obeys the following steps. In principle, we know the functional form of the partition function in terms of a generic Hamiltonian, the Green's function particularly, as we will see in the next section. Such form is, remarkably, a Gaussian integral. The observable is then included in the Hamiltonian by coupling it with a source term (e.g. density–scalar potential, current–vector potential). The statistical average of the observable is then simply obtained by performing functional derivatives of Gaussian integrals, shown in Eqs.(A.9) and (A.10).

The action

Our next big jump is the presentation of the many-body partition function in the continuum limit, defined as

$$Z = \int \mathcal{D}[\bar{\psi}\psi] e^{\mathrm{i}S(H)}, \tag{A.19}$$

where

$$\mathcal{D}[\bar{\psi}\psi] = \lim_{N\to\infty} \prod_{j=1}^{2N} [d\bar{\psi}_j d\psi_j] \tag{A.20}$$

denotes the integration over all paths and $S(H)$ is the *action*, the core of the functional method. For our porpoises, we can write the action as a sum of four terms,

$$S = S_0 + S_A + S_V + S_{\mathrm{dis}}, \tag{A.21}$$

where the first element encodes the bare Hamiltonian, the second and third describe the coupling with a vector and scalar potential, and the fourth includes random distributed impurities.

We begin by showing the procedure for deriving S_A, because of its relative generality and simplicity. The vector potential is coupled to the electric current as [171]

$$S_A = -\int d\mathbf{r} \int_{\mathcal{C}} dt\, \mathbf{A}(\mathbf{r},t)\cdot\mathbf{j}(\mathbf{r},t), \tag{A.22}$$

where $\mathbf{j} = \bar{\psi}(\mathbf{r},t)\,\mathbf{J}\,\psi(\mathbf{r},t)$ and $\mathbf{J} = e\partial H/\partial\mathbf{p}$ is the current operator in first quantization. We now rewrite the integral in such a way as to consider the extremes only belonging to the forward branch,

$$S_A \sim \int_{-\infty}^{+\infty} dt\, \left(\mathbf{A}^+\cdot\bar{\psi}^+\,\mathbf{J}\,\psi^+ + \mathbf{A}^-\cdot\bar{\psi}^-\,\mathbf{J}\,\psi^-\right), \tag{A.23}$$

where $\psi^{+(-)}$ is the Grassmann number in the forward (backward) branch, and, in general, it is a spinor. We now define the so-called *Keldysh rotation*,

$$\begin{cases} \psi_1 = \frac{1}{\sqrt{2}}(\psi^+ + \psi^-) \\ \psi_2 = \frac{1}{\sqrt{2}}(\psi^+ - \psi^-) \end{cases}, \tag{A.24a}$$

$$\begin{cases} \bar{\psi}_1 = \frac{1}{\sqrt{2}}(\bar{\psi}^+ - \bar{\psi}^-) \\ \bar{\psi}_2 = \frac{1}{\sqrt{2}}(\bar{\psi}^+ + \bar{\psi}^-) \end{cases}, \tag{A.24b}$$

which finally leads to

$$S_A = -\frac{1}{2}\int dt\, d\mathbf{r}\left[\mathbf{A}^{\mathrm{cl}}\cdot\left(\bar{\psi}_1\mathbf{J}\psi_1 + \bar{\psi}_2\mathbf{J}\psi_2\right) + \mathbf{A}^{\mathrm{q}}\cdot\left(\bar{\psi}_1\mathbf{J}\psi_2 + \bar{\psi}_2\mathbf{J}\psi_1\right)\right], \tag{A.25}$$

where $\mathbf{A}^{\mathrm{cl(q)}} = \frac{1}{2}\left(\mathbf{A}^+ \pm \mathbf{A}^-\right)$ is called classical (quantum) vector field; while a classical field has the same form in both $\mathcal{C}$-branches, the same does not hold for the quantum version. Also, the field operators are now 2D vectors in the Keldysh space, i.e., $\mathbf{\Psi} = (\psi_1, \psi_2)$. The fields coupled to the quantum vector potential are proportional to $\sim \bar{\psi}^+\psi^+ + \bar{\psi}^-\psi^-$, which therefore is the *physical* current density. On the contrary, the classical vector potential is coupled to the *quantum* current density, which has no physical meaning [178]. As a small remark, in the absence of external fields, nonequilibrium currents can still be present due, for example, to gradients of temperature and carriers' concentrations. In this case, the physical current operator is still coupled to the quantum vector potential, while the classical counterpart is equal to zero.

The scalar action has an identical form,

$$S_V = -\frac{1}{2}\int dt\, d\mathbf{r}\left[V^{\mathrm{cl}}\left(\bar{\psi}_1 P\psi_1 + \bar{\psi}_2 P\psi_2\right) + V^{\mathrm{q}}\left(\bar{\psi}_1 P\psi_2 + \bar{\psi}_2 P\psi_1\right)\right]. \tag{A.26}$$

On the other hand, the disorder action does not describe the coupling between an observable and an external field and it is therefore purely classical,

$$S_{\mathrm{dis}} = \int dt\, d\mathbf{r}\, V_{\mathrm{dis}}(\mathbf{r})\bar{\psi}_a(\mathbf{r},t)\psi_a(\mathbf{r},t), \tag{A.27}$$

where V_{dis} is the disorder potential.

Finally, we are ready to present S_0, describing the clean system,

$$S_0 = \int dt\, d\mathbf{r}\, dt'\, d\mathbf{r}'\, \bar{\psi}_a(\mathbf{r},t)[\hat{G}^{-1}]^{ab}(\mathbf{r}-\mathbf{r}',t-t')\psi_b(\mathbf{r}',t'), \tag{A.28}$$

where

$$\hat{G} = \begin{pmatrix} G^R & G^K \\ 0 & G^A \end{pmatrix}, \tag{A.29a}$$

$$\hat{G}^{-1} = \begin{pmatrix} (G^R)^{-1} & (G^K)^{-1} \\ 0 & (G^A)^{-1} \end{pmatrix}, \tag{A.29b}$$

are Green's function in the 2×2 Keldysh space, in particular

$$(G^{R(A)})^{-1}(\mathbf{r},\mathbf{r}';t,t') = \left(\mathrm{i}\partial_t - H(\mathbf{r}) \pm \mathrm{i}0^+\right)\delta(\mathbf{r}-\mathbf{r}',t-t') \tag{A.30}$$

is the retarded (advanced) Green's function, and

$$G^K = (1-2f(\epsilon))(G^R - G^A), \tag{A.31}$$

is the Keldysh propagator, with $f(\epsilon)$ being the Fermi-Dirac distribution function at equilibrium. To conclude, we write the bare action S_0 in reciprocal space, defining the Green's functions in terms of energy and momentum. The real-space field operators, in the standard basis [223], are defined as $\psi(\bar{\psi})(\mathbf{r},t) = \int d\mathbf{k}\, e^{\pm \mathrm{i}\mathbf{k}\mathbf{r}}\, e^{\mp \mathrm{i}\epsilon t}\psi(\bar{\psi})(\mathbf{p},\epsilon)$, therefore Eq.(A.28) can be rewritten as

$$\begin{aligned} S_0 = \int dt dt' d\mathbf{r} d\mathbf{r}' \int d\mathbf{p}_1 d\mathbf{p}_2 d\epsilon_1 d\epsilon_2 \\ \bar{\psi}_a(\mathbf{p}_1,\epsilon_1)e^{-\mathrm{i}\mathbf{k}_1\mathbf{r}}e^{\mathrm{i}\epsilon_1 t}[\hat{G}^{-1}]^{ab}(\mathbf{r}-\mathbf{r}',t-t')e^{\mathrm{i}\mathbf{k}_2\mathbf{r}'}e^{\mathrm{i}\epsilon_2 t'}\psi_b(\mathbf{p_2},\epsilon_2). \end{aligned} \tag{A.32}$$

Applying the Green's function operator and evaluating the integrals, we finally obtain

$$S_0 = \int d\epsilon\, d\mathbf{p}\, \bar{\psi}_a(\mathbf{p},\epsilon)[\hat{G}^{-1}]^{ab}(\mathbf{p},\epsilon)\psi_b(\mathbf{p},\epsilon), \tag{A.33}$$

where

$$(G^{R(A)})^{-1}(\mathbf{p},\epsilon) = \left(\epsilon - H(\mathbf{p}) \pm \mathrm{i}0^+\right). \tag{A.34}$$

Now that we have delineated the partition function's structure in the presence of disorder, vector, and scalar fields, we can evaluate statistical averages of observables under the effect of such interactions. In particular, as we will show in the following sections, we can derive the diagrammatic expansion of dressed Green's functions, which are renormalized by the disorder potential and the charge/spin density/current response to external perturbations, the Kubo formula.

Dressed Green's function

We now explain the procedure to find renormalized propagators in the presence of disorder, resulting in the diagrammatic expansion presented in Chap.(4). The form of the statistical average of two field operators is controlled by the Gaussian integral, Eq.(A.10), where the generic invertible matrix $\hat{A}_{ij}$ is replaced by the action $\mathrm{i}S(H)$, Eq.(A.21). Particularly, in the obsence of any interaction, we have that

$$\langle \psi_a(\mathbf{x})\bar{\psi}_b(\mathbf{x}')\rangle_{S_0} = \mathrm{i}\, G^{ab}(\mathbf{x}-\mathbf{x}'), \tag{A.35}$$

where $\mathbf{x} = (\mathbf{r}, t)$, $ab = 11(22)$ returns the retarded (advanced) clean Green's function, and $ab = 12$ produces the Keldysh component of the propagator. The bracket $\langle ... \rangle_S$ denotes the type of action included in the partition function. The corresponding operator in momentum space is obtained by performing a Fourier transform, e.g., $\int d(\mathbf{x}-\mathbf{x}') e^{\mathrm{i}(\mathbf{x}-\mathbf{x}')\mathbf{g}}(-\mathrm{i})\langle \psi_a(\mathbf{x})\bar{\psi}_b(\mathbf{x}')\rangle$, with $\mathbf{g}$ being the four-momentum. Writing the field operators in momentum representation, and using the Gaussian integrals with respect to the reciprocal bare action, Eq.(A.33), we obtain,

$$\langle \psi_a(\mathbf{g})\bar{\psi}_b(\mathbf{g})\rangle_{S_0} = \mathrm{i}\, G^{ab}(\mathbf{g}), \tag{A.36}$$

where $G^{ab}(\mathbf{g})$ is the inverse of Eq.(A.34).

The disorder is included by considering the interaction S_{dis}, which, for simplicity, we expand up to the second order in the weak impurity potential regime and consider to be scalar. Also, we examine, without loss of generality, the retarded dressed propagator $\mathcal{G}(\mathbf{x}-\mathbf{x}')$. Under these assumption, the average of two field operators becomes

$$\begin{aligned}\langle \psi_1(\mathbf{x})\bar{\psi}_1(\mathbf{x}')\rangle_{S_0+S_{\mathrm{dis}}} \sim \langle \psi_1(\mathbf{x})\bar{\psi}_1(\mathbf{x}')\rangle_{S_0} + \int d\mathbf{x}'' V_{\mathrm{dis}}(\mathbf{r}'')\langle \psi_1(\mathbf{x})\psi_a(\mathbf{x}'')\bar{\psi}_1(\mathbf{x}')\bar{\psi}_a(\mathbf{x}'')\rangle_{S_0} \\ - \frac{1}{2}\int d\mathbf{x}'' d\mathbf{x}''' V_{\mathrm{dis}}(\mathbf{r}'')V_{\mathrm{dis}}(\mathbf{r}''')\langle \psi_b(\mathbf{x}''')\psi_a(\mathbf{x}'')\psi_1(\mathbf{x})\bar{\psi}_b(\mathbf{x}''')\bar{\psi}_a(\mathbf{x}'')\bar{\psi}_1(\mathbf{x}')\rangle_{S_0},\end{aligned} \tag{A.37}$$

which can be decomposed in terms of propagators using the Wick's theorem, taking also into account the average

$$\begin{aligned}\langle \psi_a\psi_b\psi_c\bar{\psi}_d\bar{\psi}_e\bar{\psi}_f\rangle = A^{-1}_{af}A^{-1}_{be}A^{-1}_{cd} - A^{-1}_{ae}A^{-1}_{bf}A^{-1}_{cd} - A^{-1}_{af}A^{-1}_{bd}A^{-1}_{ce} \\ + A^{-1}_{ae}A^{-1}_{bd}A^{-1}_{cf} + A^{-1}_{ad}A^{-1}_{bf}A^{-1}_{ce} - A^{-1}_{ad}A^{-1}_{be}A^{-1}_{cf}.\end{aligned} \tag{A.38}$$

The second term in Eq.(A.37), that we call $\mathcal{G}^{(1)}$, becomes

$$\mathcal{G}^{(1)}(\mathbf{x}-\mathbf{x}') = n_i V \int d\mathbf{x}'' G^R(\mathbf{x}'-\mathbf{x}'')G^R(\mathbf{x}''-\mathbf{x}), \tag{A.39}$$

where we performed the disorder average $\langle V(\mathbf{x}'')\rangle_{\mathrm{dis}} = n_i V$ and, in momentum space, we finally obtain

$$\mathcal{G}^{(1)}(\mathbf{p},\epsilon) = n_i V G^R(\mathbf{p},\epsilon)G^R(\mathbf{p},\epsilon). \tag{A.40}$$

We stress that the disorder average must be performed *after* the Wick's decomposition of the statistical average [222, 171, 178]. The third term requires some more work, but eventually can be rewritten as

$$\mathcal{G}^{(2)}(\mathbf{x}-\mathbf{x}') = -\int d\mathbf{x}''d\mathbf{x}''' \\ G^R(\mathbf{x}'-\mathbf{x}'')V(\mathbf{r}'')G^R(\mathbf{x}''-\mathbf{x}''')V(\mathbf{r}''')G^R(\mathbf{x}'''-\mathbf{x}), \tag{A.41}$$

describing the double insertion of an impurity potential in a single propagator. We now use the single scattering impurity potential distribution, $\langle V(\mathbf{r}'')V(\mathbf{r}''')\rangle = n_i V^2 \delta(\mathbf{x}''-\mathbf{x}''')$, and perform the Fourier transform in momentum and energy space, finding

$$\mathcal{G}^{(2)}(\mathbf{q},\epsilon) = G^R(\mathbf{q},\epsilon)\left(n_i V^2 \int d\mathbf{p}\, G^R(\mathbf{p},\epsilon)\right) G^R(\mathbf{q},\epsilon), \tag{A.42}$$

which represents the leading order rainbow diagram in first Born approximation. The mathematical object inside brackets, which contains information about the disordered averaged impurity potential, is an *irreducible* diagram because it cannot be split into two disconnected diagrams when a line is cut. This means that all the diagrams with several impurity insertions of the same form can be rearranged into a *Dyson equation*. The special object above takes the name of *self-energy* [178], in which we can sum the first-order contribution in Eq.(A.40). The renormalized Green's function becomes

$$\mathcal{G}^{R(A)}_{\mathrm{FBA}}(\mathbf{q},\epsilon) = \frac{1}{(G^{R(A)})^{-1} - \Sigma^{R(A)}_{\mathrm{FBA}}}, \tag{A.43}$$

where $\Sigma^{R(A)}_{\mathrm{FBA}} = n_i V + n_i V^2 \int d\mathbf{p}\, G^{R(A)}(\mathbf{p},\epsilon)$. Following the same idea but with different single-scattering statistics, i.e., non-Gaussian, we would recover the T-matrix approximation, which simply generates a different self-energy.

This section showed how to renormalize the free propagator in the presence of disorder by using simple expansions of the coupling action and Wick's theorem. The following section applies the same technique to find the system's response function to external perturbations, in which the disorder average dresses both the propagators and the vertices.

The Kubo-Streda formula

In this section, we derive the Kubo-Streda formula in disordered systems using the functional approach. For simplicity, we specialize in the current-current response function, i.e., the conductivity, also considering a diagonal current operator.

From the definition of partition function, including the vector potential action s_A, we see that the i-th component of the statistically-averaged current is the functional derivative with respect to A^{q}_i

$$\langle J\rangle = \frac{\delta Z}{\delta A^q_i}\bigg/_{A^q_i=0} = \int \mathcal{D}[\psi\bar{\psi}] e^{\mathrm{i}(S_0+S_{\mathrm{dis}})} e^{\mathrm{i}S_{A^{\mathrm{cl}}}} (\bar{\psi}_1(\mathbf{x})J_i(\mathbf{x})\psi_2(\mathbf{x}) + \bar{\psi}_2(\mathbf{x})J_i(\mathbf{x})\psi_1(\mathbf{x})), \tag{A.44}$$

where $\mathrm{i}S_{A^{\mathrm{cl}}}$ is the vector potential action including only the classical field.

In the linear response theory, A^{cl} is considered to be weak, thus the exponential can be expanded linearly in the classical field,

$$\langle J\rangle = \mathrm{i}\int d\mathbf{x}'\int \mathcal{D}[\psi\bar{\psi}]e^{\mathrm{i}(S_0+S_{\mathrm{dis}})}(\bar{\psi}_1(\mathbf{x})J_i(\mathbf{x})\psi_2(\mathbf{x})+\bar{\psi}_2(\mathbf{x})J_i(\mathbf{x})\psi_1(\mathbf{x})) \tag{A.45}$$

$$\times(\bar{\psi}_1(\mathbf{x}')J_j(\mathbf{x}')\psi_1(\mathbf{x}')+\bar{\psi}_2(\mathbf{x}')J_j(\mathbf{x}')\psi_2(\mathbf{x}'))A_j^{\mathrm{cl}}(\mathbf{x}'), \tag{A.46}$$

where we assumed that the current is zero at equilibrium. The object inside the functional integral, containing the field operators, is therefore the response function R_{ij}, as shown in Eq.(4.94). The conductivity and the response function are related as $\sigma^{ij}(\omega,\mathbf{q})=\mathrm{R}^{ij}(\omega,\mathbf{q})/\mathrm{i}\omega$, thus the current-current Kubo formula can be defined as

$$\sigma_{ij}=\frac{1}{i\omega}\frac{1}{2\pi\mathrm{i}}\left.\frac{\delta Z[A^{cl},A^q]}{\delta A_j^{cl}\delta A_i^q}\right|_{A=0}, \tag{A.47}$$

and our aim is now to find its explicit expression.

The functional derivative in the clean system, i.e., zeroth order of the disorder action, produces only two terms different from zero,

$$\mathrm{R}_{ij}(\mathbf{x}'-\mathbf{x})=-\frac{e^2}{2\mathrm{i}\pi}\,\mathrm{v}_i(\mathbf{x})\mathrm{v}_j(\mathbf{x}') \tag{A.48}$$

$$\times\left[\langle\psi_1(\mathbf{x})\psi_1(\mathbf{x}')\bar{\psi}_2(\mathbf{x})\bar{\psi}_1(\mathbf{x}')\rangle+\langle\psi_1(\mathbf{x})\psi_2(\mathbf{x}')\bar{\psi}_2(\mathbf{x})\bar{\psi}_2(\mathbf{x}')\rangle\right],$$

where $\mathbf{v}(\mathbf{x})=-\frac{\mathrm{i}}{m}\boldsymbol{\nabla}$ acts only on the *annihilation* fields. Using the the Wick's contraction theorem and considering only connected diagrams, we find

$$\mathrm{R}_{ij}(\mathbf{x}'-\mathbf{x})=\frac{e^2}{2m^2\mathrm{i}}\left[\partial_{x_i}G^R(\mathbf{x}'-\mathbf{x})\partial_{x_j'}G^K(\mathbf{x}-\mathbf{x}')+\partial_{x_i}G^K(\mathbf{x}'-\mathbf{x})\partial_{x_j'}G^A(\mathbf{x}-\mathbf{x}')\right]. \tag{A.49}$$

As shown in this thesis, it is more convenient to work in the reciprocal space; we thus perform a Fourier transformation of the response function and then looking for the dynamic limit, i.e., $\mathbf{q}\to 0$, where $\mathbf{q}$ is the external momentum. Also, we neglect contributions from products of Green's functions of the same sector since they contribute at the next order in the presence of disorder. We finally find

$$\sigma_{ij}(\mathbf{q},\omega)=\frac{-e^2}{2\pi m^2\omega}\int d\omega_1 d\mathbf{p_1}\,p_{1i}\,p_{1j} \tag{A.50}$$

$$\left[F(\omega_1-\omega)G^R(\mathbf{p}_1,\omega_1)G^A(\mathbf{p}_1,\omega_1-\omega)-F(\omega_1)G^R(\mathbf{p}_1,\omega_1)G^A(\mathbf{p}_1,\omega_1-\omega)\right].$$

Assuming small external frequencies, we can expand each term inside the squared brackets linearly in ω. The zeroth order, which results in a divergent conductivity $\sim 1/\omega$, cancels out with the diamagnetic term [171], and the remaining contribution is therefore constant in the frequency,

$$\sigma_{ij}=\frac{e^2}{2\pi m^2}\int d\epsilon\,d\mathbf{p}\,p_i\,p_j\,\partial_\epsilon F(\epsilon)G^R(\mathbf{p},\epsilon)G^A(\mathbf{p},\epsilon), \tag{A.51}$$

which is the surface contribution response shown in Eq.(4.109), i.e., the bubble diagram.

We follow the same procedure to find the conductivity in the presence of random impurities, after expanding the disorder action up to the desired order. For simplicity, we show only the second order, where we get

$$\mathrm{R}^{(2)}_{ij}(\mathbf{x}'-\mathbf{x}) = \int d\mathbf{x}''d\mathbf{x}'''\langle V_{\mathrm{dis}}(\mathbf{r}'')V_{\mathrm{dis}}(\mathbf{r}''')\bar{\psi}_a(\mathbf{x}'')\psi_a(\mathbf{x}'')\bar{\psi}_b(\mathbf{x}''')\psi_b(\mathbf{x}''') \\ \big(\bar{\psi}_1(\mathbf{x})J_i(\mathbf{x})\psi_2(\mathbf{x}) + \bar{\psi}_2(\mathbf{x})J_i(\mathbf{x})\psi_1(\mathbf{x})\big) \\ \big(\bar{\psi}_1(\mathbf{x}')J_j(\mathbf{x}')\psi_1(\mathbf{x}') + \bar{\psi}_2(\mathbf{x}')J_j(\mathbf{x}')\psi_2(\mathbf{x}')\big)\rangle. \quad \text{(A.52)}$$

We continue following the same procedure applied in the former section which is, essentially, the implementation of the Wick's theorem. Already at this initial stage, we already obtain many diagrams with different impurity insertions. Neglecting crossed diagrams, which provide small quantum corrections to the leading order of the semiclassical response [51], we obtain

$$\sigma^{(2)}_{ij} = \frac{e^2}{2\pi m^2}\int d\epsilon\, d\mathbf{p}\partial_\epsilon F(\epsilon)\Big(p_i\, G^R(\mathbf{p},\epsilon)p_j G^A(\mathbf{p},\epsilon) + p_i\,(\mathcal{G}^R)^{(2)}(\mathbf{p},\epsilon)p_j G^A(\mathbf{p},\epsilon) + \\ p_i\, G^R(\mathbf{p},\epsilon)p_j(\mathcal{G}^A)^{(2)}(\mathbf{p},\epsilon) + \tilde{p}^{(2)}_i\, G^R(\mathbf{p},\epsilon)p_j G^A(\mathbf{p},\epsilon)\Big), \quad \text{(A.53)}$$

where the first terms is the bare response, the second and third contributions are the second-order dressed Green's functions in the retarded and advanced sector, and the fourth is the first impurity contribution to the Bethe-Salpeter equation, $\tilde{p}^{(2)}_i = n_i V^2 G^R p_i G^A$. Next-order impurity insertions, that is further expansions of the disorder action, construct the complete Bethe-Salpeter for the vertex-renormalization equation, Eq.(4.108), and the dressed conductivity becomes

$$\sigma_{ij} = \frac{e^2}{2\pi m^2}\int d\epsilon\, d\mathbf{p}\,\tilde{p}_i\, p_j\,\partial_\epsilon F(\epsilon)\mathcal{G}^R(\mathbf{p},\epsilon)\mathcal{G}^A(\mathbf{p},\epsilon), \quad \text{(A.54)}$$

which is a particular case of Eq.(4.109).

This appendix concisely presented the functional Green's function method technology to evaluate the response of a generic perturbed system, narrowing down on the effect of external electric fields. However, far from being exhaustive, our analysis ignored the breadth of possibilities that such methodology can offer but provides the basic technique that can be applied to any generic problem. The knowledge of the possible interactions in play, and therefore the form of the action, is everything we need to construct the related diagrammatics, thus the response function. It is possible, for example, to derive extensions of the Landauer formula in quantum point contacts, study superconductivity, include weak localization effects, or decorate the conductivity tensor derived above with electron-phonon, electron-electron, and electron-photon interactions.

Appendix B

Graphene extrinsic SOC diffusion coefficients

The coefficients in Eq.(5.7, 5.8 and 5.9), that we used to write explicitly Eq.(5.10 and 5.13) for the standard Rashba case, are shown in the following table:

(inverse) ASP conversion	$\mathbf{\Psi}^{\mu}$	$\Psi^{x}_{x} = \Psi^{y}_{y} = \alpha_{\mathrm{ASP}}$
	$\mathbf{\Gamma}^{\nu}$	$I^{0}_{x(y)} = -\alpha_{\mathrm{IASP}}$
Spin density precession	$\mathbf{R}^{\mu\nu}$	$R^{x(y)z}_{x(y)} = -R^{zx(y)}_{x(y)} = -\alpha_{\mathrm{R}}$
Spin current swapping and spin Hall	$\mathbf{\Gamma}^{\nu\sigma}$	$\Gamma^{xy}_{x(y)} = -\beta^{xx(y)}_{\mathrm{SW}}$, $\Gamma^{yx}_{x(y)} = +\beta^{xy(x)}_{\mathrm{SW}}$, $\Gamma^{0z}_{x(y)} = \beta_{\mathrm{IsH}}$, $\Gamma^{z0}_{x(y)} = \beta^{\mathrm{AASP}}_{\mathrm{sH}}$
	$\mathbf{\Omega}^{\nu\sigma}$	$\Omega^{xy}_{x(y)} = \beta^{xx}_{\omega\mathrm{SW}}$, $\Omega^{yx}_{x(y)} = -\beta^{xx}_{\omega\mathrm{SW}}$, $\Omega^{0z}_{x(y)} = -\beta_{\omega\mathrm{IsH}}$, $\Omega^{z0}_{x(y)} = -\beta_{\omega\mathrm{sH}}$
(Spin) current transfer	$D^{\nu\mu\sigma}_{A(B)}$	$D^{0xx}_{A} = D^{0yy}_{A} = D_1$, $D^{zyx}_{A} = -D^{zxy}_{A} = D^{z}_{1}$, $D^{0yx}_{B} = -D^{0xy}_{B} = -D_2$, $D^{zxx}_{B} = D^{zyy}_{B} = -D^{z}_{2}$
	$D^{\nu\mu\sigma i}_{C}$	$D^{xx0x}_{C} = D^{yy0y}_{C} = -D_4$, $D^{xx0y}_{C} = D^{yy0x}_{C} = +D_3$, $-D^{yxzx}_{C} = D^{xyzy}_{C} = D_6$, $D^{yxzy}_{C} = -D^{xyzx}_{C} = -D_5$
	$D^{\nu\mu\sigma i}_{D}$	$D^{xxzx}_{D} = D^{yyzy}_{D} = D_5$, $D^{xxzy}_{D} = D^{yyzx}_{D} = D_6$, $-D^{yx0x}_{D} = D^{xy0y}_{D} = -D_3$, $D^{yx0y}_{D} = -D^{xy0x}_{D} = -D_4$
	$D_{\mu\nu}$	$D_{x(y)0} = D$, $D_{x(y)z} = D_z$, $D_{xy} = D_{yx}$, $D_{xx} = D_{yy}$
Relaxation times	$\mathcal{T}^{\mu\nu}$	$\mathcal{T}^{00} = 0$, $\mathcal{T}^{0x(y)} = 1/\tau_{\parallel}$, $\mathcal{T}^{0z} = 1/\tau_{\perp}$, $\mathcal{T}^{x(y)0} = 1/\tau_{J\parallel}$, $\mathcal{T}^{x(y)z} = 1/\tau_{J\perp}$, $\mathcal{T}^{xy(yx)} = 1/\tau_{Jxy}$, $\mathcal{T}^{xx(yy)} = 1/\tau_{Jxx}$

where we only listed the nonzero components, and we droped the superscript "ISOS" in the related coupling constant. The change of signs in the Rashba extrinsic SOC for hollow impurities, yields the following changes:

(inverse) ASP conversion	$\mathbf{\Psi}^{\mu}$	$\Psi^{x}_{x} = -\Psi^{y}_{y} = \alpha_{ASP}$
	$\mathbf{I}^{\nu}$	$-I^{0}_{x} = I^{0}_{y} = -\alpha_{IASP}$
Spin density precession	$\mathbf{R}^{\mu\nu}$	$R^{xz}_{x} = -R^{yz}_{y} = -R^{zx}_{x} = R^{zy}_{y} = -\alpha_{R}$
(Time dependent) Spin current swapping and spin Hall	$\mathbf{\Gamma}^{\nu\sigma}$	$\Gamma^{xy}_{x(y)} = \beta^{xx(y)}_{SW}$, $\Gamma^{yx}_{x(y)} = -\beta^{xy(x)}_{SW}$, $\Gamma^{0z}_{x(y)} = -\beta_{ISh}$, $\Gamma^{z0}_{x(y)} = -\beta_{Sh}$
	$\mathbf{\Omega}^{\nu\sigma}$	$\Omega^{xy}_{x(y)} = -\beta^{xx}_{\omega SW}$, $\Omega^{yx}_{x(y)} = \beta^{xx}_{\omega SW}$, $\Omega^{0z}_{x(y)} = \beta_{\omega ISh}$, $\Omega^{z0}_{x(y)} = \beta_{\omega Sh}$
(Spin) Current stransfer	$D^{\nu\mu\sigma}_{A(B)}$	$D^{0xx}_{A} = D^{0yy}_{A} = D_1$, $D^{zyx}_{A} = -D^{zxy}_{A} = D^{z}_{1}$, $D^{0yx}_{B} = -D^{0xy}_{B} = -D_2$, $D^{zxx}_{B} = D^{zyy}_{B} = -D^{z}_{2}$
	$D^{\nu\mu\sigma i}_{C}$	$-D^{xx0x}_{C} = D^{yy0y}_{C} = -D_4$, $-D^{xx0y}_{C} = D^{yy0x}_{C} = +D_3$, $D^{yxzx}_{C} = D^{xyzy}_{C} = D_6$, $-D^{yxzy}_{C} = -D^{xyzx}_{C} = -D_5$
	$D^{\nu\mu\sigma i}_{D}$	$D^{xxzx}_{D} = -D^{yyzy}_{D} = D_5$, $D^{xxzy}_{D} = -D^{yyzx}_{D} = D_6$, $-D^{yx0x}_{D} = -D^{xy0y}_{D} = -D_3$, $D^{yx0y}_{D} = D^{xy0x}_{D} = -D_4$
	$D_{\mu\nu}$	$D_{x(y)0} = D$, $D_{x(y)z} = D_z$, $D_{xy} = D_{yx}$, $D_{xx} = D_{yy}$
Relaxation times	$\mathcal{T}^{\mu\nu}$	$\mathcal{T}^{00} = 0$, $\mathcal{T}^{0x(y)} = 1/\tau_{\parallel}$, $\mathcal{T}^{0z} = 1/\tau_{\perp}$, $\mathcal{T}^{x(y)0} = 1/\tau_{J\parallel}$, $\mathcal{T}^{x(y)z} = 1/\tau_{J\perp}$, $\mathcal{T}^{xy(yx)} = 1/\tau_{Jxy}$, $\mathcal{T}^{xx(yy)} = 1/\tau_{Jxx}$

Here we provide some results in two key scenarios: for $u_{KM} < u_R < u_0 < 1$ (limit I) and $u_0 = u_{KM} = 0$,$u_R < 1$ (limit II). In limit I we find

Relaxation times	$1/\tau = \frac{n\epsilon u_0^2}{2\mathrm{v}^2}$, $1/\tau_{\parallel} = \frac{n\epsilon u_R^2}{\mathrm{v}^2}$, $1/\tau_{\perp} = \frac{2nu_R^2\epsilon}{\mathrm{v}^2}$, $\frac{1}{\tau_{J_{\parallel}}} = \frac{1}{2\tau}$, $\frac{1}{\tau_{J_{\perp}}} = \frac{1}{\tau_{J_{\parallel}}}$, $\frac{1}{\tau_{Jxx}} = \frac{1}{\tau_{J_{\parallel}}}$, $\frac{1}{\tau_{Jxy}} = \frac{1}{\tau_{J_{\parallel}}}$
(Spin) Current stransfer	$D = D_z = D_{xx} = D_{xy} = \mathrm{v}^2\tau$, $D_1 = \frac{8u_R\mathrm{v}^3}{nu_0^3\epsilon}$, $D_2 = \frac{64u_R^3\mathrm{v}^7}{nu_0^7\epsilon^3}$, $D_1^z = \frac{64u_R^3\mathrm{v}^9}{nu_0^8\epsilon^4}$, $D_2^z = \frac{8u_R\mathrm{v}^5}{nu_0^4\epsilon^2}$, $D_3 = \frac{2u_R\mathrm{v}^3}{nu_0^3\epsilon}$, $D_4 = \frac{16u_R^3\mathrm{v}^7}{nu_0^7\epsilon^3}$, $D_5 = \frac{8u_R\mathrm{v}^5}{nu_0^4\epsilon^2}$, $D_6 = \frac{64u_R^3\mathrm{v}^9}{nu_0^8\epsilon^4}$
(Time dependent) Spin current swapping and spin Hall	$\alpha_{\mathrm{R}} = \frac{2nu_R}{\mathrm{v}}$, $\alpha_{\mathrm{ASP}} = \frac{nu_{KM}u_R\epsilon}{\mathrm{v}^3}$, $\alpha_{\mathrm{IASP}} = \frac{8u_{KM}u_R\mathrm{v}}{u_0^2}$, $\beta_{\omega\mathrm{IsH}} = 4\beta_{\omega\mathrm{sH}} = \frac{32u_R^2\mathrm{v}^4}{nu_0^5\epsilon^2}$, $\beta_{\mathrm{IsH}} = 4\beta_{\mathrm{sH}} = \beta_{\omega\mathrm{IsH}}\frac{1}{\tau}$, $\alpha_{\mathrm{zR}} = \frac{4u_R\mathrm{v}^3}{u_0^2\epsilon}$, $\beta^{xx}_{\omega\mathrm{SW}} = \frac{16u_R^2\mathrm{v}^6}{nu_0^6\epsilon^3}$, $\beta^{xx}_{\mathrm{SW}} = \beta^{xy}_{\mathrm{SW}} = \beta^{xx}_{\omega\mathrm{SW}}\frac{1}{\tau}$, $\alpha_{\mathrm{xyR}} = \frac{4\mathrm{v}^3u_R}{\epsilon u_0^2}$

In this limit, some terms match, including β_{sH} and β_{IsH}. In limit II we get

Relaxation times	$1/\tau = \frac{n\epsilon u_R^2}{\mathrm{v}^2}$, $1/\tau_\parallel = \frac{n\epsilon u_R^2}{\mathrm{v}^2}$, $1/\tau_\perp = \frac{2nu_R^2\epsilon}{\mathrm{v}^2}$, $\frac{1}{\tau_{J_\parallel}} = \frac{1}{\tau}$, $\frac{1}{\tau_{J_\perp}} = -\frac{1}{\tau_{Jx}}$, $\frac{1}{\tau_{Jxx}} = \frac{2}{3\tau}$
(Spin) Current stransfer	$D = \frac{1}{2}\mathrm{v}^2\tau$, $D_{xx} = \frac{1}{4}\mathrm{v}^2\tau$, $D_{xy} = \frac{1}{2}\mathrm{v}^2\tau$, $D_z = \frac{\epsilon}{4n}$ $D_1 = 0$, $D_2 = 0$ $D_2^z = 2D_1^z = \frac{u_R\epsilon^2}{8n\mathrm{v}^3}$, $D_3 = 0$, $D_4 = 0$, $D_5 = -\frac{\mathrm{v}}{4nu_R}$, $D_6 = \frac{\mathrm{v}^5}{2nu_R^3\epsilon^2}$
Spin current swapping and spin Hall	$\alpha_R = \frac{2nu_R}{\mathrm{v}}$, $\alpha_{\mathrm{ASP}} = 0$, $\alpha_{\mathrm{IASP}} = 0$, $\beta_{\omega\mathrm{sH}} = \beta_{\omega\mathrm{IsH}} = 0$, $\beta_{\mathrm{sH}} = -\beta_{\mathrm{IsH}} = 0$, $\alpha_{zR} = \frac{\mathrm{v}^3}{u_R\epsilon}$, $\beta_{\omega SW}^{xy} = 2\beta_{\omega SW}^{xx} = \frac{\mathrm{v}^2}{4nu_R^2\epsilon}$, $\beta_{\mathrm{SW}}^{xx} = \frac{u_R^2\epsilon^2}{8\mathrm{v}^4}$, $\beta_{\mathrm{SW}}^{xy} = 1$, $\alpha_{xyR} = \frac{\epsilon u_R}{2\mathrm{v}}$

The Diffuson Hamiltonian (Eq.(**??**)) describing our system in FBA and expressed in an implicit form in Eq.(5.7, 5.8 and 5.9), reads (here we only show the standard Rashba case):

$$H_D = \begin{pmatrix} H_{11}^D & H_{12}^D & H_{13}^D \\ H_{21}^D & H_{22}^D & H_{23}^D \\ H_{31}^D & H_{32}^D & H_{33}^D \end{pmatrix} \tag{B.1}$$

where

$$H_{11}^D = \partial_t \mathbb{I} + \begin{pmatrix} 0 & 0 & 0 & 0 \\ 0 & \frac{1}{\tau_\parallel} & 0 & 0 \\ 0 & 0 & \frac{1}{\tau_\parallel} & 0 \\ 0 & 0 & 0 & \frac{1}{\tau_\perp} \end{pmatrix}, \qquad H_{12}^D = \partial_x \mathbb{I} + \begin{pmatrix} 0 & 0 & 0 & 0 \\ 0 & 0 & 0 & -\alpha_{\mathrm{R}} \\ \alpha_{\mathrm{ASP}} & 0 & 0 & 0 \\ 0 & \alpha_{\mathrm{R}} & 0 & 0 \end{pmatrix}, \tag{B.2}$$

$$H_{13}^D = \partial_y \mathbb{I} + \begin{pmatrix} 0 & 0 & 0 & 0 \\ -\alpha_{\mathrm{ASP}} & 0 & 0 & 0 \\ 0 & 0 & 0 & -\alpha_{\mathrm{R}} \\ 0 & 0 & \alpha_{\mathrm{R}} & 0 \end{pmatrix}, \qquad H_{21}^D = \begin{pmatrix} D\partial_x & 0 & \alpha_{\mathrm{IASP}} & 0 \\ 0 & D_{xx}\partial_x & 0 & -\alpha_{\mathrm{zR}} \\ 0 & 0 & D_{xy}\partial_x & 0 \\ 0 & \alpha_{\mathrm{xyR}} & 0 & D_z\partial_x \end{pmatrix}, \tag{B.3}$$

$$H_{22}^D = \begin{pmatrix} \tau_{J_\parallel}\partial_t + 1 & -D_1\partial_y & D_1\partial_x & 0 \\ -D_3\partial_y & \tau_{Jxx}\partial_t + 1 & 0 & D_5\partial_x \\ D_3\partial_x & 0 & \tau_{Jxy}\partial_t + 1 & D_5\partial_y \\ 0 & -D_2^z\partial_x & -D_2^z\partial_y & \tau_{J_\perp}\partial_t + 1 \end{pmatrix}, \tag{B.4}$$

$$H_{23}^D = \begin{pmatrix} 0 & D_2\partial_x & D_2\partial_y & -\beta_{\omega\mathrm{IsH}}\partial_t + \beta_{\mathrm{IsH}} \\ -D_4\partial_x & 0 & \beta_{\omega\mathrm{SW}}^{xx}\partial_t - \beta_{\mathrm{SW}}^{xx} & D_6\partial_y \\ -D_4\partial_y & -\beta_{\omega\mathrm{SW}}^{xx}\partial_t + \beta_{\mathrm{SW}}^{xy} & 0 & -D_6\partial_x \\ -\beta_{\omega\mathrm{sH}}\partial_t + \beta_{\mathrm{sH}} & D_1^z\partial_y & -D_1^z\partial_x & 0 \end{pmatrix}, \tag{B.5}$$

$$H_{13}^{D} = \begin{pmatrix} D\partial_y & -\alpha_{\mathrm{IASP}} & 0 & 0 \\ 0 & D_{xy}\partial_y & 0 & 0 \\ 0 & 0 & D_{xx}\partial_y & -\alpha_{\mathrm{zR}} \\ 0 & 0 & \alpha_{\mathrm{xyR}} & D_z\partial_y \end{pmatrix} \tag{B.6}$$

$$H_{32}^{D} = \begin{pmatrix} 0 & -D_2\partial_x & -D_2\partial_y & \beta_{\omega\mathrm{IsH}}\partial_t - \beta_{\mathrm{IsH}} \\ D_4\partial_x & 0 & -\beta_{\omega\mathrm{SW}}^{xx}\partial_t + \beta_{\mathrm{SW}}^{xy} & -D_6\partial_y \\ D_4\partial_y & \beta_{\omega\mathrm{SW}}^{xx}\partial_t - \beta_{\mathrm{SW}}^{xx} & 0 & D_6\partial_x \\ \beta_{\omega\mathrm{sH}}\partial_t - \beta_{Sh} & -D_1^z\partial_x & D_1^z\partial_x & 0 \end{pmatrix}, \tag{B.7}$$

$$H_{33}^{D} = \begin{pmatrix} \tau_{J_\parallel}\partial_t + 1 & -D_1\partial_y & D_1\partial_x & 0 \\ -D_3\partial_y & \tau_{Jxy}\partial_t + 1 & 0 & D_5\partial_x \\ D_3\partial_x & 0 & \tau_{Jxx}\partial_t + 1 & D_5\partial_y \\ 0 & -D_2^z\partial_x & -D_2^z\partial_y & \tau_{J_\perp}\partial_t + 1 \end{pmatrix}, \tag{B.8}$$

where $\mathbb{I}$ denotes the 4×4 idensity matrix.

Appendix C

Spin-orbit torque decomposition in 2DEGs and TIs

This section provides a simple derivation for the SOT decomposition in two-dimensional gases and topological insulators, i.e., Eqs.(7.4) and (7.5). To begin with, we derive the symmetry properties of the $\hat{K}$-tensor, Eq.(7.3), following the procedure in Ref. [75]. The density-current response function has the form

$$K_{ij} \sim \int d\mathbf{p}\, tr\{s_\alpha G[\mathbf{p}] v_j[\mathbf{p}] G[\mathbf{p}]\}, \tag{C.1}$$

where v_j is the velocity operator. The GFs depend on the system's Hamltonian, which in the 2DEG(TI) case takes the form

$$H_{\text{2DEG(TI)}} = \left(\frac{p^2}{2m}\right)_{\text{2DEG}} + \alpha\left(p_y s_x - p_x s_y\right) + \Delta_{\text{xc}}\left(m_x s_x + m_z s_z\right), \tag{C.2}$$

where the first term is present only in the 2DEG case but absent in TIs, and we chose the reference frame's x-axis as the projection of the magnetization on the 2D plane. The corresponding velocity operator is

$$\mathbf{v} = \left(\frac{\mathbf{p}}{m}\right)_{\text{2DEG}} + \alpha\, \mathbf{e}_z \times \mathbf{s}. \tag{C.3}$$

The idea is now to find symmetry transformations able to convert $\hat{K}(\mathbf{m}) \to \hat{K}(-\mathbf{m})$, and deduct whether a given entry of the response function is even or odd in the magnetization. Since only the Hamiltonian, thus the GFs, depend on the magnetization, the chosen transformations are

$$s_x H_{\text{2DEG(TI)}}[-p_x, m_z] s_x = H_{\text{2DEG(TI)}}[p_x, -m_z], \tag{C.4a}$$
$$s_z H_{\text{2DEG(TI)}}[-\mathbf{p}, m_x] s_z = H_{\text{2DEG(TI)}}[\mathbf{p}, -m_x]. \tag{C.4b}$$

The next step is to change the momentum variable in the integral, Eq.(C.1), and insert the symmetry operators:

$$K_{ij} \to K_{ij}[-m_{z(x)}] \sim \int d\mathbf{p}\, tr\{s_{x(z)} s_\alpha s_{x(z)} G[-p_x(-\mathbf{p})] s_{x(z)} v_j[-p_x(-\mathbf{p})] s_{x(z)} G[-p_x(-\mathbf{p})] s_{x(z)}\}, \tag{C.5}$$

where we used that $\int_A^B dp \to \int_B^A d(-p) = \int_A^B dp$. We than need to establish the transformations for the velocity operator, which simply are

$$s_x v_x[-p_x] s_x = -v_x[p_x], \tag{C.6a}$$
$$s_x v_y[-p_x] s_x = -v_y[p_x], \tag{C.6b}$$
$$s_z \mathbf{v}[-\mathbf{p}] s_z = -\mathbf{v}[\mathbf{p}]. \tag{C.6c}$$
$$\tag{C.6d}$$

For illustrative porpoises, we analyze the collinear component of the $\hat{K}$-tensor, κ_{xx}. We apply the transformation in Eq.(C.4a) to establish the parity of this term with respect to the magnetization component m_z. We obtain

$$K_{xx}[m_z] = \int d\mathbf{p}\, tr\{s_x G[-m_z](-v_x) G[-m_z]\} = -K_{xx}[-m_z], \tag{C.7}$$

where in the first passage we applied the transformation which leave the trace invariant. This relation shows that by changing the sign of the out-of-plane magnetization, also the response changes sign and thus it is odd in m_z, i.e., $K_{xx} = m_z \kappa_{xx}$. Applying the same procedure to all the components of the density-current response function, we obtain the result in Eq.(7.3)

We are now ready to derive the convenient decomposition of the SOT illustrated in Eq.(7.4). From Eqs.(7.1), (7.2), and (7.3), the even (FL) components of the SOT are

$$\begin{cases} T_x^o = \frac{\Delta_{\mathrm{xc}}\gamma}{t\, M_s} m_z \kappa_{yx} E_x \\ T_y^o = \frac{\Delta_{\mathrm{xc}}\gamma}{t\, M_s} (m_x^2 m_z \kappa_{zy} - \kappa_{xy} m_z) E_y \\ T_z^o = -\frac{\Delta_{\mathrm{xc}}\gamma}{t\, M_s} m_x \kappa_{yx} E_x \end{cases}, \tag{C.8}$$

and the odd (DL) contribution is

$$\begin{cases} T_x^{\mathrm{e}} = \frac{\Delta_{\mathrm{xc}}\gamma}{t\, M_s} m_z^2 \kappa_{yy} E_y \\ T_y^{\mathrm{e}} = \frac{\Delta_{\mathrm{xc}}\gamma}{t\, M_s} (m_x^2 (\kappa_{zx} + \kappa_{xx}) - \kappa_{xx}) E_x \\ T_z^{\mathrm{e}} = -\frac{\Delta_{\mathrm{xc}}\gamma}{t\, M_s} m_x m_z \kappa_{yy} E_y \end{cases}. \tag{C.9}$$

By focusing on Eq.(C.8) first, we notice that

$$\mathbf{m} \times (\mathbf{e}_z \times \mathbf{E}) = \begin{pmatrix} -E_x m_z \\ -E_y m_z \\ E_x m_x \end{pmatrix}, \tag{C.10a}$$
$$\mathbf{m} \times (\mathbf{m} \times \mathbf{e}_z)(\mathbf{m} \cdot \mathbf{E}) = \begin{pmatrix} m_x m_z \\ 0 \\ -m_x^2 \end{pmatrix} m_x E_x, \tag{C.10b}$$

leading to Eq.(7.4b). On the other hand, the damping-like contribution produces terms

of the form

$$\mathbf{m} \times (\mathbf{m} \times (\mathbf{e}_z \times \mathbf{E})) = \begin{pmatrix} m_z^2 E_y \\ -E_x \\ -m_x m_z E_y \end{pmatrix} \tag{C.11a}$$

$$(\mathbf{m} \times \mathbf{e}_z)\mathbf{m} \cdot \mathbf{E} = \begin{pmatrix} 0 \\ -m_x^2 \\ 0 \end{pmatrix} E_x, \tag{C.11b}$$

that simply yields Eq.(7.4a). We notice that the result shown in this section does not agree with Ref. [75] even though their final result for the density-current response remains unaffected since most entries are zero.

Bibliography

[1] K. C. Chun, H. Zhao, J. D. Harms, T.-H. Kim, J.-P. Wang, and C. H. Kim, "A Scaling Roadmap and Performance Evaluation of In-Plane and Perpendicular MTJ Based STT-MRAMs for High-Density Cache Memory," *IEEE Journal of Solid-State Circuits*, vol. 48, pp. 598–610, Feb. 2013. Conference Name: IEEE Journal of Solid-State Circuits.

[2] H. Liu, D. Bedau, D. Backes, J. A. Katine, J. Langer, and A. D. Kent, "Ultrafast switching in magnetic tunnel junction based orthogonal spin transfer devices," *Applied Physics Letters*, vol. 97, p. 242510, Dec. 2010. Publisher: American Institute of Physics.

[3] N. Locatelli, V. Cros, and J. Grollier, "Spin-torque building blocks," *Nature materials*, vol. 13, pp. 11–20, Dec. 2013.

[4] G. Binasch, P. Grünberg, F. Saurenbach, and W. Zinn, "Enhanced magnetoresistance in layered magnetic structures with antiferromagnetic interlayer exchange," *Physical Review B*, vol. 39, pp. 4828–4830, Mar. 1989. Publisher: American Physical Society.

[5] F. Meier and B. P. Zakharchenia, *Optical orientation*. Amsterdam; New York; New York: North-Holland ; Sole distributors for the U.S.A. and Canada, Elsevier Science Pub. Co., 1984. OCLC: 10925249.

[6] R. J. Elliott, "Theory of the Effect of Spin-Orbit Coupling on Magnetic Resonance in Some Semiconductors," *Physical Review*, vol. 96, pp. 266–279, Oct. 1954. Publisher: American Physical Society.

[7] M. I. Dyakonov and V. I. Perel, "Current-induced spin orientation of electrons in semiconductors," *Physics Letters A*, vol. 35, pp. 459–460, July 1971. ADS Bibcode: 1971PhLA...35..459D.

[8] M. Offidani and A. Ferreira, "Anomalous Hall Effect in 2D Dirac Materials," *Physical Review Letters*, vol. 121, p. 126802, Sept. 2018. Publisher: American Physical Society.

[9] Y. K. Kato, R. C. Myers, A. C. Gossard, and D. D. Awschalom, "Current-Induced Spin Polarization in Strained Semiconductors," *Physical Review Letters*, vol. 93, p. 176601, Oct. 2004. Publisher: American Physical Society.

[10] A. Y. Silov, P. A. Blajnov, J. H. Wolter, R. Hey, K. H. Ploog, and N. S. Averkiev, "Current-induced spin polarization at a single heterojunction," *Applied Physics Letters*, vol. 85, pp. 5929–5931, Dec. 2004. Publisher: American Institute of Physics.

[11] V. Sih, R. C. Myers, Y. K. Kato, W. H. Lau, A. C. Gossard, and D. D. Awschalom, "Spatial imaging of the spin Hall effect and current-induced polarization in two-dimensional electron gases," *Nature Physics*, vol. 1, pp. 31–35, Oct. 2005. Bandiera_abtest: a Cg_type: Nature Research Journals Number: 1 Primary_atype: Research Publisher: Nature Publishing Group.

[12] R. H. Silsbee, "Spin–orbit induced coupling of charge current and spin polarization," *Journal of Physics: Condensed Matter*, vol. 16, pp. R179–R207, Feb. 2004. Publisher: IOP Publishing.

[13] J. E. Hirsch, "Spin Hall Effect," *Physical Review Letters*, vol. 83, no. 9, pp. 1834–1837, 1999. Publisher: American Physical Society.

[14] J. Sinova, D. Culcer, Q. Niu, N. A. Sinitsyn, T. Jungwirth, and A. H. MacDonald, "Universal Intrinsic Spin Hall Effect," *Physical Review Letters*, vol. 92, p. 126603, Mar. 2004. Publisher: American Physical Society.

[15] J. Wunderlich, B. Kaestner, J. Sinova, and T. Jungwirth, "Experimental Observation of the Spin-Hall Effect in a Two-Dimensional Spin-Orbit Coupled Semiconductor System," *Physical Review Letters*, vol. 94, p. 047204, Feb. 2005. Publisher: American Physical Society.

[16] D. Xiao, M.-C. Chang, and Q. Niu, "Berry phase effects on electronic properties," *Reviews of Modern Physics*, vol. 82, pp. 1959–2007, July 2010.

[17] V. M. Edelstein, "Spin polarization of conduction electrons induced by electric current in two-dimensional asymmetric electron systems," *Solid State Communications*, vol. 73, pp. 233–235, Jan. 1990.

[18] L. D. Landau and E. M. Lifshitz, *Quantum Mechanics: Non-Relativistic Theory: 3*. Singapore: Butterworth-Heinemann, 3rd edition ed., Jan. 1981.

[19] M. Milletarì and A. Ferreira, "Quantum diagrammatic theory of the extrinsic spin Hall effect in graphene," *Physical Review B*, vol. 94, p. 134202, Oct. 2016. Publisher: American Physical Society.

[20] F. Sousa, G. Tatara, and A. Ferreira, "Skew-scattering-induced giant antidamping spin-orbit torques: Collinear and out-of-plane Edelstein effects at two-dimensional material/ferromagnet interfaces," *Physical Review Research*, vol. 2, p. 043401, Dec. 2020. Publisher: American Physical Society.

[21] M. Dyakonov, *Spin Physics in Semiconductors*, vol. 1. July 2008. Journal Abbreviation: Spin Physics in Semiconductors Publication Title: Spin Physics in Semiconductors.

[22] J. C. R. Sánchez, L. Vila, G. Desfonds, S. Gambarelli, J. P. Attané, J. M. De Teresa, C. Magén, and A. Fert, "Spin-to-charge conversion using Rashba coupling at the interface between non-magnetic materials," *Nature Communications*, vol. 4, p. 2944, Dec. 2013. Publisher: Nature Publishing Group.

[23] C. R. Ast, J. Henk, A. Ernst, L. Moreschini, M. C. Falub, D. Pacilé, P. Bruno, K. Kern, and M. Grioni, "Giant Spin Splitting through Surface Alloying," *Physical Review Letters*, vol. 98, no. 18, p. 186807, 2007. Publisher: American Physical Society.

[24] Y. M. Koroteev, G. Bihlmayer, J. E. Gayone, E. V. Chulkov, S. Blügel, P. M. Echenique, and P. Hofmann, "Strong Spin-Orbit Splitting on Bi Surfaces," *Physical Review Letters*, vol. 93, no. 4, p. 046403, 2004. Publisher: American Physical Society.

[25] M. Morota, Y. Niimi, K. Ohnishi, D. H. Wei, T. Tanaka, H. Kontani, T. Kimura, and Y. Otani, "Indication of intrinsic spin Hall effect in 4d and 5d transition metals," *Physical Review B*, vol. 83, p. 174405, May 2011. Publisher: American Physical Society.

[26] L. Liu, C.-F. Pai, Y. Li, H. W. Tseng, D. C. Ralph, and R. A. Buhrman, "Spin-Torque Switching with the Giant Spin Hall Effect of Tantalum," *Science*, vol. 336, pp. 555–558, May 2012. Publisher: American Association for the Advancement of Science.

[27] H. Wang, J. Kally, J. S. Lee, T. Liu, H. Chang, D. R. Hickey, K. A. Mkhoyan, M. Wu, A. Richardella, and N. Samarth, "Surface-State-Dominated Spin-Charge Current Conversion in Topological-Insulator–Ferromagnetic-Insulator Heterostructures," *Physical Review Letters*, vol. 117, no. 7, p. 076601, 2016. Publisher: American Physical Society.

[28] M. V. Kamalakar, C. Groenveld, A. Dankert, and S. P. Dash, "Long distance spin communication in chemical vapour deposited graphene," *Nature Communications*, vol. 6, p. 6766, Apr. 2015. Applied physics;Graphene;Spintronics applied-physics;graphene;spintronics.

[29] W. Yan, L. C. Phillips, M. Barbone, S. J. Hämäläinen, A. Lombardo, M. Ghidini, X. Moya, F. Maccherozzi, S. van Dijken, S. S. Dhesi, A. C. Ferrari, and N. D. Mathur, "Long Spin Diffusion Length in Few-Layer Graphene Flakes," *Physical Review Letters*, vol. 117, no. 14, p. 147201, 2016. Publisher: American Physical Society.

[30] Z. M. Gebeyehu, S. Parui, J. F. Sierra, M. Timmermans, M. J. Esplandiu, S. Brems, C. Huyghebaert, K. Garello, M. V. Costache, and S. O. Valenzuela, "Spin communication over 30 μm long channels of chemical vapor deposited graphene on SiO 2," *2D Materials*, vol. 6, p. 034003, May 2019. Publisher: IOP Publishing.

[31] A. Ferreira, T. G. Rappoport, M. A. Cazalilla, and A. H. Castro Neto, "Extrinsic Spin Hall Effect Induced by Resonant Skew Scattering in Graphene," *Physical Review Letters*, vol. 112, p. 066601, Feb. 2014. Publisher: American Physical Society.

[32] J. Balakrishnan, G. K. W. Koon, A. Avsar, Y. Ho, J. H. Lee, M. Jaiswal, S.-J. Baeck, J.-H. Ahn, A. Ferreira, M. A. Cazalilla, A. H. C. Neto, and B. Özyilmaz, "Giant spin Hall effect in graphene grown by chemical vapour deposition," *Nature Communications*, vol. 5, p. 4748, Sept. 2014. Publisher: Nature Publishing Group.

[33] M. Gmitra, D. Kochan, P. Högl, and J. Fabian, "Trivial and inverted Dirac bands and the emergence of quantum spin Hall states in graphene on transition-metal dichalcogenides," *Physical Review B*, vol. 93, p. 155104, Apr. 2016. Publisher: American Physical Society.

[34] J. O. Island, X. Cui, C. Lewandowski, J. Y. Khoo, E. M. Spanton, H. Zhou, D. Rhodes, J. C. Hone, T. Taniguchi, K. Watanabe, L. S. Levitov, M. P. Zaletel, and A. F. Young, "Spin–orbit-driven band inversion in bilayer graphene by the van der Waals proximity effect," *Nature*, vol. 571, pp. 85–89, July 2019. Publisher: Nature Publishing Group.

[35] A. Ferreira, "Theory of spin–charge-coupled transport in proximitized graphene: an SO(5) algebraic approach," *Journal of Physics: Materials*, vol. 4, p. 045006, Oct. 2021. Publisher: IOP Publishing.

[36] M. Milletarì, M. Offidani, A. Ferreira, and R. Raimondi, "Covariant Conservation Laws and the Spin Hall Effect in Dirac-Rashba Systems," *Physical Review Letters*, vol. 119, p. 246801, Dec. 2017. Publisher: American Physical Society.

[37] M. Offidani, M. Milletarì, R. Raimondi, and A. Ferreira, "Optimal Charge-to-Spin Conversion in Graphene on Transition-Metal Dichalcogenides," *Physical Review Letters*, vol. 119, p. 196801, Nov. 2017. Publisher: American Physical Society.

[38] C. Huang, Y. D. Chong, and M. A. Cazalilla, "Direct coupling between charge current and spin polarization by extrinsic mechanisms in graphene," *Physical Review B*, vol. 94, p. 085414, Aug. 2016. Publisher: American Physical Society.

[39] B. H. Bransden and C. J. Joachain, *Physics of Atoms and Molecules*. Harlow, England ; New York: Pearson, 2nd edition ed., Apr. 2003.

[40] Y. A. Bychkov and É. I. Rashba, "Properties of a 2D electron gas with lifted spectral degeneracy," *Soviet Journal of Experimental and Theoretical Physics Letters*, vol. 39, p. 78, Jan. 1984. ADS Bibcode: 1984JETPL..39...78B.

[41] D. Kochan, S. Irmer, and J. Fabian, "Model spin-orbit coupling Hamiltonians for graphene systems," *Physical Review B*, vol. 95, p. 165415, Apr. 2017. Publisher: American Physical Society.

[42] G. P. Fisher, "The Thomas Precession," *American Journal of Physics*, vol. 40, pp. 1772–1781, Dec. 1972. Publisher: American Association of Physics Teachers.

[43] P. Pfeffer and W. Zawadzki, "Conduction electrons in GaAs: Five-level $\mathbf{k} \cdot \mathbf{p}$ theory and polaron effects," *Physical Review B*, vol. 41, pp. 1561–1576, Jan. 1990. Publisher: American Physical Society.

[44] H. Mayer and U. Rössler, "Spin splitting and anisotropy of cyclotron resonance in the conduction band of GaAs," *Physical Review B*, vol. 44, pp. 9048–9051, Oct. 1991. Publisher: American Physical Society.

[45] C. L. Kane and E. J. Mele, "Quantum Spin Hall Effect in Graphene," *Physical Review Letters*, vol. 95, p. 226801, Nov. 2005. Publisher: American Physical Society.

[46] D. Huertas-Hernando, F. Guinea, and A. Brataas, "Spin-orbit coupling in curved graphene, fullerenes, nanotubes, and nanotube caps," *Physical Review B*, vol. 74, p. 155426, Oct. 2006. Publisher: American Physical Society.

[47] C. L. Kane and E. J. Mele, "$\mathcal{Z}_2$ Topological Order and the Quantum Spin Hall Effect," *Physical Review Letters*, vol. 95, p. 146802, Sept. 2005. Publisher: American Physical Society.

[48] L. Tian, Y. Liu, W. Meng, X. Zhang, X. Dai, and G. Liu, "Spin–Orbit Coupling-Determined Topological Phase: Topological Insulator and Quadratic Dirac Semimetals," *The Journal of Physical Chemistry Letters*, vol. 11, pp. 10340–10347, Dec. 2020. Publisher: American Chemical Society.

[49] H. Zhang, C.-X. Liu, X.-L. Qi, X. Dai, Z. Fang, and S.-C. Zhang, "Topological insulators in Bi2Se3, Bi2Te3 and Sb2Te3 with a single Dirac cone on the surface," *Nature Physics*, vol. 5, pp. 438–442, June 2009. Number: 6 Publisher: Nature Publishing Group.

[50] G. Dresselhaus, "Spin-Orbit Coupling Effects in Zinc Blende Structures," *Physical Review*, vol. 100, pp. 580–586, Oct. 1955. Publisher: American Physical Society.

[51] M. Offidani and A. Ferreira, "Microscopic theory of spin relaxation anisotropy in graphene with proximity-induced spin-orbit coupling," *Physical Review B*, vol. 98, p. 245408, Dec. 2018. Publisher: American Physical Society.

[52] M. Offidani, R. Raimondi, and A. Ferreira, "Microscopic Linear Response Theory of Spin Relaxation and Relativistic Transport Phenomena in Graphene," *Condensed Matter*, vol. 3, p. 18, June 2018. Number: 2 Publisher: Multidisciplinary Digital Publishing Institute.

[53] C. Weeks, J. Hu, J. Alicea, M. Franz, and R. Wu, "Engineering a Robust Quantum Spin Hall State in Graphene via Adatom Deposition," *Physical Review X*, vol. 1, p. 021001, Oct. 2011. Publisher: American Physical Society.

[54] A. Pályi, C. Péterfalvi, and J. Cserti, "Two-dimensional electron scattering in regions of nonuniform spin-orbit coupling," *Physical Review B*, vol. 74, p. 073305, Aug. 2006. Publisher: American Physical Society.

[55] X. Xu, W. Yao, D. Xiao, and T. F. Heinz, "Spin and pseudospins in layered transition metal dichalcogenides," *Nature Physics*, vol. 10, pp. 343–350, May 2014. Number: 5 Publisher: Nature Publishing Group.

[56] D. L. Huffaker, G. Park, Z. Zou, O. B. Shchekin, and D. G. Deppe, "1.3 μm room-temperature GaAs-based quantum-dot laser," *Applied Physics Letters*, vol. 73, pp. 2564–2566, Nov. 1998. Publisher: American Institute of Physics.

[57] S. Iijima, "Helical microtubules of graphitic carbon," *Nature*, vol. 354, pp. 56–58, Nov. 1991. Number: 6348 Publisher: Nature Publishing Group.

[58] A. J. Huh and Y. J. Kwon, ""Nanoantibiotics": a new paradigm for treating infectious diseases using nanomaterials in the antibiotics resistant era," *Journal of Controlled Release: Official Journal of the Controlled Release Society*, vol. 156, pp. 128–145, Dec. 2011.

[59] A. Schindler, J. Brill, N. Fruehauf, J. P. Novak, and Z. Yaniv, "Solution-deposited carbon nanotube layers for flexible display applications," *Physica E: Low-dimensional Systems and Nanostructures*, vol. 1-2, no. 37, pp. 119–123, 2007.

[60] J. E. Moore, "The birth of topological insulators," *Nature*, vol. 464, pp. 194–198, Mar. 2010. Number: 7286 Publisher: Nature Publishing Group.

[61] M. Z. Hasan and J. E. Moore, "Three-Dimensional Topological Insulators," *Annual Review of Condensed Matter Physics*, vol. 2, pp. 55–78, Mar. 2011.

[62] A. A. Burkov and D. G. Hawthorn, "Spin and Charge Transport on the Surface of a Topological Insulator," *Physical Review Letters*, vol. 105, p. 066802, Aug. 2010. Publisher: American Physical Society.

[63] N. D. Mermin, "Crystalline Order in Two Dimensions," *Physical Review*, vol. 176, pp. 250–254, Dec. 1968. Publisher: American Physical Society.

[64] K. S. Novoselov, A. K. Geim, S. V. Morozov, D. Jiang, Y. Zhang, S. V. Dubonos, I. V. Grigorieva, and A. A. Firsov, "Electric Field Effect in Atomically Thin Carbon Films," *Science*, vol. 306, pp. 666–669, Oct. 2004. Publisher: American Association for the Advancement of Science.

[65] M. I. Katsnelson, "Graphene: carbon in two dimensions," *Materials Today*, vol. 10, pp. 20–27, Jan. 2007.

[66] J. N. Coleman, M. Lotya, A. O'Neill, S. D. Bergin, P. J. King, U. Khan, K. Young, A. Gaucher, S. De, R. J. Smith, I. V. Shvets, S. K. Arora, G. Stanton, H.-Y. Kim, K. Lee, G. T. Kim, G. S. Duesberg, T. Hallam, J. J. Boland, J. J. Wang, J. F. Donegan, J. C. Grunlan, G. Moriarty, A. Shmeliov, R. J. Nicholls, J. M. Perkins,

E. M. Grieveson, K. Theuwissen, D. W. McComb, P. D. Nellist, and V. Nicolosi, "Two-Dimensional Nanosheets Produced by Liquid Exfoliation of Layered Materials," *Science*, vol. 331, pp. 568–571, Feb. 2011. Publisher: American Association for the Advancement of Science.

[67] P. Miró, M. Audiffred, and T. Heine, "An atlas of two-dimensional materials," *Chemical Society Reviews*, vol. 43, pp. 6537–6554, Aug. 2014. Publisher: The Royal Society of Chemistry.

[68] R. Mas-Ballesté, C. Gómez-Navarro, J. Gómez-Herrero, and F. Zamora, "2D materials: to graphene and beyond," *Nanoscale*, vol. 3, pp. 20–30, Jan. 2011. Publisher: The Royal Society of Chemistry.

[69] A. K. Geim and K. S. Novoselov, "The rise of graphene," *Nature Materials*, vol. 6, pp. 183–191, Mar. 2007. Number: 3 Publisher: Nature Publishing Group.

[70] A. H. Castro Neto, F. Guinea, N. M. R. Peres, K. S. Novoselov, and A. K. Geim, "The electronic properties of graphene," *Reviews of Modern Physics*, vol. 81, pp. 109–162, Jan. 2009. Publisher: American Physical Society.

[71] S. Konschuh, M. Gmitra, and J. Fabian, "Tight-binding theory of the spin-orbit coupling in graphene," *Physical Review B*, vol. 82, p. 245412, Dec. 2010. Publisher: American Physical Society.

[72] Y. A. Bychkov and E. I. Rashba, "Oscillatory effects and the magnetic susceptibility of carriers in inversion layers," *Journal of Physics C: Solid State Physics*, vol. 17, pp. 6039–6045, Nov. 1984.

[73] D. Stein, K. v. Klitzing, and G. Weimann, "Electron Spin Resonance on GaAs − $Al_xGa_{1-x}As$ Heterostructures," *Physical Review Letters*, vol. 51, pp. 130–133, July 1983. Publisher: American Physical Society.

[74] H. L. Stormer, Z. Schlesinger, A. Chang, D. C. Tsui, A. C. Gossard, and W. Wiegmann, "Energy Structure and Quantized Hall Effect of Two-Dimensional Holes," *Physical Review Letters*, vol. 51, pp. 126–129, July 1983. Publisher: American Physical Society.

[75] I. A. Ado, O. A. Tretiakov, and M. Titov, "Microscopic theory of spin-orbit torques in two dimensions," *Physical Review B*, vol. 95, p. 094401, Mar. 2017. Publisher: American Physical Society.

[76] L. L. Tao and E. Y. Tsymbal, "Persistent spin texture enforced by symmetry," *Nature Communications*, vol. 9, p. 2763, July 2018. Number: 1 Publisher: Nature Publishing Group.

[77] C. G. Péterfalvi, A. David, P. Rakyta, G. Burkard, and A. Kormányos, "Quantum interference tuning of spin-orbit coupling in twisted van der Waals trilayers," Tech. Rep. arXiv:2111.02781, arXiv, Mar. 2022.

[78] B. A. Lippmann and J. Schwinger, "Variational Principles for Scattering Processes. I," *Physical Review*, vol. 79, pp. 469–480, Aug. 1950. Publisher: American Physical Society.

[79] M. Born, "Quantenmechanik der Stoßvorgänge," *Zeitschrift fur Physik*, vol. 38, pp. 803–827, Nov. 1926. ADS Bibcode: 1926ZPhy...38..803B.

[80] A. Ferreira, J. Viana-Gomes, J. Nilsson, E. R. Mucciolo, N. M. R. Peres, and A. H. Castro Neto, "Unified description of the dc conductivity of monolayer and bilayer graphene at finite densities based on resonant scatterers," *Physical Review B*, vol. 83, p. 165402, Apr. 2011. Publisher: American Physical Society.

[81] C. Gorini, A. Maleki Sheikhabadi, K. Shen, I. V. Tokatly, G. Vignale, and R. Raimondi, "Theory of current-induced spin polarization in an electron gas," *Physical Review B*, vol. 95, p. 205424, May 2017. Publisher: American Physical Society.

[82] E. L. Ivchenko and G. E. Pikus, "New photogalvanic effect in gyrotropic crystals," *Soviet Journal of Experimental and Theoretical Physics Letters*, vol. 27, p. 604, June 1978. ADS Bibcode: 1978JETPL..27..604I.

[83] O. Rousseau, C. Gorini, F. Ibrahim, J.-Y. Chauleau, A. Solignac, A. Hallal, S. Tölle, M. Chshiev, and M. Viret, "Spin-charge conversion in ferromagnetic Rashba states," *Physical Review B*, vol. 104, p. 134438, Oct. 2021. Publisher: American Physical Society.

[84] A. Veneri, D. T. S. Perkins, and A. Ferreira, "Nonperturbative approach to interfacial spin-orbit torques induced by Rashba effect," Aug. 2022. arXiv:2208.07296 [cond-mat].

[85] E. Lesne, Y. Fu, S. Oyarzun, J. C. Rojas-Sánchez, D. C. Vaz, H. Naganuma, G. Sicoli, J.-P. Attané, M. Jamet, E. Jacquet, J.-M. George, A. Barthélémy, H. Jaffrès, A. Fert, M. Bibes, and L. Vila, "Highly efficient and tunable spin-to-charge conversion through Rashba coupling at oxide interfaces," *Nature Materials*, vol. 15, pp. 1261–1266, Dec. 2016.

[86] J.-C. Rojas-Sánchez, S. Oyarzún, Y. Fu, A. Marty, C. Vergnaud, S. Gambarelli, L. Vila, M. Jamet, Y. Ohtsubo, A. Taleb-Ibrahimi, P. Le Fèvre, F. Bertran, N. Reyren, J.-M. George, and A. Fert, "Spin to Charge Conversion at Room Temperature by Spin Pumping into a New Type of Topological Insulator: $\ensuremath{\alpha}$-Sn Films," *Physical Review Letters*, vol. 116, p. 096602, Mar. 2016. Publisher: American Physical Society.

[87] Y. Tserkovnyak, A. Brataas, and G. E. W. Bauer, "Enhanced Gilbert Damping in Thin Ferromagnetic Films," *Physical Review Letters*, vol. 88, p. 117601, Feb. 2002. Publisher: American Physical Society.

[88] G. Y. Luo, J. G. Lin, W.-C. Chiang, and C.-R. Chang, "Spin pump and probe in lanthanum strontium manganite/platinum bilayers," *Scientific Reports*, vol. 7, p. 6612, July 2017. Number: 1 Publisher: Nature Publishing Group.

[89] K. Shen, G. Vignale, and R. Raimondi, "Microscopic Theory of the Inverse Edelstein Effect," *Physical Review Letters*, vol. 112, p. 096601, Mar. 2014. Publisher: American Physical Society.

[90] C. Gorini, P. Schwab, R. Raimondi, and A. L. Shelankov, "Non-Abelian gauge fields in the gradient expansion: Generalized Boltzmann and Eilenberger equations," *Physical Review B*, vol. 82, p. 195316, Nov. 2010. Publisher: American Physical Society.

[91] C. Gorini, R. Raimondi, and P. Schwab, "Onsager Relations in a Two-Dimensional Electron Gas with Spin-Orbit Coupling," *Physical Review Letters*, vol. 109, p. 246604, Dec. 2012. Publisher: American Physical Society.

[92] \. I. Adagideli, M. Scheid, M. Wimmer, G. E. W. Bauer, and K. Richter, "Extracting current-induced spins: spin boundary conditions at narrow Hall contacts," *New Journal of Physics*, vol. 9, pp. 382–382, Oct. 2007. Publisher: IOP Publishing.

[93] I. Žutić, J. Fabian, and S. Das Sarma, "Spin-Polarized Transport in Inhomogeneous Magnetic Semiconductors: Theory of Magnetic/Nonmagnetic $p-n$ Junctions," *Physical Review Letters*, vol. 88, p. 066603, Jan. 2002. Publisher: American Physical Society.

[94] T. Kondo, J.-j. Hayafuji, and H. Munekata, "Investigation of Spin Voltaic Effect in a p–n Heterojunction," *Japanese Journal of Applied Physics*, vol. 45, p. L663, June 2006. Publisher: IOP Publishing.

[95] S. A. Cavill, C. Huang, M. Offidani, Y.-H. Lin, M. A. Cazalilla, and A. Ferreira, "Proposal for Unambiguous Electrical Detection of Spin-Charge Conversion in Lateral Spin Valves," *Physical Review Letters*, vol. 124, p. 236803, June 2020. Publisher: American Physical Society.

[96] M. Cubukcu, O. Boulle, M. Drouard, K. Garello, C. Onur Avci, I. Mihai Miron, J. Langer, B. Ocker, P. Gambardella, and G. Gaudin, "Spin-orbit torque magnetization switching of a three-terminal perpendicular magnetic tunnel junction," *Applied Physics Letters*, vol. 104, p. 042406, Jan. 2014. Publisher: American Institute of Physics.

[97] D. Pesin and A. H. MacDonald, "Spintronics and pseudospintronics in graphene and topological insulators," *Nature Materials*, vol. 11, pp. 409–416, May 2012.

[98] P. Zhang and M. W. Wu, "Electron spin diffusion and transport in graphene," *Physical Review B*, vol. 84, p. 045304, July 2011. Publisher: American Physical Society.

[99] N. Tombros, C. Jozsa, M. Popinciuc, H. T. Jonkman, and B. J. van Wees, "Electronic spin transport and spin precession in single graphene layers at room temperature," *Nature*, vol. 448, pp. 571–574, Aug. 2007. Number: 7153 Publisher: Nature Publishing Group.

[100] P. J. Zomer, M. H. D. Guimarães, N. Tombros, and B. J. van Wees, "Long-distance spin transport in high-mobility graphene on hexagonal boron nitride," *Physical Review B*, vol. 86, p. 161416, Oct. 2012. Publisher: American Physical Society.

[101] B. Dlubak, M.-B. Martin, C. Deranlot, B. Servet, S. Xavier, R. Mattana, M. Sprinkle, C. Berger, W. A. De Heer, F. Petroff, A. Anane, P. Seneor, and A. Fert, "Highly efficient spin transport in epitaxial graphene on SiC," *Nature Physics*, vol. 8, pp. 557–561, July 2012. Number: 7 Publisher: Nature Publishing Group.

[102] S. Roche and S. O. Valenzuela, "Graphene spintronics: puzzling controversies and challenges for spin manipulation," *Journal of Physics D: Applied Physics*, vol. 47, p. 094011, Feb. 2014. Publisher: IOP Publishing.

[103] H. Dery, H. Wu, B. Ciftcioglu, M. Huang, Y. Song, R. Kawakami, J. Shi, I. Krivorotov, I. Zutic, and L. J. Sham, "Nanospintronics Based on Magnetologic Gates," *IEEE Transactions on Electron Devices*, vol. 59, pp. 259–262, Jan. 2012.

[104] W. Han, K. Pi, K. M. McCreary, Y. Li, J. J. I. Wong, A. G. Swartz, and R. K. Kawakami, "Tunneling Spin Injection into Single Layer Graphene," *Physical Review Letters*, vol. 105, p. 167202, Oct. 2010. Publisher: American Physical Society.

[105] S. Sugahara and M. Tanaka, "A spin metal–oxide–semiconductor field-effect transistor using half-metallic-ferromagnet contacts for the source and drain," *Applied Physics Letters*, vol. 84, pp. 2307–2309, Mar. 2004. Publisher: American Institute of Physics.

[106] S. Ringer, M. Rosenauer, T. Völkl, M. Kadur, F. Hopperdietzel, D. Weiss, and J. Eroms, "Spin field-effect transistor action via tunable polarization of the spin injection in a Co/MgO/graphene contact," *Applied Physics Letters*, vol. 113, p. 132403, Sept. 2018. Publisher: American Institute of Physics.

[107] A. Hirohata and K. Takanashi, "Future perspectives for spintronic devices," *Journal of Physics D: Applied Physics*, vol. 47, p. 193001, Apr. 2014. Publisher: IOP Publishing.

[108] J. Schliemann, J. C. Egues, and D. Loss, "Nonballistic Spin-Field-Effect Transistor," *Physical Review Letters*, vol. 90, p. 146801, Apr. 2003. Publisher: American Physical Society.

[109] P. Blanchard and D. Volchenkov, *Random Walks and Diffusions on Graphs and Databases: An Introduction*. Berlin: Springer, 2011th edition ed., May 2011.

[110] A. Pachoud, A. Ferreira, B. Özyilmaz, and A. H. Castro Neto, "Scattering theory of spin-orbit active adatoms on graphene," *Physical Review B*, vol. 90, p. 035444, July 2014. Publisher: American Physical Society.

[111] H. Ochoa, A. H. Castro Neto, and F. Guinea, "Elliot-Yafet Mechanism in Graphene," *Physical Review Letters*, vol. 108, p. 206808, May 2012. Publisher: American Physical Society.

[112] D. Huertas-Hernando, F. Guinea, and A. Brataas, "Spin-Orbit-Mediated Spin Relaxation in Graphene," *Physical Review Letters*, vol. 103, p. 146801, Sept. 2009. Publisher: American Physical Society.

[113] I. Žutić, J. Fabian, and S. Das Sarma, "Spintronics: Fundamentals and applications," *Reviews of Modern Physics*, vol. 76, pp. 323–410, Apr. 2004. Publisher: American Physical Society.

[114] M. W. Wu, J. H. Jiang, and M. Q. Weng, "Spin dynamics in semiconductors," *Physics Reports*, vol. 493, pp. 61–236, Aug. 2010.

[115] H. J. Zhu, M. Ramsteiner, H. Kostial, M. Wassermeier, H.-P. Schönherr, and K. H. Ploog, "Room-Temperature Spin Injection from Fe into GaAs," *Physical Review Letters*, vol. 87, p. 016601, June 2001. Publisher: American Physical Society.

[116] R. Fiederling, M. Keim, G. Reuscher, W. Ossau, G. Schmidt, A. Waag, and L. W. Molenkamp, "Injection and detection of a spin-polarized current in a light-emitting diode," *Nature*, vol. 402, pp. 787–790, Dec. 1999. ADS Bibcode: 1999Natur.402..787F.

[117] Y. Ohno, D. K. Young, B. Beschoten, F. Matsukura, H. Ohno, and D. D. Awschalom, "Electrical spin injection in a ferromagnetic semiconductor heterostructure," *Nature*, vol. 402, pp. 790–792, Dec. 1999. ADS Bibcode: 1999Natur.402..790O.

[118] M. I. Miah, "Observation of the anomalous Hall effect in GaAs," *Journal of Physics D: Applied Physics*, vol. 40, pp. 1659–1663, Mar. 2007. Publisher: IOP Publishing.

[119] Y. K. Kato, R. C. Myers, A. C. Gossard, and D. D. Awschalom, "Observation of the Spin Hall Effect in Semiconductors," *Science*, vol. 306, pp. 1910–1913, Dec. 2004. Publisher: American Association for the Advancement of Science.

[120] E. Saitoh, M. Ueda, H. Miyajima, and G. Tatara, "Conversion of spin current into charge current at room temperature: Inverse spin-Hall effect," *Applied Physics Letters*, vol. 88, p. 182509, May 2006. Publisher: American Institute of Physics.

[121] S. O. Valenzuela and M. Tinkham, "Direct electronic measurement of the spin Hall effect," *Nature*, vol. 442, pp. 176–179, July 2006. Number: 7099 Publisher: Nature Publishing Group.

[122] L. Onsager, "Reciprocal Relations in Irreversible Processes. I.," *Physical Review*, vol. 37, pp. 405–426, Feb. 1931. Publisher: American Physical Society.

[123] O. Mosendz, V. Vlaminck, J. E. Pearson, F. Y. Fradin, G. E. W. Bauer, S. D. Bader, and A. Hoffmann, "Detection and quantification of inverse spin Hall effect from spin pumping in permalloy/normal metal bilayers," *Physical Review B*, vol. 82, p. 214403, Dec. 2010. Publisher: American Physical Society.

[124] K. Ando and E. Saitoh, "Observation of the inverse spin Hall effect in silicon," *Nature Communications*, vol. 3, p. 629, Jan. 2012. Number: 1 Publisher: Nature Publishing Group.

[125] L. A. Benítez, W. Savero Torres, J. F. Sierra, M. Timmermans, J. H. Garcia, S. Roche, M. V. Costache, and S. O. Valenzuela, "Tunable room-temperature spin galvanic and spin Hall effects in van der Waals heterostructures," *Nature Materials*, vol. 19, pp. 170–175, Feb. 2020. Bandiera_abtest: a Cg_type: Nature Research Journals Number: 2 Primary_atype: Research Publisher: Nature Publishing Group Subject_term: Electronic and spintronic devices;Electronic properties and devices;Spintronics;Two-dimensional materials Subject_term_id: electronic-and-spintronic-devices;electronic-properties-and-devices;spintronics;two-dimensional-materials.

[126] J. M. Luttinger and W. Kohn, "Motion of Electrons and Holes in Perturbed Periodic Fields," *Physical Review*, vol. 97, pp. 869–883, Feb. 1955. Publisher: American Physical Society.

[127] T. Jungwirth, J. Wunderlich, and K. Olejník, "Spin Hall effect devices," *Nature Materials*, vol. 11, pp. 382–390, May 2012. Number: 5 Publisher: Nature Publishing Group.

[128] M.-C. Chang and Q. Niu, "Berry phase, hyperorbits, and the Hofstadter spectrum: Semiclassical dynamics in magnetic Bloch bands," *Physical Review B*, vol. 53, pp. 7010–7023, Mar. 1996. Publisher: American Physical Society.

[129] G. Sundaram and Q. Niu, "Wave-packet dynamics in slowly perturbed crystals: Gradient corrections and Berry-phase effects," *Physical Review B*, vol. 59, pp. 14915–14925, June 1999. Publisher: American Physical Society.

[130] J. Smit, "The spontaneous hall effect in ferromagnetics II," *Physica*, vol. 24, pp. 39–51, Jan. 1958.

[131] L. Berger, "Influence of spin-orbit interaction on the transport processes in ferromagnetic nickel alloys, in the presence of a degeneracy of the 3d band," *Physica*, vol. 30, pp. 1141–1159, June 1964.

[132] K. Ando, S. Takahashi, K. Harii, K. Sasage, J. Ieda, S. Maekawa, and E. Saitoh, "Electric Manipulation of Spin Relaxation Using the Spin Hall Effect," *Physical Review Letters*, vol. 101, p. 036601, July 2008. Publisher: American Physical Society.

[133] P. Wadley, B. Howells, J. Železný, C. Andrews, V. Hills, R. P. Campion, V. Novák, K. Olejník, F. Maccherozzi, S. S. Dhesi, S. Y. Martin, T. Wagner, J. Wunderlich, F. Freimuth, Y. Mokrousov, J. Kuneš, J. S. Chauhan, M. J. Grzybowski, A. W. Rushforth, K. W. Edmonds, B. L. Gallagher, and T. Jungwirth, "Electrical switching of an antiferromagnet," *Science*, vol. 351, pp. 587–590, Feb. 2016. Publisher: American Association for the Advancement of Science.

[134] A. Brataas, A. D. Kent, and H. Ohno, "Current-induced torques in magnetic materials," *Nature Materials*, vol. 11, pp. 372–381, May 2012.

[135] G. Yu, P. Upadhyaya, Y. Fan, J. G. Alzate, W. Jiang, K. L. Wong, S. Takei, S. A. Bender, L.-T. Chang, Y. Jiang, M. Lang, J. Tang, Y. Wang, Y. Tserkovnyak, P. K. Amiri, and K. L. Wang, "Switching of perpendicular magnetization by spin–orbit torques in the absence of external magnetic fields," *Nature Nanotechnology*, vol. 9, pp. 548–554, July 2014. Bandiera_abtest: a Cg_type: Nature Research Journals Number: 7 Primary_atype: Research Publisher: Nature Publishing Group Subject_term: Spintronics Subject_term_id: spintronics.

[136] K. Garello, C. O. Avci, I. M. Miron, M. Baumgartner, A. Ghosh, S. Auffret, O. Boulle, G. Gaudin, and P. Gambardella, "Ultrafast magnetization switching by spin-orbit torques," *Applied Physics Letters*, vol. 105, p. 212402, Nov. 2014. Publisher: American Institute of Physics.

[137] D. C. Ralph and M. D. Stiles, "Spin Transfer Torques," *Journal of Magnetism and Magnetic Materials*, vol. 320, pp. 1190–1216, Apr. 2008. arXiv: 0711.4608.

[138] Y. Wang, D. Zhu, Y. Wu, Y. Yang, J. Yu, R. Ramaswamy, R. Mishra, S. Shi, M. Elyasi, K.-L. Teo, Y. Wu, and H. Yang, "Room temperature magnetization switching in topological insulator-ferromagnet heterostructures by spin-orbit torques," *Nature Communications*, vol. 8, p. 1364, Nov. 2017. Number: 1 Publisher: Nature Publishing Group.

[139] R. Ramaswamy, J. M. Lee, K. Cai, and H. Yang, "Recent advances in spin-orbit torques: Moving towards device applications," *Applied Physics Reviews*, vol. 5, p. 031107, Sept. 2018. Publisher: American Institute of Physics.

[140] K. Dolui, M. D. Petrović, K. Zollner, P. Plecháč, J. Fabian, and B. K. Nikolić, "Proximity Spin–Orbit Torque on a Two-Dimensional Magnet within van der Waals Heterostructure: Current-Driven Antiferromagnet-to-Ferromagnet Reversible Nonequilibrium Phase Transition in Bilayer CrI3," *Nano Letters*, vol. 20, pp. 2288–2295, Apr. 2020. Publisher: American Chemical Society.

[141] K. Jabeur, G. Prenat, G. Di Pendina, L. D. Buda-Prejbeanu, I. Prejbeanu, and B. Dieny, "Compact model of a three-terminal MRAM device based on Spin Orbit Torque switching," in *2013 International Semiconductor Conference Dresden - Grenoble (ISCDG)*, pp. 1–4, Sept. 2013.

[142] A. Manchon, J. Železný, I. M. Miron, T. Jungwirth, J. Sinova, A. Thiaville, K. Garello, and P. Gambardella, "Current-induced spin-orbit torques in ferromagnetic and antiferromagnetic systems," *Reviews of Modern Physics*, vol. 91, p. 035004, Sept. 2019.

[143] V. P. Amin, J. Zemen, and M. D. Stiles, "Interface-Generated Spin Currents," *Physical Review Letters*, vol. 121, p. 136805, Sept. 2018. Publisher: American Physical Society.

[144] L. Zhu, D. C. Ralph, and R. A. Buhrman, "Spin-Orbit Torques in Heavy-Metal–Ferromagnet Bilayers with Varying Strengths of Interfacial Spin-Orbit Coupling," *Physical Review Letters*, vol. 122, p. 077201, Feb. 2019. Publisher: American Physical Society.

[145] A. R. Mellnik, J. S. Lee, A. Richardella, J. L. Grab, P. J. Mintun, M. H. Fischer, A. Vaezi, A. Manchon, E.-A. Kim, N. Samarth, and D. C. Ralph, "Spin Transfer Torque Generated by the Topological Insulator Bi_2se_3," *Nature*, vol. 511, pp. 449–451, July 2014. arXiv: 1402.1124.

[146] E. J. Duplock, M. Scheffler, and P. J. D. Lindan, "Hallmark of Perfect Graphene," *Physical Review Letters*, vol. 92, p. 225502, June 2004. Publisher: American Physical Society.

[147] F. J. Jedema, A. T. Filip, and B. J. van Wees, "Electrical spin injection and accumulation at room temperature in an all-metal mesoscopic spin valve," *Nature*, vol. 410, pp. 345–348, Mar. 2001.

[148] I. Malajovich, J. M. Kikkawa, D. D. Awschalom, J. J. Berry, and N. Samarth, "Coherent Transfer of Spin through a Semiconductor Heterointerface," *Physical Review Letters*, vol. 84, no. 5, pp. 1015–1018, 2000. Publisher: American Physical Society.

[149] J. M. Kikkawa and D. D. Awschalom, "Resonant Spin Amplification in n-Type GaAs," *Physical Review Letters*, vol. 80, no. 19, pp. 4313–4316, 1998. Publisher: American Physical Society.

[150] P. R. Hammar and M. Johnson, "Detection of Spin-Polarized Electrons Injected into a Two-Dimensional Electron Gas," *Physical Review Letters*, vol. 88, no. 6, p. 066806, 2002. Publisher: American Physical Society.

[151] C. Tang, B. Cheng, M. Aldosary, Z. Wang, Z. Jiang, K. Watanabe, T. Taniguchi, M. Bockrath, and J. Shi, "Approaching quantum anomalous Hall effect in proximity-coupled YIG/graphene/h-BN sandwich structure," *APL Materials*, vol. 6, p. 026401, Feb. 2018. Publisher: American Institute of Physics.

[152] Z. Wang, C. Tang, R. Sachs, Y. Barlas, and J. Shi, "Proximity-Induced Ferromagnetism in Graphene Revealed by the Anomalous Hall Effect," *Physical Review Letters*, vol. 114, p. 016603, Jan. 2015. Publisher: American Physical Society.

[153] Y. Li and M. Koshino, "Twist-angle dependence of the proximity spin-orbit coupling in graphene on transition-metal dichalcogenides," *Physical Review B*, vol. 99, p. 075438, Feb. 2019. Publisher: American Physical Society.

[154] A. David, P. Rakyta, A. Kormányos, and G. Burkard, "Induced spin-orbit coupling in twisted graphene–transition metal dichalcogenide heterobilayers: Twistronics meets spintronics," *Physical Review B*, vol. 100, p. 085412, Aug. 2019. Publisher: American Physical Society.

[155] D. A. Abanin and D. A. Pesin, "Ordering of Magnetic Impurities and Tunable Electronic Properties of Topological Insulators," *Physical Review Letters*, vol. 106, p. 136802, Mar. 2011. Publisher: American Physical Society.

[156] J. Honolka, A. A. Khajetoorians, V. Sessi, T. O. Wehling, S. Stepanow, J.-L. Mi, B. B. Iversen, T. Schlenk, J. Wiebe, N. B. Brookes, A. I. Lichtenstein, P. Hofmann, K. Kern, and R. Wiesendanger, "In-Plane Magnetic Anisotropy of Fe Atoms on $Bi_2Se_3(111)$," *Physical Review Letters*, vol. 108, p. 256811, June 2012. Publisher: American Physical Society.

[157] G. Grosso and G. P. Parravicini, *Solid State Physics*. Elsevier, Feb. 2000. Google-Books-ID: L5RrQbbvWn8C.

[158] E. McCann, "Staying or going? Chirality decides!," *Physics*, vol. 2, p. 98, Nov. 2009.

[159] V. V. Cheianov and V. I. Fal'ko, "Selective transmission of Dirac electrons and ballistic magnetoresistance of $n\text{\ensuremath{-}}p$ junctions in graphene," *Physical Review B*, vol. 74, p. 041403, July 2006. Publisher: American Physical Society.

[160] C. W. J. Beenakker, "Colloquium: Andreev reflection and Klein tunneling in graphene," *Reviews of Modern Physics*, vol. 80, pp. 1337–1354, Oct. 2008. Publisher: American Physical Society.

[161] K. S. Novoselov, A. K. Geim, S. V. Morozov, D. Jiang, M. I. Katsnelson, I. V. Grigorieva, S. V. Dubonos, and A. A. Firsov, "Two-dimensional gas of massless Dirac fermions in graphene," *Nature*, vol. 438, pp. 197–200, Nov. 2005. Number: 7065 Publisher: Nature Publishing Group.

[162] F. D. M. Haldane, "Model for a Quantum Hall Effect without Landau Levels: Condensed-Matter Realization of the "Parity Anomaly"," *Physical Review Letters*, vol. 61, pp. 2015–2018, Oct. 1988. Publisher: American Physical Society.

[163] J.-H. Chen, W. G. Cullen, C. Jang, M. S. Fuhrer, and E. D. Williams, "Defect Scattering in Graphene," *Physical Review Letters*, vol. 102, no. 23, p. 236805, 2009. Publisher: American Physical Society.

[164] A. K. Geim and I. V. Grigorieva, "Van der Waals heterostructures," *Nature*, vol. 499, pp. 419–425, July 2013. Number: 7459 Publisher: Nature Publishing Group.

[165] C. R. Dean, A. F. Young, I. Meric, C. Lee, L. Wang, S. Sorgenfrei, K. Watanabe, T. Taniguchi, P. Kim, K. L. Shepard, and J. Hone, "Boron nitride substrates for high-quality graphene electronics," *Nature Nanotechnology*, vol. 5, pp. 722–726, Oct. 2010. Number: 10 Publisher: Nature Publishing Group.

[166] C. Huang, M. Milletarì, and M. A. Cazalilla, "Spin-charge conversion in disordered two-dimensional electron gases lacking inversion symmetry," *Physical Review B*, vol. 96, p. 205305, Nov. 2017. Publisher: American Physical Society.

[167] V. M. Edelstein, "Inverse Faraday effect in conducting crystals caused by a broken mirror symmetry," *Physica B: Condensed Matter*, vol. 284-288, pp. 1217–1218, July 2000.

[168] C.-X. Liu, X.-L. Qi, H. Zhang, X. Dai, Z. Fang, and S.-C. Zhang, "Model Hamiltonian for topological insulators," *Physical Review B*, vol. 82, p. 045122, July 2010. Publisher: American Physical Society.

[169] J. Han, A. Richardella, S. A. Siddiqui, J. Finley, N. Samarth, and L. Liu, "Room-Temperature Spin-Orbit Torque Switching Induced by a Topological Insulator," *Physical Review Letters*, vol. 119, p. 077702, Aug. 2017. Publisher: American Physical Society.

[170] D. Hsieh, D. Qian, L. Wray, Y. Xia, Y. S. Hor, R. J. Cava, and M. Z. Hasan, "A topological Dirac insulator in a quantum spin Hall phase," *Nature*, vol. 452, pp. 970–974, Apr. 2008. Number: 7190 Publisher: Nature Publishing Group.

[171] C. Di Castro and R. Raimondi, *Statistical Mechanics and Applications in Condensed Matter*. Cambridge: Cambridge University Press, 2015.

[172] D. Culcer, E. M. Hankiewicz, G. Vignale, and R. Winkler, "Side jumps in the spin Hall effect: Construction of the Boltzmann collision integral," *Physical Review B*, vol. 81, p. 125332, Mar. 2010. Publisher: American Physical Society.

[173] J. Moser, J. Ehlers, K. Hepp, H. A. Weidenmüller, and W. Beiglböck, eds., *Dynamical Systems, Theory and Applications: Battelle Seattle 1974 Rencontres*, vol. 38 of *Lecture Notes in Physics*. Berlin, Heidelberg: Springer, 1975.

[174] M. Trushin and J. Schliemann, "Anisotropic current-induced spin accumulation in the two-dimensional electron gas with spin-orbit coupling," *Physical Review B*, vol. 75, p. 155323, Apr. 2007. Publisher: American Physical Society.

[175] D. . Khaetskii, "Relaxation of nonequilibrium carrier-density matrix in semiconductors with degenerate bands," *Journal of Experimental and Theoretical Physics*, vol. 86, May 1984.

[176] N. A. Sinitsyn, A. H. MacDonald, T. Jungwirth, V. K. Dugaev, and J. Sinova, "Anomalous Hall effect in a two-dimensional Dirac band: The link between the Kubo-Streda formula and the semiclassical Boltzmann equation approach," *Physical Review B*, vol. 75, no. 4, p. 045315, 2007. Publisher: American Physical Society.

[177] M. Milletari and A. Ferreira, "Crossover to the Anomalous Quantum Regime in the Extrinsic Spin Hall Effect of Graphene," *Physical Review B*, vol. 94, p. 201402, Nov. 2016. arXiv: 1601.08076.

[178] A. Kamenev, *Field Theory of Non-Equilibrium Systems*. Cambridge ; New York: Cambridge University Press, illustrated edition ed., Sept. 2011.

[179] J. Rammer, *Quantum Field Theory of Non-equilibrium States*. Cambridge: Cambridge University Press, 2007.

[180] L. Fu, "Hexagonal Warping Effects in the Surface States of the Topological Insulator ${\mathrm{Bi}}_{2}{\mathrm{Te}}_{3}$," *Physical Review Letters*, vol. 103, p. 266801, Dec. 2009. Publisher: American Physical Society.

[181] A. Manchon and S. Zhang, "Theory of nonequilibrium intrinsic spin torque in a single nanomagnet," *Physical Review B*, vol. 78, p. 212405, Dec. 2008. Publisher: American Physical Society.

[182] N. A. Sinitsyn, Q. Niu, and A. H. MacDonald, "Coordinate shift in the semiclassical Boltzmann equation and the anomalous Hall effect," *Physical Review B*, vol. 73, p. 075318, Feb. 2006. Publisher: American Physical Society.

[183] D. Culcer and R. Winkler, "Weak momentum scattering and the conductivity of graphene," *Physical Review B*, vol. 78, p. 235417, Dec. 2008. arXiv: 0807.3051.

[184] R. Kubo, "Statistical-Mechanical Theory of Irreversible Processes. I. General Theory and Simple Applications to Magnetic and Conduction Problems," *Journal of the Physical Society of Japan*, vol. 12, pp. 570–586, June 1957. Publisher: The Physical Society of Japan.

[185] P. Streda, "Theory of quantised Hall conductivity in two dimensions," *Journal of Physics C: Solid State Physics*, vol. 15, pp. L717–L721, Aug. 1982. Publisher: IOP Publishing.

[186] V. Bonbien and A. Manchon, "Symmetrized decomposition of the Kubo-Bastin formula," *Physical Review B*, vol. 102, p. 085113, Aug. 2020. Publisher: American Physical Society.

[187] A. A. Burkov, A. S. Núñez, and A. H. MacDonald, "Theory of spin-charge-coupled transport in a two-dimensional electron gas with Rashba spin-orbit interactions," *Physical Review B*, vol. 70, p. 155308, Oct. 2004. Publisher: American Physical Society.

[188] E. I. Rashba, "Spin currents in thermodynamic equilibrium: The challenge of discerning transport currents," *Physical Review B*, vol. 68, p. 241315, Dec. 2003. Publisher: American Physical Society.

[189] J. Balakrishnan, G. Kok Wai Koon, M. Jaiswal, A. H. Castro Neto, and B. Özyilmaz, "Colossal enhancement of spin–orbit coupling in weakly hydrogenated graphene," *Nature Physics*, vol. 9, pp. 284–287, May 2013. Number: 5 Publisher: Nature Publishing Group.

[190] Z. Jia, B. Yan, J. Niu, Q. Han, R. Zhu, D. Yu, and X. Wu, "Transport study of graphene adsorbed with indium adatoms," *Physical Review B*, vol. 91, p. 085411, Feb. 2015. Publisher: American Physical Society.

[191] C. Huang, Y. D. Chong, and M. A. Cazalilla, "Anomalous Nonlocal Resistance and Spin-Charge Conversion Mechanisms in Two-Dimensional Metals," *Physical Review Letters*, vol. 119, p. 136804, Sept. 2017.

[192] O. Chalaev and D. Loss, "Spin-Hall conductivity due to Rashba spin-orbit interaction in disordered systems," *Physical Review B*, vol. 71, p. 245318, June 2005. Publisher: American Physical Society.

[193] N. S. Averkiev and L. E. Golub, "Spin relaxation anisotropy: microscopic mechanisms for 2D systems," *Semiconductor Science and Technology*, vol. 23, p. 114002, Oct. 2008. Publisher: IOP Publishing.

[194] K. Shen, R. Raimondi, and G. Vignale, "Theory of coupled spin-charge transport due to spin-orbit interaction in inhomogeneous two-dimensional electron liquids," *Physical Review B*, vol. 90, p. 245302, Dec. 2014. Publisher: American Physical Society.

[195] S. Carr, D. Massatt, S. Fang, P. Cazeaux, M. Luskin, and E. Kaxiras, "Twistronics: Manipulating the electronic properties of two-dimensional layered structures through their twist angle," *Physical Review B*, vol. 95, p. 075420, Feb. 2017. Publisher: American Physical Society.

[196] A. Veneri, D. T. S. Perkins, C. G. Péterfalvi, and A. Ferreira, "Twist angle controlled collinear Edelstein effect in van der Waals heterostructures," *Physical Review B*, vol. 106, p. L081406, Aug. 2022. Publisher: American Physical Society.

[197] S. Lee, D. J. P. de Sousa, Y.-K. Kwon, F. de Juan, Z. Chi, F. Casanova, and T. Low, "Charge-to-spin conversion in twisted $\mathrm{graphene}/{\mathrm{WSe}}_{2}$ heterostructures," *Physical Review B*, vol. 106, p. 165420, Oct. 2022. Publisher: American Physical Society.

[198] L. Li, J. Zhang, G. Myeong, W. Shin, H. Lim, B. Kim, S. Kim, T. Jin, S. Cavill, B. S. Kim, C. Kim, J. Lischner, A. Ferreira, and S. Cho, "Gate-Tunable Reversible Rashba–Edelstein Effect in a Few-Layer Graphene/2H-TaS2 Heterostructure at Room Temperature," *ACS Nano*, vol. 14, pp. 5251–5259, May 2020. Publisher: American Chemical Society.

[199] O. V. Dimitrova, "Spin-Hall conductivity in a two-dimensional Rashba electron gas," *Physical Review B*, vol. 71, p. 245327, June 2005. Publisher: American Physical Society.

[200] T. P. Cysne, A. Ferreira, and T. G. Rappoport, "Crystal-field effects in graphene with interface-induced spin-orbit coupling," *Physical Review B*, vol. 98, p. 045407, July 2018. Publisher: American Physical Society.

[201] S. Fang, R. Kuate Defo, S. N. Shirodkar, S. Lieu, G. A. Tritsaris, and E. Kaxiras, "Ab initio tight-binding Hamiltonian for transition metal dichalcogenides," *Physical Review B*, vol. 92, p. 205108, Nov. 2015. Publisher: American Physical Society.

[202] A. Uri, S. Grover, Y. Cao, J. A. Crosse, K. Bagani, D. Rodan-Legrain, Y. Myasoedov, K. Watanabe, T. Taniguchi, P. Moon, M. Koshino, P. Jarillo-Herrero, and E. Zeldov, "Mapping the twist angle and unconventional Landau levels in magic angle graphene," *Nature*, vol. 581, pp. 47–52, May 2020. arXiv: 1908.04595.

[203] I. M. Vicent, H. Ochoa, and F. Guinea, "Spin relaxation in corrugated graphene," *Physical Review B*, vol. 95, p. 195402, May 2017. Publisher: American Physical Society.

[204] J. Xu, A. Habib, S. Kumar, F. Wu, R. Sundararaman, and Y. Ping, "Spin-phonon relaxation from a universal ab initio density-matrix approach," *Nature Communications*, vol. 11, p. 2780, June 2020. Number: 1 Publisher: Nature Publishing Group.

[205] V. P. Amin, P. M. Haney, and M. D. Stiles, "Interfacial spin–orbit torques," *Journal of Applied Physics*, vol. 128, p. 151101, Oct. 2020. Publisher: American Institute of Physics.

[206] S. Zhang, "Spin Hall Effect in the Presence of Spin Diffusion," *Physical Review Letters*, vol. 85, pp. 393–396, July 2000. Publisher: American Physical Society.

[207] V. P. Amin and M. D. Stiles, "Spin transport at interfaces with spin-orbit coupling: Phenomenology," *Physical Review B*, vol. 94, p. 104420, Sept. 2016. Publisher: American Physical Society.

[208] P. B. Ndiaye, C. A. Akosa, M. H. Fischer, A. Vaezi, E.-A. Kim, and A. Manchon, "Dirac spin-orbit torques and charge pumping at the surface of topological insulators," *Physical Review B*, vol. 96, p. 014408, July 2017. Publisher: American Physical Society.

[209] J. Kim, J. Sinha, M. Hayashi, M. Yamanouchi, S. Fukami, T. Suzuki, S. Mitani, and H. Ohno, "Layer thickness dependence of the current-induced effective field vector in Ta|CoFeB|MgO," *Nature Materials*, vol. 12, pp. 240–245, Mar. 2013. Number: 3 Publisher: Nature Publishing Group.

[210] K. Garello, I. M. Miron, C. O. Avci, F. Freimuth, Y. Mokrousov, S. Blügel, S. Auffret, O. Boulle, G. Gaudin, and P. Gambardella, "Symmetry and magnitude of spin–orbit torques in ferromagnetic heterostructures," *Nature Nanotechnology*, vol. 8, pp. 587–593, Aug. 2013.

[211] T. Schlenk, M. Bianchi, M. Koleini, A. Eich, O. Pietzsch, T. O. Wehling, T. Frauenheim, A. Balatsky, J.-L. Mi, B. B. Iversen, J. Wiebe, A. A. Khajetoorians, P. Hofmann, and R. Wiesendanger, "Controllable Magnetic Doping of the Surface State of a Topological Insulator," *Physical Review Letters*, vol. 110, p. 126804, Mar. 2013. Publisher: American Physical Society.

[212] Q. Liu, C.-X. Liu, C. Xu, X.-L. Qi, and S.-C. Zhang, "Magnetic Impurities on the Surface of a Topological Insulator," *Physical Review Letters*, vol. 102, p. 156603, Apr. 2009. Publisher: American Physical Society.

[213] I. Miron, K. Garello, G. Gaudin, P.-J. Zermatten, M. Costache, S. Auffret, S. Bandiera, B. Rodmacq, A. Schuhl, and P. Gambardella, "Perpendicular Switching of a Single Ferromagnetic Layer Induced by In-Plane Current Injection," *Nature*, vol. 476, pp. 189–93, Aug. 2011.

[214] T. D. Skinner, M. Wang, A. T. Hindmarch, A. W. Rushforth, A. C. Irvine, D. Heiss, H. Kurebayashi, and A. J. Ferguson, "Spin-orbit torque opposing the Oersted torque in ultrathin Co/Pt bilayers," *Applied Physics Letters*, vol. 104, p. 062401, Feb. 2014. Publisher: American Institute of Physics.

[215] X. Wang and A. Manchon, "Diffusive spin dynamics in ferromagnetic thin films with a Rashba interaction," *Physical Review Letters*, vol. 108, p. 117201, Mar. 2012. arXiv: 1111.1216.

[216] P. M. Haney, H.-W. Lee, K.-J. Lee, A. Manchon, and M. D. Stiles, "Current induced torques and interfacial spin-orbit coupling: Semiclassical modeling," *Physical Review B*, vol. 87, p. 174411, May 2013. Publisher: American Physical Society.

[217] C. Zener, "Interaction Between the d Shells in the Transition Metals," *Physical Review*, vol. 81, pp. 440–444, Feb. 1951. Publisher: American Physical Society.

[218] V. Y. Irkhin and S. V. Streltsov, "S. Vonsovsky and the Dawn of the Theory of Strongly Correlated Systems," *Journal of Superconductivity and Novel Magnetism*, vol. 35, pp. 2135–2140, Aug. 2022.

[219] I. V. Tokatly and E. Y. Sherman, "Duality of the spin and density dynamics for two-dimensional electrons with a spin-orbit coupling," *Physical Review B*, vol. 82, p. 161305, Oct. 2010. Publisher: American Physical Society.

[220] A. R. Mellnik, J. S. Lee, A. Richardella, J. L. Grab, P. J. Mintun, M. H. Fischer, A. Vaezi, A. Manchon, E.-A. Kim, N. Samarth, and D. C. Ralph, "Spin-transfer torque generated by a topological insulator," *Nature*, vol. 511, pp. 449–451, July 2014. Number: 7510 Publisher: Nature Publishing Group.

[221] L. Liu, O. J. Lee, T. J. Gudmundsen, D. C. Ralph, and R. A. Buhrman, "Current-Induced Switching of Perpendicularly Magnetized Magnetic Layers Using Spin Torque from the Spin Hall Effect," *Physical Review Letters*, vol. 109, p. 096602, Aug. 2012. Publisher: American Physical Society.

[222] J. Rammer, *Quantum Transport Theory*. Boulder, Colo.: Westview Press, 1st edition ed., Oct. 2008.

[223] J. J. Sakurai and J. Napolitano, *Modern Quantum Mechanics*. Cambridge: Cambridge University Press, 3rd edition ed., Oct. 2020.